Titre: Title:	Analysis of Through-Thickness Injection in Liquid Composite Molding Based on Digital Material Twins
Auteur: Author:	Wei Huang
Date:	2020
Type:	Mémoire ou thèse / Dissertation or Thesis
Référence: Citation:	Huang, W. (2020). Analysis of Through-Thickness Injection in Liquid Composite Molding Based on Digital Material Twins [Ph.D. thesis, Polytechnique Montréal]. PolyPublie. https://publications.polymtl.ca/5366/

POLYTECHNIQUE MONTRÉAL
affiliée à l'Université de Montréal
ET
UNIVERSITÉ DE WUHAN

ANALYSIS OF THROUGH-THICKNESS INJECTION IN LIQUID COMPOSITE MOLDING BASED ON DIGITAL MATERIAL TWINS

WEI HUANG
Département de génie mécanique

Thèse présentée en vue de l'obtention du diplôme de *Philosophiæ Doctor*
Génie mécanique

Août 2020

POLYTECHNIQUE MONTRÉAL
affiliée à l'Université de Montréal
ET
UNIVERSITÉ DE WUHAN

Cette thèse intitulée :

ANALYSIS OF THROUGH-THICKNESS INJECTION IN LIQUID COMPOSITE MOLDING BASED ON DIGITAL MATERIAL TWINS

présentée par **Wei HUANG**
en vue de l'obtention du diplôme de *Philosophiæ Doctor*
a été dûment acceptée par le jury d'examen constitué de :

Rachid BOUKHILI, président
François TROCHU, membre et directeur de recherche
Heng HU, membre et codirecteur de recherche
Philippe CAUSSE, membre et codirecteur de recherche
Cédric BÉGUIN, membre
Pascal HUBERT, membre externe

DEDICATION

Enjoy the sadness as fun,
thank the darkness before dawn.

ACKNOWLEDGEMENTS

First of all, I would like to express my deepest and most sincere gratitude to my supervisor, Professor François Trochu. Ever since our first encounter, I knew that this was going to be an exceptional journey. And now three years after, he has indeed had such a big influence in my life that no words can truly describe. With his guidance, his patience and his generosity throughout my whole research time, he has helped me become a better and stronger man. He will always be a significant character in my life.

I would also like to thank my co-supervisors, Professors Heng Hu and Philippe Causse, for their constant help and support. Professor Hu has always been a role model of mine. He takes challenges in his academic life with freshness and rigour, he genuinely cares about all his students. From him I learn what a true scientist should be like, and from him I learn how to be a human being with dignity and integrity. My genuine appreciation also goes to Professor Philippe Causse. During my entire PhD program, Philippe has always been a kind colleague, a helpful guide, and more importantly, a dear friend. The passionate talks and heated discussions over all kinds of scientific topics have truly lighten up the road, and they will most certainly be missed.

I would also like to take the chance to thank the other friends and colleagues. First of all, I wish to salute the team of Professor Heng Hu at Wuhan University, Kun, Jie, Qun, Yanchuan and Rui, they have offered selfless help during our collaboration. I am pleased also to acknowledge the team of the Luxembourg Institute of Science and Technology (LIST) around Dr. Salim Belouettar with Dr. Gaetano Giunta, Dr. Ahmed Makradi, Dr. Lyazid Bouhala, Dr. Yao Koutsawa and Dr. Gaston Rauchs, who have been such dear friends during my internship at LIST in Luxembourg. They helped make my time there both productive and enjoyable. I would like also to give a special thank to Professor Vladimir Brailovski and Morgan Letenneur at ETS, for providing access to the X-ray microtomograph to help with my research, and for all the other help they have offered during our collaboration.

And of course, I wish to thank the team at Polytechnique. Anna Madra, Bin Yang, Yixun Sun, Sami Hillal, Zaynab Grofti, Grégory Martinez, Béliny Bonnard, Jérome Tixier, and Christian-Charles Martel, who have supported each other in every way, in research and in life.

I would like to give a special acknowledgement to the Department of Mechanical Engineering at Polytechnique Montreal for offering me this opportunity to come and study in this world class university. Getting a doctorate here is what I could only dream of, I will take this as

the starting point of the next journey of my life, I will try my best to make myself useful to society.

My most sincere gratitude goes to my family and friends, both in Canada, in Europe, in India, around the whole world, and back at home in China. Yang, Jingwen, Yuwei, Gabrielle, Rohan, Arpan, Sachin, Their constant support has got me through this splendid yet challenging time, especially my parents, they have without doubt supported me in every possible way.

Finally, I would like to thank my wife, for her lovely voice that lights up the room, for her constant support that soothes the rugged path, and for her sweet smile that warms my soul during this rough journey.

RÉSUMÉ

Les composites à base de renforts tissés possèdent des propriétés mécaniques exceptionnelles et sont largement appliqués dans les domaines aérospatiaux et automobiles. Leur fabrication par moulage de liquide (LCM) compte parmi les procédés de mise en forme courants. Même après une optimisation continue à travers des décennies de développement, des défauts peuvent exister dans les pièces finales. L'une des raisons principales est que le textile possède une architecture spéciale à l'échelle méso-microscopique, ce qui présente des difficultés dans l'analyse de plusieurs phases critiques de fabrication, comme l'imprégnation et le compactage. En outre, dans le cas des fabrications sous membrane comme dans l'injection flexible par exemple, des défauts peuvent apparaître en raison de flambements locaux de la membrane.

Cette thèse vise à combiner des méthodes expérimentales fondées sur la microtomographie aux rayons X avec de nouvelles approches numériques pour construire un système d'analyse multi-échelle d'une série de problèmes mécaniques critiques dans les procédés de moulage liquide LCM. Les différents objectifs ont été réalisés à travers 6 articles présentés dans les chapitres suivants :

1. Une nouvelle approche de modélisation géométrique est développée dans l'article 1 pour générer un modèle mésostructural des renforts fibreux tissé à partir de la microtomographie au rayons X. Cette nouvelle approche appelée «*Micro-CT Aided Geometric Modeling*» (Micro-CT AGM) permet de créer des modèles géométriques des composites à fibres continues appelés "*Digital Material Twin*" (DMT), qui fournissent une description morphologique détaillée de la structure mésoscopique des renforts tissés. Un élément original ici consiste à évaluer la précision du DMT au moyen d'une analyse multi-critères.

2. Dans le deuxième article, plusieurs facteurs critiques sont pris en compte, comme la pression d'injection et l'imbrication entre les couches («*nesting*»), pour améliorer la méthode de mesure de la perméabilité transversale saturée d'un renfort tissé. Les modèles géométriques créés sont utilisés pour simuler l'écoulement à l'échelle mésoscopique et prédire la perméabilité des renforts. Les prédictions numériques réalisés à partir des DMT sont comparées avec succès avec des résultats expérimentaux.

3. L'évolution des caractéristiques morphologiques de la mésostructure d'un renfort tissé pendant la phase de compaction à travers l'épaisseur a été analysée dans les articles 3

et 4. Une nouvelle approche de corrélation de points a été développée pour analyser quantitativement la déformation mésoscopique des mèches d'un renfort tissé.

4. Enfin, pour étudier les problèmes de flambement des membranes utilisées dans certains procédés LCM, un modèle réduit fondé sur un développement en série de Fourier est construit dans l'article 5 pour simuler efficacement et avec précision l'ensemble du processus d'instabilité. Le modèle est ensuite amélioré dans l'article 6 pour étudier les mécanismes de flambement d'une membrane circulaire sous diverses charges.

En résumé, plusieurs nouvelles approches numériques et expérimentales ont été développées à différentes échelles afin de fournir des outils pour analyser plusieurs problèmes mécaniques critiques dans les procédés d'injection flexible à travers l'épaisseur et sous membrane déformable dans la fabrication des composites à haute performance par moulage liquide LCM.

ABSTRACT

Woven fabric reinforced composites possess outstanding mechanical properties and are thus widely used in the aerospace and automobile fields. *Liquid Composite Molding* (LCM) has now become a common composite manufacturing process. However, even after decades of development and optimization, defects still exist in final parts. One of the principal reasons is that the textile has a special architecture at the meso-microscopic scale, which makes difficult the analysis of several key stages in LCM such as the impregnation and compaction of the fibrous reinforcement. Besides, problems arising in manufacturing might also lead to defects, such as the wrinkling of the deformable membrane employed in some LCM processes like *Flexible Injection* for example.

The thesis aims at combining advanced experimental testing methods based on X-ray microtomography with novel numerical approaches to conduct multi-scale analyses of critical mechanical issues in LCM processes. The objectives are achieved through 6 articles as follows:

1. Based on Micro-CT scanning, a novel geometric modeling approach was developed in article 1 to generate mesostructural models of woven fibrous reinforcement in the first article, called *Micro-CT Aided Geometric Modeling* (Micro-CT AGM). A new concept known as "*Digital Material Twin*" (DMT) is proposed to provide a detailed morphological description of the material structure at the mesoscopic scale.

2. In the second article, several key factors are taken into account to evaluate the transverse permeability of fibrous reinforcements such as the injection pressure and nesting between fabric layers. Digital material twins of different fiber volume contents are constructed to conduct flow simulations in fabrics at the mesoscopic scale and predict the transverse permeability. Numerical predictions of transverse permeability based on DMT are compared with success with experimental measurements.

3. Based on digital material twins, the evolution of the morphological features of fabrics under transverse compaction is studied in articles 3 and 4. A new contour point correlation method is developed to quantitatively evaluate the mesoscopic deformation of fiber tows, which illustrates the effect of material variability on the compressibility of fibrous reinforcements.

4. Concerning membrane wrinkling problems in LCM processes, a reduced model based on Fourier series expansion is constructed in article 5 to efficiently and accurately

simulate the entire instability process. The model is then further improved in article 6 to investigate the wrinkling mechanisms of a circular membrane under various loads.

In summary, several numerical and experimental approaches were developed at different scales to provide analytical tools to study critical mechanical issues arising in flexible injection (through the thickness of the composite under a deformable membrane) during the fabrication by LCM. This new approach can improve advanced numerical predictions of composite manufacturing processes based on through-thickness impregnation and contribute to develop more efficient LCM processes with parts of improved quality.

TABLE OF CONTENTS

LIST OF TABLES

LIST OF FIGURES

CHAPTER 1 INTRODUCTION

1.1 Manufacturing of woven fabric reinforced polymer composites

In recent years, high performance composites have been widely used in the aerospace and automobile fields, because of their light weight, high strength, design flexibility and long life. *Liquid Composite Molding* (LCM) is a common process in composite manufacturing, which uses a liquid thermoset resin to saturate a dry preformed reinforcing material. Compared to particle and short fiber reinforcements, woven fibrous reinforcements possess outstanding mechanical properties. Thus it is widely used in LCM processes for high-performance composite manufacturing.

Various LCM processes exist, which can be essentially differentiated based on the impregnation, for example *Resin Transfer Molding* (RTM) when injection takes place in a rigid and closed mold, *Vacuum Assisted Resin Transfer Molding* (VARTM) also known as resin infusion when the resin is infused by gravity under vacuum, *Compression Resin Transfer Molding* (CRTM) when the resin is injected in a partially opened closed mold and *Flexible Injection* (FI) when the mold cavity is deformed to facilitate the liquid flow. Generally speaking, the processes can be classified into two main groups based on the flow direction during the liquid impregnation, which may occur in the plane of the part or through its thickness.

1.1.1 Fabrication process by in-plane liquid injection

RTM is a typical LCM process based on in-plane resin impregnation: the liquid polymer is injected into the fibrous preform placed in a closed and rigid mold. The RTM process is used to produce composite materials of complex geometric shapes in less time and at a reduced cost compared to other more traditional composite manufacturing techniques such as autoclave processing or hand lay-up. Because of its rigid mold, RTM presents several advantages, for example less material waste, low environmental impact and savings in labor costs. Though RTM has the potential of offering composite products of reasonable quality, for parts of large dimensions, this process has limitations because the length of the flow paths is limited. It depends in fact on the injection pressure and on the fiber volume content. The maximum flow path should remain between 1 and 1.5 m. Tooling costs become excessive because of the pressure drop required to impregnate fibrous reinforcements at high fiber volume contents. Besides, the velocity of the liquid becomes rapidly very slow in large parts, which reduces the efficiency in production. These drawbacks are common as well in other LCM processes based

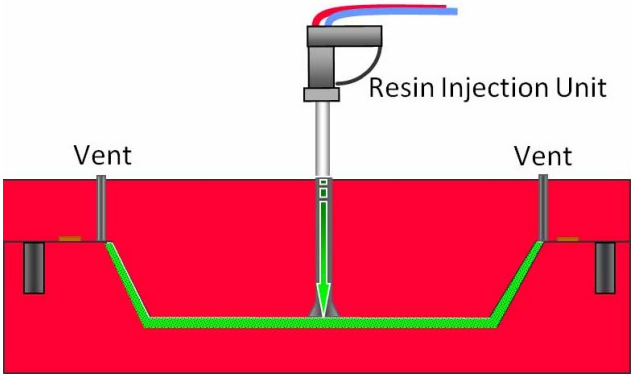

(a)

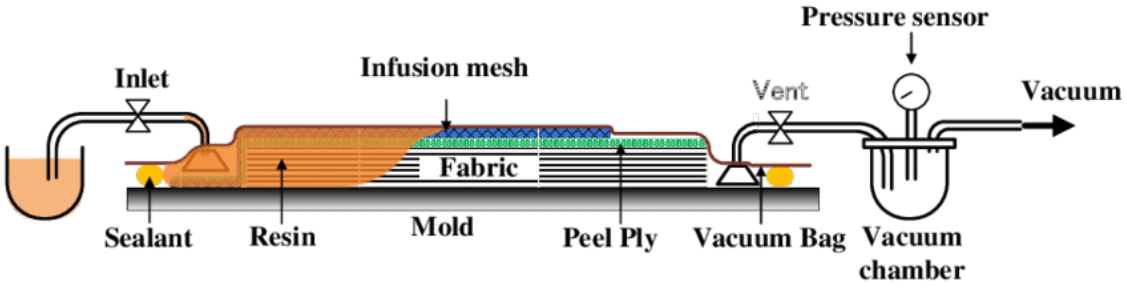

(b)

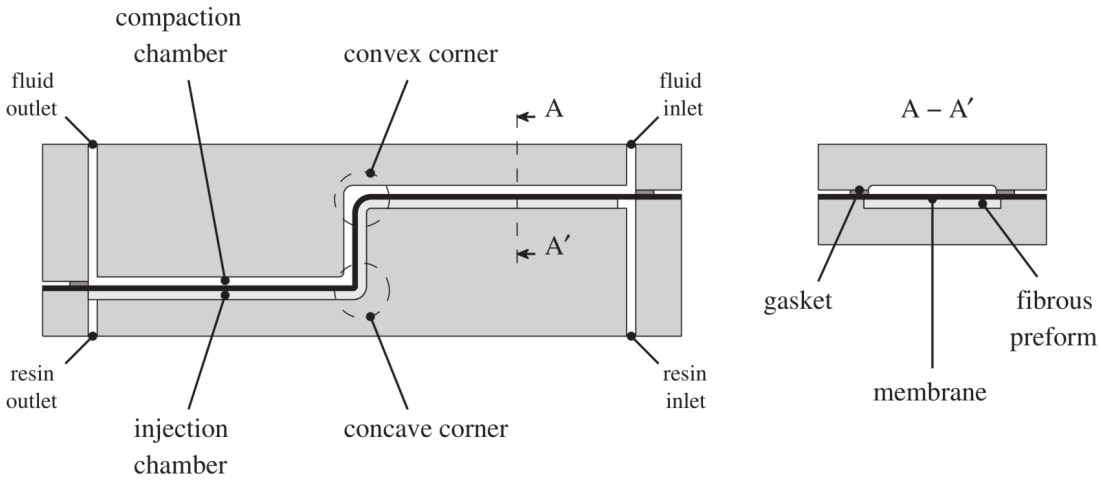

(c)

Figure 1.1 Various LCM methods: (a) Resin Transfer Molding (RTM) [1]; (b) Vacuum Assisted Resin Transfer Molding (VARTM) [2]; (c) Flexible Injection (FI) [3].

on in-plane liquid injections. To overcome these difficulties, several LCM process variants were devised to achieve transverse rather than in-plane liquid impregnation of the fiber bed, which results in decreasing considerably the average length of the flow paths.

1.1.2 Injection process based on transverse flows

Two popular LCM processes, VARTM and CRTM, attempt to carry out transverse injection. VARTM is a family of low pressure LCM processes, in which the composite is molded in a rigid cavity to give its geometry to the part with a thin flexible membrane over the fiber bed. Sealing the flexible cover and pulling partial vacuum compresses the fibers and holds the reinforcement tight against the rigid mold surface. Hence the liquid resin can flow by gravity through the fibrous reinforcement. Sometimes a distribution layer of high permeability is set above the reinforcement, allowing not only partial in-plane liquid flow, but also mainly transverse impregnation. VARTM is often used to manufacture large-scale composite parts. However, it is difficult to make thick parts or achieve a higher fiber volume content than in RTM. In recent years, VARTM improved much thanks to a series of consumable and mold settings to ensure robust and durable sealing of the cavity. However, using a flexible vacuum bag under a pressure lower than one atmosphere makes it difficult to control the final thickness of the preform and its uniformity, and thus, the fiber volume content of the composite.

CRTM is another process variant of LCM, in which the mold is not completely closed before injection, thus, if the reinforcement was preformed properly, there is a gap allowing resin to flow between the fibers and the top rigid mold. After resin injection, the rigid cover moves to completely close the mold, which results in transverse flow through the fibrous reinforcement. Although this process is delicate to set up and requires a very precise parallelism of the press governing the vertical motion of the mold cover, it was demonstrated to be effective. However, it remains much easier to implement and also more widely used for nearly flat parts. The reason is the non-uniform compression in the case of complex 3D shells. In addition, when the reinforcement was not initially preformed, a more important contribution of the pressure field is required to consolidate the fiber bed, hence reducing the liquid pressure necessary to impregnate the fiber bundles.

FI is another advanced injection process based on transverse flow proposed by Ruiz and Trochu [4]. A mold with two chambers separated by a flexible membrane is used in FI. Firstly, the resin is injected in the lower chamber containing the fibrous reinforcement, after which an incompressible fluid is injected in the top chamber to compress the flexible membrane. This generates a transverse flow to impregnate the fibers. FI is one order of magnitude

faster than standard RTM [5, 6]. It can be used also to manufacture complex 3D shells, which is an obvious advantage compared to CRTM. Since the compaction of the membrane is provided by an exterior fluid and not only by the atmospheric pressure like in VARTM, the impregnation process can be controlled, which improves part quality while reducing cycle time. This promising new process provides a good reason to study transverse flows to improve the fabrication of high performance composites by resin injection.

1.2 Defects in composite products

Even after continuous optimization of LCM processes after decades of development, defects still remain in the final composite parts. The origins of defects involve various aspects at different scales, such as the formation of air bubbles during the impregnation at the microscale and mesoscale levels, and the wrinkling of membranes at the macroscale in the processes using flexible membranes (VARTM and FI). A brief introduction on defects will be presented in the sequel.

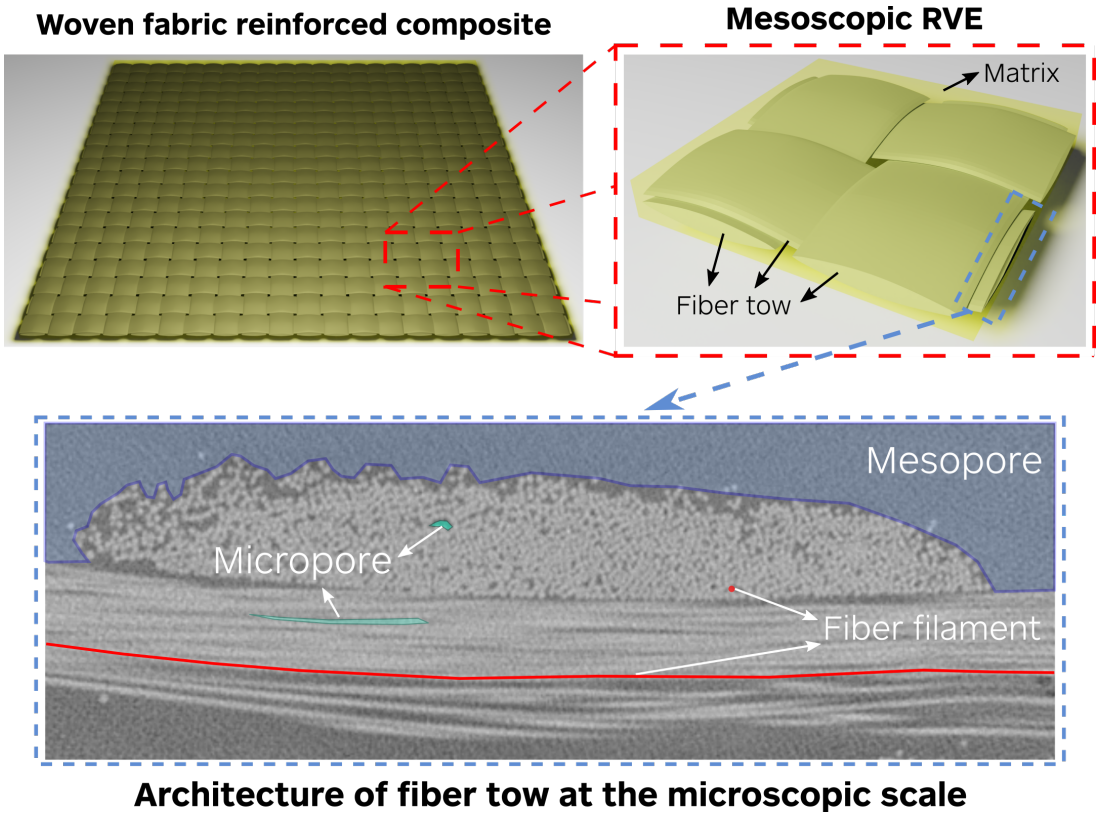

Figure 1.2 Multi-scale architecture of woven fibrous reinforcement.

1.2.1 Dual-scale flow induced defects

Figure 1.2 illustrates the multi-scale architecture of woven fibrous reinforcements. Since the woven fabric reinforcement is generally a periodic material, it is possible to find the simplest repeating unit cells at the mesoscopic scale, also called representative elementary volume (REV), to form composite parts at the macroscopic scale. The REV consists of the matrix and fiber tows, which are the basic elements at the mesoscopic scale. By employing sophisticated apparatus such as scanning electron microscope (SEM) or X-ray microtomography (Micro-CT) to study the fiber architecture at the microscopic scale, fiber tows can be observed with their hundreds or thousands of fiber filaments. Micropores exist between the fibers inside the tows, while the much larger inter-tow spaces are called mesopores (about two orders of magnitude larger than micropores).

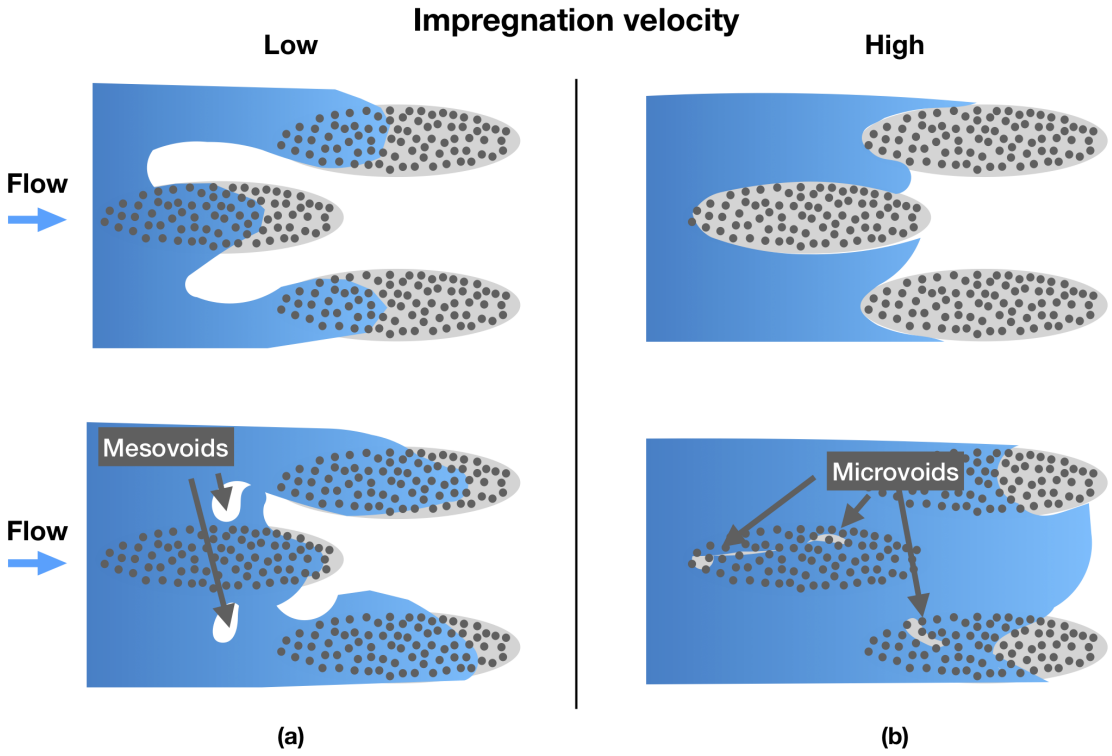

Figure 1.3 Void formation caused by dual-scale flow under low and high impregnation velocity.

During the impregnation process, the dual-scale architecture results in two possible flow patterns. If the injection is performed under pressure as shown in the right hand side of Figure 1.3, the liquid flows faster in the mesopores. Viscous effects dominate and microscopic voids tend to be created in fiber tows. On the contrary, if the velocity of the flow front is low such as in VARTM for example, then capillary effects come into play. The fiber bundles

are filled before the mesopores, which tends to entrap mesoscopic voids.

If the air bubbles cannot be squeezed out of the mold before the resin gets cured, microscopic or mesoscopic defects will be generated in the final composite part (see Figure 1.4). Based on the experimental study of Bowles and Frimpong [7], voids degrade matrix dominated mechanical properties such as the inter-laminar shear strength and the flexural strength. Every 1% increase in void content decreases mechanical properties by more than 5%. In addition, voids decrease durability and fatigue resistance, and thus can lead to failure.

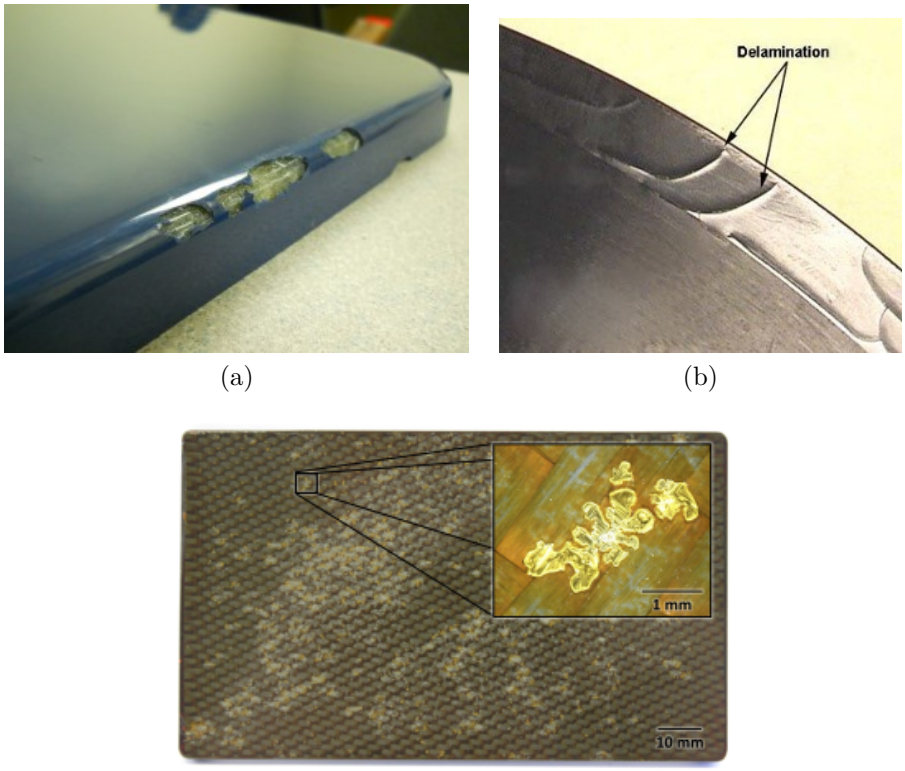

(a) (b)

(c)

Figure 1.4 Various defects [8, 9]: (a) macroscopic defects; (b) delamination; (c) mesoscopic defects.

1.2.2 Transverse compaction induced architecture change

In LCM, the compaction of fibers occurs during the entire process, whether it is during the preparation of the preform before resin injection or during the impregnation of the fiber bed in the transverse direction. The fibrous reinforcement is rearranged under compaction in two ways, resulting in changes in its dual-scale architecture: (1) the volume of the micropores is reduced inside the fiber tows due to the movements and deformation of fiber filaments; (2)

as the fiber volume content increases during compaction, the size and shape of mesopores are reorganized.

Since the dual-scale flow is determined by the fiber architecture, the compaction of the fiber bed affects the impregnation process. As presented in [10] for transverse impregnation, flow-induced compaction appears as the result of high injection pressure, leading to a rearrangement of the fiber bed. Therefore, a strong interaction exists between the flow and the fiber bed as illustrated in Fig. 1.5, making rather complex the prediction of liquid impregnation in dual-scale fibrous reinforcements. This leads to difficulties in optimizing the manufacturing process and improving part quality.

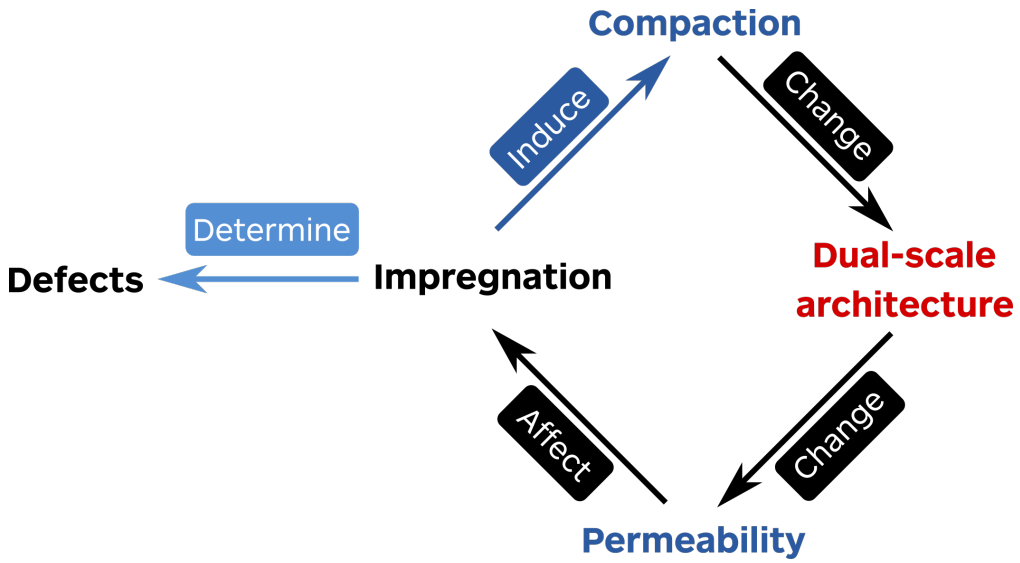

Figure 1.5 Interactive effects between the impregnation flow and the architecture of the fibrous reinforcement.

1.2.3 Membrane wrinkling induced defects

Deformable membranes are used in several injection processes to create partial transverse flows such as a vacuum bag in VARTM or a flexible membrane in FI. As soft material with almost negligible bending stiffness, membranes easily lose their mechanical stability and may wrinkle when submitted to in-plane compressive stresses. Membrane wrinkling might appear during the entire process, for example during the injection in FI [11] (see Figure 1.6a), in the layup and post-filling of VARTM as described by Simacek and Advani [12] (see Figures 1.6b and 1.6c).

Figure 1.6a shows the deformation of the membrane leading to a non-uniform resin distribution, indicating that membrane wrinkling may cause external defects in the final composites.

Excessive deformations caused by wrinkles might also alter the geometric dimensions of the parts. Meanwhile, stress distributions in the parts can also be affected by wrinkles, which may create difficulties to predict the injection process and assess part quality. Considering the thermal stresses that occur in the curing process, the effect of membrane wrinkling can become rather complex to evaluate. As a result, wrinkling induced geometric distortions may create difficulties to assemble final products. In practical applications, the mechanical properties of composites can also be affected by wrinkling-induced stress concentrations.

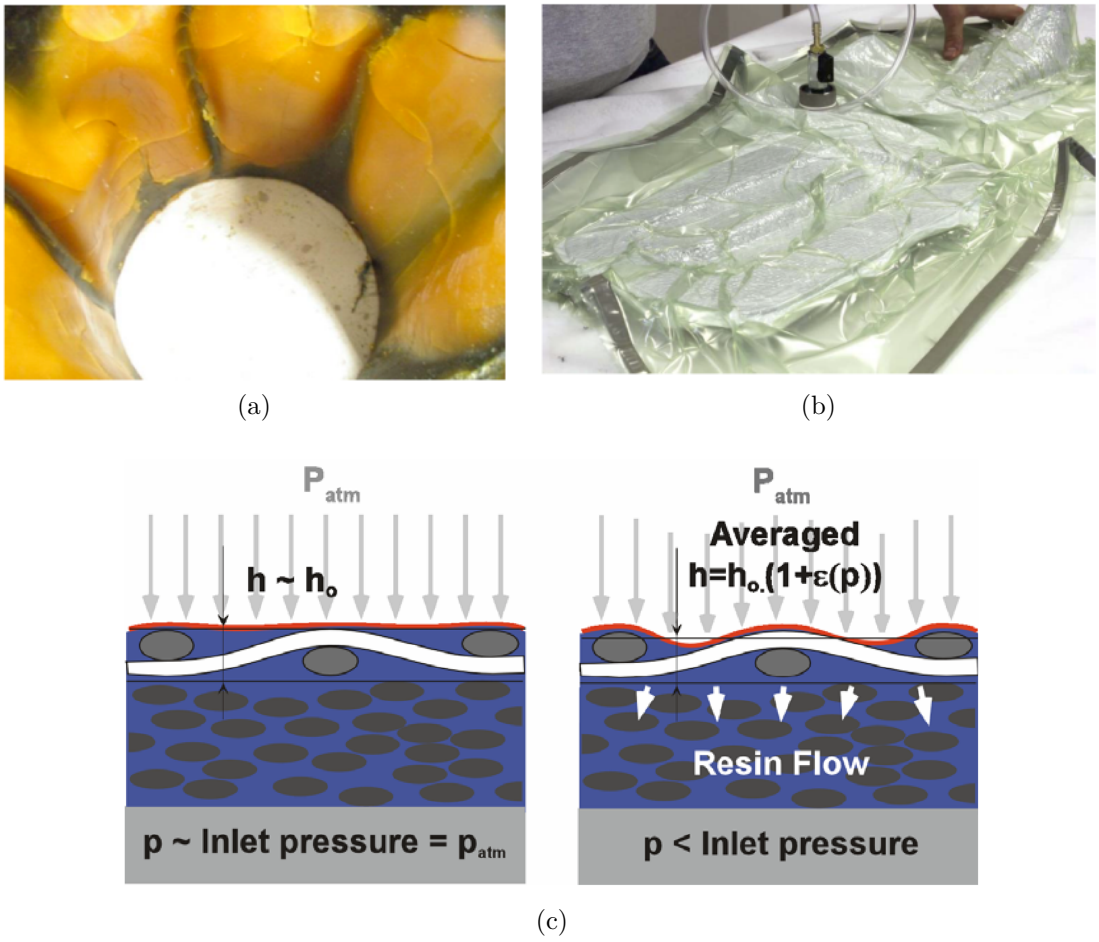

Figure 1.6 (a) Membrane wrinkling in injection process of FI [11]; (b) vacuum bag wrinkling in lay-up process of VARTM [13]; (c) distribution media collapse in post-filling process of VARTM [12].

1.3 Scope of works

This thesis will focus on through-thickness injection under a deformable membrane (FI) or plastic film (VARTM). After a review in Chapter 2 in the state-of-the-art on this issue, the

different topics covered will be presented in Chapter 3 together with the objectives and an outline of the thesis.

Bibliography

[1] "https://poly-matrix.hu/zartszerszamos-eljaras-rtm-resin-transfer-moulding."

[2] M. R. Abusrea and K. Arakawa, "Enhanced tensile strength cfrp adhesive joint constructed from carbon fiber-reinforced plastic and dry carbon fiber laminates," in *Proceedings of the 17th International Conference on Composite Materials (ICCM17)*, 2016.

[3] P. Causse, E. Ruiz, and F. Trochu, "Spring-in behavior of curved composites manufactured by Flexible Injection," *Composites Part A: Applied Science and Manufacturing*, vol. 43, no. 11, pp. 1901–1913, 2012.

[4] E. Ruiz and F. Trochu, "Manufacture of composites by a flexible injection process using a double or multiple cavity mold," Jan. 11 2011, uS Patent 7,866,969.

[5] E. Ruiz, L. Briones, E. Allard, and F. Trochu, "Flexible injection: a novel LCM technology for low cost manufacturing of high performance composites. Part I: experimental investigation," in *The 9th International Conference on Flow Processes in Composite Materials*, 2008.

[6] F. Trochu, S. Soukane, and B. Touraine, "Flexible injection: a novel LCM technology for low cost manufacturing of high performance composites. Part II: numerical model," in *9 th Int. Conf. on Flow Proc. in Comp. Mat*, 2008.

[7] K. J. Bowles and S. Frimpong, "Void effects on the interlaminar shear strength of unidirectional graphite-fiber-reinforced composites," *Journal of composite materials*, vol. 26, no. 10, pp. 1487–1509, 1992.

[8] "https://www.rtmcomposites.com/blog/process-troubleshooting-air-pockets-causing-mold-defects."

[9] "https://www.patterson-rothwell.co.uk/in-pursuit-of-the-perfect-injection-moulded-part-nine-delamination."

[10] F. Klunker, M. Danzi, and P. Ermanni, "Fiber deformation as a result of fluid injection: modeling and validation in the case of saturated permeability measurements in through thickness direction," *Journal of Composite Materials*, vol. 49, no. 9, pp. 1091–1105, 2015.

[11] V. S. Loiselle, "Fabrication par injection flexible de pièces coniques pour des applications aérospatiales," Ph.D. dissertation, École Polytechnique de Montréal, 2013.

[12] P. Simacek and S. G. Advani, "Modeling resin flow and fiber tow saturation induced by distribution media collapse in VARTM," *Composites science and technology*, vol. 67, no. 13, pp. 2757–2769, 2007.

[13] "http://www.easycomposites.cn/beginners-guide-to-out-of-autoclave-part-3.aspx."

CHAPTER 2 LITERATURE REVIEW

To understand and prevent defects, different analytical tools are required at the specific scale (or multi-scale). Though many efforts have addressed the problems mentioned above, they involve many different fields and remain complex to solve, so several key issues still need to be considered.

2.1 Geometric architecture of fibrous reinforcements

In the section, investigations on the introduction and analysis of the geometric architecture of fibrous reinforcements are reviewed. Understanding the dual-scale architecture of fibrous reinforcements guides the development of geometric modeling approaches. It reveals also the complex mechanical behaviors of fibrous reinforcements during liquid impregnation and compaction. Therefore, this part of the thesis is related to article 1, in which the novel geometric modeling approach called Micro-CT Aided Geometric Modelling (Micro-CT AGM) was presented. It is also connected to articles 2 to 4, in which Micro-CT AGM is applied to predict the permeability and compressibility of engineering fabrics.

As illustrated in Figure 1.2, the mesostructural architectures of fibrous reinforcements are quite complex. Therefore, a comprehensive review of the architecture of fibrous reinforcements is necessary. In high performance composite materials, depending on the forming technique used, fibrous reinforcements (also named textiles) can be separated in three main categories [1]: woven-, knitted- and braided fabrics as illustrated in Figure 2.1. Traditionally, 2D fabrics are formed layer by layer and preformed to produce composite parts, which provide excellent in-plane mechanical properties, such as high specific stiffness and high strength. However, laminated composites have poor mechanical properties in the transverse direction, therefore they offer a low delamination resistance. In order to overcome this drawback, 3D fibrous reinforcements have attracted interest in the composites community. Thanks to the addition of yarns, known as binders, 3D fabrics in a single layer can provide better mechanical properties in the transverse direction compared to 2D fabrics. Besides, 3D fabrics possess other advantages, such as easy handling and significantly improved impact resistance [2]. For these reasons, 3D fabrics find more applications in various industrial fields.

Composites reinforced by 3D fabrics exhibit a complex geometric architecture of interlaced tows. For example, the orthogonal 3D fabric shown in Figure 2.2 displays a fiber architecture that governs its mechanical and flow properties, as well as its failure mechanisms. As studied

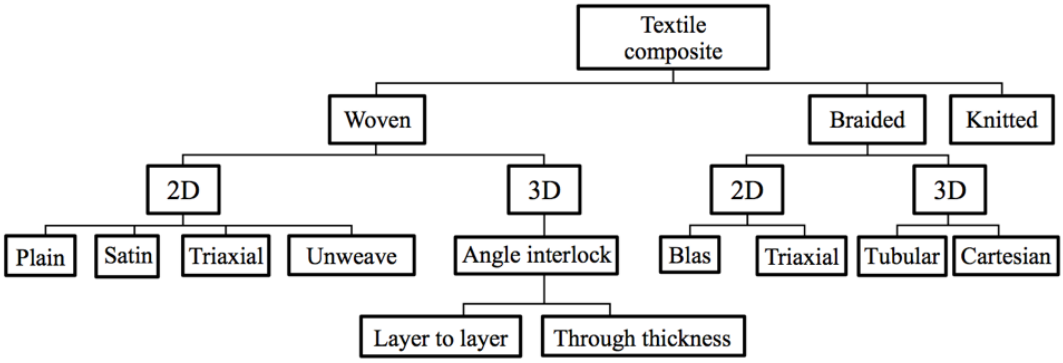

Figure 2.1 Classification of textile [1].

by Leong at el. [3], different interlock weave patterns produce large variations in mechanical properties, which are closely connected with different yarn crimps. Therefore, it is important to study the internal structure of engineering fabrics and investigate the relationship between their geometric architecture and the mechanical properties.

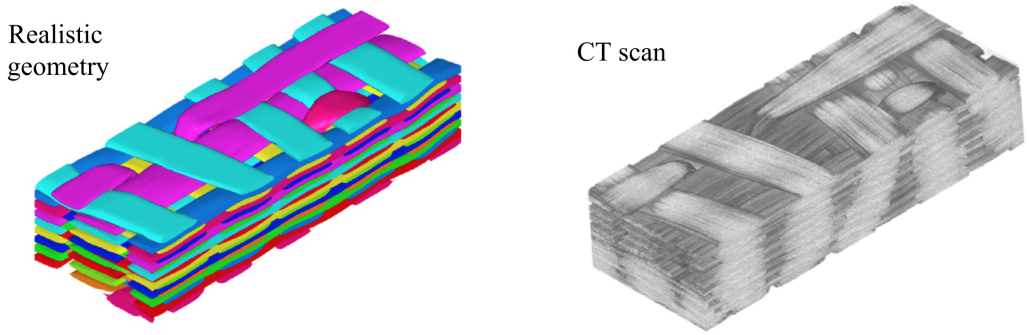

Figure 2.2 Geometry of an orthogonal 3D woven composite: geometric modelling and computed tomography scan [4].

Desplentere et al. [5] used microtomography (Micro-CT) to characterize the geometric variability of four different 3D warp-interlaced fabrics. They compared measured values of yarn thickness, width and spacing between yarns with measurements obtained from optical micrographs. The comparison did not show significant differences between the two measurements, which means that the X-ray Micro-CT is a reliable technique to acquire geometric information on engineering textiles. The experiments showed a maximum standard deviation of 16% for the geometric dimensions of yarns and of 6% for the spacing between yarns. This non-negligible variability has a strong influence on material parameters.

Mahadik et al. [6] used Micro-CT to scan two different 3D interlock fabrics and analyze their geometric characteristics. They defined a local angle as shown in Figure 2.3 and studied the relationship between yarn crimp, resin channel size and fiber volume content based on the information obtained from tomographic images. They found that warp yarns cause local areas of high crimp in weft yarns. This phenomenon is exacerbated at lower fiber volume fractions due to yarn nesting. However, it decreases sharply at high volume fraction close to 65% because of the flattening effect of compaction. They also found that major resin channels exist between warp yarns. With the increase of fiber volume fraction, resin channels change in shape. For example, the evolution of resin pockets highly associated with the weave pattern of the fabric.

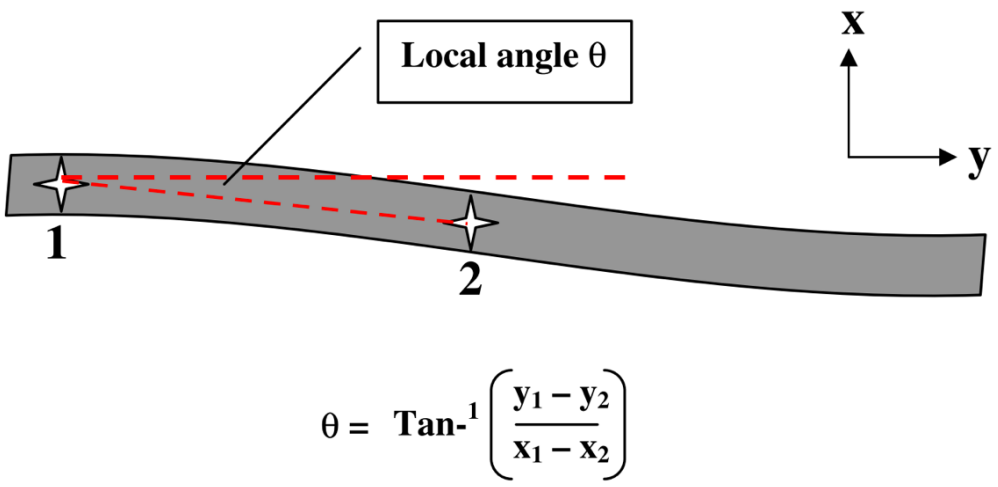

Figure 2.3 Calculation of the local angle from two points on the yarn centerline [6].

In order to develop an analytical model to predict the transverse permeability of 3D-woven fabrics, Xiao et al. [7] used optical microscopy to measure various geometric parameters of the textile, for example the spacing and width of yarns, the height and width of binder yarns, and the cross-section area of inter-yarn gap. Based on these geometric parameters, they proposed some other parameters, for example a hydraulic radius R was used to characterize the actual gap cross-section:

$$R = \frac{(S_w - D_w)(S_j - D_j) - B_w B_j}{2(S_w - D_w - B_w + S_j - D_j - B_j)} \tag{2.1}$$

where S_j, D_j, (S_w, D_w) characterize the measured spacing and the width of warp (weft) yarns, B_j, B_w are the height and width of binder yarns. These parameters provide the necessary information to develop an analytical model which agreed well with the experimental data of seven fabrics.

Considering that the Micro-CT is only feasible on very small samples and has a limited resolution, Gommer et al. [8] used conventional optical microscopy to study local material variations in carbon fiber bundles. Automatic image analysis of optical micrographs was carried out on cross-sections of the material to quantify the random and systematic changes in local filament arrangements along the bundle path. For example, they investigated the local area and fiber ratio of fiber bundle as shown in Figure 2.4. These local variations affect the fiber bundle properties differently. For example, in the high fiber density region, permeability is low and may locally prevent full saturation during the impregnation process. Thus the obtained data can be employed in multi-scale modelling approaches to improve the accuracy in the assessment of the local properties of fiber bundles.

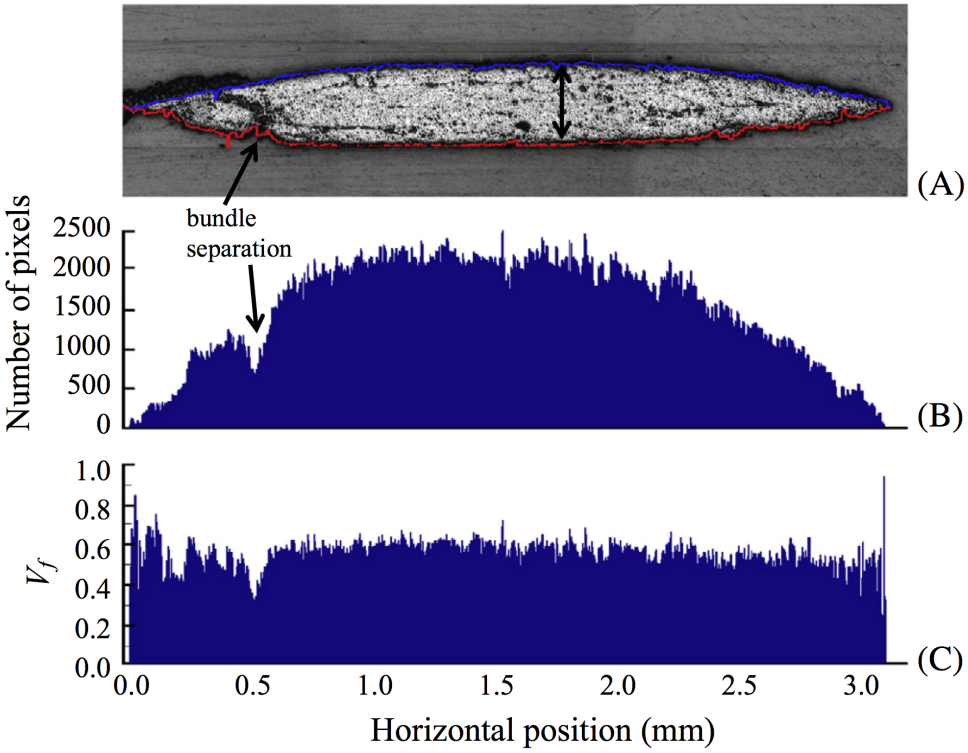

Figure 2.4 (a) Fiber bundle with estimated boundaries; (b) total filament area in pixels within the fiber bundle cross section; (c) fiber volume fraction V_f within the boundaries of the fiber bundle [8].

2.2 Geometric modeling of fibrous reinforcements

Since the performance of engineering textiles is closely related to fiber architecture, precise geometric models are critical to conduct numerical flow or mechanical simulations, such as

liquid impregnation in LCM or compaction of dry fibrous reinforcements. In this section, investigations on the geometric modeling of fibrous reinforcements are reviewed, which is the central goal of article 1. Microstructural and mesostructural geometric models exist for fibrous reinforcements. Mesostructural models take into account yarns with their geometry (shape, dimensions, area, etc.) including cross-sectional contours and local orientations along their central lines. The complement of yarns in the model is the porous network. Microstructural models include a detailed 3D representation of the filaments inside the yarns. These models are much more complex and require recording a very large amount of data. Therefore, in engineering textiles, they are usually limited to regions of less or equal to the unit cell of the fabric material.

2.2.1 Microstructural modeling

Wang and Sun [9] were among the first investigators to create microstructural models of fibrous reinforcements. They proposed the concept of digital element and used it to develop a numerical simulation approach named as "digital element simulation", which is different from the conventional finite element method because of a special yarn discretization process. In digital element simulation, the physical properties of the material are not included in the element. In contrast to the finite element method, the physical properties are initiated by an element link. As shown in Figure 2.5, this element was used to model yarns by a pin-connected digital-rod-element chain. The approach considered the contact mechanisms including yarn tension and inter-yarn friction and compression to simulate the textile fabrication process, which was regarded as a non-linear problem of solid mechanics. The model performed well in the simulation of twisting, weaving and knitting, but not so well for braiding.

This methodology was improved over the years and became a widely used approach called "multi-chain digital element analysis" [10]. In this method, the fabric is considered as an assembly of yarns. Furthermore, a yarn is formed from a bundle of fibers. Each fiber is modelled by a digital element chain. Therefore, the yarn is modelled as an assembly of digital chains as shown in Figure 2.6. Due to limitations of the current computer performance, it is not possible to simulate the mechanical response of fiber tows consisting of thousands of fiber filaments. Therefore, fiber filaments with larger radius were used to represent the real fiber filaments inside fiber tows for numerical simulations. These enlarged filaments are called effective fibers. The approach can trace both detailed yarn paths and cross-sectional shape changes during the textile fabrication process or during fabric deformation. This methodology was further improved [11, 12] and is now widely used to study the mechanical response of woven textiles submitted to different kinds of loads [13–15].

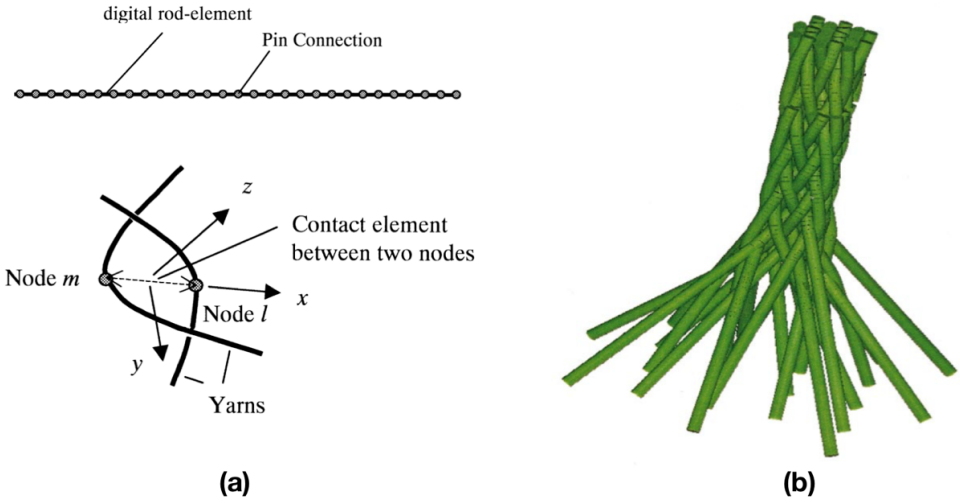

Figure 2.5 (a) Fiber bundle with estimated boundaries; (b) total filament area in pixels within the fiber bundle cross section; (c) fiber volume fraction V_f within the boundaries of the fiber bundle [9].

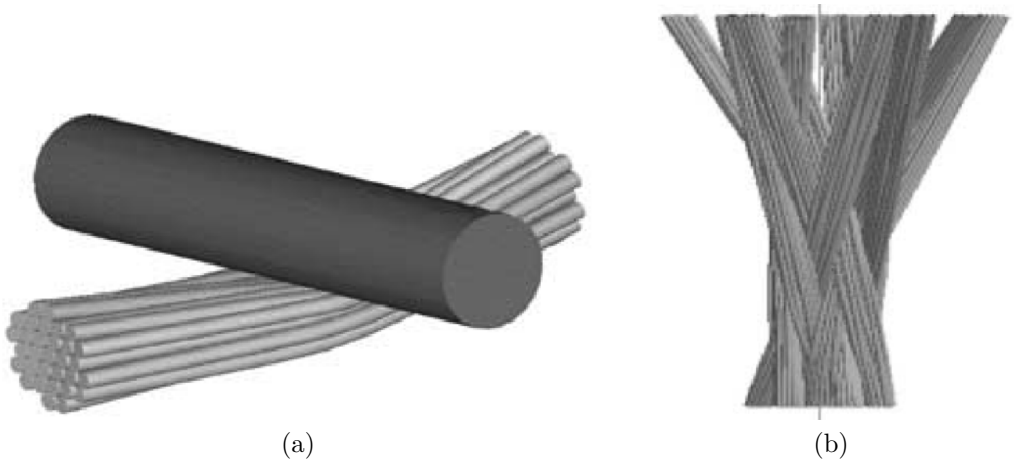

Figure 2.6 (a) Yarn under single side compression; (b) 3D braided preform [10].

Since the contact between fiber filaments is quite complex, it is not easy to efficiently carry out different kinds of computational analyses such as preform compression or resin injection through fibrous reinforcements. A good extension to powerful commercial numerical simulation software (such as ABAQUS and ANSYS) or open-source ones (such as Code Aster) is very important to promote the microstructural approach. Mahadik and Hallett [6] proposed a similar kinematic model to predict the internal architectural features in a commercial numerical simulation software. Beam-element chains were used to replace the digital element chain in [10]. A loose model was regarded as the initial model and a thermal loading was applied in the model to apply a tensile force on all the yarns. After the model was compressed to reach the measured thickness of a real fabric sample, numerical simulations were carried out. Since the approach was developed with existing commercial software, it is user-friendly and can be easily combined with other advanced methods of complex numerical simulations. Note that this approach was also applied to study different kinds of mechanical problems [4, 16–18].

2.2.2 Mesostructural modeling

Traditionally, idealized mesostructural models are created by textile software such as TexGen [19, 20], WiseTex [21, 22] or other specialized software. These geometric models are a simplified version of the actual fiber architecture based on a series of critical geometric parameters. TexGen is an open source software developed by the University of Nottingham [19, 20] dedicated to the 3D modelling of textile composites. The software uses a kinematic modelling approach based on the definition of yarn centrale lines with specified cross-sectional shapes along the yarn length. TexGen allows easy modelling of most textile fabric structures.

WiseTex is a software package developed by the team from Katholieke Universiteit Leuven [21, 22], which generates a generalized description of the internal structure of textile reinforcements at the unit cell level. In this software package, not only mechanical models of relaxed textiles, namely fibrous reinforcements in their free state before processing, are created, but also deformed textiles can be modelled. The internal textile geometry can be described based on a minimum number of topological information, such as the weave pattern and the inter-yarn distances. Since the package is integrated with resin flow models, micro-mechanical calculations of textile material properties and flow behavior can be carried out. Hence, it is possible to use the software to analyze the evolution of the geometric characteristics during fabric deformation.

Although idealized models provide an automatic and robust way of constructing simplified geometric representations of a material for numerical simulations, they still differ from the architecture of real reinforcements at the mesoscopic scale. To generate more realistic models,

several approaches are developed, which can be classified into two types:

1. Combine TexGen and digital element approach [9, 10] to introduce the randomness of fiber filaments at the microscopic scale into the geometric models at the mesoscopic scale [4, 16] (see Figure 2.7a).

2. Employ X-ray microtomography (or Micro-CT) [23] to scan the fibrous reinforcements, then apply image processing techniques on the microtomographic images to reconstruct mesostructural models [24, 25] (see Figure 2.7b).

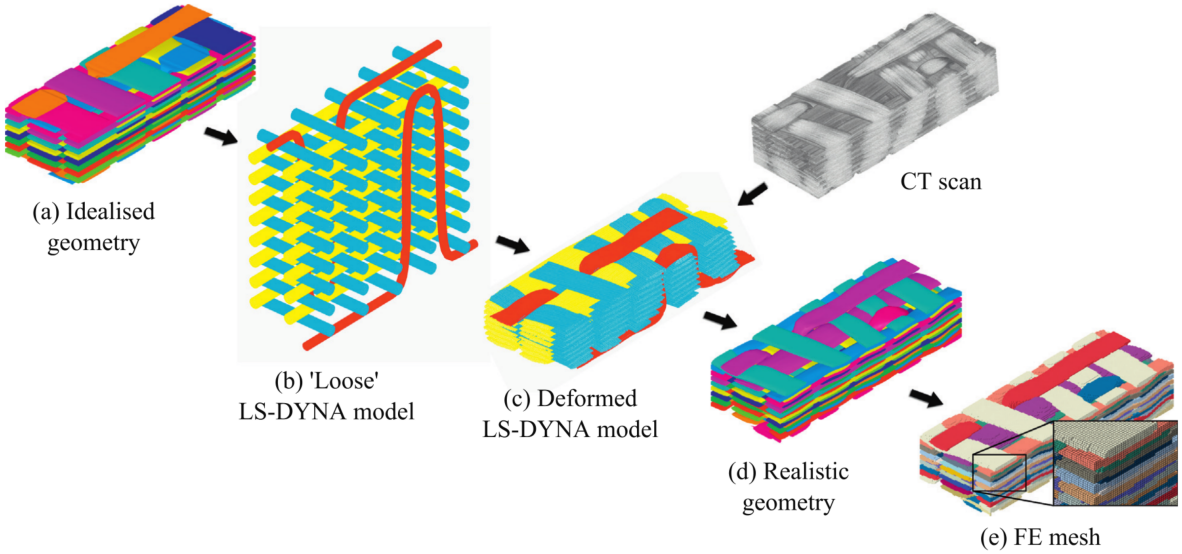

(a)

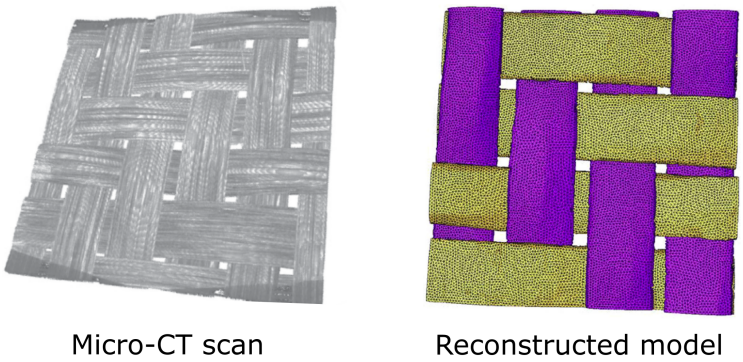

(b)

Figure 2.7 (a) Geometric model generated by combing TexGen and digital element approach [4]; (b) mesostructural model of 2D woven fabric reconstructed from microtomographic images [24].

By combining TexGen and digital elements, Green et al. [4] developed an interesting new

procedure to construct the 3D geometric model based on a realistic unit cell geometry. The workflow of the method is shown in Figure 2.7a. Firstly, an idealized geometric model is generated by TexGen. Then a "loose" LS-DYNA (commercial simulation software) model is generated from the TexGen file, which is processed by a Python script. After that, the LS-DYNA model is compacted between two rigid plates to the target fiber ratio V_f to produce a "deformed" LS-DYNA model. Then a unit cell obtained by CT scan is introduced as a reference to refine the "deformed" model and obtain realistic geometric data for numerical simulations. The geometric model is visually nice, showing waviness in the fabric and shape variations of tow cross-sections. However, there are still some drawbacks with this approach:

1. Since the construction of the geometric model involves simulation of fabric compaction, the entire procedure can be time consuming. As mentioned in [4], the model was run on a high performance computing system using eight 2.8 GHz cores taking 8 h and 55 min to complete one simulation.

2. The microstructure of the model is based on digital elements. Considering the computational feasibility, only 61 chains of beam elements are used in each yarn. Thus the microstructure of the yarn is not realistic, resulting in problems in the simulation of liquid impregnation in dual-scale fibrous reinforcements.

3. Since the modeling parameters are not extracted directly from the CT scans, some geometric details in the model differ from the actual unit cell. Therefore, using Micro-CT to reconstruct the microscopic architecture of the textile as proposed in this thesis can provide more realistic geometric models for computer simulation.

Differing from the modeling approaches only based on mathematical methods, Naouar et al. [24] firstly employ image processing techniques to generate geometric models from micro-tomographic images based on a structure tensor [26]. This approach allows creating finite element meshes ready for numerical simulations. They conducted simulations of a single layer woven fabric under compaction using the TexGen model and the reconstructed model respectively, and then compared the results with the experimental test. The reconstructed model performs much better than the TexGen model, indicating that a more realistic model is able to describe more accurately the actual mechanical behavior of fibrous reinforcements. However, this approach did not perform well for 3D textiles, when the tows are held together by a binding thread. Therefore, another technique was developed in Naouar et al. [25] to construct the mesostructural model of a 3D textile based on the calculation of Grey Level Co-occurrence matrix (GLC Matrix) [27].

The key factor in the modeling above mentioned approach is microtomography (Micro-CT), since it allows non-destructive characterization of the material microstructure in three dimensions at the microscopic level. A refined spatial resolution is obtained readily without requiring sample preparation, staining or thin slicing, which is required by standard microscopic techniques limited to surface observations. Desplentere et al. [5], Schilling et al. [28], Schell et al. [29, 30] were among the first investigators who demonstrated the potential of Micro-CT to characterize the geometric features of 3D textiles at the mesoscopic scale. For example, Schell et al. [29] applied Micro-CT to study the mesoscopic structure of glass fiber reinforced polymers. The proportion of the different phases was analyzed to distinguish, based on the distribution of scaled absorptions values, between air, resin and glass.

In recent years, increased interest in Micro-CT has led to a broad range of new applications in the field of composite materials. Madra et al. [31] applied various methods of image segmentation to study the porosity distribution in a woven glass fiber composite. On the other hand, Ali et al. [32–34] proposed a non-destructive modeling framework to predict the in-plane and transverse permeability of 3D woven fabrics based on the analysis of the mesoporous network between fiber tows. Using digital volume correlation, Mendoza et al. [35] proposed a technique to characterize quantitatively the distortions of woven composites, which was recently employed to measure yarn deformations induced by the manufacturing process [36].

Note that in the reconstruction approaches proposed in [24, 25], only one textile ply was reconstructed. It was not implemented for fabric stacks. In this case, nesting between neighboring plies still impedes an automatic recognition and separation of fiber tows. Moreover, as presented by Straumit et al. [37], the structure tensor method possesses a constraint on the lower voxel size required for Micro-CT images to attain a specific accuracy. According to this investigation, the standard deviation of the calculated orientation angle for a voxel size of 20.5 µm is nearly ten times larger than for 8.3 µm voxels. Therefore, although image processing techniques might still perform well at high resolution in the case of multiple fabric layers, the scanned specimens seem too small to represent the real geometric textile features and reflect material variability [38].

Another common problem in reconstructed models is that no basic geometric criterion is available to assess their accuracy. The reconstructed models are usually verified indirectly by comparing the results of mechanical simulations with experiments. No accuracy analysis of geometric features has yet been carried out. This leads to a lack of geometrical consistency in the proposed models, which might create numerical problems or inaccurate results in computer simulations, such as for example in LCM flow models based on the textile

mesostructure.

2.3 Permeability measurement of fibrous reinforcements

Production quality and capacity are two key issues in manufacturing. In LCM processes, the permeability of the fibrous reinforcement is one of the critical factors that determines the production efficiency and quality. As a material property, permeability depends on the cross-section and tortuosity of the flow paths in the porous material. In general, permeability is investigated as a function of the local fiber fraction of the fiber bed. Therefore, permeability can be isotropic or anisotropic based on the fibrous architecture of the reinforcement. For example, continuous fiber mats (CFM) exhibit an isotropic permeability, while woven textiles usually display an anisotropic permeability. In these reinforcements, different flow directions may lead to defects in final parts. Hence, permeability plays a key role in LCM impregnation processes. It is one important parameter to control the quality of high performance composites. This section reviews the state-of-the-art on permeability measurement, which provides important information and references for article 2. Besides, according to the articles reviewed, the through-thickness permeability is difficult to measure. Therefore, it is difficult to analyze LCM process variants using deformable membranes or plastic films such as FI or VARTM, especially when membrane wrinkling exists as discussed in articles 5 and 6.

Transient unsaturated phenomena occur during the impregnation of a fibrous reinforcement by a liquid. To model these phenomena, knowledge of the unsaturated permeability of engineering textiles is needed. However, to model saturated steady state flows through porous media, the standard Darcy permeability (also called saturated permeability) is required. In conclusion, before the mold is completely filled, the flow behavior in time depends on the position of the flow front, which is characterized by the unsaturated permeability. After the mold is completely filled, the saturated standard Darcy permeability comes into play.

In unsaturated permeability measurements, the basic idea is to acquire the position of flow front as a function of time. Many investigations have focused on measuring the unsaturated permeability based on 1D, 2D and 3D injection experiments. In 1D permeability measurements, the liquid is injected from one side of the composite preform [39]. In 2D permeability measurements, the liquid is injected at a given location of the composite structure [40, 41]. In 3D permeability measurements, the liquid is injected from the top of the fibrous reinforcement and a 3D impregnation flow is tracked through the thickness and in the plane of the fiber bed [42]. Achieving proper 2D or 3D flow configurations is rather difficult. Especially in the 3D case, a thick preform is usually needed to get meaningful results.

Because the thickness of the fibrous reinforcement is usually much smaller than the in-plane geometric dimensions, it is easier to observe the displacement of the flow front during in-plane unsaturated injections carried out to measure permeability rather than in the transverse direction. Therefore, various means have been implemented to acquire the positions of the flow front in time, which are needed to evaluate the transverse unsaturated permeability. A standard way to follow the motion of the flow front is to measure the changes of mass of the test liquid in the mold containing the measurement samples. Li et al. [43] proposed to calculate the position of the flow front based on the liquid mass absorbed during the measurement. They developed an apparatus based on this idea to estimate the unsaturated transverse permeability. They found that taking capillary pressure into consideration could help to obtain relatively accurate measurement results. Ahn et al. [42] applied embedded fiber optic sensors to detect the position of the flow front inside the preform. The idea is to embed optical fibers containing bare spots in the fabrics, and transmit a laser light through the optical fiber. When the test fluid reaches the bare spot, the intensity of light changes, which can be recorded to track as the position of the flow front in time. Nedanov and Advani [44] proposed a SMART weave sensor system to measure the unsaturated transverse permeability. Weave sensors are imbedded in the reinforcing fabrics and send information to a data acquisition system. However, the weave sensor itself results in race tracking and disturbance of the flow, leading to measurement errors.

Magnetic resonance imaging (MRI) is a non-invasive technique which can be used to monitor liquid distribution without tracer. It has been received considerable attention since it can provide flow front information with a high resolution every few seconds. Leisen and Beckham [45] used MRI to characterize the movement of fluids in textiles. Neacsu et al. [46] applied this technique to visualize the impregnation due to capillary forces across aligned cylinders. Endruweit et al. [47] used also MRI to study the local fluid concentration during liquid impregnation. However, this technique remains expensive, and only liquid containing hydrogen and fluorine can be used as test fluid in the measurement.

Saturated permeability measurements rely on several basic assumptions: the flow conditions are stable; the flow behavior is independent of time and distance; and Darcy's law applies, i.e., a linear relationship exists between the flow rate and the pressure drop. Most transverse measurement procedures [41–45] are based on these assumptions. However, they are not always valid based on our preliminary measurements. For example, if the injection pressure exceeds a specific critical value, the saturated transverse permeability tends to depend upon time. This can be explained by the deformation of the fiber bed caused by flow-induced compaction. Hence measurement results might be incorrect without taking this phenomenon into consideration.

Endruweit et al. [48] measured the transverse permeability for injection pressure values between 0.1 MPa and 0.5 MPa for various initial porosity after 5 pressure cycles. They observed a significant hysteretic behavior, especially for the first cycle. They defined the saturated permeability by averaging the permeability values for increasing and decreasing pressures in the range of 0.1 MPa to 0.5 MPa for a high cycle number to neglect the hysteretic effects. However, as mentioned above, a high injection pressure might lead to compaction of the fiber bed, resulting in a decrease of porosity. The real porosity of the sample is lower than the one designed before the measurement. Therefore, averaging the measurement results will underestimate the permeability. Besides, the permeability under a high injection pressure depends on time, so it is difficult to define the right delay to reach the steady state or select the saturated permeability at a given pressure level.

Scholz et al. [49] developed an apparatus to measure the saturated permeability of fibrous preforms using both gas and liquid flows. They pointed out that because of the mold configuration, the flow is not one-dimensional and thus the measurement method underestimates the permeability of the reinforcement (see Figure 2.8), which is no longer governed by the one-dimensional Darcy model. Therefore, they recommended to add a flow enhancement medium to ensure a 1D fluid flow. To measure the permeability for different fiber fractions, they used a hydraulic testing machine to control the thickness of the mold cavity. Hence, a continuous change in fiber volume fraction can be obtained giving the permeability as a function of fiber fraction in one measurement. Ouagne et al. [50, 51] developed a similar experimental setup to conduct continuous permeability measurements. This is a much more efficient method compared to other approaches which only investigate one fiber volume fraction for each measurement. However, this approach might lead to a significant error resulting from the compression of the mold or from flow-induced compaction. As a matter of fact, the deformation of the fiber bed gives a time-dependent permeability.

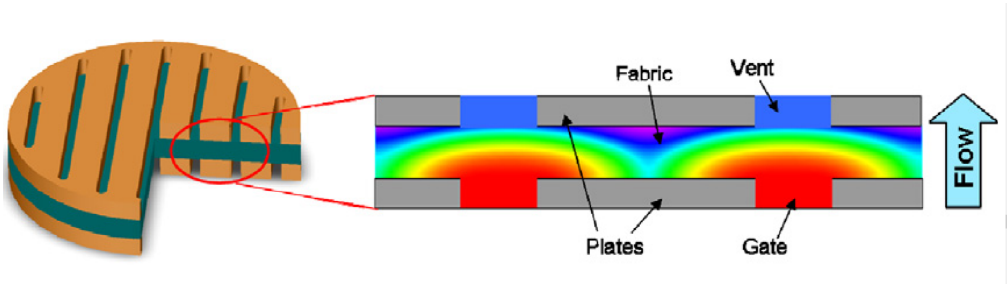

Figure 2.8 Two-dimensional flow due to the geometry of the permeability cell [49].

Klunker et al. [52] investigated this flow-induced compaction of the fiber bed, which explains why the transverse permeability depends on pressure. As shown in Figure 2.9, the fibrous

reinforcement deforms under fluid-induced compaction. Therefore, the fiber volume fraction increases in the impregnation process under high injection pressure, resulting in a decrease of the saturated transverse permeability. Based on this point, they proposed a simulation approach coupling the flow with the fiber deformation in LCM to predict the apparent saturated transverse permeability. They recommended to impose a very low injection pressure in order to ensure a homogeneous fiber volume content, but they did not define the exact value of this low pressure.

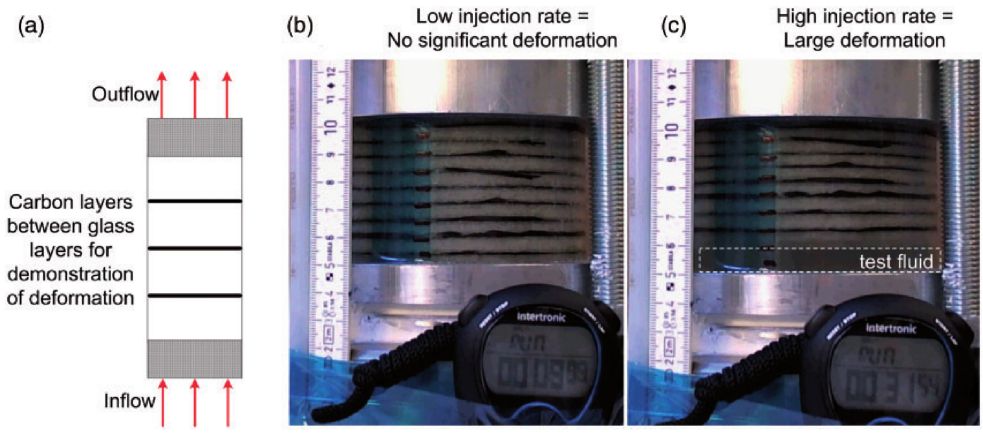

Figure 2.9 Demonstration of textile deformation as a result of transverse fluid flow [52].

The transverse permeability of fabrics is affected by many factors, such as the nesting between fabric layers [53], the deformation of fiber tows resulting from flow-induced compaction [48, 54, 55], reinforcement distortions [56, 57], and dual-scale flow [58–62]. Affected by these factors and also by the intrinsic features of different fabrics, such as the material and the woven pattern, the range of saturated trans- verse permeability can be very large, which generally varies from $10^{-10}\mathrm{m}^2$ ([32, 34, 49, 63, 64]), $10^{-11}\mathrm{m}^2$ ([50, 51, 65, 66]) to $10^{-12}\mathrm{m}^2$ or even lower ([48, 52, 54, 67, 68]). No standard procedure has yet been proven to measure the saturated transverse permeability of fibrous reinforcements. Therefore, an international benchmark exercise was performed recently to compare measurement results of compression and the transverse permeability obtained by 26 different research laboratories. However, as reported in a conference paper of 2018 summing up and comparing the experimental results [69], differences of about two orders of magnitude were observed between the experimental results of participants for the measurement of the same fabrics. Although transverse permeability measurements have been routinely performed for some time, these significant discrepancies show that some experimental issues still need to be clarified. In order to develop an accurate and robust measurement procedure, it is necessary to take into

account the physical phenomena that come into play in liquid flows through stacks of fibrous reinforcements.

2.4 Transverse compaction of fibrous reinforcements

In this section, the works on the transverse compaction of fibrous reinforcements are reviewed, which is directly connected with articles 3 and 4. According to the references, the complex mechanical behaviors of fibrous reinforcements under the transverse compaction due to their dual-scale architectures are clearly presented. Considering the complexity of the geometric modeling and the constitutive relation of the fabrics, we decided to analyze the problems directly based on the digital material twins generated from microtomographic images.

The compression of fibrous reinforcement has been studied for decades. Van Wyk [70] proposed a "1/3" power law $V = \alpha P^{-1/3}$ (where V is the assembly volume and P is the external pressure applied) to describe the compaction of fibrous material, which was extensively used by other investigators. This formula is simple and describes well most parts of the non-linear elastic compaction process. However, it was found that a typical compression curve of a woven fabric consists of three stages (see Figure 2.10), while the formula proposed by Van Wyk can only describe the first two. The first stage is linear: the space between the fibers decreases rapidly and the yarn offers little resistance to the reduction in thickness. In the second stage, which is modelled by an exponential function, the fiber-to-fiber contacts increase, which results in more inter-fiber friction. Consequently, the resistance to an external compressive pressure grows rapidly and the compression becomes a non-linear phenomenon with energy lost in friction. Hence, an hysteresis appears if the compressive load is removed. Finally, in the last stage, the fiber filaments are fully compressed: there are nearly no open spaces left, and the compression curve becomes nearly linear and parallel to the X-axis.

Based on these typical phenomena, many investigations have focused on developing compaction models for computer simulation. Saunders et al. [72] experimentally studied the compression of fabrics, and found in microscopic observations that both the yarn cross-section and waviness change. Hence, the resistance of the yarn in a fabric under compression is higher than without compression. This highlights the importance of considering the contacts between the yarns and the variations of their material properties in the simulation of compaction.

Lomov and Verpoest [73] assumed that the contact width between yarns is equal to the width of the yarns. They investigated experimentally the transverse force between two yarns under compaction to provide a reference for the simulation. This is an interesting approach

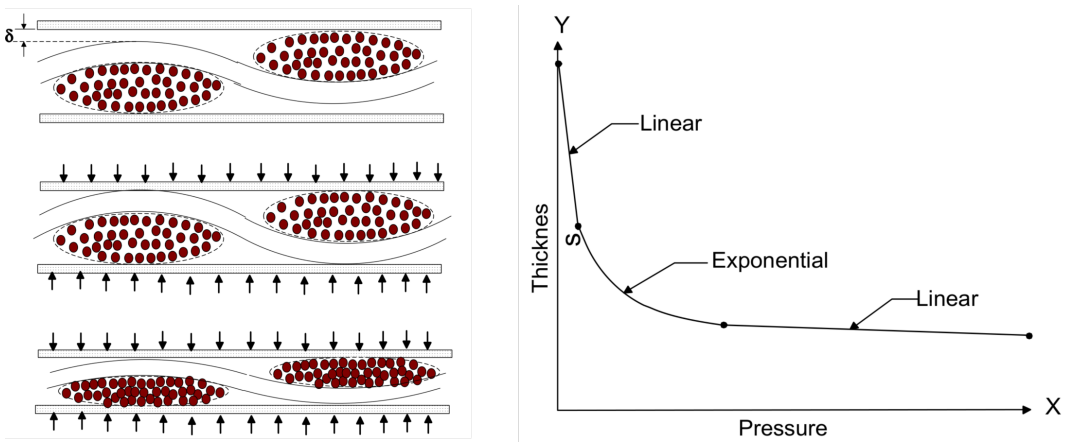

Figure 2.10 Typical compression curve of a woven fabric [71].

to connect numerical and experimental results. However, it is valid only at high pressure. Jeong and Kang [74] constructed a 3D finite element model to simulate the compaction of fabrics, which was verified in experiments for wool and nylon fabrics. However, this method is only applicable for solid polymers with a significantly high transverse modulus. Potluri and Sagar [71] developed a 3D representative volume element for finite element analysis. Considering the simulation efficiency and the symmetry of a plain weave reinforcement, only one quarter of the unit cell is used. They simulated the compaction of fabrics between two rigid plates, considering the geometric non-linearity and friction contact. However, this model is highly idealized and cannot represent the behavior of a bundle of fibers in a real yarn.

A critical issue to construct a finite element model to simulate the compaction of fibrous reinforcements consists of obtaining the real material properties of yarns or of bundles of fiber filaments. Their non-linear bending behavior can be modelled by Kawabata Evaluation System (KES) as mentioned in [4, 71, 75, 76]. Maurin et al. [77] measured experimentally the transverse mechanical properties of carbon fibers by nano-indentation, and used the results in computer simulations [78]. Green et al. [16] assumed that the yarn is a transversely isotropic material and calculated the yarn elastic constants by using a micromechanical *Finite Element* (FE) model with hexagonal fiber packing.

Nguyen et al. [79] followed the method developed by Hivet and Boisse [80] to generate mesostructural geometric models of 2D woven fabrics to simulate transverse compaction. Numerical simulations with a hypoelastic material law based on fiber rotation were in good agreement with experiments. In another approach based on the discrete homogenization method of Goda et al. [81], Rahali et al. [82] could predict the effective mechanical properties of 2.5D and 3D interlock textiles. Zhang et al. [83] developed a mesoscale finite element based

model to predict the mechanical responses and the failure locus under uniaxial and biaxial loads. However, these approaches are based on idealized geometric models, and hence cannot describe mesostructural changes in fiber architecture, namely study in detail how fiber tows are deformed under compaction. Assumptions and simplifications are usually necessary to conduct numerical simulations, which reduce the computational cost, facilitate modeling and provide computer predictions. However, these simplifications may prevent the investigation of some phenomena occurring in real applications, especially in the case of mesoscopic and microscopic issues.

2.5 Wrinkling in membranes and film substrates

Wrinkles are widely observed both in nature and in engineered products. The most common example occurs in elastic membranes under unidirectional tension, in which wrinkles appear in a perpendicular direction as shown in Figure 2.11a. In this specific example, Cerda et al. [84] explained that the sheet buckles to accommodate the in-plane strain incompatibility generated by Poisson effect. As described by Li et al. [85], wrinkles not only exist in pure membranes, but also in membrane related structures, for example film-substrate systems [86, 87] as shown in Figure 2.11b. Since one of the main objectives of this thesis is to develop numerical tools for the analysis of through-thickness injection in LCM variants using deformable membranes, investigations on membrane wrinkling are reviewed in this section, especially works on numerical simulation. As exposed in articles 5 and 6, this will provide an important background information on the numerical methods devised to model membrane wrinkling.

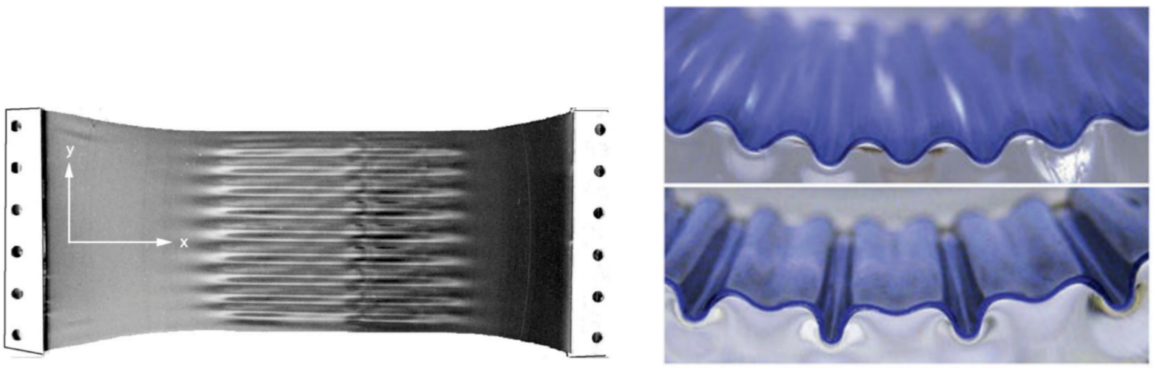

(a) (b)

Figure 2.11 (a) Wrinkles in a rectangular polyethylene sheet [88]; (b) wrinkles and folds in a Polydimethylsiloxane (PDMS) film-substrate system [89].

As discussed by Bowden et al. [90] and Cerda and Mahadevan [88], wrinkling may affect significantly the mechanical, optical and other properties of membranes. Therefore, undesired problems might occur in membranes. For example, in a manufacturing process, wrinkling might lead to production defects [91]. For this reason, instability phenomena in membranes have been widely studied. In a pioneering work, Wagner [92] developed a tension field theory, which assumed that there was no in-plane compressive stress throughout the membrane. It defined a uniaxial tension field with only one nonzero principal stress component in a perpendicular direction with respect to the wrinkles. The tension field theory was widely applied and improved over time. Pipkin [93] proposed a relaxed energy density to replace the strain energy function of the tension field theory for partially wrinkled membranes. This approach was used by Steigmann and Pipkin [94] to investigate the wrinkling of pressurized membranes. In order to study anisotropic membranes in the case of large deformations, Roddeman et al. [95] proposed a new approach with a special deformation tensor modified by a fictive non-wrinkled model. This method was used to correctly describe the stress distribution in anisotropic membranes.

Although the essential cause of wrinkling in membranes is their negligible bending stiffness and the in-plane compressive stress, the occurrence and evolution of wrinkles differ with the geometric shapes of membrane specimens. Wrinkling problems in annular and circular membranes have been widely investigated. Plaut [96] analyzed the large unwrinkled axisymmetric deformations of circular membranes under several different loadings with three different theories, namely the Generalized Reissner theory, Reissner theory and Föppl-von Kármán (FvK) theory. Analytical solutions of wrinkling in annular membranes under different boundary conditions were thoroughly studied by Coman [97, 98]. Géminard et al. [99] experimentally investigated the main features of wrinkles in a prestretched annular membrane under axisymmetric traction in the center. Wang et al. [100] proposed a theoretical model which could accurately predict the critical wrinkling behavior and post-buckling characteristics. This model was verified by comparison with experiments.

Most of the above mentioned studies are based on analytical solutions, which correctly predict the critical wrinkling behavior and stress distribution before bifurcation. However, in some cases, especially in manufacturing applications, monitoring the evolution of wrinkles is important to control the phenomenon and keep it at an acceptable level. For that purpose, a post-buckling analysis is necessary. Since the evolution of wrinkles and stress distribution becomes more complex after bifurcation, which might even cause multiple subsequent bifurcations [101], *Finite Element Analysis* (FEA) has become more suited to analyze wrinkling than analytical methods. In order to solve circumferential wrinkling problems in circular membranes, it is natural to consider the geometric axisymmetric property of membranes as

did Oden and Key [102]. However, the deformations resulting from these instability phenomena are not axisymmetric. Therefore, general axisymmetric finite elements are no longer applicable. Since the wrinkling patterns can be complex and the wave length of the wrinkles remains short, intensive calculations are required for the simulation, especially in the case of a large amount of wave numbers. Combescure [103, 104] developed an efficient and robust finite element procedure to simulate the buckling phenomena in large thin cylindrical shells.

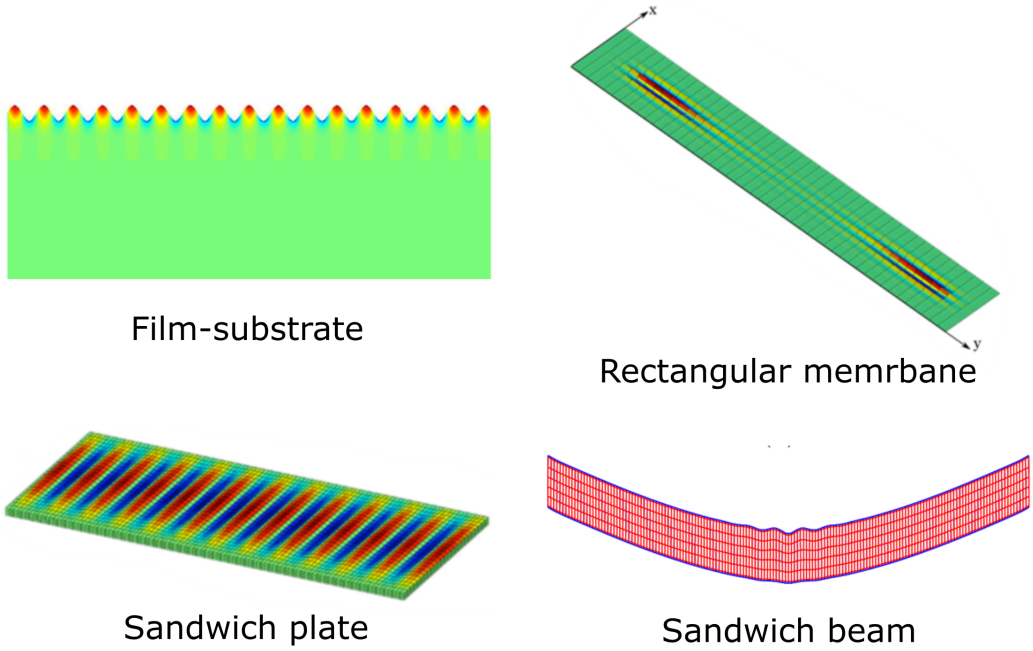

Figure 2.12 Wrinkling of different structures simulated by the Fourier-based reduced model [105–108].

The approximation assumes that there are two different structures, namely a perfect ideal structure and the actual structure with defects, so an initial imperfection can be introduced to simulate the buckling patterns. However, it is difficult to choose a proper imperfection for a specific problem. In order to overcome these difficulties, a new finite element based reduced-order model was proposed by Damil and Potier-Ferry [109] based on multiple scale analysis, which performs well in terms of accuracy and efficiency. This approach was applied to several kinds of instability problems, such as in thin films deposited on compliant substrates [107], in rectangular membranes [108, 110, 111] or in rectangular sandwich plates [105, 106, 112].

2.6 Summary of literature review

The articles reviewed above can be briefly summed up in the following four aspects:

- Accurate simulations of flow properties and mechanical behaviors of fibrous reinforcements need precise mesostructural geometric models. Although idealized models provide an automatic and robust way to construct simplified geometric representations of a material, more realistic models obtained by Micro-CT can describe the geometric details and the variability of real textiles. However, the existing reconstruction approaches still meet some problems when processing relatively large fabric specimens. Besides, no basic geometric criterion is available to assess the accuracy of the reconstructed model.

- Accurate permeability measurements of fibrous reinforcements are important for both manufacturing and academic purposes. Thanks to the contributions of the research institutions participating in the last three international benchmarks on permeability measurements, standard procedures are nearly confirmed for in-plane textile permeability. However, the measurement results of saturated through-thickness permeability still exhibit two orders of magnitude differences among the different research teams who participated in Benchmark III. The main reason is that the transverse permeability of fibrous reinforcements might be affected by several factors. Note that very few studies have investigated relevant possible sources of errors.

- Through-thickness compaction of fibrous reinforcements occurs in several LCM processes. Mesoscopic simulations of transverse compaction have attracted recent interest. A series of assumptions and simplifications are usually necessary to investigate these issues. However, this may prevent from studying some mesoscopic and microscopic phenomena occurring in real applications. Therefore, Micro-CT has been widely used to direct study the mesoscopic deformation of fibrous reinforcements under different loads. However, no research investigation has been reported up to now concerning deformation analyses based on reconstructed models of fabrics at different compaction levels when the fiber tows have been identified and labelled.

- Both local and global wrinkling phenomena might appear in VARTM and FI processes, leading to various defects in final composite parts. In order to investigate these phenomena, numerical simulation is a powerful tool. However, general methods either present intensive computations especially in the case of small wave length or suffer difficulties of choosing a proper imperfection. Although a new Fourier based reduced model was already developed, only rectangular domains have been considered up to now. Fourier based reduced models for local and global wrinkling problems in circular domains need to be developed.

Bibliography

[1] A. Dixit and H. S. Mali, "Modeling techniques for predicting the mechanical properties of woven-fabric textile composites: a review," *Mechanics of composite Materials*, vol. 49, no. 1, pp. 1–20, 2013.

[2] D. P. C. Aiman, M. F. Yahya, and J. Salleh, "Impact properties of 2D and 3D woven composites: a review," in *AIP Conference Proceedings*, vol. 1774, no. 1. AIP Publishing LLC, 2016, p. 020002.

[3] K. H. Leong, B. Lee, I. Herszberg, and M. K. Bannister, "The effect of binder path on the tensile properties and failure of multilayer woven CFRP composites," *Composites Science and Technology*, vol. 60, no. 1, pp. 149–156, 2000.

[4] S. D. Green, A. C. Long, B. S. F. El Said, and S. R. Hallett, "Numerical modelling of 3D woven preform deformations," *Composite Structures*, vol. 108, pp. 747–756, 2014.

[5] F. Desplentere, S. V. Lomov, D. L. Woerdeman, I. Verpoest, M. Wevers, and A. Bogdanovich, "Micro-CT characterization of variability in 3D textile architecture," *Composites Science and Technology*, vol. 65, no. 13, pp. 1920–1930, 2005.

[6] Y. Mahadik and S. R. Hallett, "Finite element modelling of tow geometry in 3D woven fabrics," *Composites Part A: Applied Science and Manufacturing*, vol. 41, no. 9, pp. 1192–1200, 2010.

[7] X. L. Xiao, A. Endruweit, X. S. Zeng, J. L. Hu, and A. Long, "Through-thickness permeability study of orthogonal and angle-interlock woven fabrics," *Journal of Materials Science*, vol. 50, no. 3, pp. 1257–1266, 2015.

[8] F. Gommer, A. Endruweit, and A. C. Long, "Quantification of micro-scale variability in fibre bundles," *Composites Part A: Applied Science and Manufacturing*, vol. 87, pp. 131–137, 2016.

[9] Y. Wang and X. Sun, "Digital-element simulation of textile processes," *Composites Science and Technology*, vol. 61, no. 2, pp. 311–319, 2001.

[10] G. Zhou, X. Sun, and Y. Wang, "Multi-chain digital element analysis in textile mechanics," *Composites Science and Technology*, vol. 64, no. 2, pp. 239–244, 2004.

[11] Y. Miao, E. Zhou, Y. Wang, and B. A. Cheeseman, "Mechanics of textile composites: Micro-geometry," *Composites Science and Technology*, vol. 68, no. 7-8, pp. 1671–1678, 2008.

[12] L. Huang, Y. Wang, Y. Miao, D. Swenson, Y. Ma, and C. Yen, "Dynamic relaxation approach with periodic boundary conditions in determining the 3-D woven textile micro-geometry," *Composite Structures*, vol. 106, pp. 417–425, 2013.

[13] Z. Yousaf, P. Potluri, P. J. Withers, D. Mollenhauer, E. Zhou, and S. Duning, "Digital element simulation of aligned tows during compaction validated by computed tomography (CT)," *International Journal of Solids and Structures*, vol. 154, pp. 78–87, 2018.

[14] A. Drach, B. Drach, and I. Tsukrov, "Processing of fiber architecture data for finite element modeling of 3D woven composites," *Advances in Engineering Software*, vol. 72, pp. 18–27, 2014.

[15] S. Joglekar and M. Pankow, "Modeling of 3D woven composites using the digital element approach for accurate prediction of kinking under compressive loads," *Composite Structures*, vol. 160, pp. 547–559, 2017.

[16] S. D. Green, M. Y. Matveev, A. C. Long, D. Ivanov, and S. R. Hallett, "Mechanical modelling of 3D woven composites considering realistic unit cell geometry," *Composite Structures*, vol. 118, pp. 284–293, 2014.

[17] B. El Said, S. Green, and S. R. Hallett, "Kinematic modelling of 3D woven fabric deformation for structural scale features," *Composites Part A: Applied Science and Manufacturing*, vol. 57, pp. 95–107, 2014.

[18] A. J. Thompson, B. El Said, D. Ivanov, J. P. H. Belnoue, and S. R. Hallett, "High fidelity modelling of the compression behaviour of 2D woven fabrics," *International Journal of Solids and Structures*, vol. 154, pp. 104–113, 2018.

[19] M. Sherburn, "Geometric and mechanical modelling of textiles," Ph.D. dissertation, University of Nottingham, 2007.

[20] A. C. Long and L. P. Brown, "Modelling the geometry of textile reinforcements for composites: TexGen," in *Composite Reinforcements for Optimum Performance*, 2011, pp. 239–264.

[21] I. Verpoest and S. V. Lomov, "Virtual textile composites software WiseTex: Integration with micro-mechanical, permeability and structural analysis," *Composites Science and Technology*, vol. 65, pp. 2563–2574, 2005.

[22] S. V. Lomov, "Modelling the geometry of textile reinforcements for composites: Wisetex," in *Composite reinforcements for optimum performance*. Elsevier, 2011, pp. 200–238.

[23] E. N. Landis and D. T. Keane, "X-ray microtomography," *Materials characterization*, vol. 61, no. 12, pp. 1305–1316, 2010.

[24] N. Naouar, E. Vidal-Sallé, J. Schneider, E. Maire, and P. Boisse, "Meso-scale FE analyses of textile composite reinforcement deformation based on X-ray computed tomography," *Composite Structures*, vol. 116, no. 1, pp. 165–176, 2014.

[25] N. Naouar, E. Vidal-Sallé, J. Schneider, E. Maire, and P. Boisse, "3D composite reinforcement meso F.E. analyses based on X-ray computed tomography," *Composite Structures*, vol. 132, pp. 1094–1104, 2015.

[26] J. Bigun, T. Bigun, and K. Nilsson, "Recognition by symmetry derivatives and the generalized structure tensor," *IEEE Transactions on Pattern Analysis and Machine Intelligence*, vol. 26, no. 12, pp. 1590–1605, 2004.

[27] R. M. Haralick and L. G. Shapiro, *Computer and robot vision*. Addison-wesley Reading, 1992, vol. 1.

[28] P. J. Schilling, B. R. Karedla, A. K. Tatiparthi, M. A. Verges, and P. D. Herrington, "X-ray computed microtomography of internal damage in fiber reinforced polymer matrix composites," *Composites Science and Technology*, vol. 65, no. 14, pp. 2071–2078, 2005.

[29] J. S. U. Schell, M. Renggli, G. H. van Lenthe, R. Müller, and P. Ermanni, "Micro-computed tomography determination of glass fibre reinforced polymer meso-structure," *Composites Science and Technology*, vol. 66, no. 13, pp. 2016–2022, 2006.

[30] J. S. U. Schell, M. Deleglise, C. Binetruy, P. Krawczak, and P. Ermanni, "Numerical prediction and experimental characterisation of meso-scale-voids in liquid composite moulding," *Composites Part A: Applied Science and Manufacturing*, vol. 38, no. 12, pp. 2460–2470, 2007.

[31] A. Madra, N. El Hajj, and M. Benzeggagh, "X-ray microtomography applications for quantitative and qualitative analysis of porosity in woven glass fiber reinforced thermoplastic," *Composites Science and Technology*, vol. 95, pp. 50–58, 2014.

[32] M. A. Ali, R. Umer, K. A. Khan, S. Bickerton, and W. J. Cantwell, "Non-destructive evaluation of through-thickness permeability in 3D woven fabrics for composite fan blade applications," *Aerospace Science and Technology*, vol. 82-83, pp. 520–533, 2018.

[33] M. A. Ali, R. Umer, K. A. Khan, and W. J. Cantwell, "In-plane virtual permeability characterization of 3D woven fabrics using a hybrid experimental and numerical approach," *Composites Science and Technology*, vol. 173, pp. 99–109, 2019.

[34] M. A. Ali, R. Umer, K. A. Khan, and W. J. Cantwell, "XCT-scan assisted flow path analysis and permeability prediction of a 3D woven fabric," *Composites Part B: Engineering*, vol. 176, p. 107320, 2019.

[35] A. Mendoza, J. Schneider, E. Parra, E. Obert, and S. Roux, "Differentiating 3D textile composites: A novel field of application for Digital Volume Correlation," *Composite Structures*, vol. 208, pp. 735–743, 2019.

[36] A. Mendoza, J. Schneider, E. Parra, and S. Roux, "Measuring yarn deformations induced by the manufacturing process of woven composites," *Composites Part A: Applied Science and Manufacturing*, vol. 120, pp. 127–139, 2019.

[37] I. Straumit, S. V. Lomov, and M. Wevers, "Quantification of the internal structure and automatic generation of voxel models of textile composites from X-ray computed tomography data," *Composites Part A: Applied Science and Manufacturing*, vol. 69, pp. 150–158, 2015.

[38] A. Madra, P. Breitkopf, A. Rassineux, and F. Trochu, "Image-based model reconstruction and meshing of woven reinforcements in composites," *International Journal for Numerical Methods in Engineering*, vol. 112, no. 9, pp. 1235–1252, 2017.

[39] P. Ferland, D. Guittard, and F. Trochu, "Concurrent methods for permeability measurement in resin transfer molding," *Polymer Composites*, vol. 17, no. 1, pp. 149–158, 1996.

[40] J. R. Weitzenböck, R. A. Shenoi, and P. A. Wilson, "Radial flow permeability measurement. Part A: Theory," *Composites Part A: Applied Science and Manufacturing*, vol. 30, no. 6, pp. 781–796, 1999.

[41] J. R. Weitzenböck, R. A. Shenoi, and P. A. Wilson, "Radial flow permeability measurement. Part B: Application," *Composites part A: Applied Science and Manufacturing*, vol. 30, no. 6, pp. 797–813, 1999.

[42] S. H. Ahn, W. I. Lee, and G. S. Springer, "Measurement of the three-dimensional permeability of fiber preforms using embedded fiber optic sensors," *Journal of Composite Materials*, vol. 29, no. 6, pp. 714–733, 1995.

[43] M. Li, S. K. Wang, Y. Z. Gu, Y. X. Li, K. Potter, and Z. G. Zhang, "Evaluation of through-thickness permeability and the capillary effect in vacuum assisted liquid molding process," *Composites Science and Technology*, vol. 72, no. 8, pp. 873–878, 2012.

[44] P. B. Nedanov and S. G. Advani, "A method to determine 3D permeability of fibrous reinforcements," *Journal of Composite Materials*, vol. 36, no. 2, pp. 241–254, 2002.

[45] J. Leisen and H. W. Beckham, "Quantitative magnetic resonance imaging of fluid distribution and movement in textiles," *Textile research journal*, vol. 71, no. 12, pp. 1033–1045, 2001.

[46] V. Neacsu, J. Leisen, H. W. Beckham, and S. G. Advani, "Use of magnetic resonance imaging to visualize impregnation across aligned cylinders due to capillary forces," *Experiments in fluids*, vol. 42, no. 3, pp. 425–440, 2007.

[47] A. Endruweit, P. Glover, K. Head, and A. C. Long, "Mapping of the fluid distribution in impregnated reinforcement textiles using Magnetic Resonance Imaging: Application and discussion," *Composites Part A: Applied Science and Manufacturing*, vol. 42, no. 10, pp. 1369–1379, 2011.

[48] A. Endruweit, T. Luthy, and P. Ermanni, "Investigation of the influence of textile compression on the out-of-plane permeability of a bidirectional glass fiber fabric," *Polymer Composites*, vol. 23, no. 4, pp. 538–554, 2002.

[49] S. Scholz, J. W. Gillespie, and D. Heider, "Measurement of transverse permeability using gaseous and liquid flow," *Composites Part A: Applied Science and Manufacturing*, vol. 38, no. 9, pp. 2034–2040, 2007.

[50] P. Ouagne and J. Bréard, "Continuous transverse permeability of fibrous media," *Composites Part A: Applied Science and Manufacturing*, vol. 41, no. 1, pp. 22–28, 2010.

[51] P. Ouagne, T. Ouahbi, C. H. Park, J. Bréard, and A. Saouab, "Continuous measurement of fiber reinforcement permeability in the thickness direction: Experimental technique and validation," *Composites Part B: Engineering*, vol. 45, no. 1, pp. 609–618, 2013.

[52] F. Klunker, M. Danzi, and P. Ermanni, "Fiber deformation as a result of fluid injection: modeling and validation in the case of saturated permeability measurements in through thickness direction," *Journal of Composite Materials*, vol. 49, no. 9, pp. 1091–1105, 2015.

[53] S. V. Lomov, I. Verpoest, T. Peeters, D. Roose, and M. Zako, "Nesting in textile laminates: geometrical modelling of the laminate," *Composites Science and Technology*, vol. 63, no. 7, pp. 993–1007, 2003.

[54] D. Becker and P. Mitschang, "Measurement system for on-line compaction monitoring of textile reaction to out-of-plane impregnation," *Advanced Composites Letters*, vol. 23, no. 2, p. 096369351402300202, 2014.

[55] B. Willenbacher, A. Kabachi, D. May, P. Mitschang, and P. Ermanni, "Flow induced sample deformations in out-of-plane permeability measurement," in *ECCM18 - 18th European Conference on Composite Materials*, 2018.

[56] M. Bodaghi, S. V. Lomov, P. Simacek, N. C. Correia, and S. G. Advani, "On the variability of permeability induced by reinforcement distortions and dual scale flow in liquid composite moulding: A review," *Composites Part A: Applied Science and Manufacturing*, 2019.

[57] A. Endruweit, X. Zeng, M. Matveev, and A. C. Long, "Effect of yarn cross-sectional shape on resin flow through inter-yarn gaps in textile reinforcements," *Composites Part A: Applied Science and Manufacturing*, vol. 104, pp. 139–150, 2018.

[58] N. Kuentzer, P. Simacek, S. G. Advani, and S. Walsh, "Permeability characterization of dual scale fibrous porous media," *Composites Part A: Applied Science and Manufacturing*, vol. 37, no. 11, pp. 2057–2068, 2006.

[59] E. Ruiz, V. Achim, S. Soukane, F. Trochu, and J. Bréard, "Optimization of injection flow rate to minimize micro/macro-voids formation in resin transfer molded composites," *Composites Science and Technology*, vol. 66, no. 3-4, pp. 475–486, 2006.

[60] C. Ravey, E. Ruiz, and F. Trochu, "Determination of the optimal impregnation velocity in resin transfer molding by capillary rise experiments and infrared thermography," *Composites Science and Technology*, vol. 99, pp. 96–102, 2014.

[61] M. Imbert, S. Comas-Cardona, E. Abisset-Chavanne, and D. Prono, "Experimental investigation of intra-tow fluid storage mechanisms in dual-scale fiber reinforcements," *Composites Part A: Applied Science and Manufacturing*, vol. 107, pp. 70–82, 2018.

[62] J. Bréard, Y. Henzel, F. Trochu, and R. Gauvin, "Analysis of dynamic flows through porous media. Part I: Comparison between saturated and unsaturated flows in fibrous reinforcements," *Polymer Composites*, vol. 24, no. 3, pp. 391–408, 2003.

[63] B. Yang, S. Wang, and Y. Wang, "Effect of nesting in laminates on the through-thickness permeability of woven fabrics," *Applied Composite Materials*, vol. 25, no. 5, pp. 1237–1253, 2018.

[64] E. E. Swery, T. Allen, S. Comas-Cardona, Q. Govignon, C. Hickey, J. Timms, L. Tournier, A. Walbran, P. Kelly, and S. Bickerton, "Efficient experimental characterisation of the permeability of fibrous textiles," *Journal of Composite Materials*, vol. 50, no. 28, pp. 4023–4038, 2016.

[65] H. S. Sas, E. B. Wurtzel, P. Simacek, and S. G. Advani, "Effect of relative ply orientation on the through-thickness permeability of unidirectional fabrics," *Composites Science and Technology*, vol. 96, pp. 116–121, 2014.

[66] X. S. Zeng, A. C. Long, F. Gommer, A. Endruweit, and M. Clifford, "Modelling compaction effect on permeability of 3D carbon reinforcements," in *18th International Conference on Composites Materials, Jeju Island, Korea*, 2011.

[67] S. Drapier, A. Pagot, A. Vautrin, and P. Henrat, "Influence of the stitching density on the transverse permeability of non-crimped new concept (NC2) multiaxial reinforcements: Measurements and predictions," *Composites Science and Technology*, vol. 62, no. 15, pp. 1979–1991, 2002.

[68] M. Danzi, F. Klunker, and P. Ermanni, "Experimental validation of through-thickness resin flow model in the consolidation of saturated porous media," *Journal of Composite Materials*, vol. 51, no. 17, pp. 2467–2475, 2017.

[69] D. May, A. Aktas, and A. Yong, "International benchmark exercises of textile permeability and compressibility characterization," in *ECCM18 - 18th European Conference on Composite Materials*, 2018.

[70] C. M. van Wyk, "Note on the compressibility of wool," *Journal of the Textile Institute Transactions*, vol. 37, no. 12, pp. T285–T292, 1946.

[71] P. Potluri and T. V. Sagar, "Compaction modelling of textile preforms for composite structures," *Composite Structures*, vol. 86, no. 1-3, pp. 177–185, 2008.

[72] R. A. Saunders, C. Lekakou, and M. G. Bader, "Compression and microstructure of fibre plain woven cloths in the processing of polymer composites," *Composites Part A: Applied Science and Manufacturing*, vol. 29, no. 4, pp. 443–454, 1998.

[73] S. V. Lomov and I. Verpoest, "Compression of woven reinforcements: A mathematical model," *Journal of Reinforced Plastics and Composites*, vol. 19, no. 16, pp. 1329–1350, 2000.

[74] Y. J. Jeong and T. J. Kang, "Analysis of compressional deformation of woven fabric using finite element method," *Journal of the Textile Institute*, vol. 92, no. 1, pp. 1–15, 2001.

[75] P. Badel, E. Vidal-Sallé, E. Maire, and P. Boisse, "Simulation and tomography analysis of textile composite reinforcement deformation at the mesoscopic scale," *Composites Science and Technology*, vol. 68, no. 12, pp. 2433–2440, 2008.

[76] H. Lin, M. Sherburn, J. Crookston, A. C. Long, M. J. Clifford, and I. A. Jones, "Finite element modelling of fabric compression," *Modelling and Simulation in Materials Science and Engineering*, vol. 16, no. 3, p. 035010, 2008.

[77] R. Maurin, P. Davies, N. Baral, and C. Baley, "Transverse properties of carbon fibres by nano-indentation and micro-mechanics," *Applied Composite Materials*, vol. 15, no. 2, p. 61, 2008.

[78] X. Zeng, L. P. Brown, A. Endruweit, M. Matveev, and A. C. Long, "Geometrical modelling of 3D woven reinforcements for polymer composites: Prediction of fabric permeability and composite mechanical properties," *Composites Part A: Applied Science and Manufacturing*, vol. 56, pp. 150–160, 2014.

[79] Q. T. Nguyen, E. Vidal-Sallé, P. Boisse, C. H. Park, A. Saouab, J. Bréard, and G. Hivet, "Mesoscopic scale analyses of textile composite reinforcement compaction," *Composites Part B: Engineering*, vol. 44, no. 1, pp. 231–241, 2013.

[80] G. Hivet and P. Boisse, "Consistent 3D geometrical model of fabric elementary cell. Application to a meshing preprocessor for 3D finite element analysis," *Finite Elements in Analysis and Design*, vol. 42, no. 1, pp. 25–49, 2005.

[81] I. Goda, M. Assidi, and J. F. Ganghoffer, "Equivalent mechanical properties of textile monolayers from discrete asymptotic homogenization," *Journal of the Mechanics and Physics of Solids*, vol. 61, no. 12, pp. 2537–2565, 2013.

[82] Y. Rahali, M. Assidi, I. Goda, A. Zghal, and J. F. Ganghoffer, "Computation of the effective mechanical properties including nonclassical moduli of 2.5D and 3D interlocks by micromechanical approaches," *Composites Part B: Engineering*, vol. 98, pp. 194–212, 2016.

[83] D. Zhang, Y. Sun, X. Wang, and L. Chen, "Meso-scale finite element analyses of three-dimensional five-directional braided composites subjected to uniaxial and biaxial loading," *Journal of Reinforced Plastics and Composites*, vol. 34, no. 24, pp. 1989–2005, 2015.

[84] E. Cerda, K. Ravi-Chandar, and L. Mahadevan, "Thin films: Wrinkling of an elastic sheet under tension," *Nature*, vol. 419, no. 6907, pp. 579–580, 2002.

[85] B. Li, Y. Cao, X. Feng, and H. Gao, "Mechanics of morphological instabilities and surface wrinkling in soft materials: A review," *Soft Matter*, vol. 8, pp. 5728–5745, 2012.

[86] X. Chen and J. W. Hutchinson, "Herringbone buckling patterns of compressed thin films on compliant substrates," *Journal of Applied Mechanics*, vol. 71, p. 597, 2004.

[87] J. W. Wang, B. Li, Y. P. Cao, and X. Q. Feng, "Surface wrinkling patterns of film–substrate systems with a structured interface," *Journal of Applied Mechanics*, vol. 82, p. 051009, 2015.

[88] E. Cerda and L. Mahadevan, "Geometry and physics of wrinkling," *Physical Review Letters*, vol. 90, no. 7, p. 074302, 2003.

[89] F. Brau, H. Vandeparre, A. Sabbah, C. Poulard, A. Boudaoud, and P. Damman, "Multiple-length-scale elastic instability mimics parametric resonance of nonlinear oscillators," *Nature Physics*, vol. 7, no. 1, pp. 56–60, 2011.

[90] N. Bowden, S. Brittain, A. G. Evans, J. W. Hutchinson, and G. M. Whitesides, "Spontaneous formation of ordered structures in thin films of metals supported on an elastomeric polymer," *Nature*, vol. 393, no. May, pp. 146–149, 1998.

[91] N. Jacques, A. Elias, M. Potier-Ferry, and H. Zahrouni, "Buckling and wrinkling during strip conveying in processing lines," *Journal of Materials Processing Technology*, vol. 190, no. 1-3, pp. 33–40, 2007.

[92] H. Wagner, "Flat sheet metal girders with very thin metal web. Part I : General theories and assumptions," *Zeitschrift für Motortechnik und Luftschiffahrt*, vol. 20, no. 8, pp. 200–207, 1929.

[93] A. C. Pipkin, "Integration of an equation in membrane theory," *Zeitschrift für angewandte Mathematik und Physik ZAMP*, vol. 19, no. 5, pp. 818–819, 1968.

[94] D. J. Steigmann and A. C. Pipkin, "Wrinkling of pressurized membranes," *Journal of Applied Mechanics*, vol. 56, no. 3, p. 624, 1989.

[95] D. G. Roddeman, J. Drukker, C. W. J. Oomens, and J. D. Janssen, "The wrinkling of thin membranes : Part I — theory," *Journal of Applied Mechanics*, vol. 54, pp. 884–887, 1987.

[96] R. H. Plaut, "Linearly elastic annular and circular membranes under radial, transverse, and torsional loading. Part I: Large unwrinkled axisymmetric deformations," *Acta Mechanica*, vol. 202, pp. 79–99, 2009.

[97] C. D. Coman, "On the applicability of tension field theory to a wrinkling instability problem," *Acta Mechanica*, vol. 190, pp. 57–72, 2007.

[98] C. D. Coman, "Some applications of the WKB method to the wrinkling of bi-annular plates in tension," *Acta Mechanica*, vol. 224, pp. 399–423, 2013.

[99] J. C. Géminard, R. Bernai, and F. Melo, "Wrinkle formations in axi-symmetrically stretched membranes," *European Physical Journal E*, vol. 15, pp. 117–126, 2004.

[100] C. G. Wang, Y. P. Liu, L. Lan, L. Li, and H. F. Tan, "Post-wrinkling analysis of a torsionally sheared annular thin film by using a compound series method," *International Journal of Mechanical Sciences*, vol. 110, pp. 22–33, 2016.

[101] F. Xu, M. Potier-Ferry, S. Belouettar, and H. Hu, "Multiple bifurcations in wrinkling analysis of thin films on compliant substrates," *International Journal of Non-Linear Mechanics*, vol. 76, pp. 203–222, 2015.

[102] J. T. Oden and J. E. Key, "Numerical analysis of finite axisymmetric deformations of incompressible elastic solid of revolution," *International Journal of Solids and Structures*, vol. 6, pp. 497–518, 1970.

[103] A. G. Combescure, "Static and dynamic buckling of large thin shells," *Nuclear Engineering and Design*, vol. 92, pp. 339–354, 1986.

[104] A. G. Combescure, "Modeling elastic-plastic buckling of sandwich axisymmetric shells: On the limits of " shell " models and analytical solutions," *Advanced Modeling and Simulation in Engineering Sciences*, pp. 1–27, 2014.

[105] Y. Liu, K. Yu, H. Hu, S. Belouettar, M. Potier-Ferry, and N. Damil, "A new Fourier-related double scale analysis for instability phenomena in sandwich structures," *International Journal of Solids and Structures*, vol. 49, no. 22, pp. 3077–3088, 2012.

[106] Q. Huang, Y. Liu, H. Hu, Q. Shao, K. Yu, G. Giunta, S. Belouettar, and M. Potier-Ferry, "A Fourier-related double scale analysis on the instability phenomena of sandwich plates," *Computer Methods in Applied Mechanics and Engineering*, vol. 318, pp. 270–295, 2017.

[107] Q. Huang, J. Yang, W. Huang, Y. Liu, H. Hu, G. Giunta, and S. Belouettar, "A new Fourier-related double scale analysis for wrinkling analysis of thin films on compliant substrates," *Composite Structures*, vol. 160, pp. 613–624, 2017.

[108] Q. Huang, H. Hu, K. Yu, M. Potier-Ferry, S. Belouettar, and N. Damil, "Macroscopic simulation of membrane wrinkling for various loading cases," *International Journal of Solids and Structures*, vol. 64-65, pp. 246–258, 2015.

[109] N. Damil and M. Potier-Ferry, "Influence of local wrinkling on membrane behaviour: A new approach by the technique of slowly variable Fourier coefficients," *Journal of the Mechanics and Physics of Solids*, vol. 58, no. 8, pp. 1139–1153, 2010.

[110] N. Damil, M. Potier-ferry, and H. Hu, "New nonlinear multi-scale models for wrinkled membranes," *Comptes Rendus Mecanique*, vol. 341, no. 8, pp. 616–624, 2013.

[111] N. Damil, M. Potier-Ferry, and H. Hu, "Membrane wrinkling revisited from a multi-scale point of view," *Advanced Modeling and Simulation in Engineering Sciences*, vol. 1, no. 1, p. 6, 2014.

[112] K. Yu, H. Hu, S. Chen, S. Belouettar, and M. Potier-Ferry, "Multi-scale techniques to analyze instabilities in sandwich structures," *Composite Structures*, vol. 96, pp. 751–762, 2013.

CHAPTER 3 OBJECTIVES OF THE THESIS

According to the literature review carried out above, a series of research issues in LCM have been identified. In order to solve these issues, several objectives are proposed in the sequel. Finally, an outline of the thesis will be presented.

3.1 Research issues

3.1.1 Mesostructural geometric reconstruction

Setting up a geometric model of the material is the basic requirement to conduct computer simulations. With the development of computer visualization and advanced image analysis, X-ray microtomography has become more widely used in recent years to study composite materials. It is possible to generate more realistic models of woven fibrous reinforcements from microtomographic images, but the construction of mesostructural geometric models based on existing image processing techniques bears the following limitations:

1. A relatively high resolution scan is required for accurate segmentation, which limits the geometric dimensions of observed specimens.
2. One single fabric layer can be successfully reconstructed by existing methods. However, processing specimens containing stacks of multiple fabric layers with nesting remains arduous.
3. Unpredictable and uncontrollable errors are introduced when employing standard image processing techniques, especially in lower resolution images.
4. The geometrical accuracy of reconstructed geometric models is not systematically assessed.

3.1.2 Saturated transverse permeability measurement

Knowledge of transverse permeability is important not only for process simulation, but also to set up the fabrication procedure. However, transverse permeability is rather complex to measure compared to in-plane permeability, which can be routinely and reliably evaluated. As mentioned above, differences of about two orders of magnitude were observed between the experimental results of transverse permeability measured by the 26 participants of Benchmark III for the same fabrics [1]. It is difficult to precisely measure the transverse permeability,

because it is simultaneously affected by diverse factors, for example the geometric features of the test mold, nesting between fabric layers, and flow-induced compaction of the fiber bed. Numerical simulations provide an efficient way to study the permeability of engineering fabrics and reveal the critical phenomena occurring during the liquid impregnation of the fibrous reinforcement. However, in LCM processes, numerical simulations at the mesoscale and microscale levels cannot take into account the effect of material variability, whereas this is possible in experiments.

3.1.3 Analysis of transverse compaction at the mesoscopic scale

As mentioned above, two different compaction phenomena appear in LCM processes based on transverse flows, namely fiber compaction during mold closing and flow-induced compression during liquid impregnation. Both phenomena are related to the dual-scale architecture of engineering fabrics. Thus it is necessary to study the transverse compactions of fibrous reinforcements during the entire processing cycle. However, fabrics exhibit a highly non-linear, viscoelastic compaction behavior in the transverse direction. Elastic bending and compression of fiber tows as well as friction forces result from their rearrangement under transverse compaction loads. Many efforts have been devoted to construct empirical models based on experiments. However, to reach a better understanding of the compaction behavior of dual-scale fibrous reinforcements, it is necessary to integrate the numerical tools with experiments.

3.1.4 Membrane wrinkling simulation

The deformation of membranes can be complex to assess if wrinkling occurs during the injection process. In manufacturing processes, a proper solution may not be to prevent wrinkling, since it can be difficult, but rather to monitor and control the level of wrinkling. Therefore, the analysis after wrinkling, also called post-buckling analysis, might be more important than just predicting the bifurcation point associated to the critical instability load. However, the simulation of membrane wrinkling requires a fairly large number of computations and high number of finite elements, especially in the case of short wave lengths. In some cases, the standard finite element models have problems in correctly predicting the wrinkling patterns. Besides, no investigations were found on the effects of membrane wrinkling in LCM processes. Therefore, finite element models are needed to correctly predict the wrinkling patterns and capture efficiently the entire instability phenomena.

3.2 Objectives

The thesis aims to investigate the above-mentioned research issues and carry out a multi-scale analysis to deal with key issues of LCM processes, especially the ones connected with transverse flows during through-thickness liquid impregnation such as in VARTM and FI. It is possible to employ the methods developed here to analyze the mechanical response of deformable membranes, obtain precise values of saturated transverse permeability, characterize the dual-scale architecture of engineering fabrics, and analyze the deformation of woven fibrous reinforcements under the transverse compaction. Several more specific objectives are introduced in the sequel.

1. In order to resolve the issues of mesostructural geometric reconstruction, the first objective of the current work is to develop a geometric modeling framework based on microtomographic scans, named *Micro-CT Aided Geometric Modeling* (Mico-CT AGM), and use the geometric features of real textile specimens to generate material twins of multi-layer woven fabrics. Besides, a multiple morphological factor criterion is developed to assess the model accuracy directly from a series of selected geometric features. Thus, the relative accuracy of the reconstructed geometric models can be evaluated with respect to the resolution of the microtomographic scan directly from their geometric features instead of indirectly from the results of numerical simulations.

2. The second objective is to improve the existing experimental measurement approach and conduct flow simulations on the novel material twins to study the saturated transverse permeability of 2D woven fabrics. The original in situ compaction device developed by Hilal [2] for microtomographic investigations was used to scan a stack of fabric layers at different levels of compaction. The Micro-CT AGM is then employed to construct, from X-ray microtomographic voxel images of fibrous reinforcements, material twins for several increasing fiber volume contents.

3. The third objective of this thesis is to analyze of the mesoscopic deformation of fibrous reinforcements directly based on the observation of their mesoscopic architecture. Material twins of increasing fiber volume content are reconstructed and employed to extract the geometric features of fiber tows and study their evolution with the compaction levels. Besides, in order to quantitatively evaluate the mesoscopic deformations of fiber tows, a new correlation technique based on material twin is proposed to track the displacements of contour points in the cross-sections of fiber tows during compaction.

4. The final objective consists of developing a Fourier based reduced model to analyze membrane wrinkling in LCM. Considering that reduced models in Cartesian coordinates were already devised to study wrinkling in rectangular membranes [3–10], the current work focused on the development of an efficient model for circular membranes. The accuracy and efficiency of reduced models are verified by comparing numerical predictions obtained with ABAQUS with analytical results. Based on the modeling results, the instability mechanism in circular membranes were thoroughly investigated for different geometries and loading conditions.

3.3 Outline of the thesis

Solutions to the four above-mentioned objectives are described in 6 articles presented in the following chapters:

- Chapter 4 presents the first article published in *Composites Part A: Applied Science and Manufacturing*, which introduce the proposed *Micro-CT Aided Geometric Modeling* (Micro-CT AGM) to generate the material twin models of the multiple-layer 2D woven fabrics and 3D orthogonal textiles. A multiple factor morphological criterion is developed to assess the accuracy of the reconstructed model.

- Chapter 5 contains the second article published in *Polymer Composites*, in which the numerical and experimental investigations of saturated transverse permeability of 2D woven glass fabrics were carried out based on material twins. Several key issues were considered to improve the existing experimental procedures. Both approaches are employed to discuss the effect of nesting between fabric layers on the saturated transverse permeability of specimens.

- Chapters 6 and 7 respectively present the third and fourth articles that are an article in two parts published in *Composite Structures*. The mesoscopic deformation of 2D woven fibrous reinforcements under the transverse compaction was analyzed based on material twin models. In the first part, the evolution of the geometric features of fiber tows with the compaction levels is investigated. In the second part, a new correlation approach is proposed to quantitatively evaluate the deformation of fiber tows.

- Chapter 8 presents the fifth article published in *Computer Methods in Applied Mechanics and Engineering*, which introduces the development of the Fourier-based reduced model for the wrinkling analysis of circular membranes. The efficiency and accuracy of the model are verified by comparing the numerical simulations with results obtained by

ABAQUS. Besides, several wrinkling problems in circular membranes under different loads are also discussed to reveal the mechanisms of wrinkling.

- Chapter 9 is the last article submitted to *Thin-Walled Structures*, in which the reduced model is further improved by accounting for several Fourier harmonics. The instability mechanisms of an annular membrane under in-plane stretching is investigated.

- Chapter 11 is the conclusion of the thesis, which provides a general synthesis of the work. The approaches and the results are briefly summed up, while the limitations and possible extensions of the works are discussed.

Bibliography

[1] D. May, A. Aktas, and A. Yong, "International benchmark exercises of textile permeability and compressibility characterization," in *ECCM18 - 18th European Conference on Composite Materials*, 2018.

[2] S. Hilal, "Caractérisation par microtomographie de la mésostructure des renforts fibreux pour la fabrication de composites par injection," Ph.D. dissertation, École Polytechinque de Montréal, 2018.

[3] N. Damil and M. Potier-Ferry, "Influence of local wrinkling on membrane behaviour: A new approach by the technique of slowly variable Fourier coefficients," *Journal of the Mechanics and Physics of Solids*, vol. 58, no. 8, pp. 1139–1153, 2010.

[4] Q. Huang, J. Yang, W. Huang, Y. Liu, H. Hu, G. Giunta, and S. Belouettar, "A new Fourier-related double scale analysis for wrinkling analysis of thin films on compliant substrates," *Composite Structures*, vol. 160, pp. 613–624, 2017.

[5] N. Damil, M. Potier-ferry, and H. Hu, "New nonlinear multi-scale models for wrinkled membranes," *Comptes Rendus Mecanique*, vol. 341, no. 8, pp. 616–624, 2013.

[6] N. Damil, M. Potier-Ferry, and H. Hu, "Membrane wrinkling revisited from a multi-scale point of view," *Advanced Modeling and Simulation in Engineering Sciences*, vol. 1, no. 1, p. 6, 2014.

[7] Q. Huang, H. Hu, K. Yu, M. Potier-Ferry, S. Belouettar, and N. Damil, "Macroscopic simulation of membrane wrinkling for various loading cases," *International Journal of Solids and Structures*, vol. 64-65, pp. 246–258, 2015.

[8] Y. Liu, K. Yu, H. Hu, S. Belouettar, M. Potier-Ferry, and N. Damil, "A new Fourier-related double scale analysis for instability phenomena in sandwich structures," *International Journal of Solids and Structures*, vol. 49, no. 22, pp. 3077–3088, 2012.

[9] K. Yu, H. Hu, S. Chen, S. Belouettar, and M. Potier-Ferry, "Multi-scale techniques to analyze instabilities in sandwich structures," *Composite Structures*, vol. 96, pp. 751–762, 2013.

[10] Q. Huang, Y. Liu, H. Hu, Q. Shao, K. Yu, G. Giunta, S. Belouettar, and M. Potier-Ferry, "A Fourier-related double scale analysis on the instability phenomena of sandwich

plates," *Computer Methods in Applied Mechanics and Engineering*, vol. 318, pp. 270–295, 2017.

CHAPTER 4 ARTICLE 1 : RECONSTRUCTION OF MESOSTRUCTURAL MATERIAL TWIN MODELS OF ENGINEERING TEXTILES BASED ON MICRO-CT AIDED GEOMETRIC MODELING

W. Huang, P. Causse, V. Brailovski, H. Hu*, F. Trochu

Published in *Composites Part A: Applied Science and Manufacturing, Volume 124, 105481, 1 September 2019.*

4.1 Chapter overview

This chapter presents the article published in *Composites Part A: Applied Science and Manufacturing*, which introduce the originally proposed concept of "material twin". Based on X-ray microtomography, a novel geometric modeling approach named *Micro-CT Aided Geometric Modeling* (Micro-CT AGM) is developed to generate the material twins of the multiple-layer 2D woven fabrics and 3D orthogonal textiles. A multiple factor morphological criterion is implemented to assess the accuracy of the reconstructed model. Since material twins precisely represent the geometric details of real fabrics at the mesoscopic scale, they allow predicting accurately permeability as discussed in Chapter 5. Besides, material twins can accurately reflect contact between fiber tows, thus they play a key role to analyze the mesoscopic deformation of fabrics under through-thickness compaction as presented in Chapters 6 and 7.

4.2 Abstract

Engineering textiles are used as fibrous reinforcements in high performance polymer composites. The mechanical properties of composite materials depend on their dual-scale porous structure: long and elongated microscopic open spaces (micropores) appear between the filaments of fiber tows, and up to two orders of magnitude larger mesoscopic spaces (mesopores) exist between yarns. Because of the complex structure of composites, it is difficult to establish a connection between fiber architecture and mechanical behavior. To achieve this goal, X-ray microtomography (Micro-CT) can be used to provide detailed information on the geometric mesostructure of continuous fiber composites. The objective of this paper is to present a new approach based on "Micro-CT Aided Geometric Modeling" (Micro-CT AGM) to construct detailed geometric models of engineering textiles from Micro-CT three-dimensional

(3D) images. The obtained geometric models are called "material twins" because of three distinctive features: (1) they are representative of the material variability; (2) their accuracy can be evaluated; and (3) they can be used to carry out computer simulations of mechanical behavior. This new method is applied to two industrial reinforcements: a 2D plain woven fabric and a 3D orthogonal glass textile. By introducing a new multiple factor morphological accuracy criterion, the quality of the "material twin" reconstruction can be compared to models obtained by standard image processing techniques or textile modeling software.

4.3 Introduction

Engineering textiles are used as fibrous reinforcements in high performance polymer based composites. The mechanical properties of these materials depend on their dual-scale structure: fibers belong to yarns, and yarns follow specific textile architectures. At the fiber level, microscopic pores exist inside yarns. At the yarn level, mesoscopic open spaces appear between fiber tows. The distributions of microscopic pores in the tows and of mesoscopic pores in between govern the flow properties, such as permeability, whereas the fiber volume content of the yarns and their orientation govern the mechanical properties such as stiffness or impact behavior. Due to the complexity of the mesostructure of fibrous reinforcements, the connection between macroscopic behavior and fiber architecture has not yet been fully established especially for 2D and 3D woven fabrics.

In this paper, we present a new methodology based on dual kriging interpolation to construct geometric models of the material mesostructure from 3D images obtained by X-ray microtomography. This methodology called "Micro-CT Aided Geometric Modeling" (Micro-CT AGM) is applied to two fibrous reinforcements: a 2D plain woven glass fabric and a 3D orthogonal glass textile. The objective pursued is to obtain what we propose to refer to as a "material twin" of the real specimen. This concept is a detailed morphological description of the material structure that would meet the following conditions:

1) The model takes into account the statistical variability of the material structure.

2) The accuracy of the model can be evaluated with respect to the resolution of scanned specimens. Different levels of observation are possible at different scales: nanoscopic, microscopic, mesoscopic or macroscopic.

3) The model can be used in data-driven simulations to predict mechanical or flow properties.

The definition of a "material twin" proposed above sums up several critical issues connected with data-driven numerical simulations. For example, the ability to perform readily such simulations is seldom mentioned in published papers. In fact, this capability is not straightforward since robust data processing is required to go from Micro-CT scanned 3D images to virtual models usable in computer simulations. Note however that the present study do not intend to provide a thorough assessment of this new concept but should be seen as a first step towards that goal. In particular, the variability of material structure is not quantitatively taken into account in this paper, although it still remains an important research goal. As will be shown, the lower scan resolution used here allows analyzing larger specimens than a single textile unit cell. Therefore, multiple geometric features can be averaged over a certain number of unit cells, hence providing information on material variability.

The structure of the article is arranged as follows. Section 4.4 gives a review of the scientific literature on microtomographic applications in the field of composites and the methods to construct mesostructural geometric models, then it sums up the critical issues connected with the existing methods. In Section 4.5, the new Micro-CT Aided Geometric Modeling (Micro-CT AGM) approach proposed is thoroughly described. In Section 4.6, a reasonable number of key sections are used to construct the material twins of single tows. The accuracy is verified by introducing a new multiple factor morphological criterion to compare the geometric models obtained with the original scanned images. In the sequel, Sections 4.7 and 4.8 apply the proposed methodology to construct mesostructural models of a 2D plain woven glass fabric and of a 3D orthogonal glass textile. The geometric features of the material twins are then compared with models obtained by image processing techniques previously used in the scientific literature or based on textile software models such as TexGen [1, 2].

4.4 Literature review

The mesoscopic geometric features of fibrous reinforcements govern mechanical properties. Therefore, a precise description of the morphology of engineering textiles is important to predict the mechanical behavior of continuous fiber composites and optimize manufacturing processes. A direct way to study the mesostructure of engineering textiles is to employ microscopic observation techniques to measure and analyze their geometric structure, such as X-ray micro-computed tomography (Micro-CT), a non-destructive technique providing detailed three-dimensional observations of the internal structure of materials.

Micro-CT has been widely employed to study composite materials in recent years. Desplentere et al. [3], Schilling et al. [4], Schell et al. [5, 6] were among the first investigators who demonstrated the potential of Micro-CT to characterize the geometric features of 3D textiles

at the mesoscopic scale. Two main kinds of microtomographic analyses have been conducted on long fiber reinforced composites, namely (1) characterization of the geometric features of fibrous reinforcements; and (2) analysis of porosity or voids in composite specimens.

Badel et al. [7] analyzed the spatial distribution of fibers inside fiber tows at the microscopic scale, and then proposed a hypo-elastic constitutive model which was later used to simulate the mesoscopic deformation of textile reinforcements. Pazmino et al. [8] manually measured the geometry of fiber tows on microtomographic images and studied shearing of a single layer of E-glass non-crimp 3D orthogonal woven fabric. Based on microtomographic analysis, Madra et al. [9] proposed a clustering method to analyze the geometric features of short natural fiber composites. On the other hand, Emerson et al. [10] proposed a segmentation method to segregate individual filaments inside fiber tows to analyze fiber orientation. Combined with digital volume correlation, Mendoza et al. [11] proposed a technique to quantitatively characterize the weaving distortions of woven composites, a promising new approach to characterize composite materials. Rolland et al. [12] analyzed damage mechanisms in short glass fiber composites by an in-situ Micro-CT investigation at the microscopic scale. Finally, Wan et al. [13, 14] analyzed the internal geometry of chopped carbon fiber tape composites based on Micro-CT analysis and assessed the accuracy of Micro-CT measurements.

Schell et al. [5] employed Micro-CT to observe the geometry of fiber bundles and analyze voids in glass fiber reinforced polymers based on the greyscale values of the microtomographic images. Madra et al. [15] applied various methods of image segmentation to study the porosity distribution in a woven glass fiber composite. On the other hand, Ali et al. [16, 17] proposed a non-destructive modeling framework to predict the in-plane and through-thickness permeabilities of 3D woven fabrics based on the analysis of mesopores between fiber tows. Larson and Zok [18] adopted an in-situ microtomographic analysis to observe micropores inside fiber tows and investigate the axial impregnation of unidirectional fibrous reinforcements by Liquid Composite Molding (LCM).

Since the performance of engineering textiles is closely related to fiber architecture, precise geometric models are critical to conduct numerical simulations of mechanical behavior, such as the compaction of dry fibrous reinforcements and their impregnation by LCM. Generally, two kinds of approaches have been used to construct mesostructural geometric models of composites for computer simulation:

1) Idealized models can be created by textile software such as TexGen [1, 2], WiseTex [19, 20] or the widely used multi-chain digital element approach [21, 22], which creates geometric models based on a series of critical geometric parameters combined with reasonable simplifications.

2) More realistic models obtained by Micro-CT incorporating multiple geometric features of real textiles [23,24]. The resolution selected usually allows constructing accurate and representative models at the mesoscopic scale.

Although idealized models provide an automatic and robust way to construct simplified geometric representations of a material for numerical simulations, more realistic models obtained by Micro-CT can describe the geometric details and the variability of real textiles, which are needed for precise data-driven numerical simulations. Green et al. [25,26] proposed a numerical modeling procedure to construct a realistic mesostructural model. Firstly, a compaction simulation is conducted with a "loose" LS-DYNA model constructed from a TexGen idealized model and the multi-chain digital element. The predicted deformation of this initial model is then combined with geometric information obtained from microtomographic scans to refine the analysis and generate in the end a more realistic TexGen model. This final model is then used in several mechanical simulations to show that more precise results can be obtained with such a refined model than with an idealized one.

By using image processing techniques on microtomographic images, Naouar et al. [23] successfully reconstructed the mesostructure of a 2D woven fabric. The analysis was based on the different orientations of warp and weft yarns, which were separated in the segmentation process by a methodology based on a structure tensor [27]. However, this approach did not perform well for the reconstruction of 3D textiles [28], when the tows are held together by a binding thread. The large contact zones between the binder and the tows of same orientations prevent from separating the two components in the 3D digital image. Therefore, another technique was devised in Naouar et al. [24] to construct the mesostructural model of a 3D textile. Texture analysis based on the calculation of Grey Level Co-occurrence matrix (GLC Matrix) [29] was employed to create a mesostructural model of a representative unit cell of the 3D orthogonal textile, which was then used in data-driven numerical simulations of through-thickness compaction.

Investigations reported in the scientific literature up to now show that micro-CT can be effectively used to reconstruct the mesostructure of composite specimens, which opens up the possibility of performing data-driven computer simulations of mechanical behavior. However, only one textile ply was usually reconstructed in the above-mentioned segmentation approaches, which were not implemented for fabric stacks. In this case, nesting between neighboring plies still impede an automatic recognition and separation of tows. Moreover, as presented by Straumit et al. [30], the structure tensor method possesses a constraint on the lower size of voxels required for Micro-CT images to attain a specific accuracy. According to this investigation, the standard deviation of the calculated orientation angle for a voxel

size of 20.5 µm^3 is nearly ten times larger than for 8.3 µm^3 voxels. Therefore, although image processing techniques might still perform well at high resolution in the case of multiple fabric layers, the scanned specimens seem too small to represent the real geometric textile features and variability.

A common problem in reconstructed models is that no basic geometric criterion is available to assess their accuracy. In fact, although a detailed 3D image of the composite mesostructure represents already much progress, a qualitative assessment of the quality of reconstructed models might not have been the first concern of investigators [25, 31, 32], although this task was carried out by [33] for a limited number of geometric features. In fact, most of the above-mentioned reconstructed models have been verified indirectly by comparing the results of mechanical simulations with experiments. No accuracy analysis of geometric features has yet been carried out. This leads to lack of geometric consistency in the proposed models, which might create numerical problems or inaccurate results in computer simulations, such as for example in LCM flow models, which are highly dependent on textile mesostructure.

In summary, the construction of mesostructural geometric models based on existing image processing techniques bears the following limitations:

1) A relatively high scan resolution is required for accurate segmentation, which limits the geometric dimensions of observed specimens.

2) One single fabric layer can be successfully reconstructed by existing methods. However, processing specimens containing a stack of multiple fabric layers remains arduous.

3) Unpredictable and uncontrollable errors are introduced when employing image processing techniques, especially in lower resolution cases.

4) The geometrical accuracy of reconstructed geometric models is seldom assessed.

In order to resolve these issues, this article aims to develop a geometric modeling framework based on microtomographic scans, called Micro-CT AGM and use the geometric features of real textile specimens to generate material twins of engineering textiles.

Since no appropriate existing image processing techniques could be found to separate fiber tows among a stack of fabrics at relatively lower resolution, manual separation is employed in this article in a novel way by combining three views of observed specimens. Therefore, high image resolution is no longer necessary like in previous investigations to obtain a precise mesostructural model, which turns out to be significantly different from the ones obtained by standard image processing techniques or from textile modeling software. Therefore, the

dimensions of a scanned fibrous sample can be large enough to include more than a single unit cell and hence incorporate more representative geometric features of a real material together with its intrinsic variability.

In addition, the proposed new approach allows distinguishing precisely between fiber tows in contact even in the case of complex textile configurations, which is not possible by general image processing techniques at lower resolution (22 µm/pixel) as used in this article. One particularly instructive example on this matter is provided by a stack of 2D woven fabrics with significant nesting at a relatively high fiber volume content of around 50%. Finally, a multiple morphological factor criterion is introduced to assess the model accuracy directly from a series of selected geometric features. Thus, the relative accuracy of the reconstructed geometric models can be evaluated with respect to the resolution of the microtomographic scan directly from their geometric features instead of indirectly from the results of mechanical simulations.

4.5 Description of Micro-CT Aided Geometric Modeling (Micro-CT AGM)

The different steps of the new Micro-CT Aided Geometric Modeling (Micro-CT AGM) described in this paper are illustrated in the schematics of Figure 4.1. Firstly, an original software was developed to assist in the acquisition of the contour data of tows from the 3D Micro-CT images. Then, a parametric surface model of the yarns is constructed from a series of selected representative contours by an interpolation method known as dual kriging [34]. The vector model created by parametric surface kriging is called a vector material twin. The next step consists of reconstructing a new voxel model of fiber tows from the parametric surface equations of the yarns. During this process, an iterative expansion method is proposed to prevent neighboring tows to intersect each other after interpolation. By following this approach, the 3D Micro-CT images are translated into geometric models representative of the material structure at a given scale and ready to be meshed for data-driven finite element computer simulations.

4.5.1 Contours of fiber tows

The first task consists of extracting fiber tows from the Micro-CT 3D images to construct a vector-based mesostructural textile model. The fiber tows must be separated from each other and labeled. In this article, a manual separation is performed so as to be less dependent on the scan resolution. This allows analyzing material specimens of larger geometric dimensions. Although manual separation and quantitative observations on the morphology of fiber tows

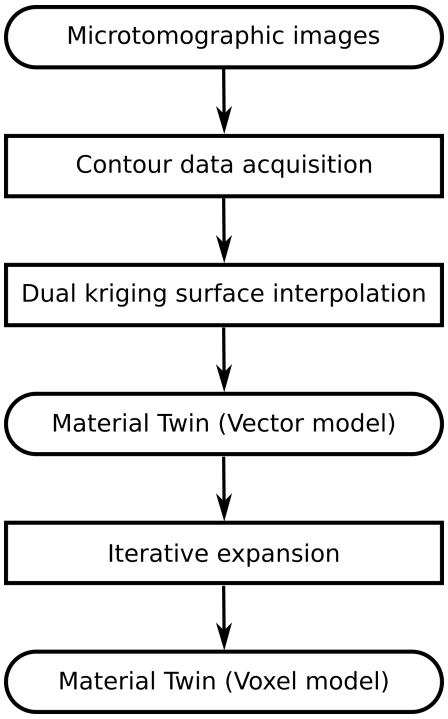

Figure 4.1 Schematics of Micro-CT Aided Geometric Modeling (Micro-CT AGM)

have been widely investigated in the scientific literature (see for example references [3, 8, 35–37]), the selection of contour points is generally based on only one view of the image. This might induce non-negligible errors, especially if the scan resolution is not high enough or where tows are in close contact. In order to reconstruct mesostructural models that represent accurately the geometric features of engineering fabrics, precise contours of fiber tows together with a sufficiently large number of cross-sections are needed.

To facilitate these operations, a software called CompoCT was developed as a platform for Micro-CT AGM. Figure 4.2a illustrates the three views employed by the software to observe the scanned textile specimen. Figure 4.2b presents the user interface of the software with the front view (top left window), side view (top right window) and top view (bottom window) of the microtomographic voxel 3D image. All the manipulations of the 3D voxel images are carried out in a local reference coordinate system in voxel unit. To make the observation and the manual separation easier, the top and side views are scaled down compared to the front view, which is the main observation view. Two straight cross-lines, whose positions correspond respectively to slices of the other two views, are placed on each window. Looking at the top view for example, moving the green line changes the slice appearing in the front view, while the blue line corresponds to the side view. The slices in the views can also be changed by moving the sliders under each window.

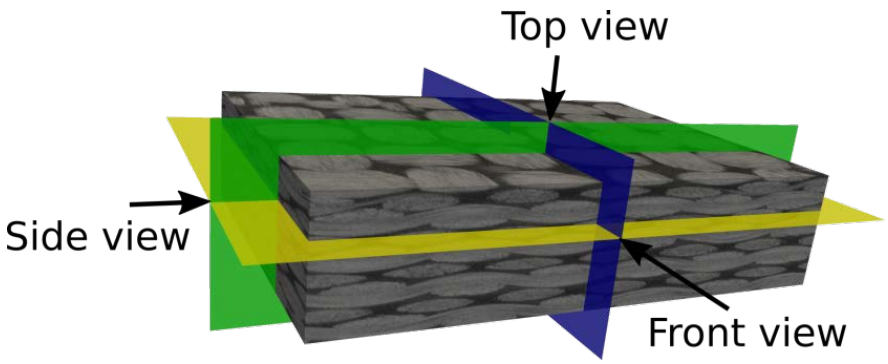

(a)

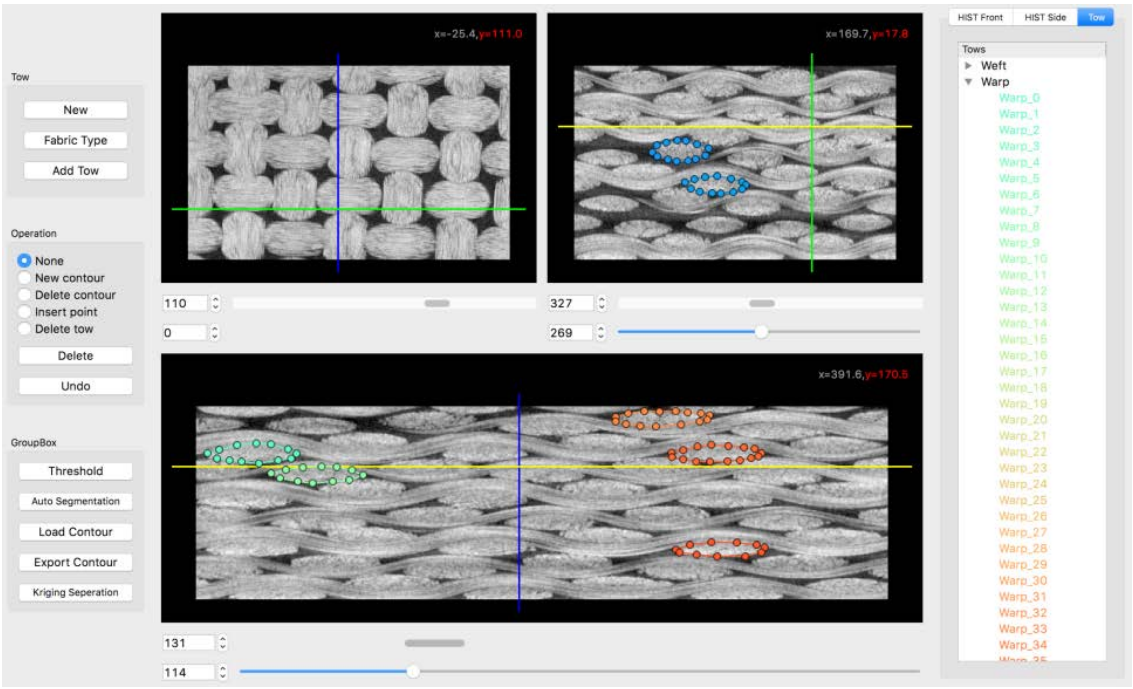

(b)

Figure 4.2 Micro-CT AGM software – CompoCT : (a) three views are used to observe composite specimens; (b) user interface of the software.

Since all the operations of the software are based on 2D images corresponding to parallel 2D planes of the 3D volume, a global 3D coordinate system is not absolutely necessary. We will work in the sequel in a 2D reference system with axes denoted X and Y. However, to make the latter analysis of geometric features more convenient, a local coordinate system is assigned to each view whose horizontal axis is denoted X and the orthogonal axis is denoted Y, while the Z axis stands in the direction of the fiber tows investigated.

Thanks to the three views available, the precision of the selection can be improved, especially to distinguish between boundaries of contacting tows. Figure 4.3 shows the procedure to select a point on the contact boundary. It is a bit difficult to distinguish the tow boundary in the front view, but the voxels of the two tows appear clearly and can be identified in the top view because of their different orientations. The intersection point of the blue line (slice of the side view), green line (slice of the front view) with the red curve (contour of the tow on the top view) is the point to be selected in the front view (see red circle on the front view). In this article, all the points on the contours used to reconstruct the geometric models were selected in this way.

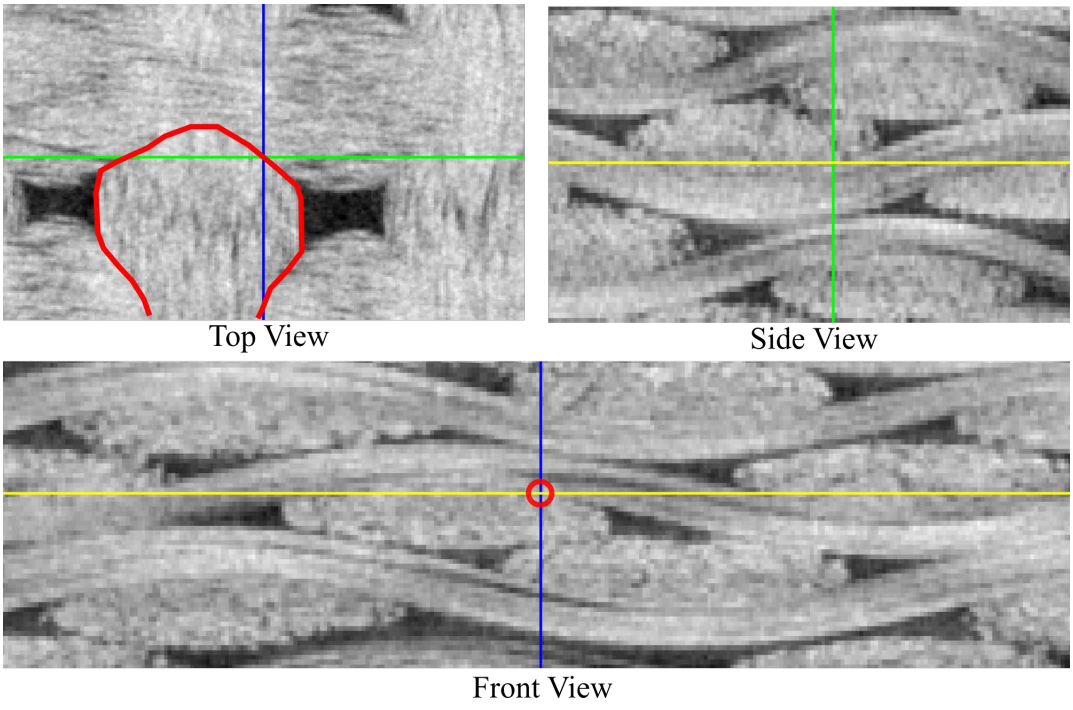

Figure 4.3 Three views based selection of contour points

4.5.2 Key sections

To reconstruct a fiber tow, the contours need to be selected on several cross-sections along the orientation of the tow. The sections representing the waviness of the tow together with contact conditions between tows are defined as key sections to create the parametric surface model. To be more specific, key sections can be defined as peaks of waviness, at edges of contact zones between intersecting tows and at additional positions where tows are not in contact. Figure 4.4 shows one example of key sections selected for one tow. To reconstruct the weft yarn highlighted in red in Figure 4.4 (side view) without significant deformation, at least 12 key sections for each waviness period should be selected, which represents a total of about 36 key sections for the tow. The number of key sections, of course, can be larger to obtain a more precise reconstruction or for tows undergoing significant deformations.

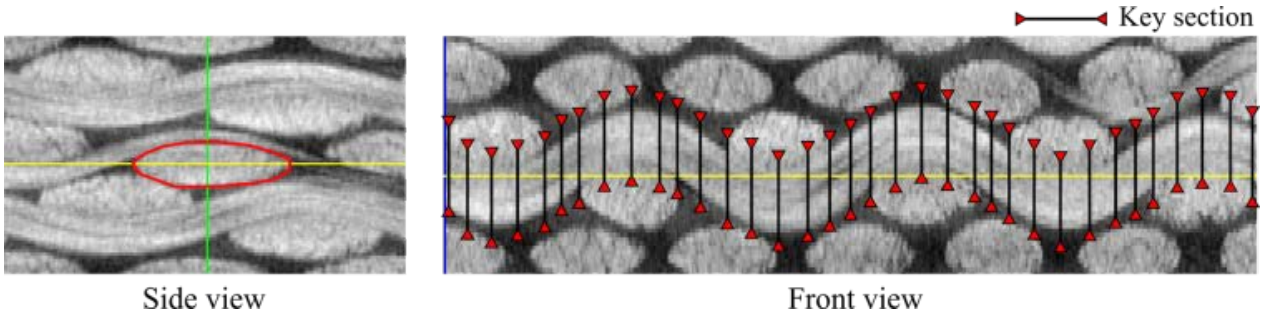

Figure 4.4 Key sections used to select the contours of a weft yarn

After having selected data points on the contours of each key section, the contour acquisition procedure is completed. All the selected points are then interpolated by parametric curve and surface kriging to generate surface parametric equations of fiber tows. Details on the use of the parametric kriging are given in Appendix A.

4.5.3 Contour expansion

After employing the parametric curve kriging to interpolate the selected contour points, the surfaces of fiber tows can be modeled by parametric surface kriging. The possible intersection of tows remains a problematic issue in the construction of mesostructural textile models by interpolation ([2, 38]). As a matter of fact, tows in contact or close to one another may intersect when interpolated. A contour expansion technique is proposed here to solve this problem.

Imagine the stack of 2D microtomographic images to be a series of superposed pixel canvases

with all the tow contours drawn on them. All the original pixels are given a first label of 0 to represent the initial matrix. Then an iterative process starts as illustrated in Figure 4.5. In the expansion algorithm, all the tows "grow" one by one from the centroids to their boundaries with preassigned expansion factors while conserving the same contour shapes. Since the interaction problems only occur at the boundaries of tows in contact, a large initial expansion factor is assigned in the first step to directly let the tows expand to a significant percentage of areas and speed up the algorithm. In this work, the initial expansion factor was chosen to be 0.85. Thus, after the first iteration, Figure 4.5 shows that 85% of the tow areas are labeled individually. In the following iterations, the tows expand with small expansion factor (in this case, 0.05) until 100% of the tow area is labeled, i.e., the total expansion factor reaches 1 after four iterative steps. During the procedure, the pixels covered by the growing tow are labeled with the coding numbers of the tows, which are presented in different colors in Figure 4.5. Once a pixel is labeled by a fiber tow, it cannot be labeled by other tows. Note that the expansions of tows are conducted one by one in the 3D space, thus the voxel data are directly updated in a 3D array. By doing this, a clear boundary between the two tows in contact in the example of Figure 4.5 (the gray and yellow ones) can be obtained at iteration 4, although the original contours of tows intersect at iteration 0. Besides, no intersection is observed between the tows with different orientations (the yellow and blue ones).

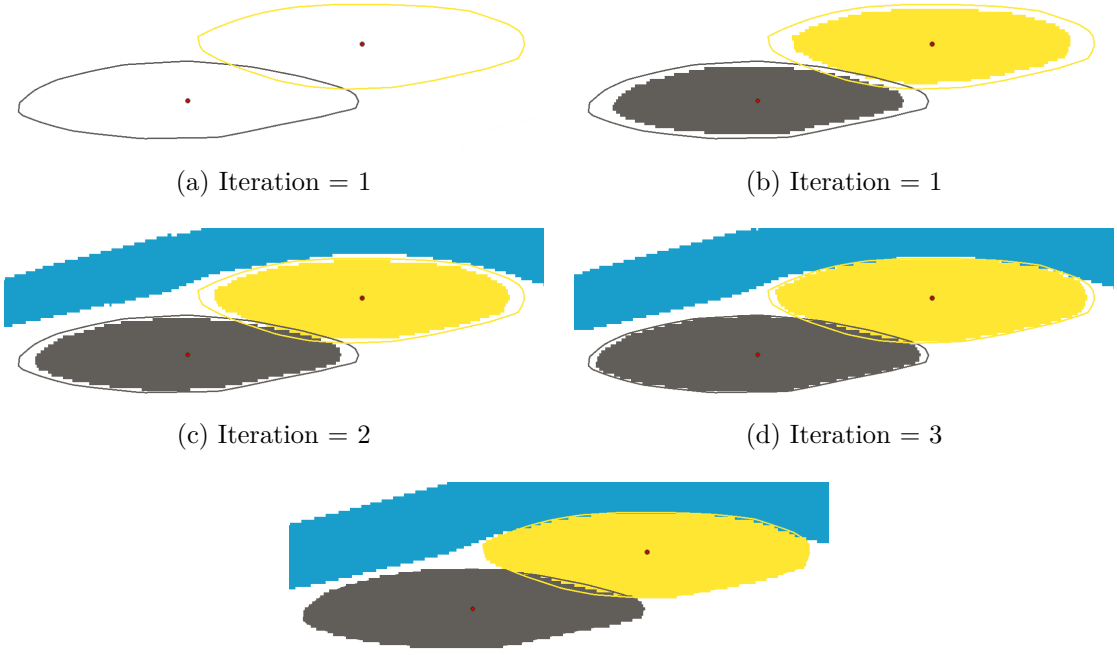

(a) Iteration = 1

(b) Iteration = 1

(c) Iteration = 2

(d) Iteration = 3

(e) Iteration = 4

Figure 4.5 Illustration of the contour expansion algorithm

4.6 Criterion of accuracy for the reconstructed geometric model

As mentioned in Section 4.3, when generating material twins, the accuracy of the geometric models needs to be evaluated. In order to do so, a procedure is proposed as illustrated in Figure 4.6. Firstly, a voxel reference model and a vector material twin can be reconstructed from the voxel file of the microtomographic images. Then the vector material twin is transferred to the voxel material twin which will be compared to the voxel reference model. By introducing a new multiple factor criterion based on a series of morphological features of fiber tows, the accuracy of the material twin can be assessed. If the accuracy is acceptable, this validates the material twin at the resolution level of the microtomographic scan; otherwise, the vector material twin should be refined. The multiple factor criterion is based on a selected series of morphological features of fiber tows that are critical to assess the accuracy of the geometric model and will be detailed hereafter.

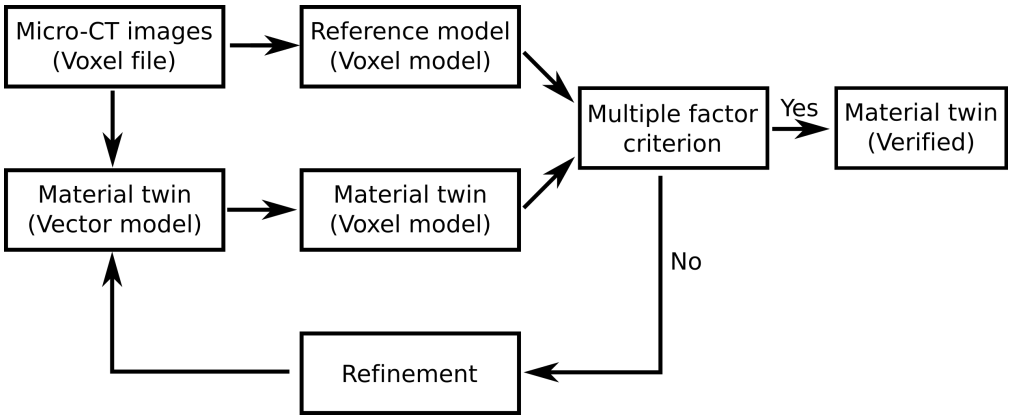

Figure 4.6 Schematics of the accuracy assessment procedure for material twins

Note that the voxel reference model and the vector material twin are both generated by Micro-CT AGM. In this article, the only difference is that the voxel reference model is reconstructed from a large number of key sections to ensure a higher accuracy. Since this is highly time consuming, it was used here only to confirm that a reasonable number of key sections may be used to generate accurate material twins (see Section 4.6.2). Therefore, a limited number of tows are reconstructed in the reference model used to assess accuracy. In the future, image processing techniques and deep learning algorithms can be introduced in the acquisition of tow contour data.

4.6.1 Morphological features

In order to assess the accuracy of the reconstructed geometric models, a series of representative morphological features of fiber tows are introduced. Considering that textile reinforcements follow specific woven patterns, the path of the centroid lines of fiber tows represents one of the most important features. As mentioned in Section 4.5.1, a local coordinate system is assigned for each view of the 3D voxel image, in which the fiber direction is oriented along the Z axis, and the cross-sections of the fiber tow lies in the $X - Y$ plane. Thus, for each cross-section, the centroid of the contour can be calculated in pixel unit as follows:

$$(XC, YC) = \left(\frac{M_{10}}{M_{00}}, \frac{M_{01}}{M_{00}}\right) \tag{4.1}$$

where XC, YC are the pixel coordinates of the centroid of the contour, and M_{ij} denotes image moments defined by:

$$M_{ij} = \sum_x \sum_y x^i y^j I(x, y), \quad (i, j = 0, 1, 2, \cdots) \tag{4.2}$$

where x, y are the pixel coordinates of all the points inside the contour, and $I(x, y)$ the pixel intensity in the greyscale image.

The shape of the contour is also a key feature in the reconstructed model. The area of the cross-section being related to the fiber volume content of fiber tows, the pixel area must also be taken into account. To characterize the shape and orientation of cross-sections, each contour is fitted with a rectangle to obtain the width and height of the contour as shown in Figure 4.7. At the same time, an ellipse is fitted to the contour to quantify the angle between its minor axis and the X axis. This angle is considered as defining the inclination of the cross-section with respect to the horizontal axis of the image.

The general shape of the cross-section represents another important morphological factor. The circularity (roundness) C of the contour is thus introduced to evaluate quantitatively how close the shape is to a mathematically perfect circle. This measure is achieved by calculating the circularity index defined as:

$$C = \frac{4\pi A}{P^2} \tag{4.3}$$

where A is the total area and P the perimeter of the contour. For a perfect circle, the circularity index is equal to 1.

To summarize, the following geometric features will be considered in the forthcoming para-

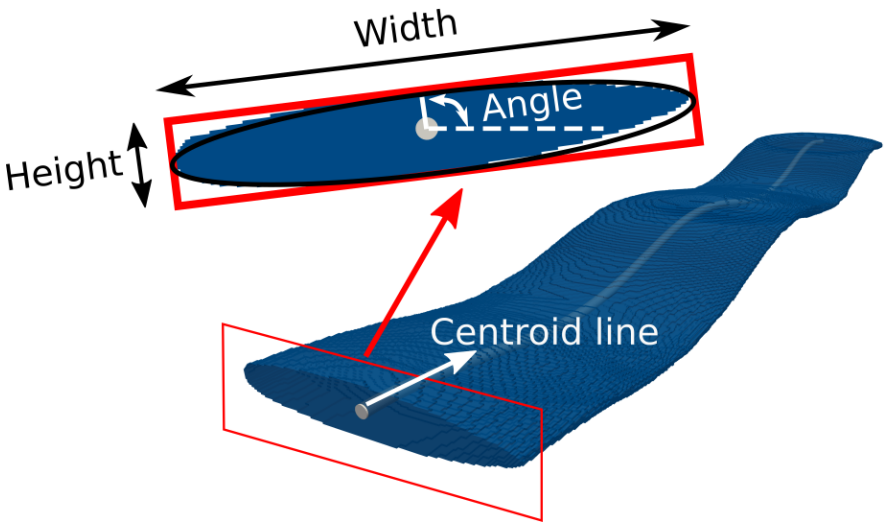

Figure 4.7 Morphological features of fiber tows

metric study: the centroid line of fiber tows, the area, width, height, inclination and circularity of contours. The centroid line indicates the longitudinal orientation of the tow. The area of key contours in pixel unit is directly connected to the volume of the tow (in voxel unit), and hence to the fiber volume content of the specimen. The width, height and angle of the representative rectangle and ellipse give information on the average shape of the tow in the transverse direction, whereas the circularity tells by how much the contour differs from a perfect circle. This morphological analysis allows evaluating quantitatively the skewness of tows in their transverse directions.

4.6.2 Number of key sections

Considering all the slices as key sections should give the most precise reconstructed model with respect to the resolution of the microtomographic scan. However, a compromise is necessary here to create representative and suitable geometric models for computer simulation. In this article, the reconstructed model is obtained by manual separation of the tows. Hence, numerous key sections would lead to a rather time-consuming operating procedure. Thus, the number of selected sections is an important parameter that must be carefully selected. Figure 4.8 shows two models reconstructed for one fiber tow of 2D woven textiles with different numbers of key sections. In fact, the reference tow contains 215 sections, the thickness of which in voxel unit depends on the resolution of the microtomographic scan. On the other hand, the approximated tow has only 40 sections. As already discussed in Section 4.5.2, the numbers of key sections selected here is based on the waviness of the fiber tow.

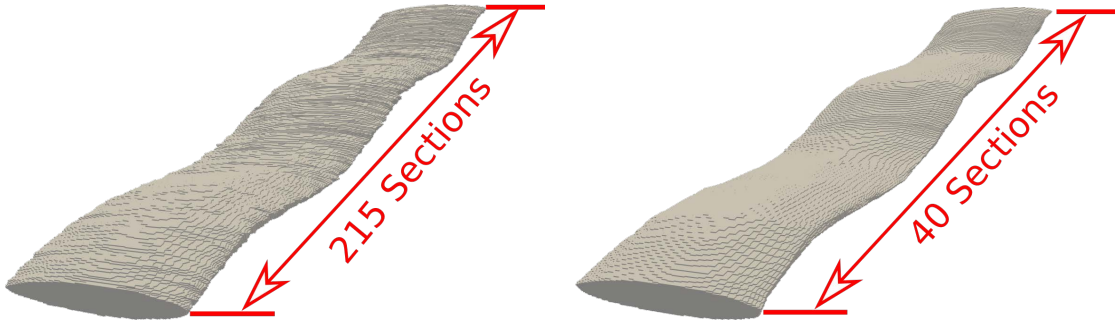

(a) (b)

Figure 4.8 Mesostructural models of a single fiber tow constructed from a stack of 501 microtomographic images with different numbers of key sections: (a) reference fiber tow with 215 sections; (b) approximated fiber tow with 40 sections.

As shown in Figure 4.8, the surface of the approximated tow is virtually smoother than that of the reference tow. This is mainly caused by two reasons: (1) the variability arising from the manual separation procedure; and (2) the noise on the boundary of tows induced by the Micro-CT scan. Whatever segmentation method used, the latter problem cannot be avoided since it comes from the scanning process. The former one can be solved in several ways. For example, the geometric features on each slice are fitted by appropriate functions in the following parametric study. Besides, the nugget effect in kriging, which represents the variance of the measurement error [34], can also be introduced in the reconstruction process such as in Madra et al. [39] to smooth the geometric models. Note that smoothing is a critical issue to ensure that the final geometric models are material twins, namely that they can be readily used in numerical simulations at reasonable computational cost.

4.6.3 Parametric study

Since waviness is a critical geometric feature of engineering textiles (determined by the fabric weave pattern), the centroid lines of tows will be the first objective of our analysis. Figure 4.9a and Figure 4.9b show the evolution of the centroid line along the tow orientation for the two models discussed above. As expected, the centroid line shows a nearly periodic evolution in the Y direction along the tow orientation, while it nearly remains linear in the X direction. In order to observe the evolution of geometric features and compare the accuracy of the geometric models, the raw data must be fitted with proper functions. Thus, the evolution of the centroid line in the Y direction (YC) may be fitted by a Fourier series function, while the centroid line in the X direction (XC) by a polynomial function.

Considering that the weave pattern might affect other geometric features, a correlation anal-

ysis is performed between the morphological characteristics to find appropriate fits. If XC or YC show a periodic evolution, their gradients (GXC and GYC) should also present similar periodic evolutions with a quarter-period shift. Considering this might also be the cases for some other morphologic features, GXC and GYC will be also taken into account in the correlation analysis and will be evaluated from the fitted functions of YC and XC. Generally speaking, except for GXC and GYC, the values of other geometric features should be positive, thus the absolute values of GYC and GXC will be the final parameters considered in the correlation analysis.

Before the correlation analysis, in order to ensure that the contribution of each feature is equally important, the values of each feature f are normalized on a $0-1$ scale as follows:

$$f_{norm} = \frac{f - min(f)}{max(f) - min(f)} \tag{4.4}$$

Then the Pearson coefficient of linear correlation ρ is calculated for each pair of normalized features f, g as follows:

$$\rho = \frac{cov(f,g)}{\sigma_f \sigma_g} = \frac{\sum_1^N (f_i - \bar{f})(g_i - \bar{g})}{\sigma_f \sigma_g} \tag{4.5}$$

where N is the number of slices, $\bar{f}$, $\bar{g}$ denote the mean values, and σ_f, σ_g are the standard deviations of the features for all the slices of the tow. Finally, the correlation matrix of geometric features of the reference tow is obtained in Figure 4.10, in which absolute correlation values ρ higher than 0.4 are highlighted in red.

The area, height and circularity show a strong correlation with GYC, while the width is highly related to XC, and the angle to YC. As expected, this analysis confirms that the fabric weave pattern strongly affects the morphological characteristics. Considering that the area also exhibits a strong correlation with the width and the height, the evolution of the centroid line is related to changes in width and height of the tow cross-section, which further affects the area. Thus, the waviness of the tow is indeed a critical geometric feature. According to the above analysis, the height, the area, the angle and the circularity should be fitted by Fourier series functions, while the width can be fitted by polynomials.

After calculating both the correlation matrices of the reference and approximated tows, the functions employed to fit the curves of geometric features can be determined. Then, the comparison of the geometric features of the reference and approximated tows can be readily obtained as illustrated in Figure 4.9. All the features are well fitted, especially the ones with Fourier series, i.e., the area, the width and YC exhibit a significant nearly periodic

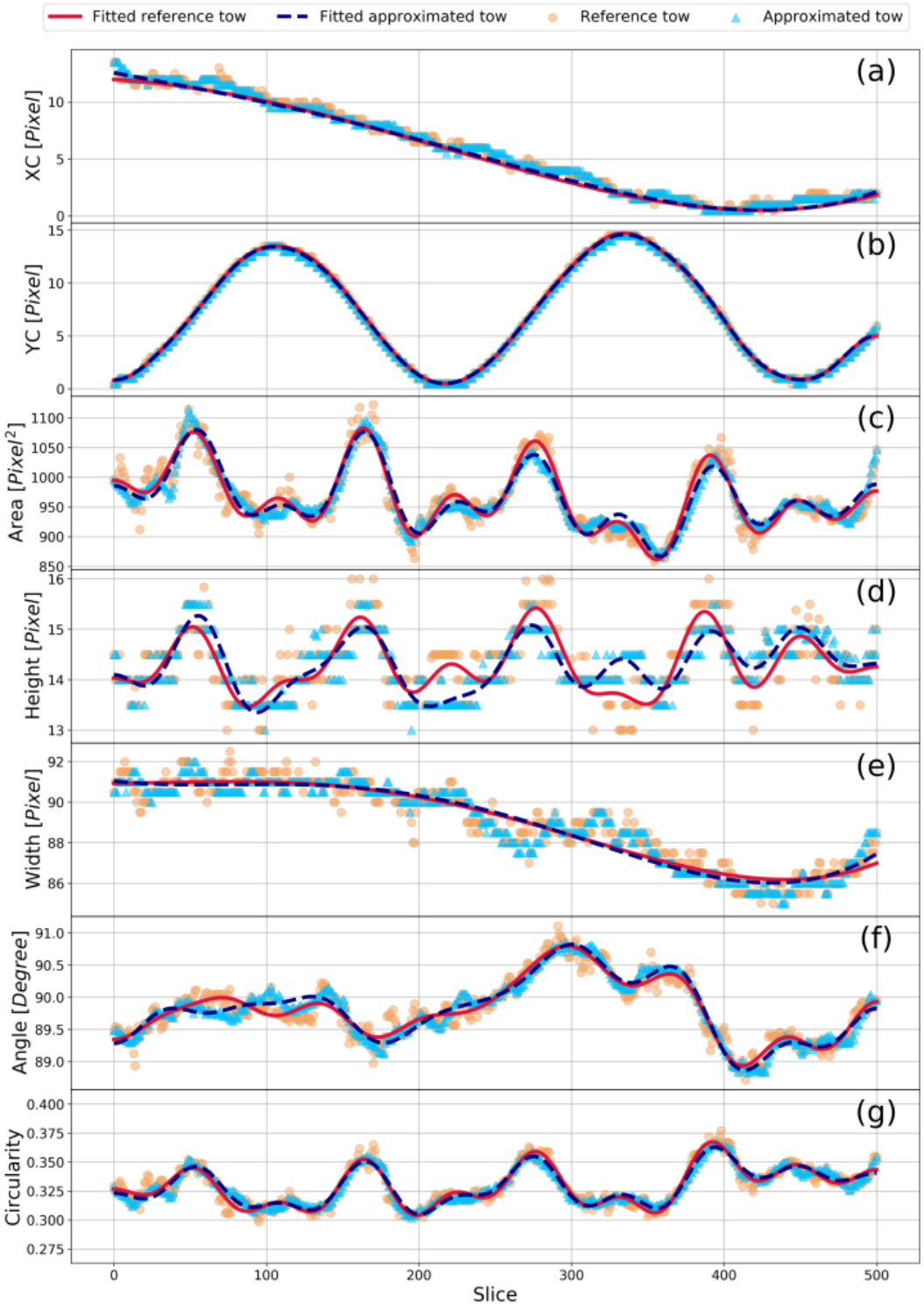

Figure 4.9 Comparison of geometric features between the reference and approximated tows: the centroid lines (a,b) are very accurate; the fitted areas (c) also (although the raw data show minor differences at peaks); the height and width (d,e) exhibit a larger variability, but averaged values remain centered; the angle and circularity (f,g) are well respected

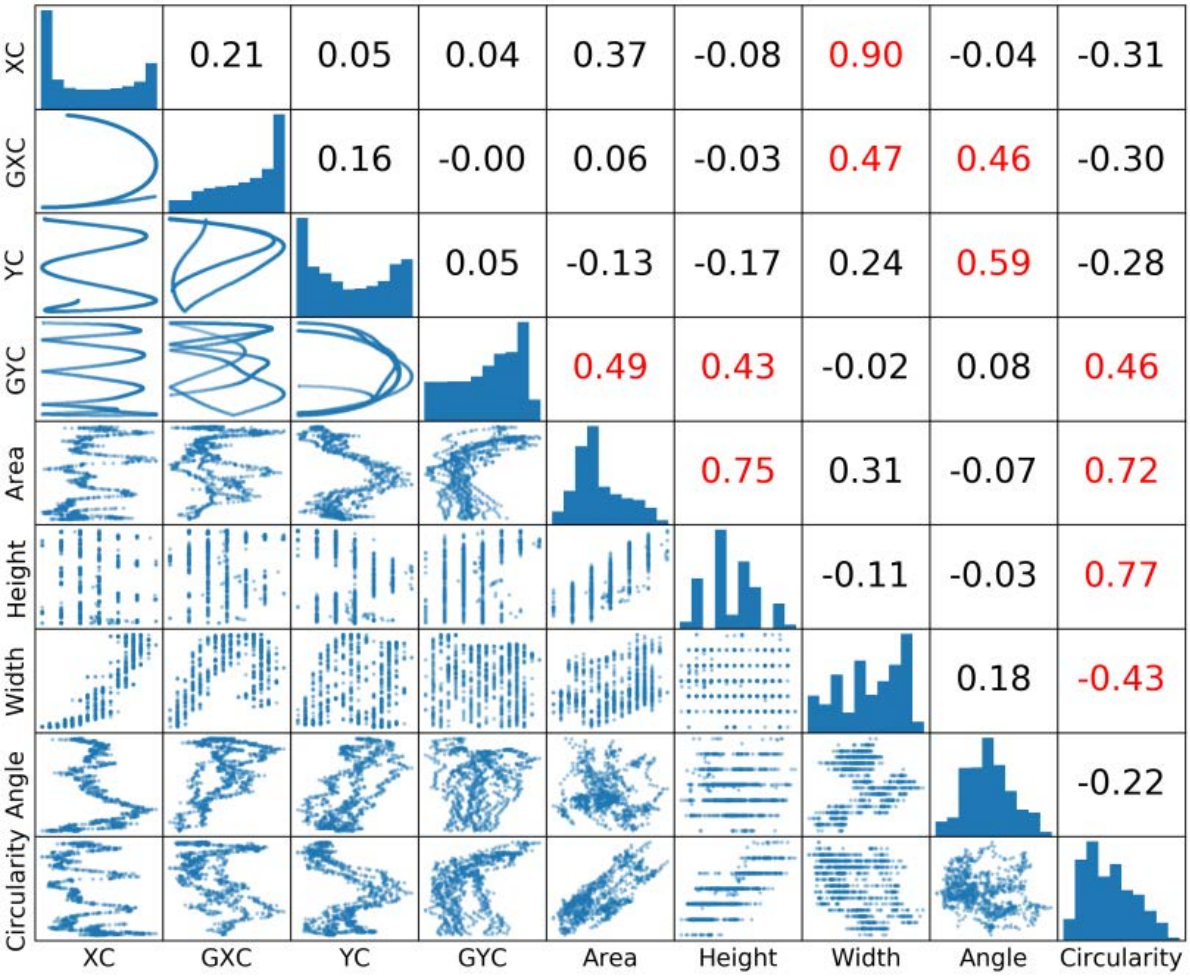

Figure 4.10 Correlation matrix of geometric features. Scatter plots of variable pairs are given in the lower part, while Pearson coefficients of linear correlation ρ are given in the upper part. The statistical distributions of each morphological feature appear in the diagonal

trend. As shown in Figure 4.9a, the value of XC does not remain constant value along the fiber orientation, because the sample analyzed here is a stack of 2D woven textiles. During the layup process, the orientations of the fabric layers were not strictly controlled, thus the orientations of some layers of the preform are not orthogonal to the direction of the microtomographic observation. Although Figure 4.10 shows that the angle is correlated with YC, there is no clear periodicity as shown in Figure 4.9f. This might be because the angle is also correlated with GXC (see Figure 4.10). This means that the angle is affected by the contact between tows as illustrated by the evolution of the centroid line. Finally, Figure 4.9g shows that the circularity vibrates within a small range, which means that in the case of low compaction, the shape of tow cross-sections remains stable.

Based on the geometric information of Figure 4.9, a multiple factor morphological criterion can now be proposed to assess the accuracy of the reconstructed geometric model. Since the reference tow is the closest model to the real tow for a given resolution of the microtomographic scan, it may be regarded as a benchmark to assess the relative precision of the approximated tow. The geometric features used to evaluate the quality of the reconstructed geometric model have all different degrees of relative importance. For example, the centroid line of the reconstructed tow should be as precise as possible, because it is a critical feature for geometric analyses and numerical simulations related to the weave pattern of the textile. The correlation between the area, width and height might lead to bias on the assessment if they are the only considered morphologic features. Their relative influence should be balanced, so that all the geometric features are taken into account to assess the accuracy of the reconstructed model.

The quality of the approximated tow can be compared to the reference one based on the errors between the values of their respective geometric features evaluated by:

$$s^j = \left(1 - \frac{SMAPE(f^j, \widehat{f}^j)}{C_{ref}}\right) \tag{4.6}$$

where s^j is the precision of the j^{th} geometric feature, f^j and $\widehat{f}^j$ are the values of the j^{th} geometric feature for the slices of the tested and reference models respectively, C_{ref} is the error criterion (20% in this article) and $SMAPE(f^j, \widehat{f}^j)$ the symmetric mean absolute percentage error of $(f^j, \widehat{f}^j)$ calculated by:

$$SMAPE(f^j, \widehat{f}^j) = \frac{1}{N}\sum_{i=1}^{N} \frac{\left|f_i^j - \widehat{f}_i^{\,j}\right|}{\left|f_i^j\right| + \left|\widehat{f}_i^{\,j}\right|} \tag{4.7}$$

where N is the number of slices.

The result of the accuracy assessment for the approximated tow is presented in Figure 4.11. The precision of each geometric feature is listed on the right, in which the closer we are to 1, the more precise is the geometric feature. A relative radar chart showing the performance of the model is presented on the left, where the area indicates the overall precision of the model considering all the geometric features. Besides, the radar chart can directly show drawbacks of a reconstructed model since it indicates also the precision of each parameter. In conclusion, the geometric features of the approximated tow with a limited number of key sections show a good agreement with the ones of the reference tow. Therefore, in the following analysis, a limited number of key sections can be used to generate material twins, which will be regarded as benchmark for further comparisons.

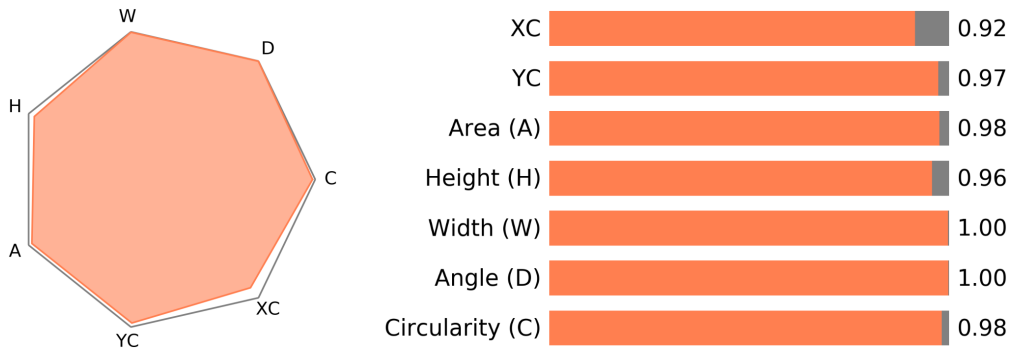

Figure 4.11 Precision of the approximated tow compared to the reference tow

4.7 Reconstruction of the dry preform of 2D woven fabrics

In this section, the methodology proposed to create a material twin from a microtomographic image is applied to a stack of 2D plain woven glass fabric layers. A geometric model of the fibrous reinforcement is reconstructed at the mesoscopic scale by Micro-CT AGM (referred to as the material twin in this article). The reconstructed model is used to analyze the geometric features of the preform and then is set as reference to assess the accuracy of another model reconstructed using standard image processing techniques, namely here based on the structure tensor method (referred to as the "ST model" in this article).

4.7.1 X-ray microtomography

Microtomographic scans of a stack of 2D fabric layers were acquired with a specially devised cylindrical observation tool. A full description of the experimental setup and measurement

can be found in [28]. The specimen comprised several circular samples (diameter 25 mm) of a glass fiber plain weave fabric from Texonic (product number L14012). During sample preparation, the different layers were carefully positioned so that the complete stack possess the same tows orientation. The sample was scanned at a resolution of 22 µm/pixel with a voltage and intensity of X-ray beam of 180 kV and 30 µA, respectively. The X-ray microtomograph was a Nikon XT H 225 located at École de Technologie Supérieure (ETS) in Montreal. In order to avoid boundary effects and observe a representative specimen, a region of interest of $15.4 \times 3.52 \times 11.2\mu m^3$ was selected for analysis in the central part of the scanned specimen. Figure 4.12a shows the region of interest which contains 8 fabric layers with 6, 7 warp yarns and 4, 5 weft yarns per layer.

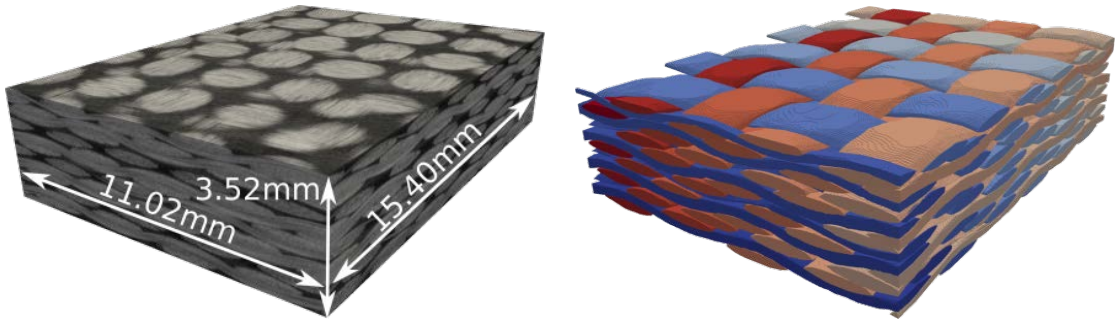

(a) (b)

Figure 4.12 Preform of the stack of 2D glass fiber woven fabrics: (a) original microtomographic image; (b) material twin (voxel model) reconstructed by Micro-CT AGM

4.7.2 Material twin

Different from the geometric models reconstructed in other studies [23, 24, 30, 31], in the voxel model of the preform obtained by the Micro-CT AGM approach, all the fiber tows are individually labeled as illustrated in Figure 4.12b. Thus, the geometric features, orientation, size and mechanical properties of each fiber tow can be taken into account for further analysis.

As performed in references [31, 40, 41], overlap superpositions of the geometric models on the microtomographic images have been done to visually verify the accuracy. Figure 4.13 shows an overlap comparison of the material twin with the stack of microtomographic images. The tows of the material twin are in transparent colors, while the image stack stands in grayscale with the air phase in light gray and the fibers in dark gray. For the three randomly selected cross-sections presented on the right, the material twin agrees well with the original image stack. This proves that the Micro-CT AGM is well suited for the multiple layer preform and

the resolution of 22 µm/pixel considered here.

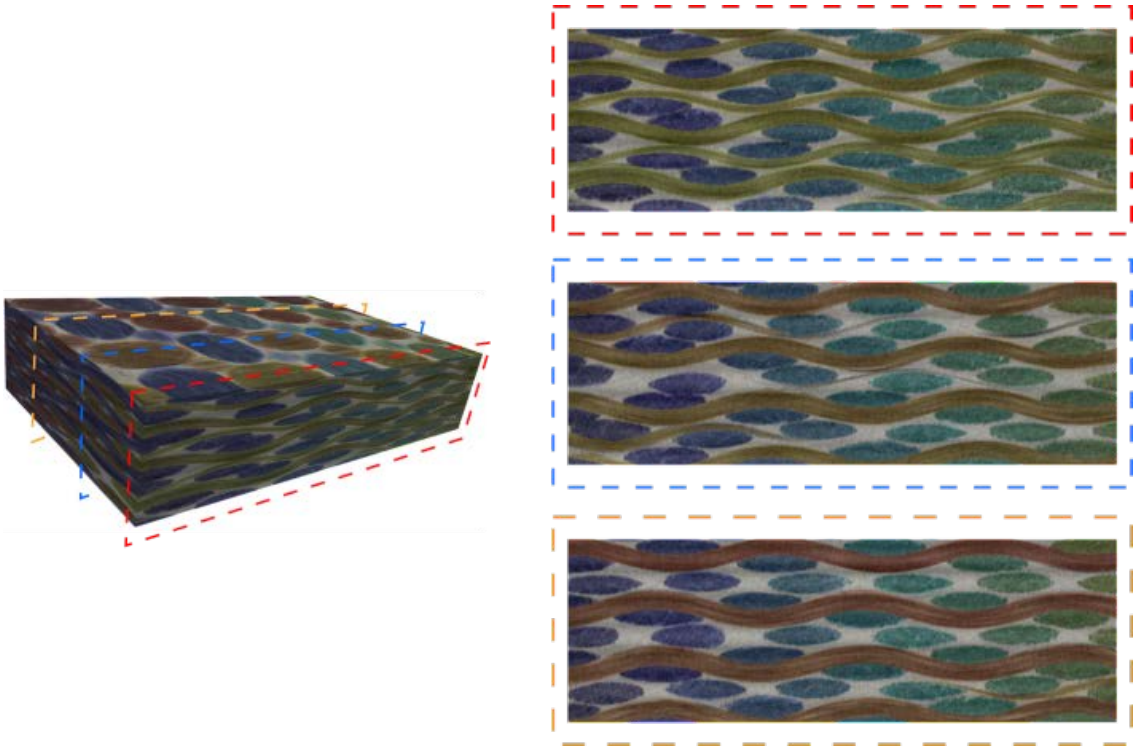

Figure 4.13 Overlap comparison of the material twin with microtomographic images. It is possible to verify the quality by superposing three cross-sections of the reconstructed model on the original pixel images. If the resulting image would appear fuzzy, this would mean that the reconstructed model is not representative of the microtomographic scan

4.7.3 Analysis of morphologic features

As a first approximation, we consider that the warp yarns of the 2D woven fabric have similar geometric features as the weft yarns, thus only the warp yarn will be analyzed here. The normalized values of the geometric features of a warp yarn in contact with four weft yarns are presented in Figure 4.14. The periodic evolution of YC shows that the waviness of the tow is determined by the weave pattern of the textile. The height and area exhibit a similar nearly periodic evolution with a period half that of YC, while the width changes without obvious periodicity.

Five cross-sections of the warp yarn are also specifically analyzed, i.e., the crest A, the troughs C and E, and two middle positions B and D. At the crest A and the trough C, the area and the height reach local minimum values, while they increase to local maxima at the middle positions B and D. According to the images at these positions, the tow is compressed by weft

yarns at A and C, thus both the height and the area are reduced, while it is not compressed by any other tow at B and D. From B to E, the width of the yarn decreases to a minimum value, but the height and area do not decrease to local minima. This is different from the idealized model, but clearly represents the variability of the real tows.

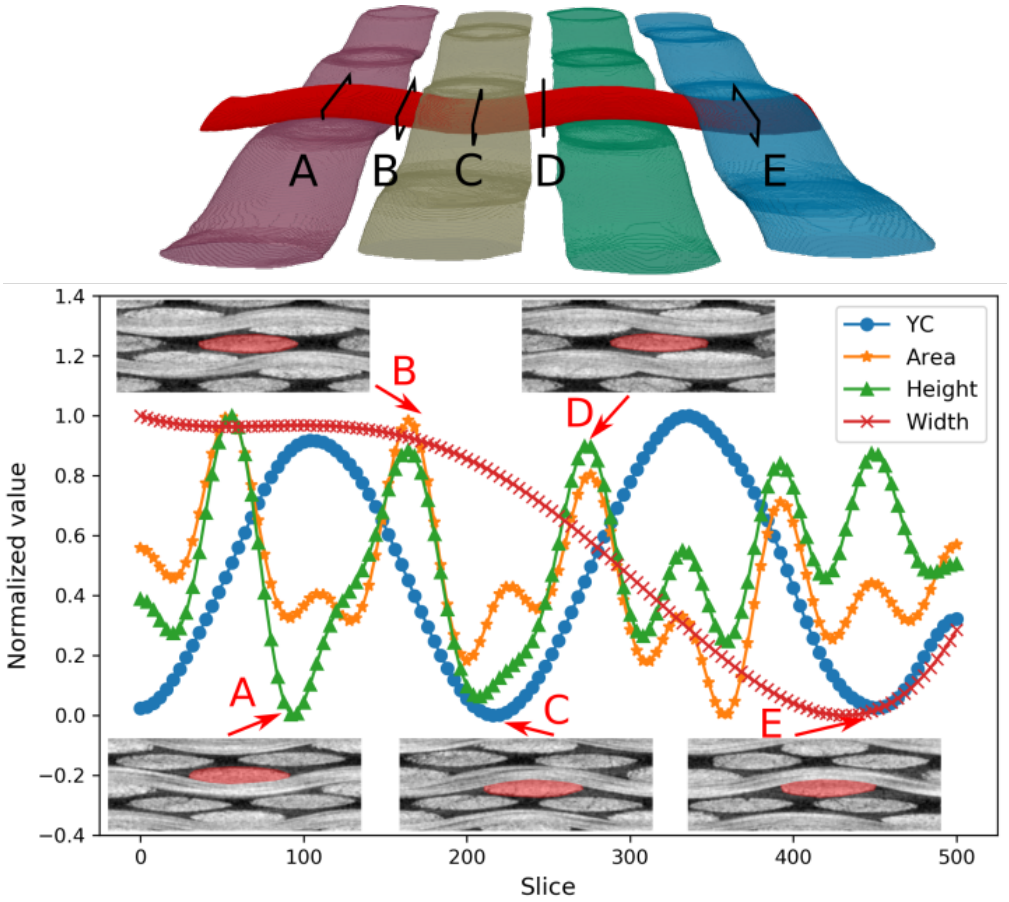

Figure 4.14 Analysis of the geometric features of a typical warp yarn in the material twin model

4.7.4 ST model

The structure tensor is a matrix devised to represent the predominant directions of the gradient in a specific neighborhood of a voxel. Since it can be employed to distinguish between fiber tows of different general orientations, it is widely used to reconstruct fabric mesostructural models ([23,24,31]). However, the precision of the geometric model reconstructed with the structure tensor was barely investigated, since no criterion of accuracy was considered. Thus, in this section, the model reconstructed by applying the structure tensor (ST model) is compared to the material twin based on the proposed multiple factor morphological criterion.

Following similar steps as in [23], several plugins from Fiji image processing software [42] have been used, namely OrietationJ [43] and 3D Segmentation [44]. As shown in Figure 4.15, the warp and weft yarns were segmented in the microtomographic image. The segmentation procedure will now be briefly described. As illustrated in Figure 4.15b, the plugin OrientationJ calculates the structure tensor for each pixel and determines the orientation of fiber tows in the original microtomographic images. Then, a color segmentation plugin is used to classify the colors into three categories for the warp and weft yarns, and the matrix. Figure 4.15c shows the result of color segmentation. The next operation is the binarization which classifies the pixels into two classes (black and white) based on a threshold value. After that, a series of morphological operations are carried out and a median filter is implemented to obtain the final image of Figure 4.15d containing the yarns of similar orientations. Since the 2D woven fabric consists of warp and weft yarns having similar geometric features, only the warp yarns are reconstructed and compared here.

As mentioned in [30], the precision of the tensor structure calculations depends on the resolution of the microtomographic images. Since the resolution in this study is not as high as in [23, 30], the orientations cannot be accurately calculated on the boundary of the tows. As shown in Figure 4.15c, noise exists on the boundary of each fiber tow. Thus the contours of the tows, which are obtained after a series of morphologic operations to eliminate the noise, are less precise compared to the results presented in the aforementioned studies. Besides, the technique based on the structure tensor does not work well for multiple layers of 2D woven fabrics, because of the significant nesting occurring between fabric layers. This makes it rather difficult to distinguish between fiber tows of similar orientation when they are in contact. For example, Figure 4.15c shows three blue tows contained in the red contour that are in contact with each other. The middle tow belongs to one fabric layer and the other two tows to another layer. This kind of nesting-induced problem complicates the separation of tows of similar orientations as illustrated in Figure 4.16. In order to evaluate the accuracy of the reconstructed ST model, only the slices with tows not in contact with other tows will be considered. Thus, the ST model will be assessed in a piecewise way, then an average value will be obtained to evaluate the quality of the reconstruction.

4.7.5 Precision of the ST model

In order to assess the precision of the model, three tows are assessed respectively, and then average values are calculated and compared with the material twin set as benchmark. According to the radar chart presented in Figure 4.17, the model poorly performs in representing the area, the circularity and XC. As already mentioned, this is because of the lower resolution

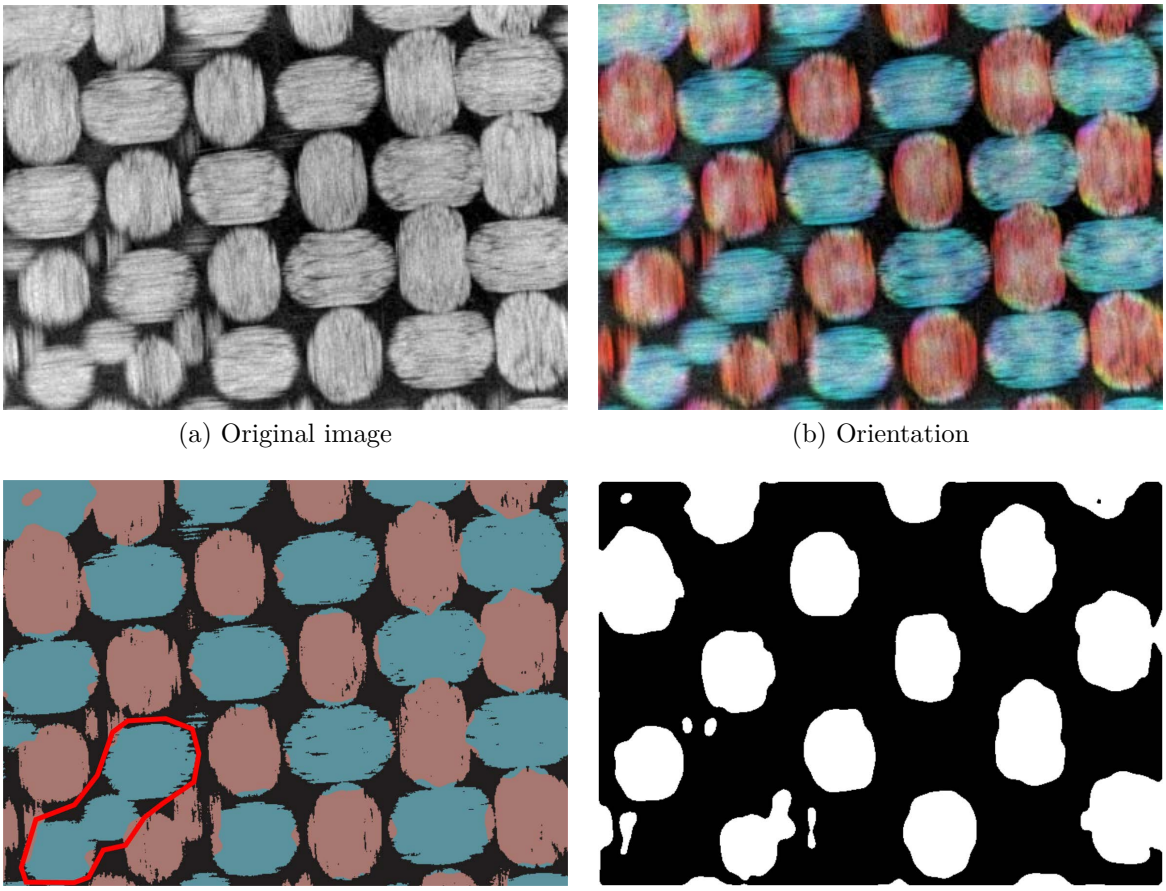

(a) Original image (b) Orientation

(c) Color segmentation (d) Warp yarns

Figure 4.15 Segmentation of the 2D woven textile to identify the warp yarns using Fiji image processing software

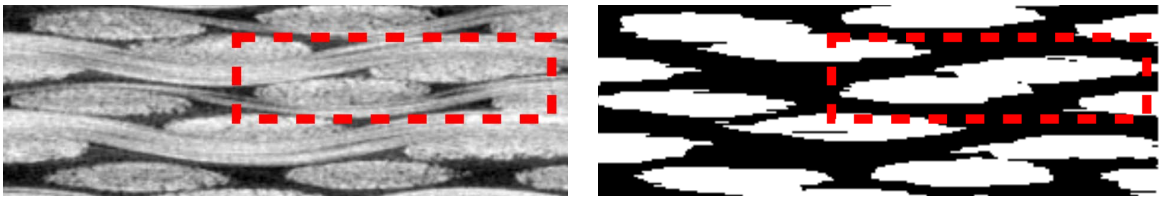

(a) Original image (b) Binary image

Figure 4.16 Warp yarns in contact cannot be separated

of the scan and of nesting which prevent from performing a precise segmentation with the structure tensor. In order to erase the noise on the binary images, the area of tows is eroded without a strict criterion during the morphological operations. As a result, the height and width are affected. However, in Figure 4.17, the precision of YC is not as bad as that of XC. This is because the main waves of the tow occur along the Y axis, hence the variations of XC are much smaller than that of YC. Consequently, the errors induced by morphological operations have more significant effects on XC than on YC.

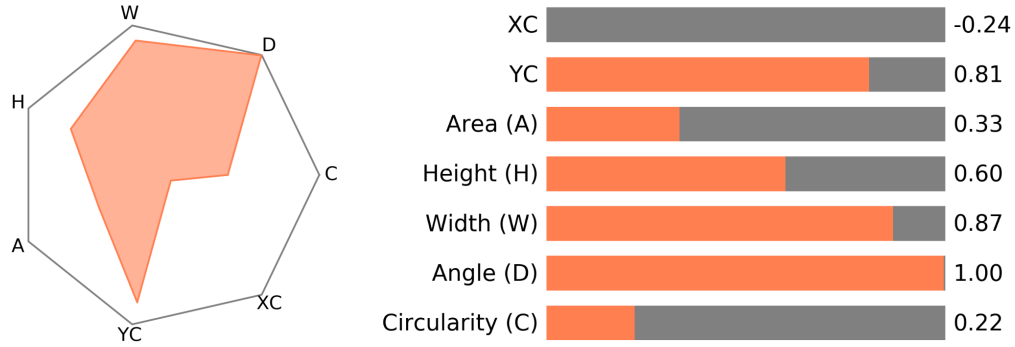

Figure 4.17 Precision of the ST preform model of 2D woven textile compared with the material twin as benchmark

4.8 Reconstruction of the 3D orthogonal textile

In this section, a preform of 3D orthogonal glass textile is reconstructed at the mesoscopic scale by Micro-CT AGM. The material twin obtained is used to analyze the geometric features of the preform and then considered as a reference model to assess the accuracy of a ST model and a refined textile model based on TexGen software.

4.8.1 X-ray microtomography

A stack of 3D orthogonal glass textile (Texonic TG96N) was scanned at the same resolution and identical conditions as the 2D fibrous reinforcement previously analyzed, except that the intensity of the X-ray beam was 40 µA (see Hilal [28] for more information). As before, a region of interest of $16.5 \times 4.95 \times 43.22\text{mm}^3$ was selected from the central part of the scanned specimen for analysis to avoid boundary effects and obtain a representative specimen of material variability. Figure 4.18a shows the preform consisting of 2 layers of fibrous reinforcement. Each layer contains 12 longitudinal tows, 4 binders and 20 transverse tows.

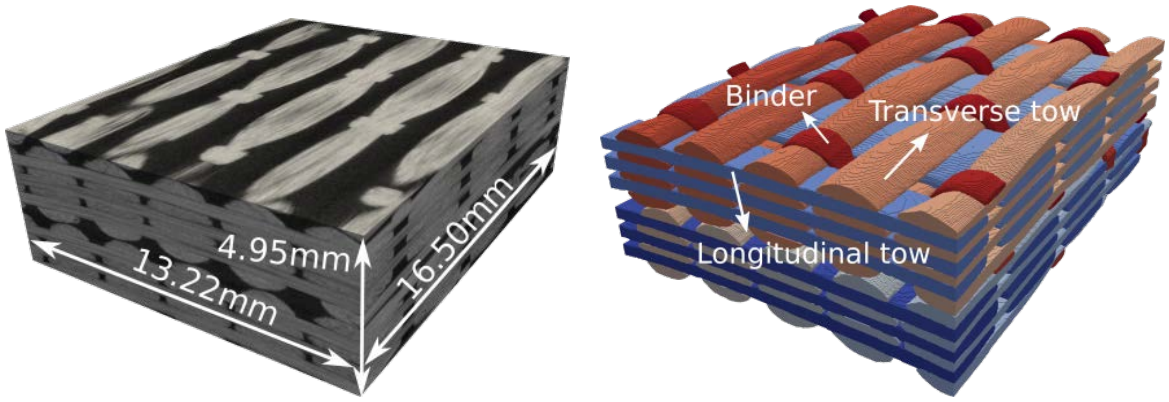

(a) (b)

Figure 4.18 Preform of the 3D glass fiber orthogonal textiles: (a) stack of microtomographic images; (b) voxel material twin constructed by Micro-CT AGM

4.8.2 Material twin

The voxel model of the preform reconstructed by Micro-CT AGM is shown in Figure 4.18b with each fiber tow labeled individually. Compared to the stack of 2D plain woven fabrics studied in Section 4.7, the nesting effect between the fabric layers of the 3D textile is much less significant.

4.8.3 Analysis of morphological features

Compared with the transverse and longitudinal tows, the shape of the binder changes a lot in the weave pattern. Thus, the geometric features of the binder are normalized to be analyzed as illustrated in Figure 4.19. These features show highly periodic evolutions along the binder orientation, in which the period of YC is twice as long as that of the other morphological characteristics. Four slices are selected to show the cross-sections of the binder at different positions, namely the crest A, the trough C and the middle points B and D. At the crest A and the trough C, the binder lies between the two fabric layers, thus it is compressed by the transverse tows of both layers, leading to a local minimum of height and area and a local maximum of width. At the middle positions B and D, the binder is compressed by the longitudinal tows on the right and left sides, thus the width reaches a local minimum. It should be pointed out that the cross-sections considered here are sections of the tows on the image slices, thus it is not strictly orthogonal to the centroid line of the tows in several slices, especially for the binders with significant waviness. This leads to significantly high values of area and height at the middle positions B and D.

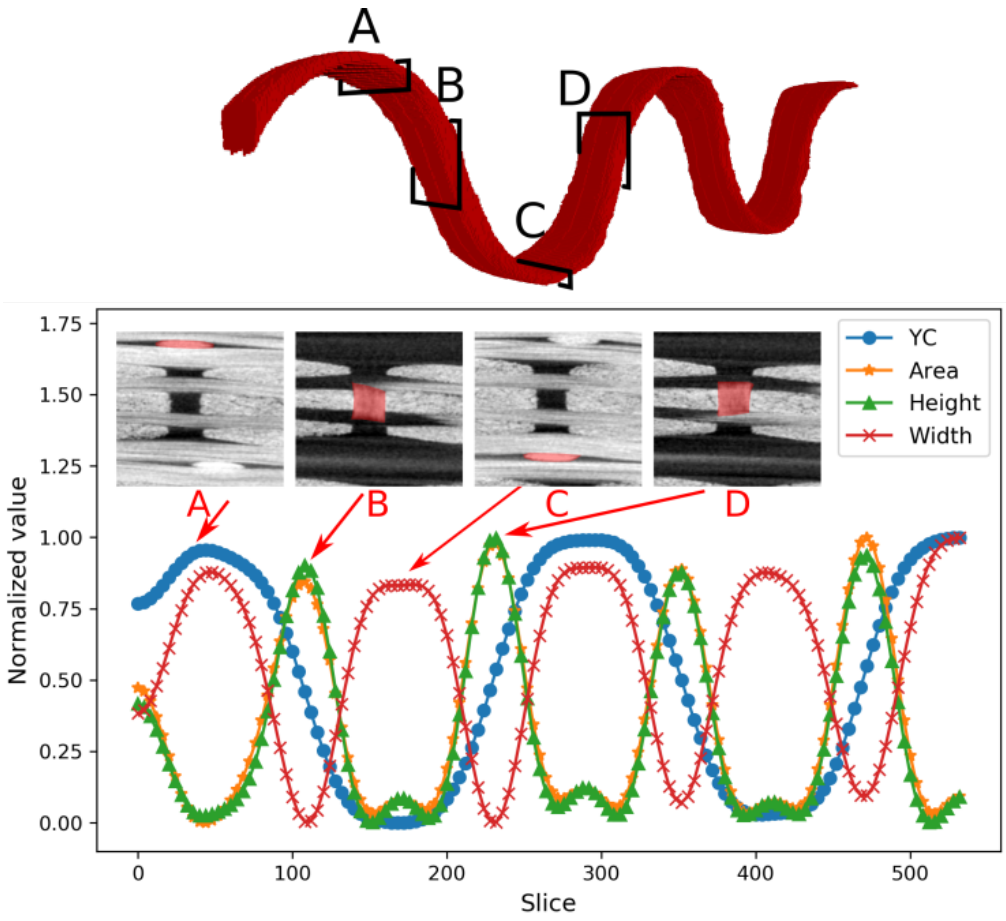

Figure 4.19 Analysis of the geometric features of the binder of the material twin

4.8.4 Assessment of the ST model

As presented in [24, 30], although the structure tensors can be used to distinguish between tows of different orientations, in 3D orthogonal textiles, the binders and the tows cannot be separated easily because they possess similar orientations. As mentioned in Section 4.7.4, slices where some tows are in contact with each other cannot be used for this assessment. Thus, in this case, only the longitudinal tows can be compared slice by slice, while the transverse tows are compared in a piecewise way and the binder cannot be assessed.

Figure 4.20 shows the overlap comparison of the longitudinal tows obtained from the two models superposed on the original image stack (matrix hidden). It is obvious that the surface of tows in the ST model is not as smooth as that of the material twin. This is because the morphologic operations make it difficult to control the quality of contours at such a low resolution. Thus, the precision of the tow of the ST model varies in the four randomly selected cross-sections as shown on the right-hand side of Figure 4.20. For sure, further operations can be performed to optimize the quality of the ST model. However, without a morphological criterion of accuracy, applying image processing techniques remains a trial-and-error procedure. Thus, the ST model is directly compared to the material twin after the same image processing steps as mentioned in Section 4.7.4.

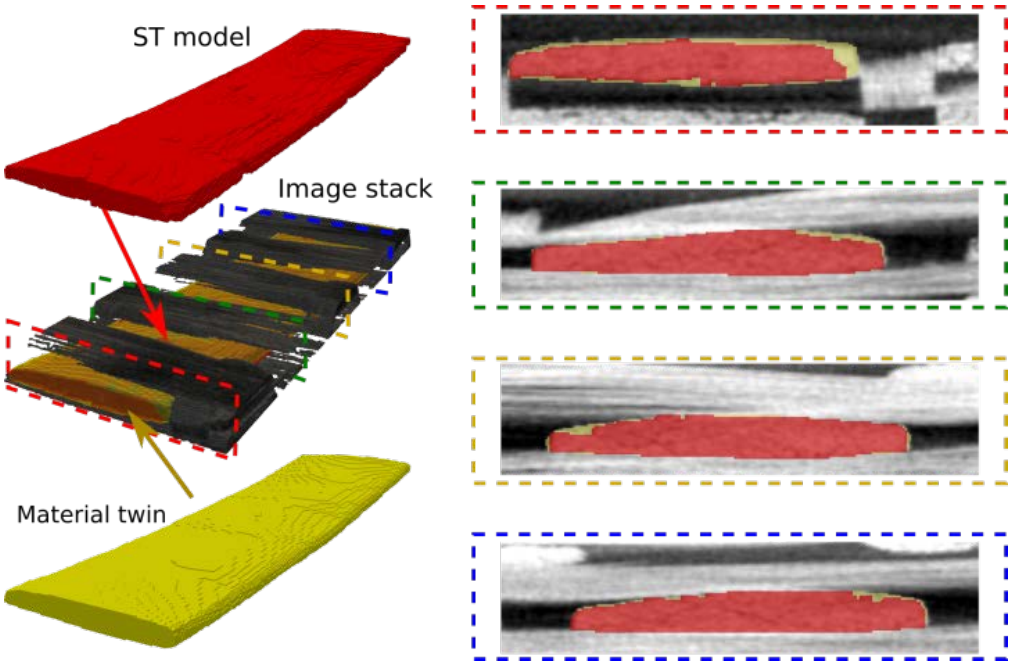

Figure 4.20 Overlap comparison of the tows of the ST model and the material twin superposed on the stack of microtomographic images

As before, three longitudinal and transverse tows are assessed respectively, and an average evaluation of the two kinds of tows of the ST model is presented in Figure 4.21. Compared to the transverse tow, the precision of the longitudinal tow is higher. Since the surface of the tow of the ST model is not as smooth as that of the material twin, the circularity of both tows is less precise. Compared to the 2D fabric ST model of Figure 4.17, the 3D textile ST model is much more precise. This means that at such a low resolution, it is more suitable to apply the structure tensor method to 3D orthogonal textiles than to 2D woven fabrics. This can be explained by the architecture of the 3D textile, since nearly no nesting exists between the fabric layers and the wavinesses of the longitudinal and transverse tows remains limited. However, applying the structure tensor is not the best technique to reconstruct the mesostructure of 3D textiles for numerical simulations, because as mentioned in [23], the binder cannot be separated easily from the tows.

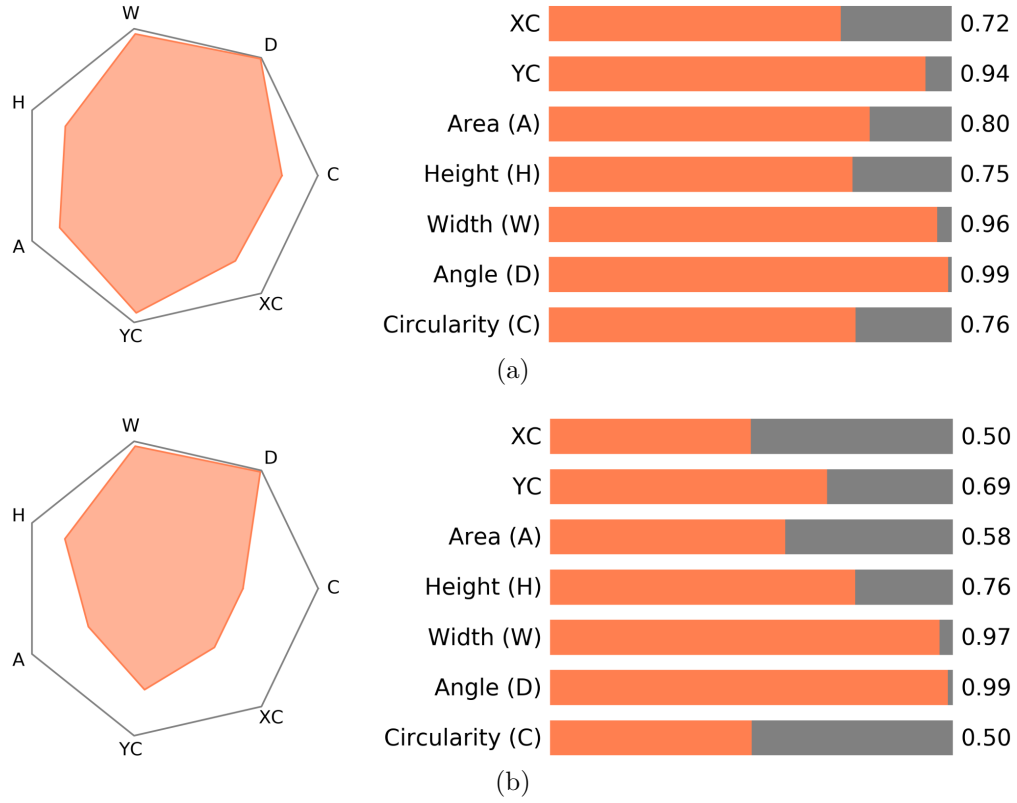

Figure 4.21 Accuracy assessment of the ST model of the 3D orthogonal textile preform compared with the material twin: (a) longitudinal tows; (b) transverse tows

4.8.5 Assessment of the refined TexGen model

TexGen [1, 2] is a widely employed geometric modeling software for engineering textiles. The default 3D weave wizard of the software allows creating, with the required geometric information, a 3D orthogonal textile model as illustrated in Figure 4.22b. Compared to the material twin of Figure 4.22a, the default TexGen model is too idealized. Thus, a Python script was developed to construct a refined TexGen model based on the geometric features obtained from the material twin. The geometric features are extracted along the tow directions every 10 slices of tows from the material twin, which means that the geometric information of about 60 slices is used here to construct the refined model. As shown in Figure 4.22c, the refined model is much more realistic than the default model. It is obvious that the precision of the default TexGen model is not comparable to that of the refined TexGen model. Therefore, only the refined TexGen model will be compared to the material twin in the sequel.

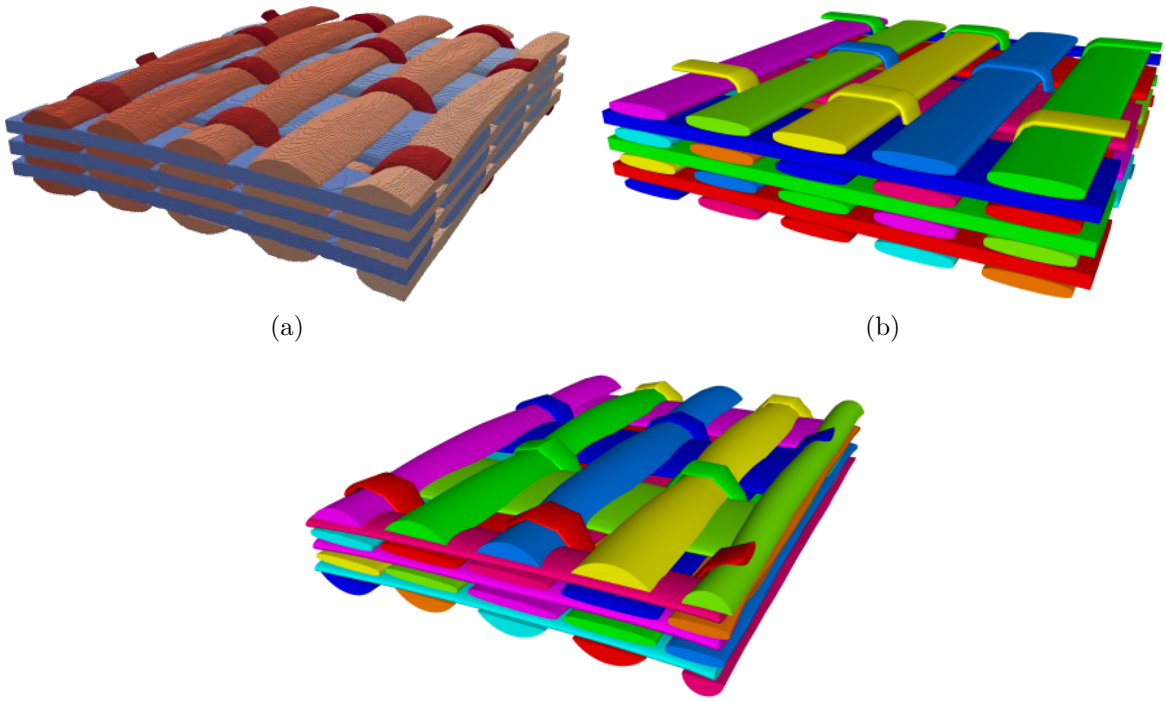

(a) (b)

(c)

Figure 4.22 Mesostructural models of the 3D orthogonal textile: (a) material twin; (b) default TexGen model; (c) refined TexGen model

Figure 4.23 shows the accuracy assessment of the refined TexGen model, in which the geometric features of three binders, longitudinal tows and transverse tows are respectively compared slice by slice with the material twin. The radar charts show that the width is generally pre-

cise while the area, height and circularity can be less precise in some cases. This indicates that the precision of the area is dominated by that of the height and circularity. Besides, compared to the binder, the precision of the transverse and longitudinal tows is much better. This can be explained by the way to assign the cross-sections of yarns in TexGen and the significant waviness of the binder.

In TexGen, the cross-sections need to be assigned for each master node. The geometric information of the cross-section contains the contour shape (such as rectangle and ellipse) and the related geometric dimensions (width and height). However, the only input for the material twin are the contours of tows without any shape definition. Thus, when the geometric information of the material twin is used to construct the refined TexGen model, it is possible to assign basic geometric dimensions such as the width and height, but it is difficult to define a proper shape for each cross-section. Thus, a uniform shape is assigned to each type of fiber tow. For example, the shapes of the binders, of the longitudinal tows, of the surface transverse tows and of the internal transverse tows are assigned as ellipse, lenticular cross-section and power ellipse respectively. Since the shape and geometric dimensions of the binder cross-sections change acutely along the binder orientation as shown in Figure 4.23a, inappropriate definition of cross-sectional shapes can severely affect the precision of binders. On the contrary, the effect is much smaller on the longitudinal and transverse tows, since the waviness and evolution of their cross-sections remain rather limited.

4.9 Conclusion

In this article, a Micro-CT Aided Geometric Modeling approach (Micro-CT AGM) was proposed to reconstruct mesostructural geometric models of continuous fiber reinforcements from microtomographic images. A software called CompoCT was developed as a platform for this specific modeling procedure. In addition, a multiple factor criterion based on a series of morphological features of fiber tows, was proposed to assess the relative accuracy of the geometric models created. Following this approach, precise mesostructural geometric models of a 2D woven fabric and a 3D orthogonal textile were successfully reconstructed at the lower scanning resolution (22 µm/pixel). These models possess several interesting features that were summarized in a new concept called "material twin", for which a tentative definition was also proposed. Considering the material twin as a benchmark, a comparison with other modeling approaches based on image processing or textile modeling such as TexGen [1, 2] showed that the Micro-CT AGM methodology allows constructing more accurate geometric models for the resolution considered.

Since Micro-CT AGM is a way to create material twins of built-in accuracy for further use in

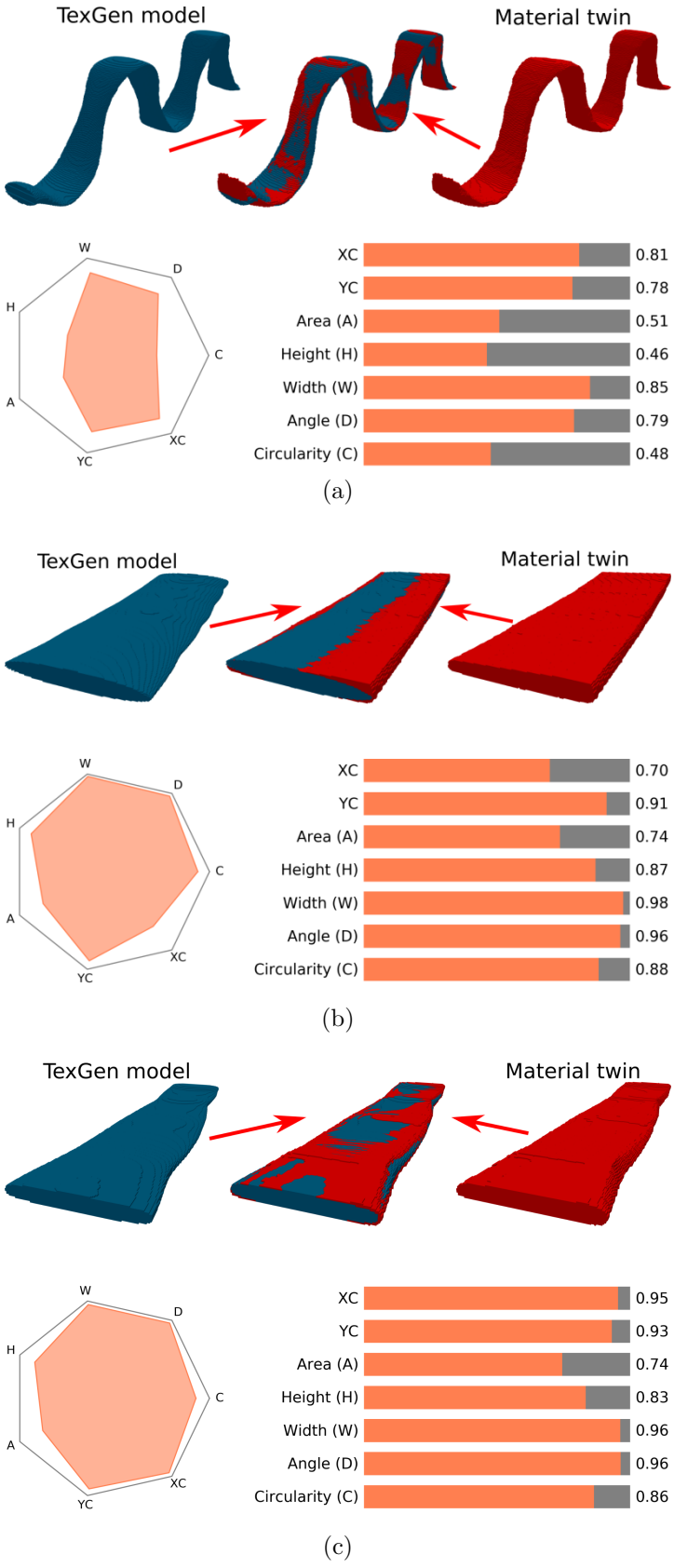

Figure 4.23 Precision of the refined TexGen model of the 3D orthogonal textile compared to the material twin: (a) binders; (b) longitudinal tows; (c) transverse tows.

data-driven simulations, it can lead to methods to tailor and predict composite mechanical properties. The geometric information extracted from material twins could be also used as input in stochastic modeling [36]. Moreover, by combining this approach with multi-scale modeling (see references [45–47] for example), advanced and automatic computer simulations taking into account the mesostructure of high performance composites can be carried out, in which detailed geometric modeling and manual assignment of material properties are no longer necessary.

In this study, the contours of tows were obtained by manual separation to reconstruct geometric models from a relatively lower resolution image, requiring significant labor. One future key issue would be to implement precise automatic or semi-automatic segmentation approaches at lower resolution to accelerate modeling procedures. Applying the Micro-CT AGM methodology to simulate and analyze the mechanical behavior of engineering textiles in compression and shear during composite manufacturing are other interesting topics of future work, as well as modeling impact behavior or flow properties to predict permeability.

4.10 Acknowledgements

This work has been partially supported by the Department of Mechanical Engineering of Polytechnique Montreal, the National Natural Science Foundation of China (Grant Nos. 11372231 and 11772238) and by the National Science & Engineering Research Council of Canada (NSERC) (Discovery Grant). Authors also gratefully acknowledge the Research Center for High Performance Polymer and Composite Systems (CREPEC), the "Fonds de recherche du Québec - Nature et technologies" (FRQNT) and the "Fonds National de la Recherche" (FNR) of Luxembourg for their financial support. Authors would also like to express their thanks to Nicolas Juillard and Texonic for providing the fiber reinforcements used in this study.

4.11 Appendix A. Parametric curve and surface kriging

After extracting the contours on a large enough number of key sections, interpolation methods are used to reconstruct the surface of the whole tow, i.e., parametric curve and surface kriging [34]. Since a different number of points was selected in each key section, parametric curve kriging is initially employed to obtain a uniform number of points in all the key sections. Assuming that the contour of the tow is defined by a set of data points $X_i = (x_i, y_i)$, $1 \leq i \leq N$, that will be used in the interpolation. By selecting an appropriate drift function $\sum_{i=0}^{L} a_i^q p_i(t)$ to represent the average shape of the contour, where $p_i(t)$ are the terms that

depend on the selection of drift function, and a covariance $K(h)$ to model the deviations with respect to the average shape, the contours of tows can be precisely interpolated by parametric dual kriging, after which a uniform number of data points can be readily obtained on each contour.

The parametric equations of the contour can be stated as follows:

$$\begin{cases} x(t) = \sum_{i=0}^{L} a_i^x p_i(t) + \sum_{j=1}^{N} b_j^x K(|t - t_j|), \\ y(t) = \sum_{i=0}^{L} a_i^y p_i(t) + \sum_{j=1}^{N} b_j^y K(|t - t_j|), \end{cases} \tag{4.8}$$

in which the parameter t_j is normalized so that:

$$0 = t_1 \leq \cdots \leq t_j \leq \cdots \leq t_N = 1 \tag{4.9}$$

and the coefficients a_i^q, $b_j^q (q = x, y)$ in Eq. (4.8) are the solution of the linear system:

$$\begin{bmatrix} 0 & \cdots & K(|t_1 - t_N|) & 1 & \cdots & p_L(t_1) \\ \vdots & \ddots & \vdots & \vdots & \ddots & \vdots \\ K(|t_N - t_1|) & \cdots & 0 & 1 & \cdots & p_L(t_N) \\ 1 & \cdots & 1 & 0 & \cdots & 0 \\ \vdots & \ddots & \vdots & \vdots & \ddots & \vdots \\ p_L(t_1) & \cdots & p_L(t_N) & 0 & \cdots & 0 \end{bmatrix} \begin{bmatrix} b_1^x & b_1^y \\ \vdots & \vdots \\ b_N^x & b_N^y \\ a_0^x & a_0^y \\ \vdots & \vdots \\ a_L^x & a_L^y \end{bmatrix} = \begin{bmatrix} x_1 & y_1 \\ \vdots & \vdots \\ x_N & y_N \\ 0 & 0 \\ \vdots & \vdots \\ 0 & 0 \end{bmatrix} \tag{4.10}$$

The contour points on a series of sections of a fiber tow can be used to reconstruct the surface of the tow by parametric surface kriging [34]. Suppose that each contour is defined by N points for a total of M cross-sections of the tow. The data points of these contours are denoted P_{ij} for $1 \leq i \leq M$, $1 \leq j \leq N$. They will be used to interpolate the surface of the tow by parametric dual kriging.

For convenience, the kriging profiles are chosen as constant drift with covariance $K_1(h)$ in the cross-section, and linear drift with covariance $K_2(h)$ in the longitudinal tow direction. Before using the surface kriging, proper parameter values should be assigned to each data point such that:

$$P(s_i, t_j) = P_{ij} \quad (1 \leq i \leq M, 1 \leq j \leq N) \tag{4.11}$$

where $\mathbf{S}$ and $\mathbf{T}$ denote two independent normalized sets of parameters between 0 and 1 along the longitudinal and transverse tow directions respectively.

The parametric equation of the surface can be obtained as follows (for convenience, only the equation for x is presented here):

$$x(s,t) = \mathbf{k}_1(s)^T \cdot \mathbf{S}^{-1} \cdot \mathbf{P}_x \cdot \mathbf{T}^{-1} \cdot \mathbf{k}_2(t) \tag{4.12}$$

where $\mathbf{S}$, $\mathbf{T}$ are the dual kriging matrices in the longitudinal and transverse directions respectively, $\mathbf{k}_1(s)$, $\mathbf{k}_2(t)$ are the vectors of the drift and covariance functions, and $\mathbf{P}_x$ is a matrix containing the abscissa of points P_{ij}:

$$\mathbf{S} = \begin{bmatrix} & & & 1 \\ & K_1(|s_i - s_j|) & & \vdots \\ & & & 1 \\ 1 & \cdots & 1 & 0 \end{bmatrix} \tag{4.13}$$

$$\mathbf{T} = \begin{bmatrix} & & & 1 & t_1 \\ & K_2(|t_i - t_j|) & & \vdots & \vdots \\ & & & 1 & t_N \\ 1 & \cdots & 1 & 0 & 0 \\ t_1 & \cdots & t_N & 0 & 0 \end{bmatrix} \tag{4.14}$$

$$\mathbf{k}_1(s) = \begin{bmatrix} K_1(|s - s_1|) & \cdots & K_1(|s - s_M|) & 1 \end{bmatrix}^T \tag{4.15}$$

$$\mathbf{k}_1(s) = \begin{bmatrix} K_2(|t - t_1|) & \cdots & K_2(|t - t_N|) & 1 & t \end{bmatrix}^T \tag{4.16}$$

$$\mathbf{P}_x = \begin{bmatrix} x(s_1,t_1) & \cdots & x(s_1,t_N) & 0 & 0 \\ \vdots & & \vdots & 0 & 0 \\ x(s_M,t_1) & \cdots & x(s_M,t_N) & 0 & 0 \\ 0 & \cdots & 0 & 0 & 0 \end{bmatrix} \tag{4.17}$$

Finally, the full parametric equation of the tow surface is obtained by applying the same method to process the y and z coordinates of points P_{ij}.

Bibliography

[1] M. Sherburn, "Geometric and mechanical modelling of textiles," Ph.D. dissertation, University of Nottingham, 2007.

[2] A. C. Long and L. P. Brown, "Modelling the geometry of textile reinforcements for composites: TexGen," in *Composite Reinforcements for Optimum Performance*, 2011, pp. 239–264.

[3] F. Desplentere, S. V. Lomov, D. L. Woerdeman, I. Verpoest, M. Wevers, and A. Bogdanovich, "Micro-CT characterization of variability in 3D textile architecture," *Composites Science and Technology*, vol. 65, no. 13, pp. 1920–1930, 2005.

[4] P. J. Schilling, B. R. Karedla, A. K. Tatiparthi, M. A. Verges, and P. D. Herrington, "X-ray computed microtomography of internal damage in fiber reinforced polymer matrix composites," *Composites Science and Technology*, vol. 65, no. 14, pp. 2071–2078, 2005.

[5] J. S. U. Schell, M. Renggli, G. H. van Lenthe, R. Müller, and P. Ermanni, "Micro-computed tomography determination of glass fibre reinforced polymer meso-structure," *Composites Science and Technology*, vol. 66, no. 13, pp. 2016–2022, 2006.

[6] J. S. U. Schell, M. Deleglise, C. Binetruy, P. Krawczak, and P. Ermanni, "Numerical prediction and experimental characterisation of meso-scale-voids in liquid composite moulding," *Composites Part A: Applied Science and Manufacturing*, vol. 38, no. 12, pp. 2460–2470, 2007.

[7] P. Badel, E. Vidal-Sallé, E. Maire, and P. Boisse, "Simulation and tomography analysis of textile composite reinforcement deformation at the mesoscopic scale," *Composites Science and Technology*, vol. 68, no. 12, pp. 2433–2440, 2008.

[8] J. Pazmino, V. Carvelli, and S. V. Lomov, "Micro-CT analysis of the internal deformed geometry of a non-crimp 3D orthogonal weave E-glass composite reinforcement," *Composites Part B: Engineering*, vol. 65, pp. 147–157, 2014.

[9] A. Madra, J. Adrien, P. Breitkopf, E. Maire, and F. Trochu, "A clustering method for analysis of morphology of short natural fibers in composites based on X-ray microtomography," *Composites Part A: Applied Science and Manufacturing*, vol. 102, pp. 184–195, 2017.

[10] M. J. Emerson, K. M. Jespersen, A. B. Dahl, K. Conradsen, and L. P. Mikkelsen, "Individual fibre segmentation from 3D X-ray computed tomography for characterising the fibre orientation in unidirectional composite materials," *Composites Part A: Applied Science and Manufacturing*, vol. 97, pp. 83–92, 2017.

[11] A. Mendoza, J. Schneider, E. Parra, E. Obert, and S. Roux, "Differentiating 3D textile composites: A novel field of application for Digital Volume Correlation," *Composite Structures*, vol. 208, pp. 735–743, 2019.

[12] H. Rolland, N. Saintier, P. Wilson, J. Merzeau, and G. Robert, "In situ X-ray tomography investigation on damage mechanisms in short glass fibre reinforced thermoplastics: Effects of fibre orientation and relative humidity," *Composites Part B: Engineering*, vol. 109, pp. 170–186, 2017.

[13] Y. Wan, I. Straumit, J. Takahashi, and S. V. Lomov, "Micro-CT analysis of internal geometry of chopped carbon fiber tapes reinforced thermoplastics," *Composites Part A: Applied Science and Manufacturing*, vol. 91, pp. 211–221, 2016.

[14] Y. Wan, I. Straumit, J. Takahashi, and S. V. Lomov, "Micro-CT analysis of the orientation unevenness in randomly chopped strand composites in relation to the strand length," *Composite Structures*, vol. 206, pp. 865–875, 2018.

[15] A. Madra, N. El Hajj, and M. Benzeggagh, "X-ray microtomography applications for quantitative and qualitative analysis of porosity in woven glass fiber reinforced thermoplastic," *Composites Science and Technology*, vol. 95, pp. 50–58, 2014.

[16] M. A. Ali, R. Umer, K. A. Khan, S. Bickerton, and W. J. Cantwell, "Non-destructive evaluation of through-thickness permeability in 3D woven fabrics for composite fan blade applications," *Aerospace Science and Technology*, vol. 82-83, pp. 520–533, 2018.

[17] M. A. Ali, R. Umer, K. A. Khan, and W. J. Cantwell, "In-plane virtual permeability characterization of 3D woven fabrics using a hybrid experimental and numerical approach," *Composites Science and Technology*, vol. 173, pp. 99–109, 2019.

[18] N. M. Larson and F. W. Zok, "Insights from in-situ X-ray computed tomography during axial impregnation of unidirectional fiber beds," *Composites Part A: Applied Science and Manufacturing*, vol. 107, pp. 124–134, 2018.

[19] I. Verpoest and S. V. Lomov, "Virtual textile composites software WiseTex: Integration with micro-mechanical, permeability and structural analysis," *Composites Science and Technology*, vol. 65, pp. 2563–2574, 2005.

[20] S. V. Lomov, "Modelling the geometry of textile reinforcements for composites: Wisetex," in *Composite reinforcements for optimum performance*. Elsevier, 2011, pp. 200–238.

[21] Y. Wang and X. Sun, "Digital-element simulation of textile processes," *Composites Science and Technology*, vol. 61, no. 2, pp. 311–319, 2001.

[22] G. Zhou, X. Sun, and Y. Wang, "Multi-chain digital element analysis in textile mechanics," *Composites Science and Technology*, vol. 64, no. 2, pp. 239–244, 2004.

[23] N. Naouar, E. Vidal-Sallé, J. Schneider, E. Maire, and P. Boisse, "Meso-scale FE analyses of textile composite reinforcement deformation based on X-ray computed tomography," *Composite Structures*, vol. 116, no. 1, pp. 165–176, 2014.

[24] N. Naouar, E. Vidal-Sallé, J. Schneider, E. Maire, and P. Boisse, "3D composite reinforcement meso F.E. analyses based on X-ray computed tomography," *Composite Structures*, vol. 132, pp. 1094–1104, 2015.

[25] S. D. Green, A. C. Long, B. S. F. El Said, and S. R. Hallett, "Numerical modelling of 3D woven preform deformations," *Composite Structures*, vol. 108, pp. 747–756, 2014.

[26] S. D. Green, M. Y. Matveev, A. C. Long, D. Ivanov, and S. R. Hallett, "Mechanical modelling of 3D woven composites considering realistic unit cell geometry," *Composite Structures*, vol. 118, pp. 284–293, 2014.

[27] J. Bigun, T. Bigun, and K. Nilsson, "Recognition by symmetry derivatives and the generalized structure tensor," *IEEE Transactions on Pattern Analysis and Machine Intelligence*, vol. 26, no. 12, pp. 1590–1605, 2004.

[28] S. Hilal, "Caractérisation par microtomographie de la mésostructure des renforts fibreux pour la fabrication de composites par injection," Ph.D. dissertation, École Polytechinque de Montréal, 2018.

[29] R. M. Haralick and L. G. Shapiro, *Computer and robot vision*. Addison-wesley Reading, 1992, vol. 1.

[30] I. Straumit, S. V. Lomov, and M. Wevers, "Quantification of the internal structure and automatic generation of voxel models of textile composites from X-ray computed tomography data," *Composites Part A: Applied Science and Manufacturing*, vol. 69, pp. 150–158, 2015.

[31] Y. Liu, I. Straumit, D. Vasiukov, S. V. Lomov, and S. Panier, "Prediction of linear and non-linear behavior of 3D woven composite using mesoscopic voxel models reconstructed from X-ray micro-tomography," *Composite Structures*, vol. 179, pp. 568–579, 2017.

[32] N. Isart, J. A. Mayugo, N. Blanco, L. Ripoll, A. Solà, and M. Soler, "Geometric model for 3D through-thickness orthogonal interlock composites," *Composite Structures*, vol. 119, pp. 787–798, 2015.

[33] N. Isart, B. El Said, D. S. Ivanov, S. R. Hallett, J. A. Mayugo, and N. Blanco, "Internal geometric modelling of 3D woven composites: A comparison between different approaches," *Composite Structures*, vol. 132, pp. 1219–1230, 2015.

[34] F. Trochu, "A contouring program based on dual kriging interpolation," *Engineering with Computers*, vol. 9, no. 3, pp. 160–177, 1993.

[35] M. Karahan, S. V. Lomov, A. E. Bogdanovich, D. Mungalov, and I. Verpoest, "Internal geometry evaluation of non-crimp 3D orthogonal woven carbon fabric composite," *Composites Part A: Applied Science and Manufacturing*, vol. 41, no. 9, pp. 1301–1311, 2010.

[36] A. Vanaerschot, B. N. Cox, S. V. Lomov, and D. Vandepitte, "Multi-scale modelling strategy for textile composites based on stochastic reinforcement geometry," *Computer Methods in Applied Mechanics and Engineering*, vol. 310, pp. 906–934, 2016.

[37] X. Yu, H. Wang, and Z. Wang, "Analysis of yarn fiber volume fraction in textile composites using scanning electron microscopy and X-ray micro-computed tomography," *Journal of Reinforced Plastics and Composites*, vol. 38, no. 5, pp. 199–210, 2019.

[38] S. V. Lomov, D. S. Ivanov, I. Verpoest, M. Zako, T. Kurashiki, H. Nakai, and S. Hirosawa, "Meso-FE modelling of textile composites: Road map, data flow and algorithms," *Composites Science and Technology*, vol. 67, no. 9, pp. 1870–1891, 2007.

[39] A. Madra, P. Breitkopf, A. Rassineux, and F. Trochu, "Image-based model reconstruction and meshing of woven reinforcements in composites," *International Journal for Numerical Methods in Engineering*, vol. 112, no. 9, pp. 1235–1252, 2017.

[40] B. El Said, S. Green, and S. R. Hallett, "Kinematic modelling of 3D woven fabric deformation for structural scale features," *Composites Part A: Applied Science and Manufacturing*, vol. 57, pp. 95–107, 2014.

[41] S. Joglekar and M. Pankow, "Modeling of 3D woven composites using the digital element approach for accurate prediction of kinking under compressive loads," *Composite Structures*, vol. 160, pp. 547–559, 2017.

[42] J. Schindelin, I. Arganda-Carreras, E. Frise, V. Kaynig, M. Longair, T. Pietzsch, S. Preibisch, C. Rueden, S. Saalfeld, B. Schmid *et al.*, "Fiji: an open-source platform for biological-image analysis," *Nature Methods*, vol. 9, no. 7, pp. 676–682, 2012.

[43] R. Rezakhaniha, A. Agianniotis, J. T. C. Schrauwen, A. Griffa, D. Sage, C. V. C. Bouten, F. N. Van De Vosse, M. Unser, and N. Stergiopulos, "Experimental investigation of collagen waviness and orientation in the arterial adventitia using confocal laser scanning microscopy," *Biomechanics and Modeling in Mechanobiology*, vol. 11, no. 3-4, pp. 461–473, 2012.

[44] J. Ollion, J. Cochennec, F. Loll, C. Escudé, and T. Boudier, "TANGO: a generic tool for high-throughput 3D image analysis for studying nuclear organization," *Bioinformatics*, vol. 29, no. 14, pp. 1840–1841, 2013.

[45] R. Xu, C. Bouby, H. Zahrouni, T. Ben Zineb, H. Hu, and M. Potier-Ferry, "A multiscale analysis on the superelasticity behavior of architected shape memory alloy materials," *Materials*, vol. 11, no. 9, p. 1746, 2018.

[46] R. Xu, Y. Hui, H. Hu, Q. Huang, H. Zahrouni, T. B. Zineb, and M. Potier-Ferry, "A Fourier-related FE^2 multiscale model for instability phenomena of long fiber reinforced materials," *Composite Structures*, vol. 211, pp. 530–539, 2019.

[47] J. Yang, R. Xu, H. Hu, Q. Huang, and W. Huang, "Structural-Genome-Driven computing for composite structures," *Composite Structures*, vol. 215, pp. 446–453, 2019.

CHAPTER 5 ARTICLE 2 : NUMERICAL AND EXPERIMENTAL INVESTIGATION OF SATURATED TRANSVERSE PERMEABILITY OF 2D WOVEN GLASS FABRICS BASED ON MATERIAL TWINS

W. Huang, P. Causse, H. Hu*, F. Trochu

Published in *Polymer Composites, Volume41, 1341-1355, 1 April 2020*

5.1 Chapter overview

This chapter presents the article published in *Polymer Composites*, in which the numerical and experimental investigations of saturated transverse permeability of 2D woven glass fabrics were carried out based on the material twins proposed in Chapter 4. Compared to traditional geometric models, material twins precisely represent the geometric features of the fiber tows and the nesting between the fabric layers. This provides a more realistic model of mesopores, which leads to more precise and reliable simulation results. Besides, thanks to the material variability that can be taken into account in material twin, variations in fiber volume content and permeability predictions occur in numerical simulations as in experiments with real fabrics. This inherent characteristic makes the material twins different from the other general geometric models. In addition, several key issues were considered to improve the existing experimental procedures and get more reliable and accurate measurement results. Finally, both the numerical and experimental approaches are employed to discuss the effect of nesting between fabric layers in saturated transverse permeability measurements.

5.2 Abstract

The through-thickness permeability of fibrous reinforcement is one of the critical parameters that govern fabrication efficiency and production quality in several Liquid Composite Molding (LCM) process variants devised to achieve through-thickness impregnation of fibrous reinforcements. It is difficult to precisely measure and predict the through-thickness permeability, because it is simultaneously affected by diverse factors, for example the geometric features of the test mold, nesting between fabric layers and flow-induced compaction of the fiber bed. In this article, the saturated through-thickness permeability of 2D woven glass fabrics is investigated using information provided by mesostructural geometric models reproducing the real textile architecture. These models are created by Micro-CT Aided Geometric Modeling

(Micro-CT AGM), a recently proposed technique to analyze three-dimensional images obtained by X-ray microtomography. They are called "material twins" because they reproduce with assessed accuracy the geometrical configuration of the textile preform, are representative of material variability and allow performing numerical simulations of flow or mechanical properties. Computer simulations of steady state through-thickness flows in material twins were carried out to evaluate the transverse permeability and compared to experiments. Issues concerning material variability due to nesting and the accuracy of through-thickness permeability measurements were considered and discussed. A good agreement was obtained between numerical and experimental values of transverse permeability. Both approaches show a significant influence of the number of layers considered, which can be explained by nesting between adjacent plies. Numerical simulations also illustrate how nesting significantly affects material variability.

5.3 Introduction

High performance polymer based composites are widely used in the aerospace and automobile fields, because of their higher strength per unit mass compared to metallic materials. The design flexibility they provide and long life are also key advantages of these materials. Liquid Composite Molding (LCM) is a generic term regrouping a family of composite manufacturing processes, in which a liquid thermoset resin is injected in a mold cavity to saturate a dry preformed fibrous reinforcement. Several LCM process variants were devised to achieve through-thickness rather than in-plane resin impregnation of the fiber bed, for example Vacuum Assisted Resin Infusion (VARI) with a distribution medium [1, 2], Compression Resin Transfer Molding (CRTM) [3–5], and Flexible Injection (FI) [6–8]. Thus, the average length of resin flow paths is considerably decreased, which makes possible to produce composite parts of large dimension with standard injection equipment. In these processes, the through-thickness permeability of fibrous reinforcement is a critical factor that governs part quality and manufacturing efficiency.

In recent years, different experimental approaches have been developed to measure the saturated through-thickness permeability. Klunker et al. [9] used experimental setups with three slightly different injection and data acquisition systems to study the permeability of fibrous reinforcements for different injection pressures. Becker and Mitschang [10] built a measurement unit to simultaneously monitor compaction and measure the transverse permeability. Without using stacks of fabric layers like in other investigations, Drapier et al. [11] designed a system with fewer fabric plies to study the influence of stitching density on permeability. A continuous method was also proposed by Ouagne et al. [12, 13] to measure in a single test

the through-thickness permeability as a function of fiber volume content. This approach is considered to better reflect the coupling phenomena between compaction and the liquid flow in Resin Film Infusion (RFI). Scholz et al. [14] followed a similar procedure to characterize the liquid and air permeability. Note that they also used highly permeable grids as surface layers on the bottom and top of the experimental samples to assist in generating a through-thickness flow as uniformly unidirectional as possible. According to their findings, the grid plays a quite important role in saturated through-thickness permeability measurements, especially for thin samples. Moreover, they found that permeability decreases when more layers of the same material are stacked. This was explained by the reduction of gaps between fiber tows in stacked layers induced by nesting [15].

The effect of nesting on through-thickness permeability of fibrous reinforcements was also investigated in several other studies. Fang et al. [16] and Jiang et al. [17] proposed theoretical models to predict the transverse permeability of unidirectional and non-crimp fabrics that were compared to experimental results. This analysis showed that layer shifts and nesting have a great effect on the permeability of these two types of fabrics. Yang et al. [18] employed a numerical model of two fabric layers to study the effect of nesting on the through-thickness permeability of woven fabrics. Sas et al. [19] conducted numerical simulations to investigate the effects of the stacking sequence and of the misalignment of layers as commonly observed in practical applications. The results show that the stacking sequence plays a significant role on the transverse permeability of engineering fabrics. However, these papers do not give a full picture on the effect of nesting on permeability, because in [16, 18] only two plies were tested which is not fully representative of real materials, and in [17, 19] only unidirectional fabrics were investigated. The effect of nesting on the transverse permeability of multilayer woven fabrics still needs to be studied. Thanks to microtomography, it is possible to carry out this investigation for fibrous reinforcements in their real deformed state under compaction. Numerical flow simulations will be conducted on three-dimensional geometric material models obtained from micro-CT scans.

Besides nesting, the through-thickness permeability of fabrics can also be affected by other factors, such as the deformation of fiber tows resulting from flow-induced compaction [10, 20, 21], reinforcement distortions [22, 23] and dual-scale flow [24–28]. Affected by these factors and also the intrinsic features of different fabrics, such as the material and the woven pattern, the range of saturated transverse permeability can be very large, which generally varies from $10^{-10}\mathrm{m}^2$ ([14, 18, 29–31]), $10^{-11}\mathrm{m}^2$ ([12, 13, 19, 32]) to $10^{-12}\mathrm{m}^2$ or even lower ([9–11, 20, 33]). No standard procedure has yet been proven to measure the saturated through-thickness permeability of fibrous reinforcements. Therefore, an international benchmark exercise was performed recently to compare measurement results of compression and through-thickness

permeability obtained by 32 different research laboratories. However, as reported in a conference paper of 2018 summing up and comparing the experimental results [34], differences of about two orders of magnitude were observed between the experimental results of participants even for the measurement of the same fabrics. Although through-thickness permeability measurements have been routinely performed for some time, these significant discrepancies show that some experimental issues still need to be clarified. In order to develop an accurate and robust measurement procedure, it is necessary to take into account the physical phenomena that come into play in liquid flows through stacks of fibrous reinforcements.

Compared to experiments, numerical simulation is an efficient way to study the permeability of engineering fabrics to reveal the critical phenomena occurring during the impregnation in LCM processes both at the mesoscale and microscale levels [19, 35–39]. However, the comparison between numerical predictions of transverse permeability and experiments still remains a challenge because the mesostructural models are generally constructed by idealized modeling approaches. Thus, most simulation results cannot take into account the effect of material variability as in experiments. Since material variability is an intrinsic feature of fabric stacks, it was always regarded as a critical factor leading to the scatter of experimental results [22]. However, few appropriate modeling tools are yet available to account for the variability of engineering fabrics [40]. Some numerical simulations based on the geometric models generated from microtomographic images allowed investigating the influence of material variability on permeability [30, 31, 41]. However, since the unit cells are extracted at different locations of the reconstructed model for a certain number of layers, only the spatial variability of permeability can be studied. It is still not possible to study the variability induced by nesting or contact between tows, since the tows are not necessarily separated during image processing.

This article studies the saturated through-thickness permeability of 2D woven fabrics using both experimental characterization and numerical predictions. The objective is to improve the comparison between the two approaches by considering in numerical simulations the effect of nesting in fabric stacks. The original in-situ compaction device developed by Hilal [42] for microtomographic investigations was used to scan a stack of fabric layers at different levels of compaction. The recently proposed technique of Micro-CT Aided Geometric Modeling [43] (Micro-CT AGM) was employed to construct, from X-ray microtomographic voxel images of fibrous reinforcements, structured geometric models of a stack of 2D woven glass fabrics for increasing fiber volume contents. These models combine the power of two representations of complex materials: (1) depending on the resolution of the micro-CT scan, the voxel file contains observed local details of the material; (2) identifying and numbering fiber tows provides in the end a structured voxel file for detailed analysis of their geometrical features.

In addition to providing a better understanding on liquid flows through continuous fiber composites, this article shows how realistic mesostructural models and numerical simulations provide relevant information on material variability.

The article is organized as follows. In Section 5.4, three geometric models of the same textile specimen are generated for different compaction levels, namely for increasing fiber volume contents. These models are subsequently used to calculate the effective thicknesses of each fabric ply and investigate the influence of the number of layers on the fiber volume content of the stack. Section 5.5 describes the experimental setup and methodology followed to measure the transverse permeability and discusses key issues connected with accuracy. Section 5.6 gives details on the numerical simulations carried out to predict the through-thickness permeability. Finally, simulation results are compared to experiments in Section 5.7.

5.4 Geometric models created from microtomographic scans

In this section, Micro-CT Aided Geometric Modeling (Micro-CT AGM) is applied to a stack of 2D plain woven glass fabric layers to construct mesostructural geometric models of textile architecture. These models were called "material twins" [1] in [43], because they possess the three following basic properties:

1. Accuracy. - The models reproduce with assessed accuracy the mesoscopic structure of fiber tows. This is possible thanks to microtomographic observations of the material structure and to the Micro-CT AGM methodology devised to construct a detailed and structured geometric model of textile architecture. The structured voxel file created allows a thorough analysis of the geometric features of the fiber tows contained in the specimen.

2. Material variability. - Lower resolution micro-CT scans enable to model larger specimens that are more representative of material variability than single unit cells like in most previous investigations ([32, 44–46]).

3. Numerical simulations. - Because the structure of the material has been identified and all the tows numbered, it is possible to create finite element meshes of the fibers and/or of the mesopores between the tows. Hence numerical simulations can be carried out to predict the mechanical or flow behavior of engineering textiles, thus establishing a

[1] There is no direct connection here with digital twins, which denote computer models of mechanical systems based on big data experimental observations.

connection between material properties and the geometric features of fibrous reinforcements.

Three geometric models of the same fabric are generated for different fiber volume contents. Based on the geometric features of material twins, the statistical concept of "effective thickness" is introduced to describe precisely the local thickness of nested plies and derive a more accurate estimation of fiber volume content.

5.4.1 X-ray microtomography

Microtomographic scans of a stack of 2D fabric layers were acquired with a specially devised cylindrical observation tool [42]. The fabric can be carefully cut with a dye in a press to provide circular samples of diameter 25.8 mm without falling apart. Since the region of interest lies inside the yellow dashed rectangles of Figure 5.1, no edge effect due to cutting may affect the analysis. The specimen includes ten circular samples of a glass fiber plain weave fabric from Texonic (product number L14012) and two metallic grids (called distribution grids in the sequel) on the top and bottom surfaces of the sample as illustrated in Figure 5.1a. The textile specimen is held between these two grids during the compaction experiments as in the through-thickness injection tests performed to measure the transverse permeability (see Section 5.5.2). During sample preparation, the different layers were positioned as carefully as possible, so that all the plies possess identical tow orientation.

The X-ray microtomographic scans were conducted with a Nikon XT H 225 at a resolution of 22 µm/pixel with a voltage and intensity of the X-ray beam of 180 kV and 30 µA respectively. Three measurements were carried out on the same sample at different levels of compaction. In order to avoid edge effects, a rectangular region of interest of area $15.82 \times 8.58 \text{mm}^2$ (around 6 unit cells in the horizontal plane) was selected for analysis in the central part of the scanned specimen (see Figure 5.1b).

5.4.2 Geometric models created for three increasing fiber volume contents

Figure 5.2 illustrates the geometric models created by Micro-CT AGM for the three increasing levels of compaction. As indicated, the overall thickness of the specimen decreases by 0.64 mm from the lowest fiber volume content of 47.4% to the highest one of 54.4%. These geometric models are different from the ones reconstructed in other studies ([45–48]), because all the fiber tows of the fibrous reinforcement are identified and individually labeled. Thus, the geometric features, orientations and mechanical properties of fiber tows can be taken into account in the analysis. Since the geometric information comes from the actual configuration

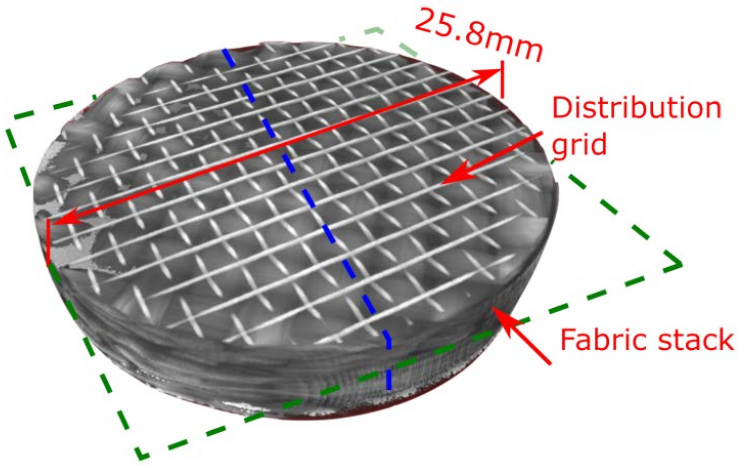

(a) 3D voxel microtomographic image

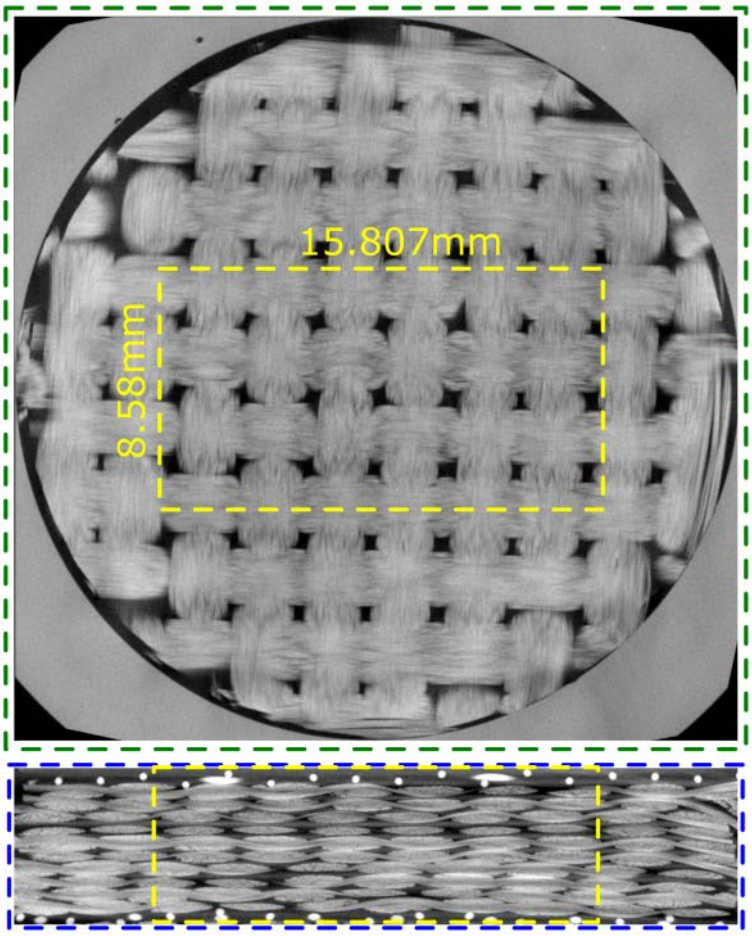

(b) (b) Top and front views of the microtomographic image

Figure 5.1 X-ray microtomographic scans of the fabric specimen: (a) reconstructed 3D voxel microtomographic image; (b) top and front views of the cross-sectional planes assigned in (a) showing the region of interest to generate material twins indicated by the dashed rectangles

of fiber tows and because of their specific properties, these structured models combining specific geometric information on fiber tows with a voxel representations of textile architecture were called material twins in [43]. They provide more precise details and general information on material variability at the mesoscopic scale compared to standard approaches based on textile modeling software such as TexGen [49, 50] or WiseTex [51, 52] for example. At the same time, similarly to the models generated by textile software, operations such as deletion, deformation and displacement of fiber tows are possible. This means that different geometric models can be extracted from one material twin. In the next section, this property is used to calculate the effective thicknesses of each layer inside the fabric stack.

5.4.3 Effective thickness

The geometric models derived from material twins allow performing mathematical operations on fiber tows so that their geometric features (such as the centroid line or cross-sectional area) can be clearly defined (see also [43] for more details). This can be used to calculate the effective thickness of any subset of n layers from the complete stack. To do so, the top and bottom surfaces of each fabric layer were generated as follows:

1. determine the centroid lines of each fiber tow;
2. extract the extremum points of all the centroid lines in the thickness direction to determine the crests and troughs, then select the top (bottom) points of contours at the crests (troughs) respectively;
3. for each fabric layer, classify the top (and bottom) points on the top (and bottom) surface;
4. apply parametric surface kriging [53] to process the surface points, then generate the top and bottom surfaces as shown in Figure 5.3a.

After generating these surfaces of each fabric layer, it is possible to calculate the average thickness between the top and bottom surfaces of any number of superposed plies. Note that since these surfaces are not necessarily flat, the thickness cannot be readily obtained from one single measurement. Therefore, the statistical concept of effective thickness is introduced as the mean value of all the distances between corresponding pixels on the top and bottom surfaces of the superposed plies. Given the material variability of composites, it is natural here to use statistics to define representative characteristic parameters of materials with significant geometric variability. For example, Figure 5.3 illustrates how an effective

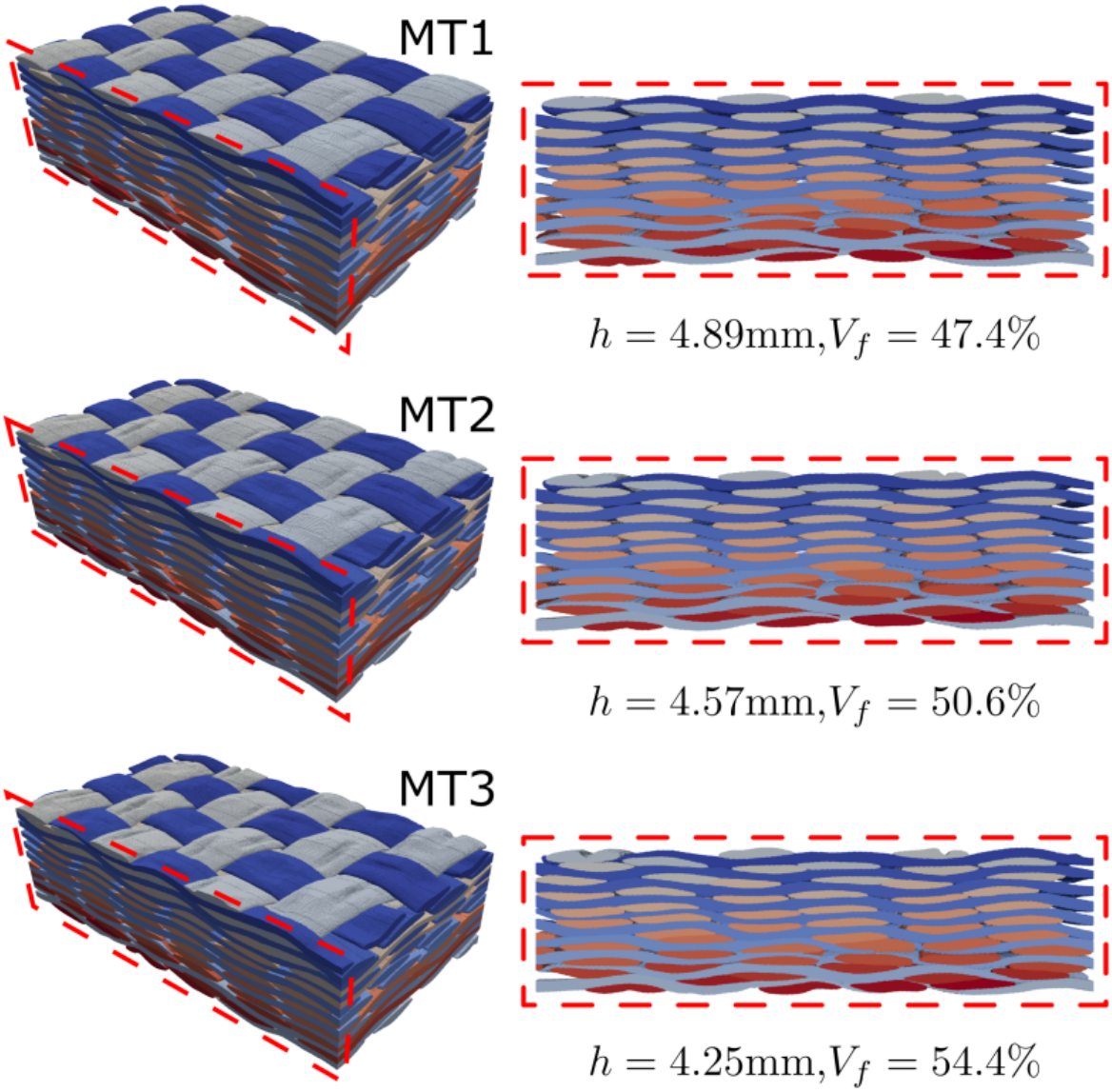

Figure 5.2 Material twins for three different fiber volume contents: the left side shows the voxel material twins; the right side displays the cross-sections identified in the voxel images

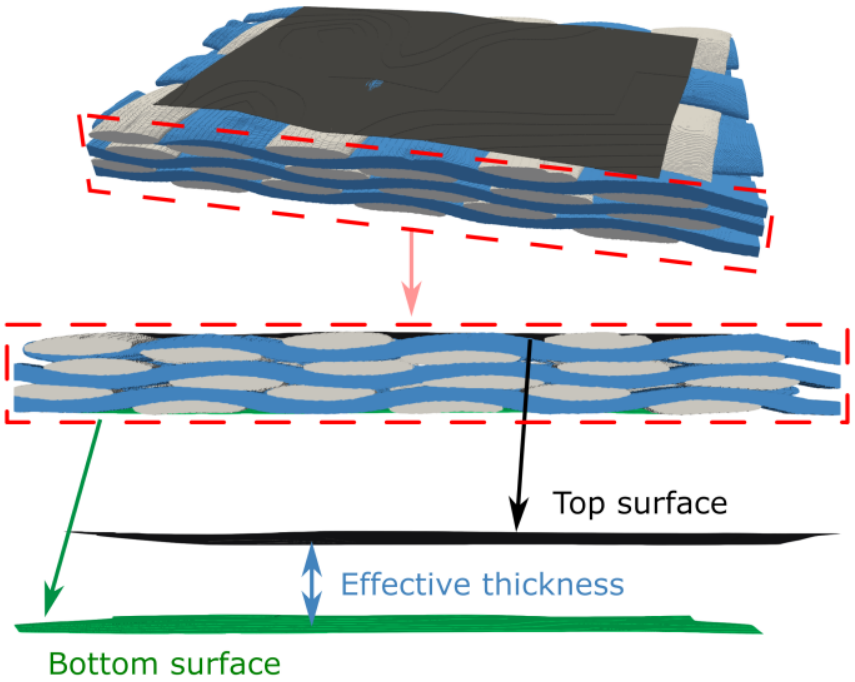

(a) Definition of the top and bottom surfaces of a three-layer fabric stack

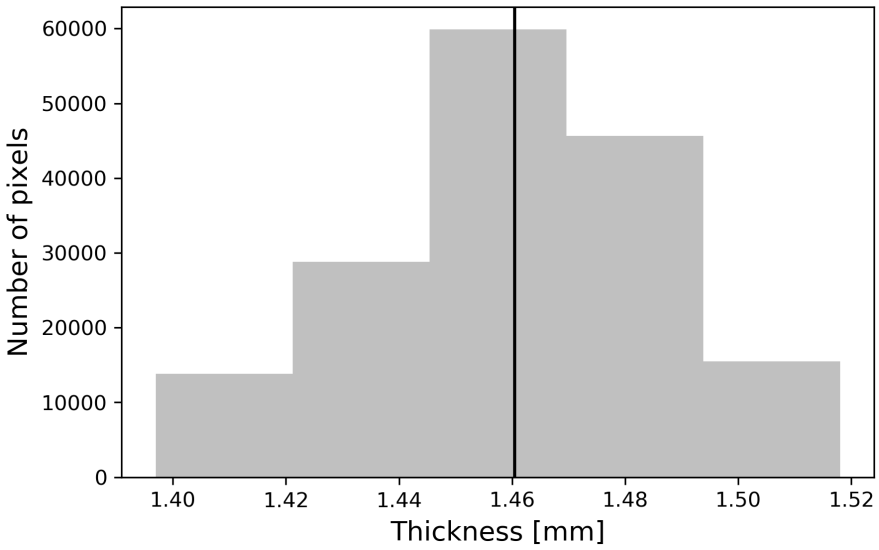

(b) Effective thickness of the three-layer fabric stack

Figure 5.3 Effective thickness of a three-layer fabric stack: (a) illustration of the top and bottom surfaces used to determine the effective thickness of a three-layer sample extracted from the ten-layer stack; (b) the effective thickness is defined as the statistical mean value (black line) of the distances between the corresponding pixels on the top and bottom surfaces of a series of fabric layers

thickness of 1.46 mm was determined for a three-layer stack extracted from the ten-layer material.

5.4.4 Analysis of fiber volume content

The fiber volume content V_f of a stack of fabric layers is calculated by the following equation:

$$V_f = \frac{n \times \rho_{surf}}{h \times \rho_{vol}} \tag{5.1}$$

in which n is the number of fabric layers, ρ_{surf} the surface density of the fabric, ρ_{vol} the volume density of glass fibers, h the thickness of the sample. As the top and bottom surfaces of all the fabric layers were determined previously, the fiber volume content can be evaluated for any number of layers in the stack. To do so, all possible models of n superposed plies, for $1 \leq n \leq 10$, were extracted from the specimen. For example, if the layers are numbered from 1 to 10 from top to bottom, then 8 three-layer models can be considered, namely with plies 1 to 3, 2 to 4, 3 to 5, 4 to 6, 5 to 7, 6 to 8, 7 to 9 and 8 to 10. Then the effective thickness and the resulting V_f can be calculated for each of these three-layer stacks. Following this methodology, the effective thickness and fiber volume content were evaluated for each number of layers (NOL). Figure 5.4 shows the average V_f values with error bars obtained for the three levels of compaction considered. In each case, V_f increases with the number of layers and converges to a constant higher value for increasing compaction levels. This means that to reach the same V_f for two fabric stacks with different numbers of layers, their overall levels of compaction will be different, especially for a low NOL. Thus the flow properties of the reinforcing material clearly depend on their level of compaction, and not only on fiber volume content.

Another particular finding in Figure 5.4 concerns the nearly identical mean values of fiber volume content obtained for the three compaction levels considered when $NOL = 1$ (however, with significantly different error bars). This means that, from a statistical point of view, the displacements of fiber tows lead to a reduction in the volume of mesopores (i.e., the open spaces between tows), which finally contributes to increase V_f for the whole stack. In order to better understand, the evolution of fiber volume content for single layer fabrics during compaction should be further investigated.

5.5 Saturated through-thickness permeability measurements

The saturated through-thickness permeability measurement technique employed in this study is presented in this section, including the theoretical background, the experimental set-up

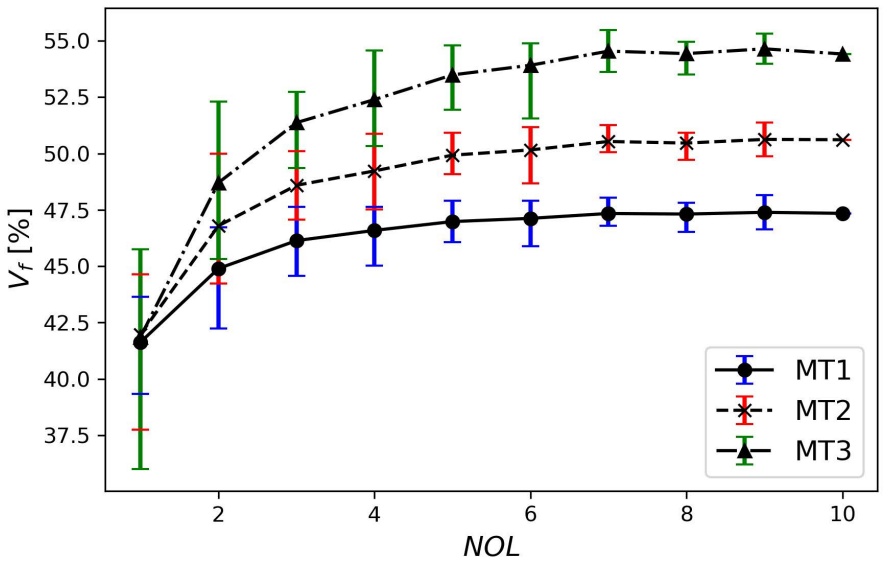

Figure 5.4 Relationship between the fiber volume content V_f and the number of layers (NOL) for the three levels of compaction MT1, MT2, MT3 considered in Figure 5.2

and several issues connected with accuracy, namely the injection pressure, test duration and the effective thickness of the distribution grids.

5.5.1 Theory

The principle of through-thickness permeability measurements is based on the linear relationship between the pressure drop and the volumetric flow rate in unidirectional flow conditions. The permeability K_z can be obtained from Darcy's law:

$$\frac{Q}{A} = \frac{K_z}{\mu}\frac{\Delta P}{h} \tag{5.2}$$

where Q is the volumetric flow rate, A the flow area of the porous medium, μ the viscosity of the fluid, ΔP the pressure drop and h the thickness of the preform.

5.5.2 Experimental setup

Figure 5.5 shows the through-thickness permeability test mold. The device consists of a stainless steel cylindrical mold of diameter 95.25 mm. Following Scholz et al. [14], two highly permeable metallic grids (called distribution grids as shown in Figure 5.1) are placed on the top and bottom surfaces of the specimen to generate a unidirectional transverse flow as uniform as possible. As presented in Eq. (5.2), the volumetric flow rate Q and the flow area A of the fabric specimen are considered here to calculate the transverse permeability K_z.

The textile specimen with the two distribution grids is then placed horizontally between two circular metallic perforated plates (see Figure 5.6a) to ensure uniform compaction. Shims are used to control the thickness of the fabric specimen and its total fiber volume content. The mold is closed by three manually tightened nuts.

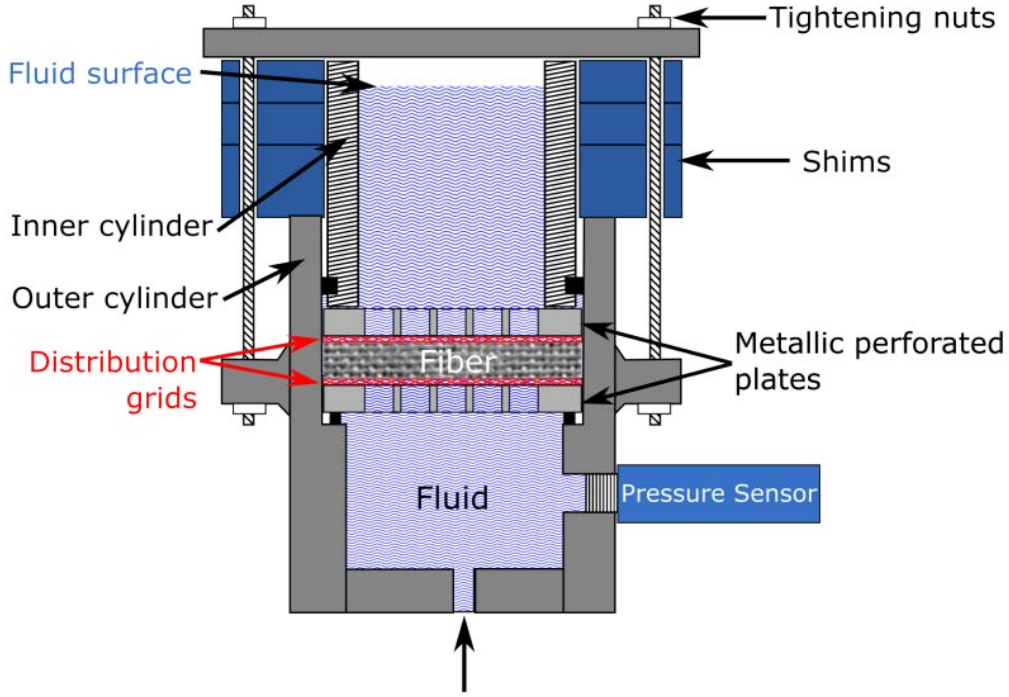

Figure 5.5 Schematics of the through-thickness permeability mold

The test liquid is injected from a cylindrical piston (PARKER Series 2MA) assembled on a universal testing machine with the capability of setting the piston velocity to generate a stable and constant injection flow rate during the measurement. As carefully checked before each test, air bubbles are completely squeezed out of the injection system (the piston and the connected tube), so that the volumetric flow rate remains constant. The liquid enters the bottom cavity of the mold, passes through the fibrous reinforcement and leaves the mold through the flow outlet pipe near the top (see Figure 5.6b). The outlet pipe is connected to a vacuum pump to draw the fluid out and ensure that the liquid surface remains stable inside the mold. A pressure sensor (Hoskin Scientific E-14 with a range from -1 to 0.6 bar) is placed at the bottom of the cavity to measure the pressure of the oil flowing into the fibrous reinforcement.

The experimental procedure can be outlined as follows: the textile specimen with the desired number of layers is placed in the mold, which is closed with a given shim combination to

(a) (b)

Figure 5.6 (a) Illustration of the metallic perforated plates mentioned in Figure 5.5; (b) top view of the closed mold showing the outlet of the mold and the outlet pipe connected with the vacuum pump

compress the specimen and reach the target fiber volume content. The piston is set into motion at an appropriate velocity to inject the oil into the mold and saturate the specimen at constant volumetric flow rate. The saturated through-thickness permeability measurement can then be launched.

Three different flow rates are needed for each permeability measurement. The corresponding piston velocities are carefully selected to ensure a relatively low pressure to prevent flow-induced fiber deformation. Figure 5.7a shows a typical pressure profile obtained during a complete test. Every injection stage at a given velocity lasted about 90 s to make sure that the pressure is stabilized. Thus a stable pressure was obtained for each injection stage. The starting and end points are labeled on the pressure curve of Figure 5.7a. Note that the oscillations coming from the pressure sensor remain low compared to the pressure level attained during each injection stage. The stages at zero pressure correspond to the time necessary to change the piston velocity on the console panel of the injection system. Based on the selected periods of the pressure curve and other data appearing in Eq. (5.2), a real-time average permeability is calculated by Darcy's law and plotted in Figure 5.7b. The three average values obtained correspond to the three stable pressure stages appearing in Figure 5.7a. Due to the noise in the signal of the pressure sensor and the mechanical vibration of the injection system, the curves of Figure 5.7b oscillate around constant values. Thus it is straightforward to calculate a mean value for each injection stage from the real-time

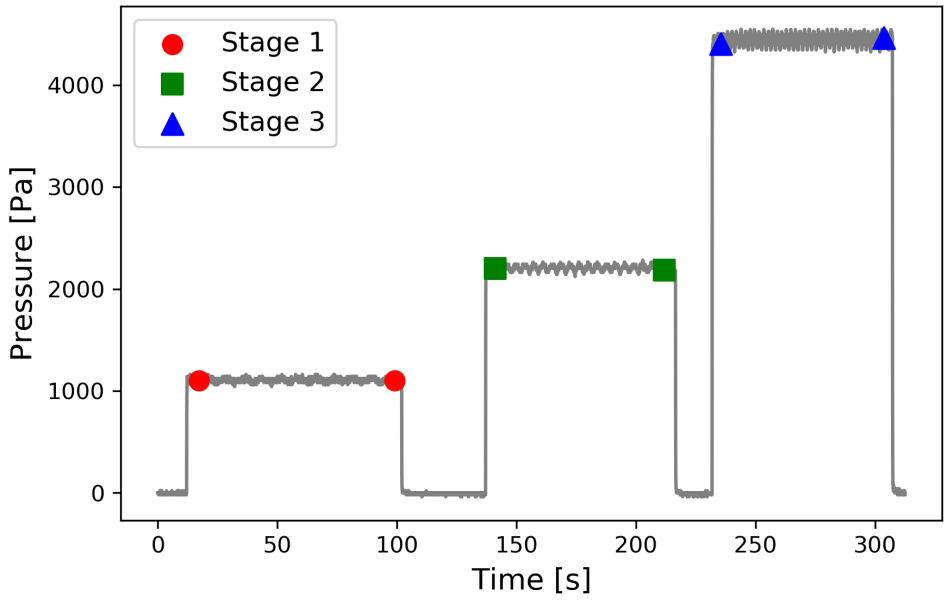

(a) Raw pressure profile and three stable injection stages considered for permeability calculation

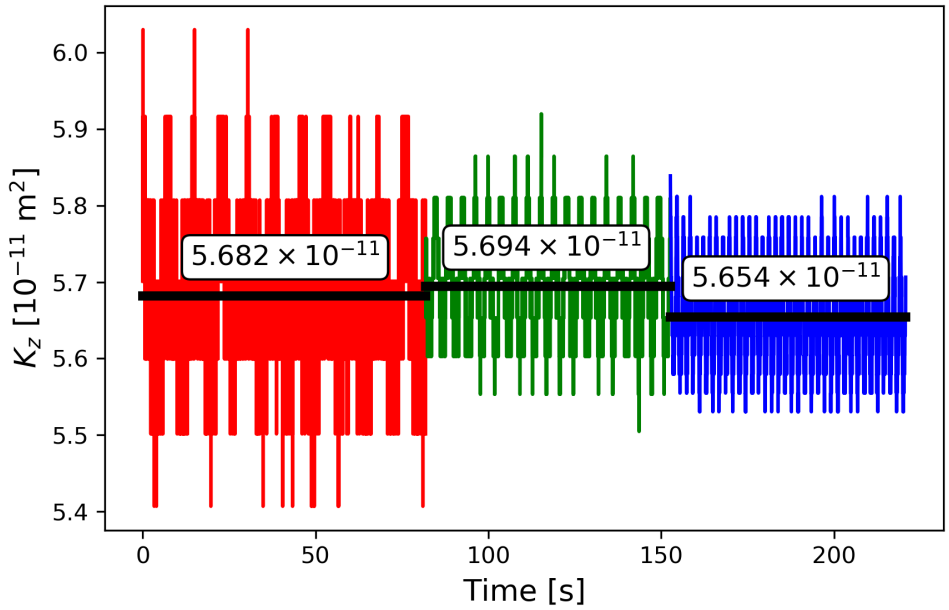

(b) Real-time through-thickness average permeability values and oscillations found for the three injection stages considered in (a)

Figure 5.7 (a) Typical example of transient pressure during the experiment: the red circles, green squares and blue triangles show the start and end points of three injection stages considered as stable to calculate permeability; (b) real-time average through-thickness permeability calculated from the pressure data of (a); the red, green and blue curves correspond to the stabilized injection stages in (a)

permeability. The final permeability value is computed as the average of the three injection stages (namely here $5.7 \times 10^{-11}\text{m}^2$ for the selected example).

5.5.3 Material description and experimental conditions

The material of the experiments was mentioned in Section 5.4, namely the glass fiber plain weave fabric from Texonic (product number L14012) of areal weight $590\,\text{g/m}^2$. The test fluid was silicone oil XIAMETER® PMX-200 100CS (Lot 0008225354). Based on the viscosity measurements performed by the Technical University of Munich (TUM) for an international benchmark exercise [34], the following power law was chosen to correct the viscosity of each measurement based on the temperature recorded during the test:

$$\mu = 528 \times T^{-0.533} \tag{5.3}$$

where μ is the viscosity (mPa.s) and T the temperature (°C).

To prevent fiber deformation which change permeability during the transverse permeability tests [9, 20, 21], low injection pressures were selected for the measurements. Since the flow rate is controlled by the injection system (and not pressure), the injection velocity is specified in the tests. The highest injection pressure is around 6000 Pa (for the tests with $V_f = 56.3\%$ and $NOL = 12$), while the injection pressure remains lower than 2000 Pa for most of the experiments. Since a pressure sensor with a small range of values from -1 to 0.6 bar was used in the measurements, the accuracy of the obtained pressure data can be confirmed.

In order to study the effect of the number of layers, three sets of fabric samples with different numbers of layers (NOL) were tested, namely for $NOL = 6$, $NOL = 8$ and $NOL = 12$. The experiments were performed at three different fiber volume contents for each NOL. All the tests were repeated three times. Considering that the injection pressure applied in this investigation is very low, flow-induced compaction was assumed negligible and the fabric specimens were used for a series of successive experiments. For $NOL = 6$ and $NOL = 8$, three tests were performed with each fabric specimen for increasing fiber volume contents. Since the injection pressure was higher with $NOL = 12$ (see above), a new stack of textile reinforcement was inserted in the mold for that configuration.

5.5.4 Thickness correction

As illustrated in Figure 5.5, the experimental setup uses a combination of calibrated shims to control the thickness of the cavity. The latter contains the textile specimen and the two distribution grids. These metallic grids play an important role to ensure a unidirectional

transverse flow as uniform as possible through the fibrous reinforcement, but their presence can change the fiber volume content of the sample. As illustrated in Figure 5.8, if no nesting occurs between the grid and the fabric layers, the thickness of the textile specimen can be calculated by using the cavity thickness h_{cavity} and subtract the thicknesses of the two distribution grids without compression, which is 2×0.57 mm. However, in practice, nesting occurs between the grids and the top and bottom layers of the fabric stack as shown in Figure 5.9. During compaction, the distribution grids are compressed inside the top and bottom surfaces of the fabric stack, inducing important local deformations of the fabric layers. This changes the thickness of the distribution grids and hence, if not taken into account, this can affect significantly the final value of permeability as a function of fiber volume content. As illustrated in Figure 5.8, the effective thickness of the distribution grid h_{DG} is defined as the distance between the surface of the distribution grid and the surface of the fabric layer at the boundary. Therefore, the effective thickness of the textile specimen can be calculated as $h_F = h_{cavity} - 2h_{DG}$. By using the calculation method of the effective thickness introduced in Section 5.4.3, the effective thickness of the distribution grid h_{DG} for different levels of compaction can be evaluated from the geometric models of the ten-layer fabric stack generated by Micro-CT AGM. Figure 5.9 illustrates the difference in preform thickness that occurs in case of nesting.

Finally, combining the relationship of Figure 5.4 between the fiber volume content V_f and the number of layers with the evolution of the effective thickness of the distribution grid with fiber volume content V_f in Figure 5.9, the effective thickness of the distribution grids for fabric stacks with different numbers of layers can be obtained as a function of the fiber volume content as illustrated in Figure 5.10. The exponential fitting functions giving these effective thicknesses are listed in Table 5.1. Figure 5.10 shows that the effective thickness h_{DG} of a distribution grid decreases significantly with the fiber volume fraction (V_f) of the fabric stack, while h_{DG} slightly increases with the number of layers (NOL).

NOL	Fitting function
6	$h_{DL} = (3.49 \times 10^6)e^{-35.52V_f} + (3.43 \times 10^{-1}), R_2 = 1.00$
8	$h_{DL} = (2.34 \times 10^6)e^{-34.55V_f} + (3.44 \times 10^{-1}), R_2 = 1.00$
10	$h_{DL} = (8.44 \times 10^5)e^{-32.32V_f} + (3.41 \times 10^{-1}), R_2 = 1.00$

Table 5.1 Fitting curve of the relation between V_f and h_{DG}

To illustrate the importance of this correction, a comparison between the experimental results of transverse permeability with and without thickness correction is presented in Figure 5.11. The same pressure data is used in this analysis for the test with $NOL = 8$. The

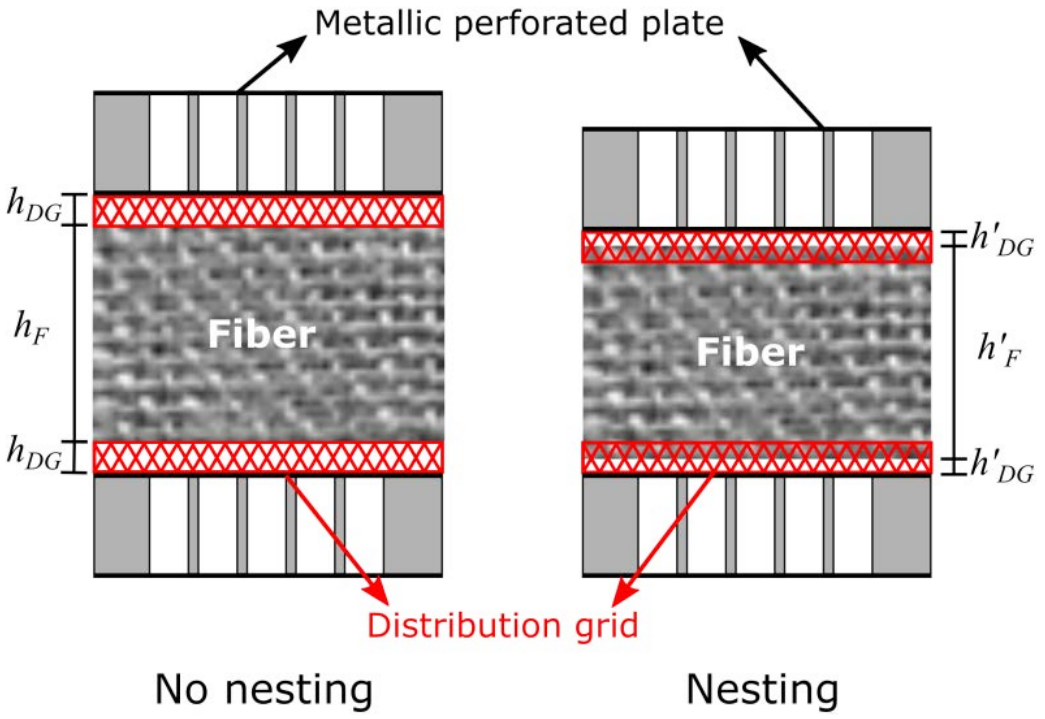

Figure 5.8 Illustration of the effect of nesting on the calculation of fiber volume content. The left side shows the case with no nesting between the distribution grids (DG) and the fabric layers, and the right side shows the case of nesting

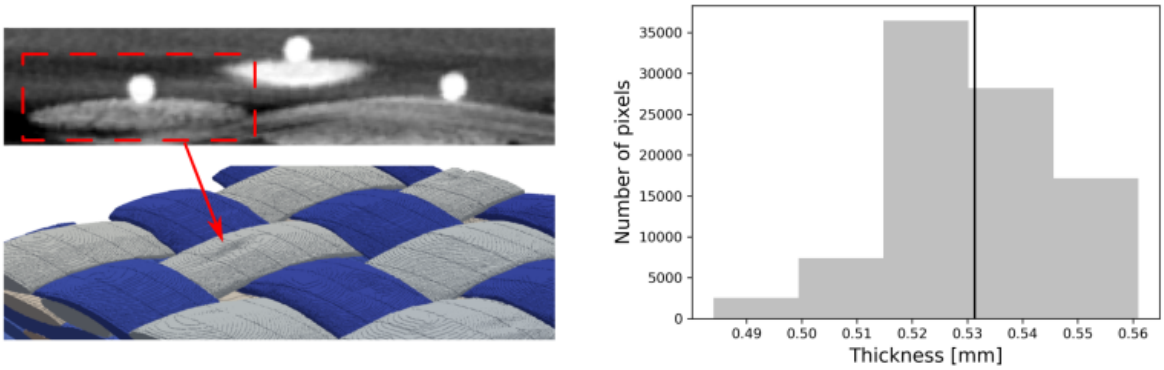

(a) Compaction at $V_f = 47.4\%$

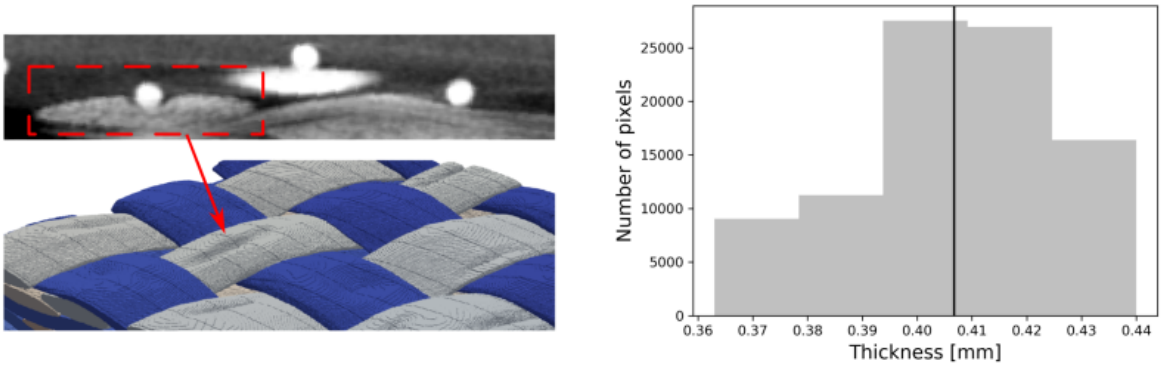

(b) Compaction at $V_f = 50.6\%$

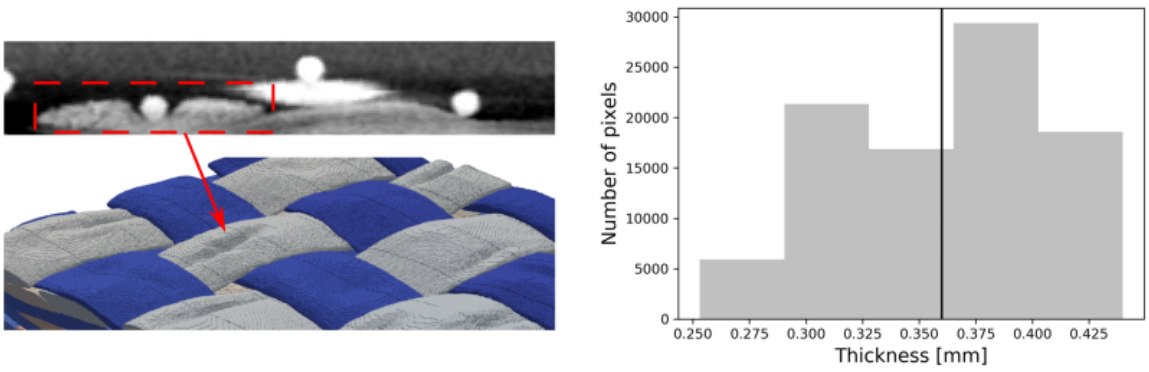

(c) Compaction at $V_f = 54.4\%$

Figure 5.9 Evolution of the effective thickness of the distribution grid for three compaction levels. On each of the figure panels (a), (b) and (c), the left side illustrates the nesting effect between the distribution grid and the adjacent fabric layer during compaction; the right side gives the corresponding effective thickness of the distribution grid. The fiber volume contents of the ten-layer textile specimen were calculated from the microtomographic images for the three compaction levels considered and take the following values: (a) $V_f = 47.4\%$; (b) $V_f = 50.6\%$; (c) $V_f = 54.4\%$

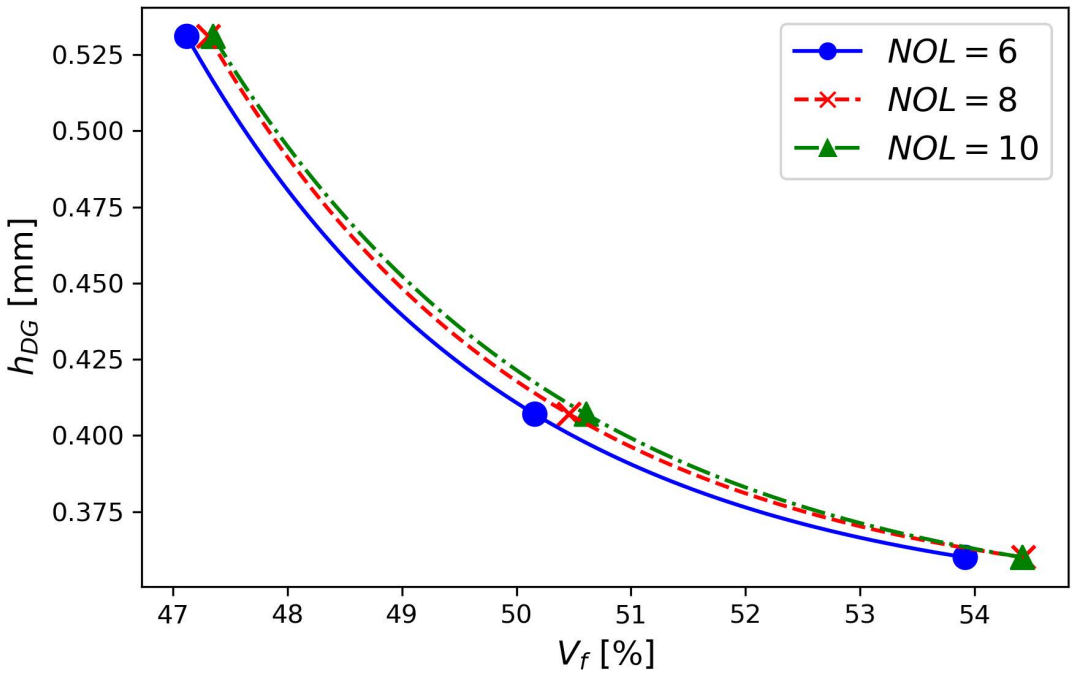

Figure 5.10 Relationship between the effective thickness of the distribution grid h_{DG} and the fiber volume contents V_f of fabric stacks with different numbers of layers (NOL)

only difference lies in the calculated thickness of the textile specimens, which leads to huge differences in fiber volume content for the two results in Figure 5.11. Since the thickness also affects transverse permeability in Darcy's law (see Eq. (5.2)), this correction leads to slightly different permeability values. Therefore, this thickness correction is absolutely necessary to process accurately transverse permeability measurements, especially when the fabric stacks are thin and if coarse metallic grids are used as distribution grids to ensure that a thorough uniform 1D flow is generated.

5.6 Numerical simulations

In this section, the geometric models generated by Micro-CT AGM presented in Section 5.4 are employed to carry out simulations of through-thickness permeability measurements with VGStudio MAX 3.0 software [54]. A convergence study is conducted to ensure that the model considered is large enough to get representative simulation results.

5.6.1 Flow model

Predictions of transverse permeability were obtained by performing numerical simulations with VGStudio MAX 3.0 software [54]. The model is based on the geometric descriptions

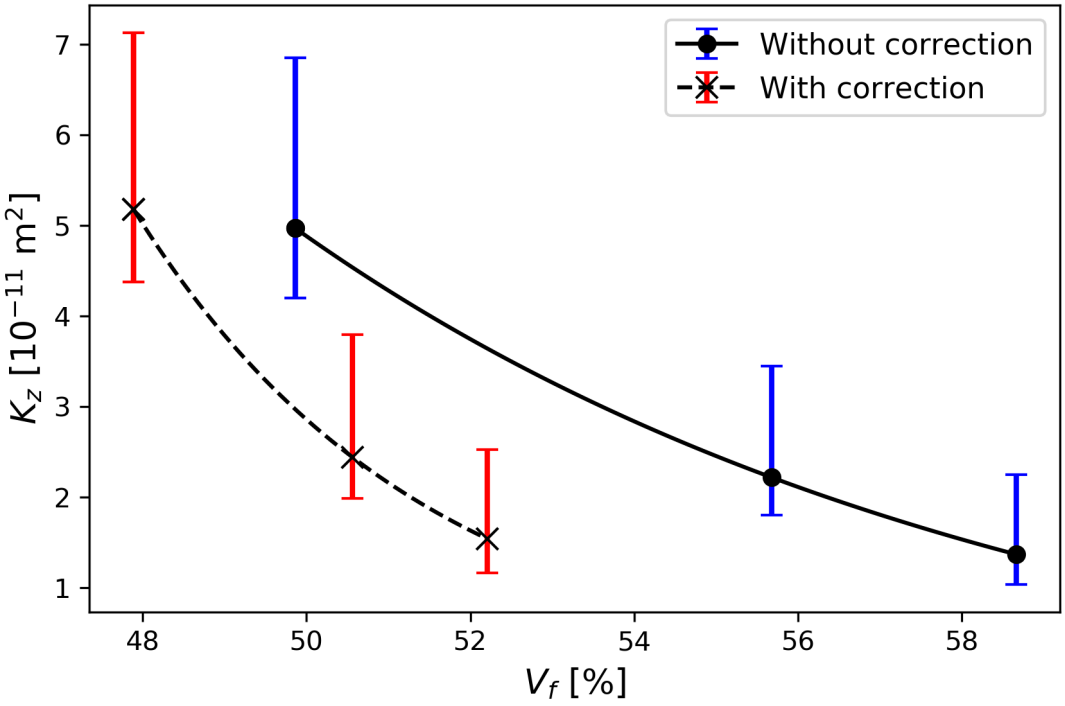

Figure 5.11 Effect of thickness correction on typical permeability measurements for $NOL = 8$

generated by Micro-CT AGM and the numerical simulation of a steady Stokes flow through the mesopores of the fibrous reinforcement. The boundary conditions and other parameters (i.e., fluid properties) used in the simulations are representative of a real experiment. As illustrated in Figure 5.12, the pressure distribution and the flow paths in the preform can be evaluated numerically, and then the saturated permeability can be computed. Note that the mesostructural models do not consider microstructural open spaces inside fiber tows. Hence the liquid can flow only through the mesopores between fiber tows. These microscopic effects can usually be neglected in the evaluation of saturated permeability [36], although this might not be the case for the unsaturated permeability as the micropores are progressively filled up during mold filling. Thus, the mesoscopic and microscopic scale flows can be decoupled, although it might lead to an underestimation of the predicted permeability. However, since the highest fiber volume content studied in this article is lower than 55%, this leaves continuous flow channels between the tows. Hence, we can consider that the permeability is dominated by the mesoscopic flow with less significant effect of the microscopic impregnation of fiber tows.

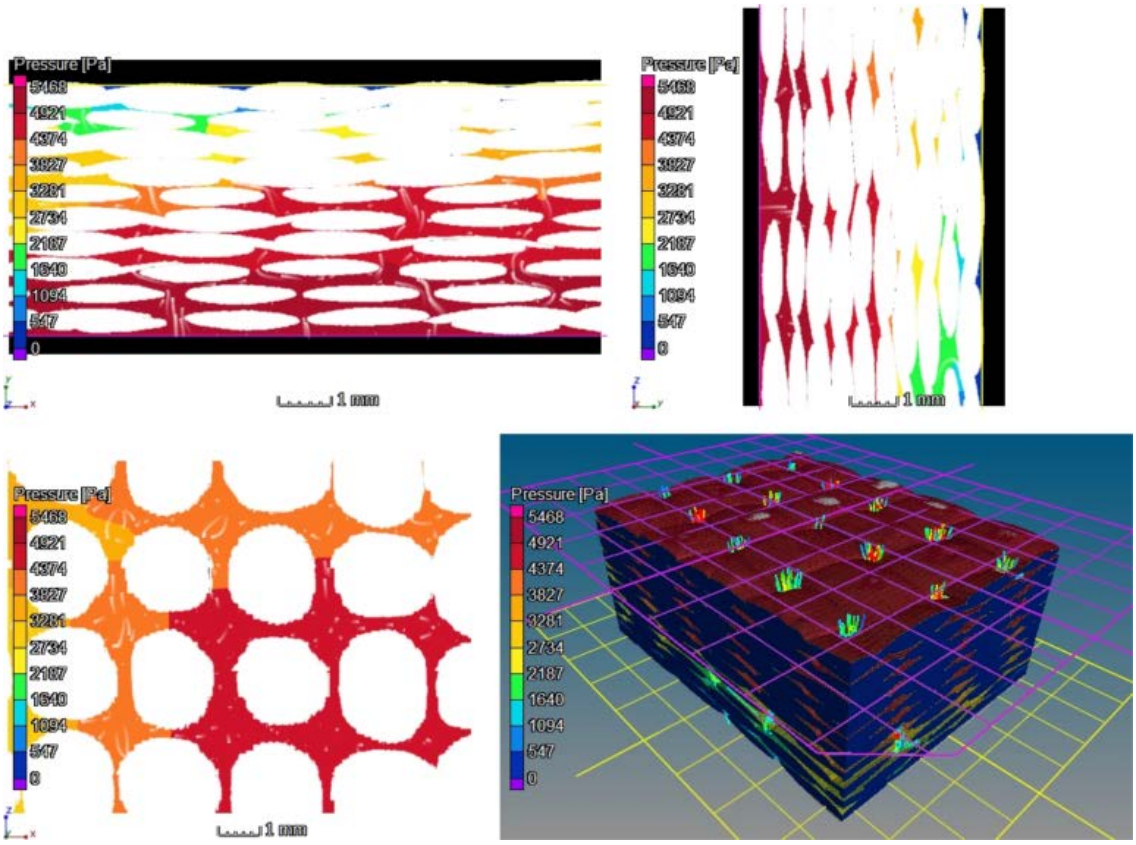

Figure 5.12 Simulation result showing the pressure distribution and flow paths in the mesopores of a mesostructural model generated by Micro-CT AGM ($NOL = 10$, $V_f = 47.4\%$) obtained with VGStudio MAX 3.0 software. The through-thickness flow is assumed to enter through the bottom surface of the fabrics stack and leave through the top surface. The top left, top right, bottom left and bottom right images show respectively the front, side, top and 3D views of the mesoporous structures of the preform

5.6.2 Convergence study

In order to prevent an overestimation of the mesopores in the region close to the boundary of the mesostructural models, regions of interest for the flow analysis need to be selected in the central parts of the geometric models. However, the cross-section of the simulation domain should be large enough to ensure that the results are representative of the real material. To verify this, a convergence study was conducted with the geometric model MT1 considered in Figure 5.2 by increasing the length and width of the region of interest, while keeping the maximum height constant in the thickness direction (see Figure 5.13). Since the geometric model consists of ten plies, significant nesting exists between fabric layers, which makes difficult to distinguish the number of unit cells in the whole fabric stack. Therefore, the geometric features (length, width and area) are used here to describe the size of the regions of interest. When the sample area becomes larger than 60 mm^2 (around 3 unit cells), the simulation results converge to a nearly constant value. The largest area in Figure 5.13, namely $11.28 \times 8.58\mathrm{mm}^2$ (around 4 unit cells), was selected to perform the numerical simulations in the sequel.

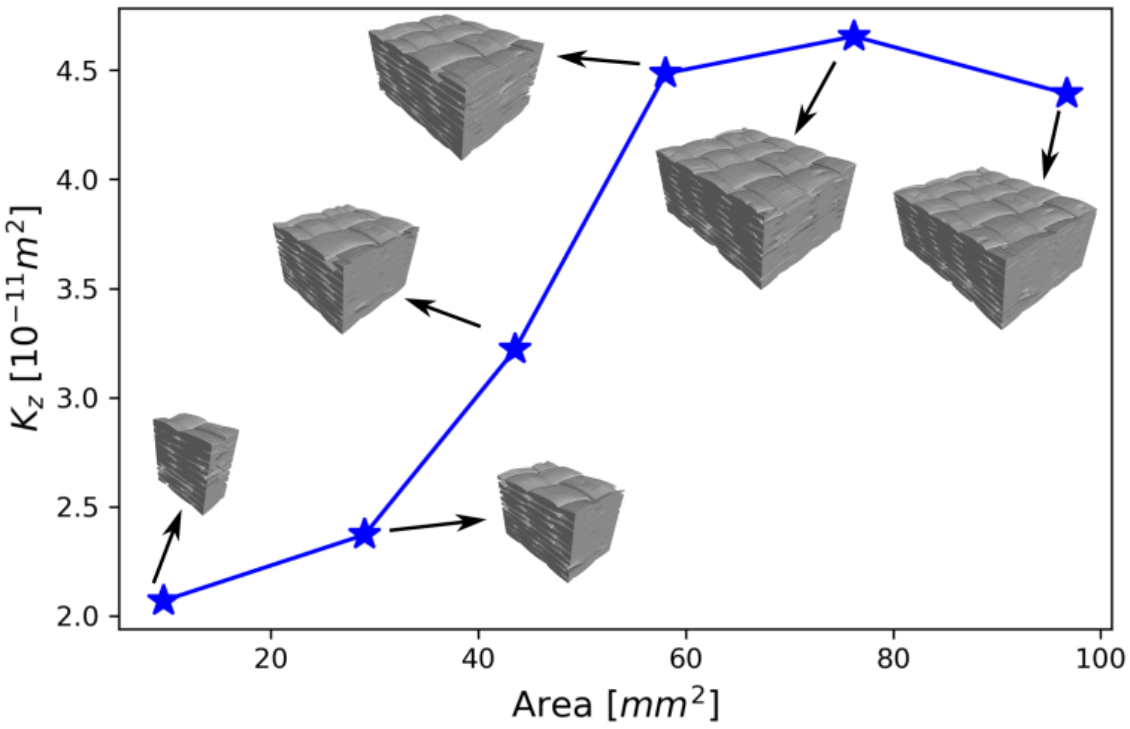

Figure 5.13 Convergence study of through-thickness permeability calculations with VGStudio software in regions of interest of increasing cross-sectional areas ($NOL = 10$, $V_f = 47.4\%$)

5.7 Analysis and discussion of experimental and simulation results

This section presents a comparison of experimental results and numerical predictions of the transverse permeability of 2D woven fabrics. The two approaches are also used to investigate the effect of the number of layers on permeability.

5.7.1 Comparison of simulations and experiments

Figure 5.14 shows the comparison of simulation with experiments for $NOL = 6$ and 8. A good agreement is found, especially for 8 fabric layers. Since the simulations are conducted in representative regions extracted from the material twins created with 10 fabric layers, five combinations of layers for $NOL = 6$ and three for $NOL = 8$ have been studied, so that error bars can be provided for simulation results along the x and y axes. Thus numerical predictions can also illustrate the variability of the material much like experiments, which was generally not possible in previous studies [19, 35–39]. Meanwhile, differently from other investigations that assume a uniform distribution of fiber volume content in one fabric stack, the geometric models used in numerical simulation are constructed from real fabrics so that the nesting and distortion between fabric layers can be precisely described without any particular assumption. As illustrated in Figure 5.14, these phenomena can cause significant variations in fiber volume content and predicted permeability, which explain the overall variability of simulation results.

The variability of experimental results might be explained in the same way, since the orientation of fibers and the nesting of fabric layers cannot be perfectly controlled during the lay-up process. However, some differences still exist between simulations and experiments, which might explain why the variability of experimental results is lower than that of simulations. For example, all the six-layer and eight-layer representative regions are extracted from the ten-layer material twins, thus their fiber volume contents cannot be controlled, but only calculated. Meanwhile, some of them do not possess the top and bottom surfaces with highly local deformation induced by the compression of the distribution grids. However, the fabric stacks used in the experiments include the effect of top, bottom and middle layers, and the exact fiber volume content of the stack can be evaluated from the measurements.

5.7.2 Effect of the number of layers on the through-thickness permeability

Figure 5.15 illustrates how the number of fabric layers affects the transverse permeability from the numerical and experimental points of view. Both results show that permeability decreases when the number of fabric layers increases. However, this effect gets smaller with

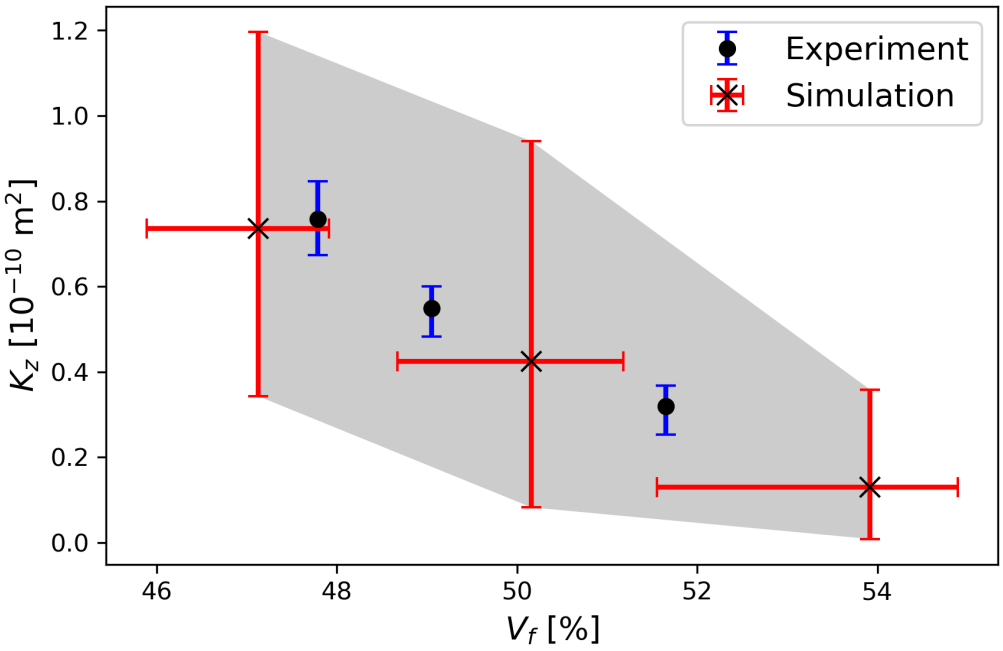

(a) Numerical and experimental through-thickness permeability for 6 fabric layers

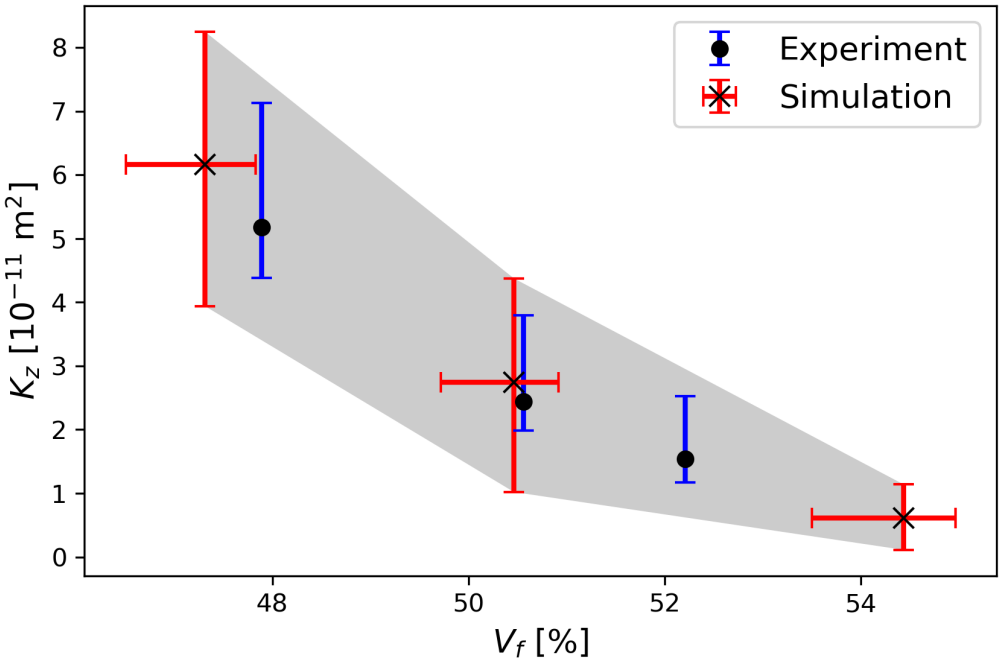

(b) Numerical and experimental through-thickness permeability for 8 fabric la

Figure 5.14 Comparison of simulation results with experiments for two stacks of 6 and 8 fabric layers: (a) $NOL = 6$; (b) $NOL = 8$

V_f. The largest difference can reach 50%, which indicates a significant effect of the number of layers on permeability. The same conclusion was observed in other investigations [14, 17]. However, it is the first time that the effect has been verified for multi-layer 2D woven fabrics simultaneously in numerical predictions and experimentally. According to these results, it is not recommended, especially for a low number of fabric layers and fiber volume content, to use a fixed cavity thickness and change the number of fabric layers to characterize the saturated transverse permeability as a function of fiber volume content, as commonly seen in other works [9, 20]. Instead, the number of layers should be selected based on practical requirements, and the fiber volume content controlled by changing the cavity thickness.

5.8 Conclusion

Saturated through-thickness permeability measurements based on unidirectional transverse injections in a cylindrical test mold were carried out experimentally and reproduced numerically. Several key issues were considered to perform the experiments: (1) highly permeable metallic distribution grids were placed on the top and bottom surfaces of the preforms to generate a unidirectional transverse flow as uniform as possible; (2) low injection pressure was applied to prevent fiber deformation; (3) the effect of nesting between the distribution grids and the fabric layers was quantified and considered for the calculation of fiber volume content. The simulations were carried out with mesostructural models generated from 3D microtomographic images of dry fabric stacks using recently proposed Micro-CT AGM [43]. This allowed extracting from one single scan geometric models for various numbers of fabric layers, which provides then a quantitative evaluation of the material variability induced by nesting without undue increase in characterization time (normally a microtomographic scan can take hours). Overall, simulation results exhibit a good agreement with experiments. Both approaches confirm that nesting explains why the number of layers in 2D woven fabrics has a strong influence on the saturated through-thickness permeability.

Although nesting between fabric layers was studied in detail in this work, it is still worth further investigating this phenomenon to better understand the variability of permeability experimental results. Only mesoscopic flows were considered here in the numerical simulations. Another interesting application would consist of simulating dual-scale flows through fibrous reinforcements [24–28]. Moreover, by combining material twins with multiscale models (see references [55,56] for example), advanced and automated computer simulations taking into account the mesostructure of fibrous reinforcements could be carried out. Finally, using material twins to predict the mechanical behavior of textiles in compression and shear in composite manufacturing are other research topics that can provide useful information for

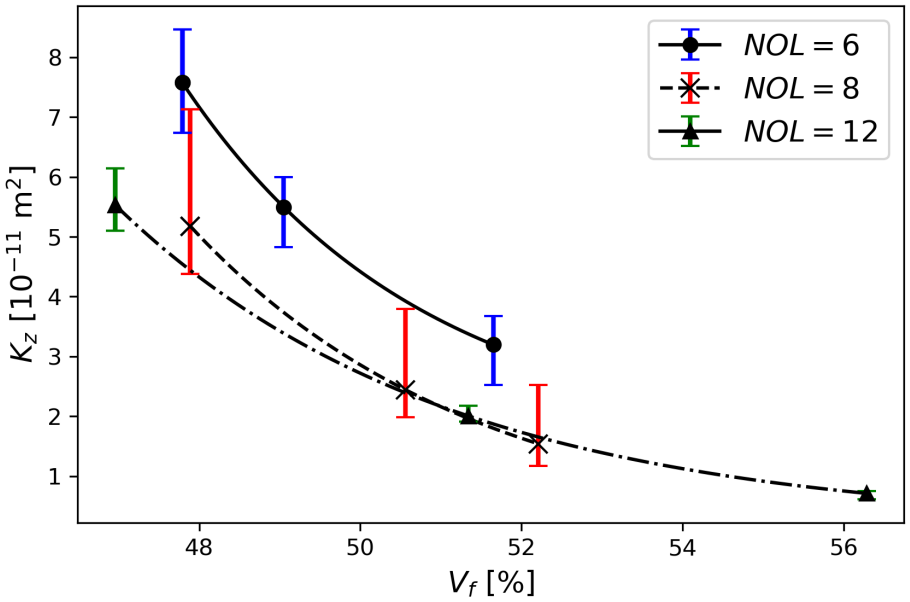

(a) Experimental values of through-thickness permeability

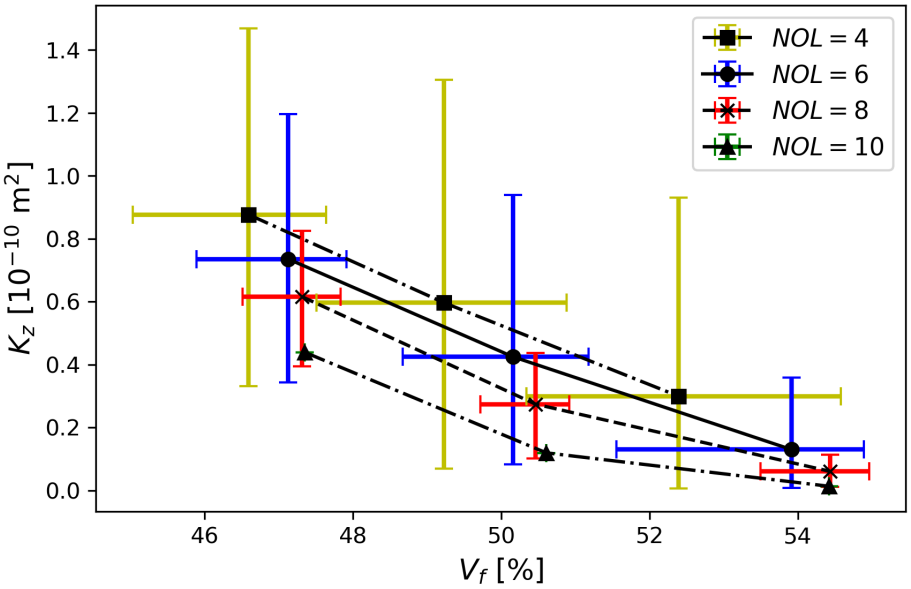

(b) Simulation results of through-thickness permeability based on material twins

Figure 5.15 Effect of the number of layers (NOL) on the through-thickness permeability of 2D woven fabrics: (a) experimental values; (b) simulation results based on material twins

high performance composite applications.

5.9 Acknowledgements

This work has been partially supported by the Department of Mechanical Engineering of Polytechnique Montreal, the National Natural Science Foundation of China (Grant Nos. 11920101002, 11372231 and 11772238) and by the National Science & Engineering Research Council of Canada (NSERC) (Discovery Grant). Authors also gratefully acknowledge the Research Center for High Performance Polymer and Composite Systems (CREPEC), the "Fonds de recherche du Québec - Nature et technologies" (FRQNT) and the "Fonds National de la Recherche" (FNR) of Luxembourg for their partial financial support. Authors would also like to express their sincere thanks to Nicolas Juillard from Texonic for providing the fibrous reinforcements used in this study. The help of Bin Yang, PhD student, is highly appreciated for the experiments. Authors are grateful to Professor Vladimir Brailovski and Morgan Letenneur for providing access to the X-ray microtomograph and to VGStudio MAX 3.0 software.

Bibliography

[1] L. Joubaud, V. Achim, and F. Trochu, "Numerical simulation of resin infusion and reinforcement consolidation under flexible cover," *Polymer composites*, vol. 26, no. 4, pp. 417–427, 2005.

[2] L. Joubaud, F. Trochu, and J. Le Corvec, "Analysis of resin flow under flexible cover in vacuum assisted resin infusion (VARI)," *Journal of advanced materials*, vol. 37, no. 3, pp. 3–10, 2005.

[3] X. Pham, F. Trochu, and R. Gauvin, "Simulation of compression resin transfer molding with displacement control," *Journal of reinforced plastics and composites*, vol. 17, no. 17, pp. 1525–1556, 1998.

[4] X. Pham and F. Trochu, "Simulation of compression resin transfer molding to manufacture thin composite shells," *Polymer composites*, vol. 20, no. 3, pp. 436–459, 1999.

[5] X. Pham and F. Trochu, "Analysis of the consolidation in flexible bladder process for thin composite parts by finite element method," *Journal of reinforced plastics and composites*, vol. 19, no. 3, pp. 182–218, 2000.

[6] E. Ruiz, L. Briones, E. Allard, and F. Trochu, "Flexible injection: a novel LCM technology for low cost manufacturing of high performance composites. Part I: experimental investigation," in *The 9th International Conference on Flow Processes in Composite Materials*, 2008.

[7] F. Trochu, S. Soukane, and B. Touraine, "Flexible injection: a novel LCM technology for low cost manufacturing of high performance composites. Part II: numerical model," in *9 th Int. Conf. on Flow Proc. in Comp. Mat*, 2008.

[8] P. Causse, E. Ruiz, and F. Trochu, "Spring-in behavior of curved composites manufactured by Flexible Injection," *Composites Part A: Applied Science and Manufacturing*, vol. 43, no. 11, pp. 1901–1913, 2012.

[9] F. Klunker, M. Danzi, and P. Ermanni, "Fiber deformation as a result of fluid injection: modeling and validation in the case of saturated permeability measurements in through thickness direction," *Journal of Composite Materials*, vol. 49, no. 9, pp. 1091–1105, 2015.

[10] D. Becker and P. Mitschang, "Measurement system for on-line compaction monitoring of textile reaction to out-of-plane impregnation," *Advanced Composites Letters*, vol. 23, no. 2, p. 096369351402300202, 2014.

[11] S. Drapier, A. Pagot, A. Vautrin, and P. Henrat, "Influence of the stitching density on the transverse permeability of non-crimped new concept (NC2) multiaxial reinforcements: Measurements and predictions," *Composites Science and Technology*, vol. 62, no. 15, pp. 1979–1991, 2002.

[12] P. Ouagne and J. Bréard, "Continuous transverse permeability of fibrous media," *Composites Part A: Applied Science and Manufacturing*, vol. 41, no. 1, pp. 22–28, 2010.

[13] P. Ouagne, T. Ouahbi, C. H. Park, J. Bréard, and A. Saouab, "Continuous measurement of fiber reinforcement permeability in the thickness direction: Experimental technique and validation," *Composites Part B: Engineering*, vol. 45, no. 1, pp. 609–618, 2013.

[14] S. Scholz, J. W. Gillespie, and D. Heider, "Measurement of transverse permeability using gaseous and liquid flow," *Composites Part A: Applied Science and Manufacturing*, vol. 38, no. 9, pp. 2034–2040, 2007.

[15] S. V. Lomov, I. Verpoest, T. Peeters, D. Roose, and M. Zako, "Nesting in textile laminates: geometrical modelling of the laminate," *Composites Science and Technology*, vol. 63, no. 7, pp. 993–1007, 2003.

[16] L. Fang, J. Jiang, J. Wang, C. Deng, D. Li, and F. Liu, "Effect of layer shift on the out-of-plane permeability of 0/90 noncrimp fabrics," *Journal of Reinforced Plastics and Composites*, vol. 33, no. 22, pp. 2073–2094, 2014.

[17] J. Jiang, Y. Su, L. Zhou, Q. Guo, C. Xu, G. Deng, X. Chen, X. Yao, and L. Fang, "Effect of nesting on the permeability of multilayer unidirectional fabrics," *Applied Composite Materials*, vol. 24, no. 3, pp. 625–642, 2017.

[18] B. Yang, S. Wang, and Y. Wang, "Effect of nesting in laminates on the through-thickness permeability of woven fabrics," *Applied Composite Materials*, vol. 25, no. 5, pp. 1237–1253, 2018.

[19] H. S. Sas, E. B. Wurtzel, P. Simacek, and S. G. Advani, "Effect of relative ply orientation on the through-thickness permeability of unidirectional fabrics," *Composites Science and Technology*, vol. 96, pp. 116–121, 2014.

[20] A. Endruweit, T. Luthy, and P. Ermanni, "Investigation of the influence of textile compression on the out-of-plane permeability of a bidirectional glass fiber fabric," *Polymer Composites*, vol. 23, no. 4, pp. 538–554, 2002.

[21] B. Willenbacher, A. Kabachi, D. May, P. Mitschang, and P. Ermanni, "Flow induced sample deformations in out-of-plane permeability measurement," in *ECCM18 - 18th European Conference on Composite Materials*, 2018.

[22] M. Bodaghi, S. V. Lomov, P. Simacek, N. C. Correia, and S. G. Advani, "On the variability of permeability induced by reinforcement distortions and dual scale flow in liquid composite moulding: A review," *Composites Part A: Applied Science and Manufacturing*, 2019.

[23] A. Endruweit, X. Zeng, M. Matveev, and A. C. Long, "Effect of yarn cross-sectional shape on resin flow through inter-yarn gaps in textile reinforcements," *Composites Part A: Applied Science and Manufacturing*, vol. 104, pp. 139–150, 2018.

[24] N. Kuentzer, P. Simacek, S. G. Advani, and S. Walsh, "Permeability characterization of dual scale fibrous porous media," *Composites Part A: Applied Science and Manufacturing*, vol. 37, no. 11, pp. 2057–2068, 2006.

[25] E. Ruiz, V. Achim, S. Soukane, F. Trochu, and J. Bréard, "Optimization of injection flow rate to minimize micro/macro-voids formation in resin transfer molded composites," *Composites Science and Technology*, vol. 66, no. 3-4, pp. 475–486, 2006.

[26] C. Ravey, E. Ruiz, and F. Trochu, "Determination of the optimal impregnation velocity in resin transfer molding by capillary rise experiments and infrared thermography," *Composites Science and Technology*, vol. 99, pp. 96–102, 2014.

[27] M. Imbert, S. Comas-Cardona, E. Abisset-Chavanne, and D. Prono, "Experimental investigation of intra-tow fluid storage mechanisms in dual-scale fiber reinforcements," *Composites Part A: Applied Science and Manufacturing*, vol. 107, pp. 70–82, 2018.

[28] J. Bréard, Y. Henzel, F. Trochu, and R. Gauvin, "Analysis of dynamic flows through porous media. Part I: Comparison between saturated and unsaturated flows in fibrous reinforcements," *Polymer Composites*, vol. 24, no. 3, pp. 391–408, 2003.

[29] E. E. Swery, T. Allen, S. Comas-Cardona, Q. Govignon, C. Hickey, J. Timms, L. Tournier, A. Walbran, P. Kelly, and S. Bickerton, "Efficient experimental characterisation of the permeability of fibrous textiles," *Journal of Composite Materials*, vol. 50, no. 28, pp. 4023–4038, 2016.

[30] M. A. Ali, R. Umer, K. A. Khan, S. Bickerton, and W. J. Cantwell, "Non-destructive evaluation of through-thickness permeability in 3D woven fabrics for composite fan blade applications," *Aerospace Science and Technology*, vol. 82-83, pp. 520–533, 2018.

[31] M. A. Ali, R. Umer, K. A. Khan, and W. J. Cantwell, "XCT-scan assisted flow path analysis and permeability prediction of a 3D woven fabric," *Composites Part B: Engineering*, vol. 176, p. 107320, 2019.

[32] X. S. Zeng, A. C. Long, F. Gommer, A. Endruweit, and M. Clifford, "Modelling compaction effect on permeability of 3D carbon reinforcements," in *18th International Conference on Composites Materials, Jeju Island, Korea*, 2011.

[33] M. Danzi, F. Klunker, and P. Ermanni, "Experimental validation of through-thickness resin flow model in the consolidation of saturated porous media," *Journal of Composite Materials*, vol. 51, no. 17, pp. 2467–2475, 2017.

[34] D. May, A. Aktas, and A. Yong, "International benchmark exercises of textile permeability and compressibility characterization," in *ECCM18 - 18th European Conference on Composite Materials*, 2018.

[35] A. Nabovati, E. W. Llewellin, and A. C. M. Sousa, "A general model for the permeability of fibrous porous media based on fluid flow simulations using the lattice Boltzmann method," *Composites Part A: Applied Science and Manufacturing*, vol. 40, no. 6-7, pp. 860–869, 2009.

[36] M. Karaki, A. Hallal, R. Younes, F. Trochu, P. Lafon, A. Hayek, A. Kobeissy, and A. Fayad, "A comparative analytical, numerical and experimental analysis of the microscopic permeability of fiber bundles in composite materials," *International Journal of Composite Materials*, vol. 7, no. 3, pp. 82–102, 2017.

[37] F. Loix, P. Badel, L. Orgéas, C. Geindreau, and P. Boisse, "Woven fabric permeability: From textile deformation to fluid flow mesoscale simulations," *Composites science and Technology*, vol. 68, no. 7-8, pp. 1624–1630, 2008.

[38] B. Verleye, R. Croce, M. Griebel, M. Klitz, S. V. Lomov, G. Morren, H. Sol, I. Verpoest, and D. Roose, "Permeability of textile reinforcements: Simulation, influence of shear and validation," *Composites Science and Technology*, vol. 68, no. 13, pp. 2804–2810, 2008.

[39] X. Zeng, L. P. Brown, A. Endruweit, M. Matveev, and A. C. Long, "Geometrical modelling of 3D woven reinforcements for polymer composites: Prediction of fabric permeability and composite mechanical properties," *Composites Part A: Applied Science and Manufacturing*, vol. 56, pp. 150–160, 2014.

[40] X. S. Zeng, A. Endruweit, L. P. Brown, and A. C. Long, "Numerical prediction of in-plane permeability for multilayer woven fabrics with manufacture-induced deformation," *Composites Part A: Applied Science and Manufacturing*, vol. 77, pp. 266–274, 2015.

[41] M. A. Ali, R. Umer, K. A. Khan, and W. J. Cantwell, "In-plane virtual permeability characterization of 3D woven fabrics using a hybrid experimental and numerical approach," *Composites Science and Technology*, vol. 173, pp. 99–109, 2019.

[42] S. Hilal, "Caractérisation par microtomographie de la mésostructure des renforts fibreux pour la fabrication de composites par injection," Ph.D. dissertation, École Polytechinque de Montréal, 2018.

[43] W. Huang, P. Causse, V. Brailovski, H. Hu, and F. Trochu, "Reconstruction of mesostructural material twin models of engineering textiles based on Micro-CT Aided Geometric Modeling," *Composites Part A: Applied Science and Manufacturing*, vol. 124, p. 105481, 2019.

[44] A. Madra, P. Breitkopf, A. Rassineux, and F. Trochu, "Image-based model reconstruction and meshing of woven reinforcements in composites," *International Journal for Numerical Methods in Engineering*, vol. 112, no. 9, pp. 1235–1252, 2017.

[45] Y. Liu, I. Straumit, D. Vasiukov, S. V. Lomov, and S. Panier, "Prediction of linear and non-linear behavior of 3D woven composite using mesoscopic voxel models reconstructed from X-ray micro-tomography," *Composite Structures*, vol. 179, pp. 568–579, 2017.

[46] I. Straumit, S. V. Lomov, and M. Wevers, "Quantification of the internal structure and automatic generation of voxel models of textile composites from X-ray computed tomography data," *Composites Part A: Applied Science and Manufacturing*, vol. 69, pp. 150–158, 2015.

[47] N. Naouar, E. Vidal-Sallé, J. Schneider, E. Maire, and P. Boisse, "Meso-scale FE analyses of textile composite reinforcement deformation based on X-ray computed tomography," *Composite Structures*, vol. 116, no. 1, pp. 165–176, 2014.

[48] N. Naouar, E. Vidal-Sallé, J. Schneider, E. Maire, and P. Boisse, "3D composite reinforcement meso F.E. analyses based on X-ray computed tomography," *Composite Structures*, vol. 132, pp. 1094–1104, 2015.

[49] M. Sherburn, "Geometric and mechanical modelling of textiles," Ph.D. dissertation, University of Nottingham, 2007.

[50] A. C. Long and L. P. Brown, "Modelling the geometry of textile reinforcements for composites: TexGen," in *Composite Reinforcements for Optimum Performance*, 2011, pp. 239–264.

[51] I. Verpoest and S. V. Lomov, "Virtual textile composites software WiseTex: Integration with micro-mechanical, permeability and structural analysis," *Composites Science and Technology*, vol. 65, pp. 2563–2574, 2005.

[52] S. V. Lomov, D. S. Ivanov, I. Verpoest, M. Zako, T. Kurashiki, H. Nakai, and S. Hirosawa, "Meso-FE modelling of textile composites: Road map, data flow and algorithms," *Composites Science and Technology*, vol. 67, no. 9, pp. 1870–1891, 2007.

[53] F. Trochu, "A contouring program based on dual kriging interpolation," *Engineering with Computers*, vol. 9, no. 3, pp. 160–177, 1993.

[54] "VGStudio MAX 3.0. Volume Graphics Inc.; https://www.volumegraphics.com."

[55] R. Xu, Y. Hui, H. Hu, Q. Huang, H. Zahrouni, T. B. Zineb, and M. Potier-Ferry, "A Fourier-related FE^2 multiscale model for instability phenomena of long fiber reinforced materials," *Composite Structures*, vol. 211, pp. 530–539, 2019.

[56] J. Yang, R. Xu, H. Hu, Q. Huang, and W. Huang, "Structural-Genome-Driven computing for composite structures," *Composite Structures*, vol. 215, pp. 446–453, 2019.

CHAPTER 6 ARTICLE 3 : TRANSVERSE COMPACTION OF 2D GLASS WOVEN FABRICS BASED ON MATERIAL TWINS – PART I: GEOMETRIC ANALYSIS

W. Huang, P. Causse, H. Hu*, S. Belouettar, F. Trochu*

Published in *Composite Structures, Volume 237, 111929, 1 April 2020*

6.1 Chapter overview

This chapter presents the first part of the article in two parts published in *Composite Structures*, in which the mesoscopic deformation of multilayered 2D woven fabrics in transverse compaction is studied. The analyses are based on three material twins of one fabric specimen at different compaction levels generated in Chapter 5 by using the Micro-CT AGM approach described in Chapter 4. The evolution of the morphological features of fiber tows was investigated during compaction. The results show that contacts between fiber tows have a strong effect on the evolution of their morphological features, which is related to the material variability of fiber tows in real fabrics. Although the geometric analyses carried out in this chapter provide a better understanding of the mechanical phenomena occurring during textile compaction, the results remain qualitative as the deformation of fiber tows is not directly evaluated. A quantitative deformation analysis of the fabrics will be carried out in Chapter 7.

6.2 Abstract

In Liquid Composite Molding (LCM), compaction of the reinforcement occurs during several stages of the entire process, including before and during resin injection, which leads to significant deformation of the fibrous architecture. This affects not only the manufacturing process, but also the mechanical properties of final parts. This article aims to study by X-ray microtomography the mesoscopic deformations of 2D glass woven fabrics under transverse compaction for a range of fiber volume fractions encountered in high performance composite applications. The analysis is based on the recently proposed Micro-CT Aided Geometric Modeling (AGM) technique [1], which is used to create, from the three-dimensional images of dry textile preforms obtained by microtomography, “material twin” geometric models representative of fiber architecture. Three “material twin” mesostructural geometric models of

a stack of multiple layer 2D woven fabrics are generated from microtomographic images at different compaction levels. Since all the fiber tows are reconstructed from real fabrics and are labeled separately, the deformation and displacement of fiber tows during compaction can be subsequently studied, which is not necessarily possible with other reconstruction methods. The results show that contacts between fiber tows have an effect on the evolution of their morphological features, which is related to the material variability of fiber tows in real fabrics. Tracking of the fiber tows positions also reveals that the vertical displacement of fiber tows are significant, while their horizontal movements are negligible.

6.3 Introduction

Liquid Composite Molding (LCM) is a generic term regrouping a family of composite manufacturing processes, in which a liquid thermoset resin is injected in a mold cavity to saturate a dry preformed fibrous reinforcement. For processes using rigid tools such as Resin Transfer Molding (RTM), compaction of the reinforcing textile is the main deformation mechanism during closure of the mold. Compaction can also be significant during preparation of the preform in other process variants such as Vacuum Assisted Resin Transfer Molding (VARTM) [2, 3], Compression Resin Transfer Molding (CRTM) [4–6], or Flexible Injection (FI) [7–9]. Rearrangement and deformation of fibrous reinforcements occur at the mesoscopic scale during compaction, leading to significant changes in the mesoporous configuration. Thus the flow paths through the fiber bed, and hence permeability, are strongly affected. The prediction of liquid impregnation in engineering fabrics remains a complex issue because of their dual-scale porosity [10–14]. The strong interaction between the liquid flow and fiber architecture plays an important role on part quality. Therefore it must be investigated to optimize manufacturing processes based on resin injection through fibrous reinforcements.

Mesoscopic simulations of transverse compaction have attracted recent interest. Geometric modeling approaches have been developed using textile modelling software such as TexGen [15,16] or WiseTex [17,18], which have been applied in different topics [19–23]. Methods based on the multi-chain digital element approach have also been implemented [24–28]. Green et al. [29, 30] proposed a numerical procedure to construct mesostructural geometric models of fabrics for simulation by combining TexGen idealized models with multi-chain digital elements. Nguyen et al. [31] followed the method developed by Hivet and Boisse [32] to generate mesostructural geometric models of 2D woven fabrics to simulate transverse compaction. Numerical simulations with a hypoelastic material law based on fiber rotation were in good agreement with experiments. In another approach based on the discrete homogenization method of Goda et al. [33], Rahali et al. [34] could predict the effective mechanical

properties of 2.5D and 3D interlock textiles. Zhang et al. [35] developed a meso-scale finite element-based model to predict the mechanical responses and the failure locus under uniaxial and biaxial loadings. However, these approaches are based on idealized geometric models, and hence cannot describe mesostructural changes in fiber architecture, namely study in detail how fiber tows are deformed under compaction. Assumptions and simplifications are usually necessary for numerical simulations, which reduce the computational cost, facilitate the modeling process and provide computer predictions. However, these simplifications may prevent the investigations of some phenomena occurring in real applications, especially in the case of mesoscopic and microscopic issues.

A direct study of the mesoscopic deformation of fibrous reinforcements can also be conducted by microscopic observations such as X-ray micro-computed tomography (Micro-CT). With this technique, it is possible to measure, model and analyze the geometric structure of fiber tows. Desplentere et al. [36] and Schell et al. [37, 38] were among the first to demonstrate the potential of Micro-CT to characterize the geometric features of 3D textiles at the mesoscopic scale. Pazmino et al. [39] manually measured geometric features of fiber tows from microtomographic images to study the shear of a single layer of non-crimp 3D orthogonal woven fabric. Naouar et al. [40, 41] successfully reconstructed mesostructural geometric models of a 2D woven fabric and 3D orthogonal textile from microtomographic images. The same approach was followed by Wang et al. [42] to study the longitudinal compression and Poisson ratio of fiber yarns. Badel et al. [43] conducted both numerical simulations and tomographic analyses of 2D woven fabrics under biaxial tension and in-plane shear deformation. Combined with digital volume correlation, Mendoza et al. [44] proposed a technique to characterize quantitatively the distortions of woven composites, which was recently employed to measure yarn deformations induced by the manufacturing process [45]. However, no research investigation has been reported up to now concerning deformation analyses based on mesostructural models of fabrics with fiber tows separated by these simplified approaches at different compaction levels.

This article aims to study the mesoscopic deformation of dry 2D glass woven fabrics under transverse compaction by modeling the fiber tows. The original in-situ compaction device developed by Hilal [46] to perform microtomographic measurements was used to scan a stack of 2D glass woven fabric layers at different compaction levels. “Material twin” geometric models of the fibrous reinforcement were created from X-ray microtomographic voxel images following the recently proposed approach called Micro-CT Aided Geometric Modeling [1] (Micro-CT AGM). Three “material twin” mesostructural geometric models of multi-layer 2D woven fabrics were generated from microtomographic images at different compaction levels (and not only a manual reconstruction from a limited number of slices like other

investigators [36, 39, 47, 48]). Since all the fiber tows are reconstructed from real fabrics and are labeled separately in the material twin geometric model, it is possible to analyze the geometric features of fiber tows to study directly their deformations at the mesoscopic scale. Note that changes in the mesoporous empty domains complementary to the fibrous reinforcement (known as flow channels in LCM) play a key role in the impregnation process as a result of the deformation of fiber tows. Therefore, it is possible to apply the approach proposed here to analyze also the evolution of mesopores during compaction as done by most other investigators [37, 38, 49–51]. However, note that it is not possible for them to analyze the deformations of fiber tows.

In summary, recalling the definition of material twins in [1], their three main features can be stated up as follows:

1. The mesoscopic structure of fiber tows is reproduced with assessed accuracy.
2. The fiber tows are identified and labeled in the voxel image, thus enabling a thorough voxel based analysis of their geometrical features.
3. Material variability is taken into account, which allows conducting representative numerical simulations of mechanical or flow properties.

Note that these models were proved effective to assess the accuracy of textile architecture [1], and in particular predict the saturated transverse permeability of 2D woven fabrics [52].

This investigation is presented in two parts:

1. Part I studies the evolution of the morphological features and the displacements of fiber tows under through-thickness compaction based on material twins geometric models representative of textile preforms. Statistical analyses of tow geometric features are also performed to evaluate material variability.
2. Part II proposes a new approach to follow the motion of points on the surfaces of fiber tows during compaction. This provides a quantitative evaluation of the mesoscopic deformations of fiber tows resulting from contact between tows or from nesting between fabric layers.

The structure of Part I is organized as follows. In Section 6.4, material twin geometric models of the same textile specimen are generated for three increasing compaction levels, namely for fiber volume contents between 47% and 55%, which lie in the range of high performance composite applications. In Section 6.5, the evolution of the morphological features of one

fiber tow is analyzed during transverse compaction. This shows how Micro-CT can analyze the geometric structure of a single tow. In Section 6.6, the geometric features of tows are evaluated statistically for different compaction levels. Section 6.7 studies the motion of the central lines of tows. Finally, the conclusion in Section 6.8 introduces Part II, which presents a new way to describe the mesoscopic deformations of textile preforms from Micro-CT images.

6.4 Material twin based geometric models

In a recent work on the saturated transverse permeability of engineering fabrics [52], the Micro-CT Aided Geometric Modeling (Micro-CT AGM) technique [1] was implemented for a stack of 2D plain glass woven fabrics to construct material twin geometric models for three different fiber volume contents. The specimen comprised several circular samples (diameter 25.2 mm) of a glass fiber plain weave fabrics from Texonic (product number L14012, the characteristics of the material are listed in Table 6.1). X-ray microtomography was conducted with a Nikon XT H 225 at a resolution of 22 µm/pixel with a voltage and intensity of the X-ray beam of 180 kV and 30 µA respectively. Three measurements were carried out on the same sample at different levels of compaction. In order to avoid boundary effects, a rectangular region of interest of area $15.82 \times 8.58\text{mm}^2$ was selected for analysis in the central part of the scanned specimen. Meanwhile, since the top and bottom fabric layers are in contact with metallic grids (see Figures 1 and 2 in [52]) to support the stack in the compaction device, the fiber tows exhibit significant local deformations which are not representative of the general compaction behavior of the fiber bed. Hence, only the middle eight layers of the ten-layer stack will be analyzed in this study (namely from the second to the ninth layer).

Figure 6.1 shows perspective views of the three material twins created to investigate the mesoscopic deformations of fiber tows under transverse compaction. For convenience, the geometric models generated for the three levels of compaction considered in this analysis will be referred to in the sequel as MT1, MT2 and MT3.

Table 6.1 Characteristics of the 2D glass woven fabrics L14012

Material	Fiber diameter (µm)	Strands per centimeter	Linear density of strands (10^{-6}kg/m)	Surface density (kg/m^2)	Volume density (kg/m^3)
Glass fiber	13	Warp: 4 Weft: 3.7	735	0.590	2550

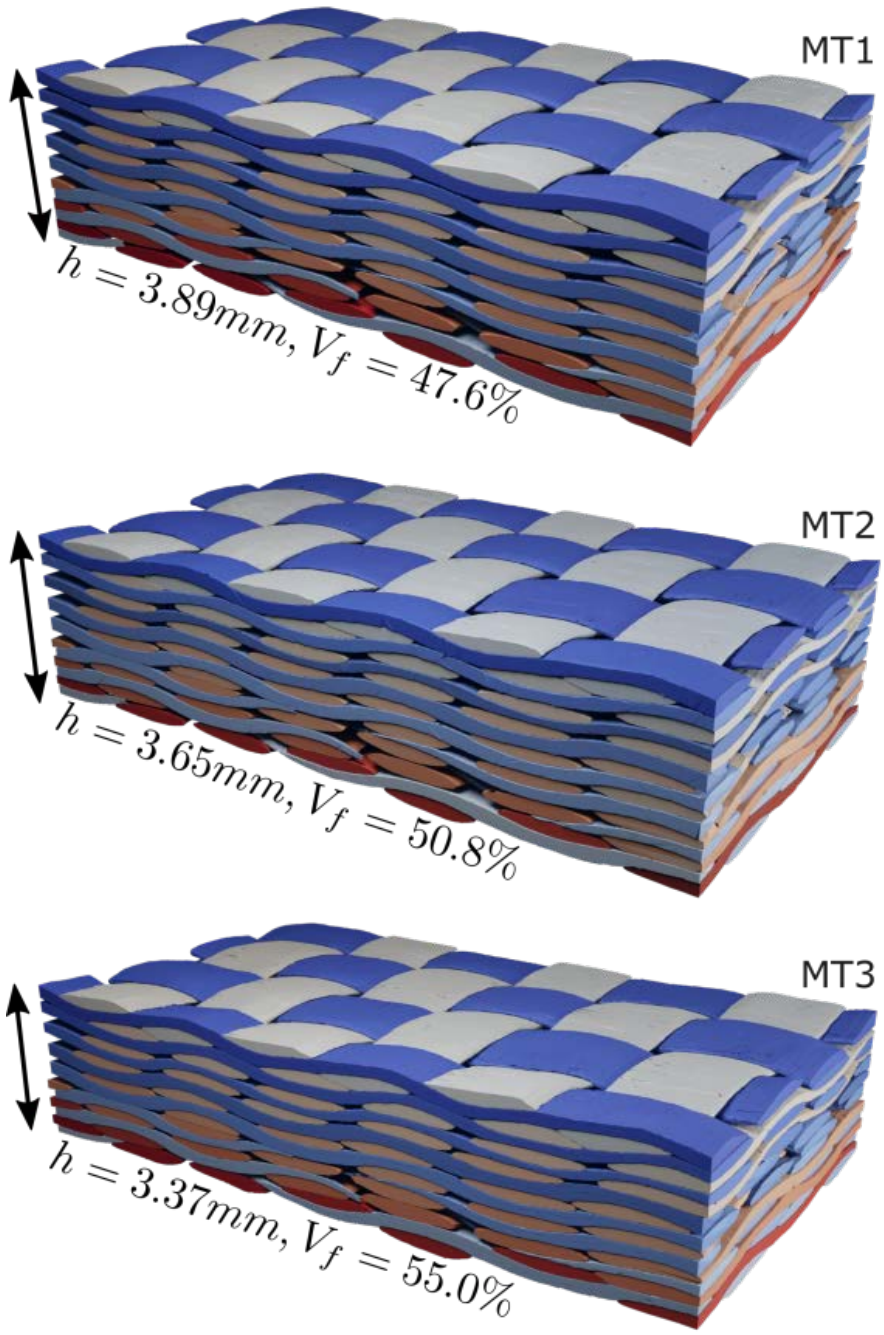

Figure 6.1 Material twins for three different fiber volume contents

In this article, the fiber tows are identified and individually labeled in the reconstructed mesostructural model. Hence the approach based on "material twin" geometric models of real textile preforms will allow to study in detail the evolution of the geometric features, orientations, changes in shape and displacements of fiber tows. This kind of analysis is different from microtomographic investigations based on standard image processing techniques [37, 38, 49–51], which provide only models of mesopores at a specific fiber volume content, without any analysis on how fiber tows are deformed and displaced.

6.5 Morphological analysis of one single tow

Figure 6.2 shows the morphological features of fiber tows analyzed in [1] to assess the accuracy of the reconstructed geometric models. This evaluation is based on a multiple factor criterion and includes the seven following morphological features: local coordinates of the centroid point, the area, height, width, angle and circularity of tow cross-sections. The shape and skewness of the transverse cross-sections of fiber tows can be evaluated quantitatively by an analysis based on the above mentioned morphological features. The first stage consists of describing the procedure followed for one weft tow.

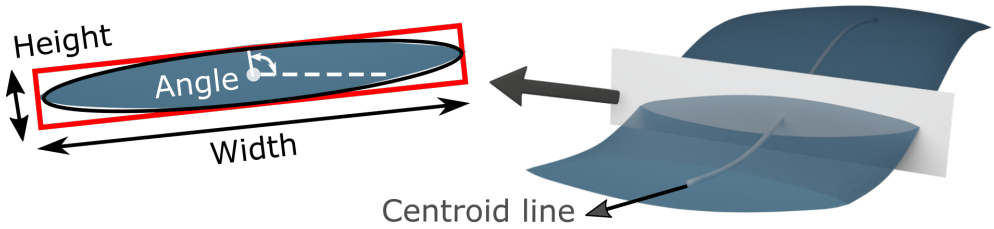

Figure 6.2 Morphological features of fiber tows

Figure 6.3 illustrates the morphological features of a typical weft tow extracted from the material twins at the three compaction levels MT1, MT2, MT3 illustrated in Figure 6.1. All these features exhibit a nearly periodic behavior in the tow direction and change during compaction. In Figure 6.3, four typical cross-sections A, B, C and D of the fiber tow are identified. Note that a detailed evolution of their contours is illustrated in Figure 6.4 for the three compaction levels considered. Let us begin by reviewing in Figure 6.3 the changes under compaction of the following five morphological features of fiber tows:

1. For larger compaction levels, the area of the tow decreases in sections A and C, where it comes in contact with its neighbors, while it increases slightly in the middle positions (sections B and D), where the tow is barely compressed.

2. As expected, the height tends to decrease with compaction in the contact regions (sections A and C), but it increases in the middle positions (sections B and D). Again, this is understandable as the tows are squeezed, deformed and may even be slightly twisted in the contact zones as shown by the evolution of the angle.

3. On the contrary to the area and height, the width increases everywhere with compaction, which means that all tow cross-sections are affected by compression even if not in direct contact with other tows. This can be explained by the structure of fiber bundles, which are made of long and continuous filaments. Although the contact between tows can enhance local effects on some features such as the area, height and circularity, compression has an influence on all the fiber bundles, and not only in contact regions between tows.

4. The angle of the fiber tow increases also slightly with compaction, especially at some crests and troughs. This indicates that local contact forces between tows cause the fiber bundles to twist during compaction. However, the maximum change in angle is about 4 degrees, thus the twist is not significant.

5. The circularity (roundness) of the contour evaluates quantitatively how close the shape is to a mathematically perfect circle. (For a perfect circle, the circularity index is equal to 1.) As shown in Figure 6.3, circularity obviously decreases at the crests and troughs, which further illustrates how contact between tows leads to local deformations and distortion.

Figure 6.4 displays the four cross-sections of the weft tow for the three levels of compaction. A local coordinate system in pixel units is introduced for each cross-section, in which the coordinates of the centroids points are set as (0,0). At the crest A and trough C, the deformation of the contour is more significant where it comes in contact with other fiber tows, but this is not the case at the middle positions B and D. Since the contours of cross-sections can be easily acquired from the material twin geometric models, it will be possible to track the displacement of contour points to evaluate quantitatively in Part II the local deformations of fiber tows.

6.6 Statistical analysis of morphological features

By comparing the geometric features of each slice of fiber tows in MT2 and MT3 with MT1, the evolution of geometric features can be analyzed statistically by evaluating relative changes with the equation $\Delta f = (f - f_1)/f_1$, where f stands for one geometric feature in configurations

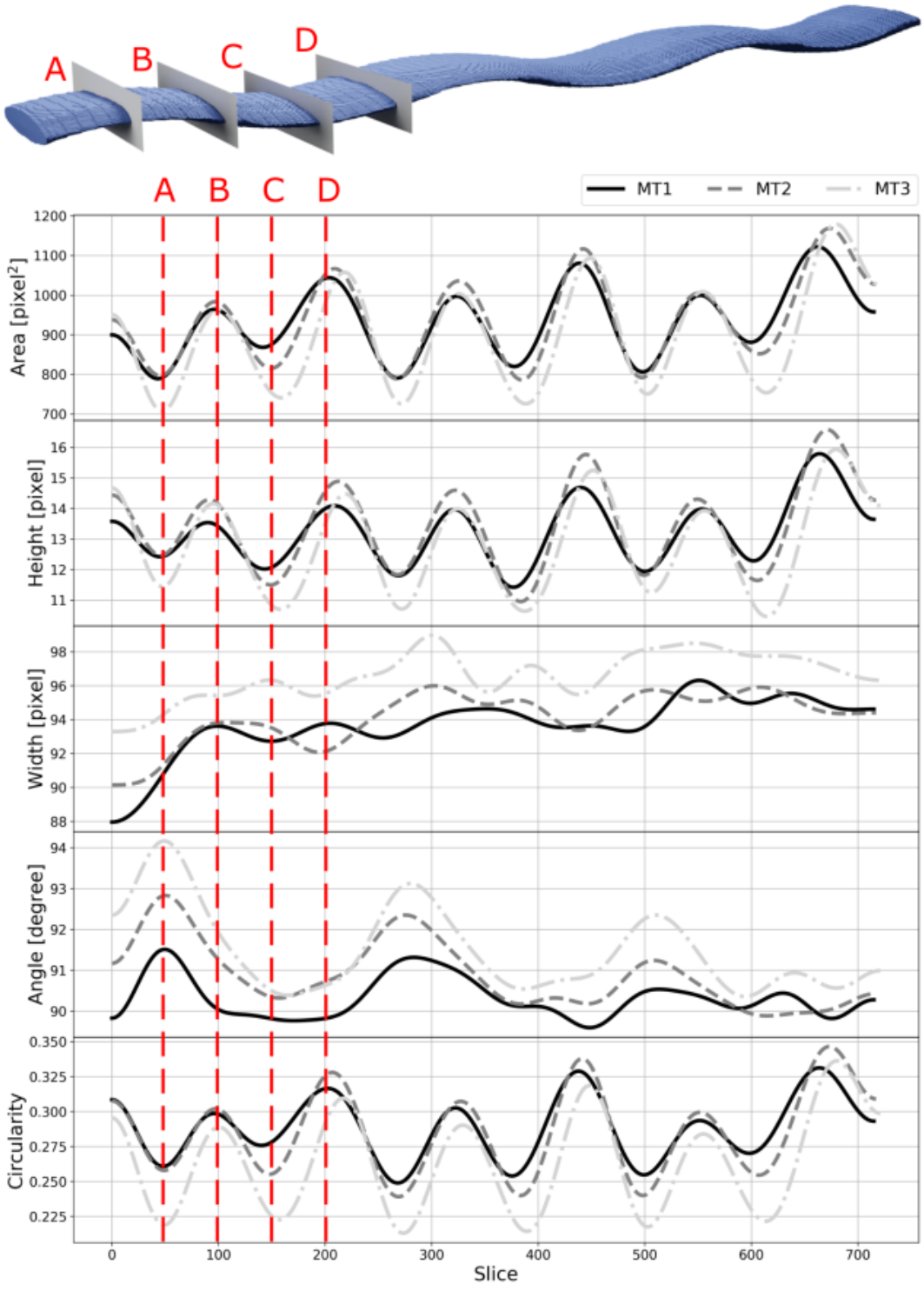

Figure 6.3 Variations of the morphological features of a weft tow in the tow direction for the three compaction levels MT1, MT2, MT3 of Figure 6.1

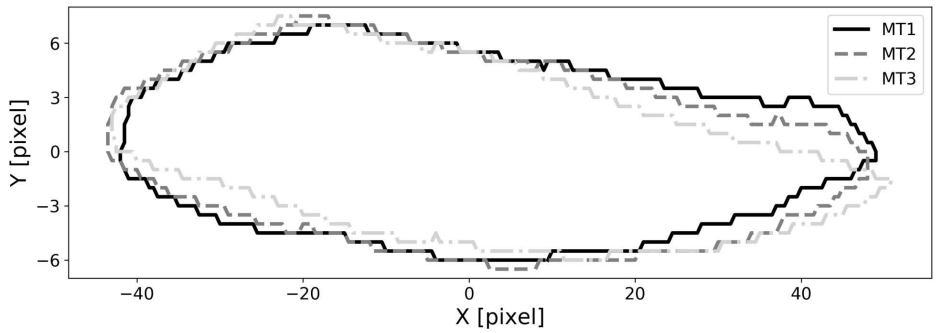

(a) Cross-section A (slice=50) at three compaction levels

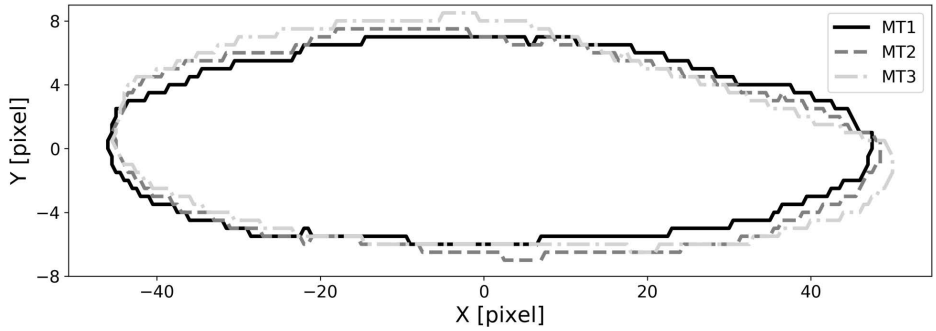

(b) Cross-section B (slice=100) at three compaction levels

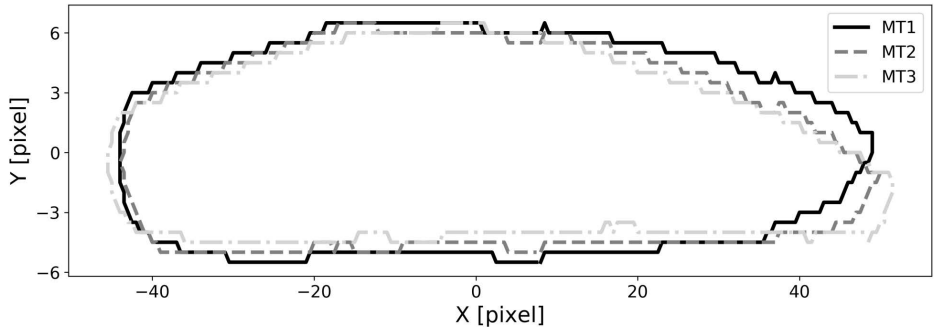

(c) Cross-section C (slice=150) at three compaction levels

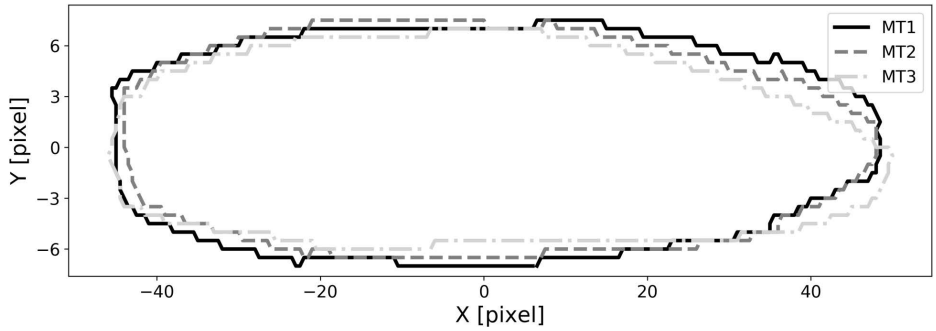

(d) Cross-section D (slice=200) at three compaction levels

Figure 6.4 Contours of the weft tow at three compaction levels for the four cross-sections A, B, C and D identified in Figure 6.3

MT2 or MT3, and f_1 is the same geometric feature in the reference configuration MT1. The maximum, minimum and average values of Δf can be calculated. Consequently, statistical results can be obtained on the evolution of the geometric features of fiber tows.

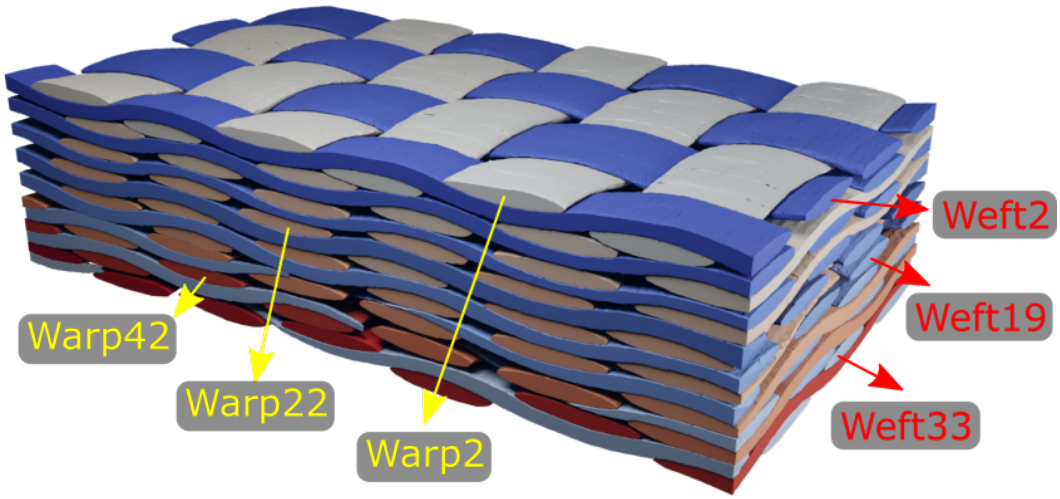

Figure 6.5 Fiber tows selected for statistical analysis to follow the evolution of morphological features at different compaction levels

As an illustration, three warp and three weft tows were randomly selected in different fabric layers of the stack (see Figure 6.5). Figure 6.6a gives statistical results on the geometric features of the warp tows at different compaction levels with average values of the relative changes Δf of geometrical features and error bars to show extreme values. The area and the height both decrease under compaction, although the mean value does not present a obvious trend with the compaction level, for example from MT2 to MT3, they increase for Warp2, nearly keep the same for Warp22, but decrease distinctly for Warp42. This can be explained by the material variability of real fabrics, which can be assessed in material twins. However, the boundaries of these two geometric features generally tend to become wider with compaction, which indicate that some parts are compressed to be thinner while some other parts expand during the process.

The evolution of the width is quite clear. For MT2, the mean value is around 0, while it increases obviously at MT3 for each warp tow presented in Figure 6.6a. It means that when the fiber volume content is high enough, namely the compaction level is quite high, the Poisson effect starts to become significant to make the fiber tows expand in horizontal direction.

The drastic change of the mean value of circularity indicates a severe deformation of the fiber tows, during which the cross-sections of fiber tows become less regular. Especially for Warp2

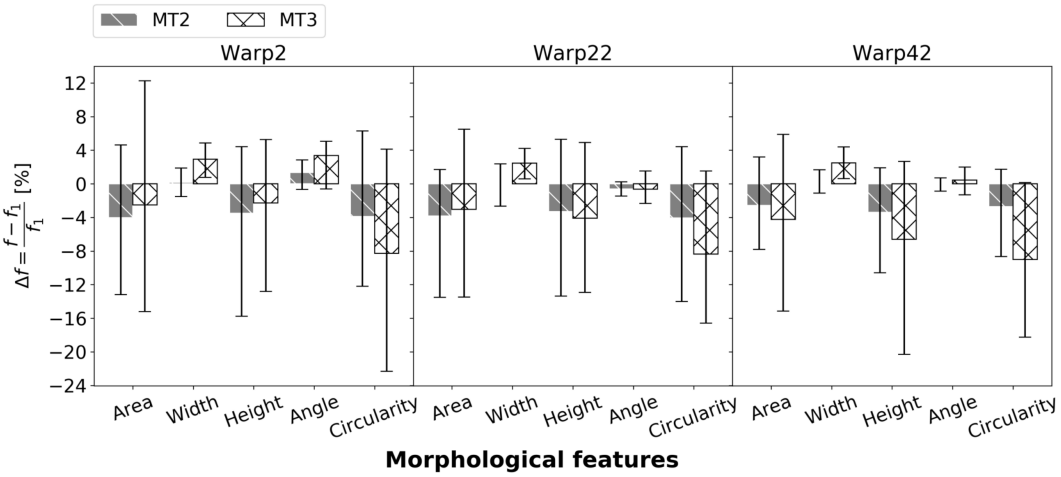

(a)

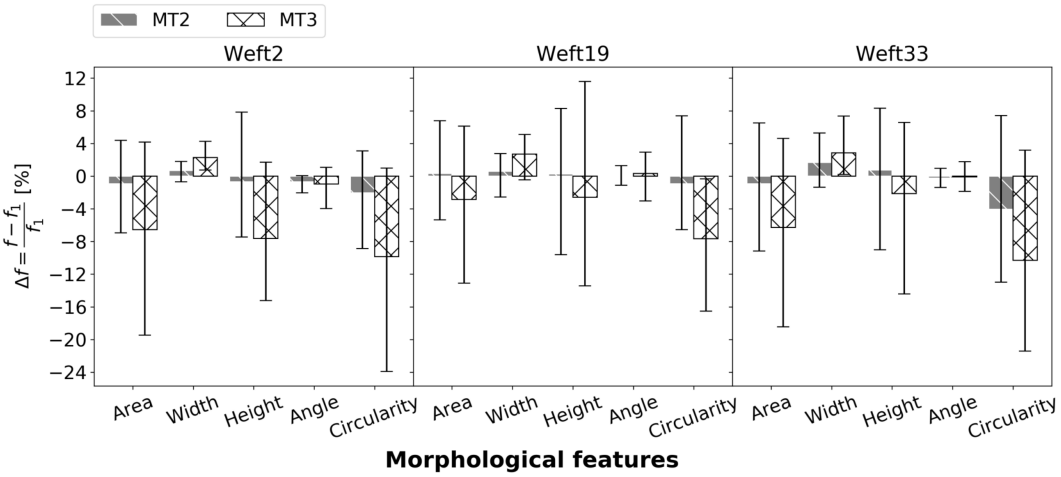

(b)

Figure 6.6 Statistical analysis to follow the evolution of the morphological features of individual warp and weft tows at different compaction levels: (a) evolution of the morphological features of three warp tows; (b) evolution of the morphological features of three weft tows

at MT3, the lowest value nearly reaches -24%, it means that some cross-sections become extremely irregular during compaction. In the contrary, the angle barely changes, especially for Warp22 and Warp42, in which the value of angle nearly keeps zero during compaction. Although the change of the angle is larger in Warp2, the upper boundary is still lower than 5%.

As shown in Figure 6.6b, the evolution of the geometric features is rather similar for the weft tows although a noticeable difference exists for MT2. In that case, the changes are quite small for most of the geometric features, which differs from the warp tows, especially for the area, height and circularity. This might be caused by the difference between the inherent properties of warp and weft tows (see Table 6.1), namely the strands per centimeter (thus the initial height and width of the fiber tows) or the woven pattern. The other possible reason might just be the particularity of the three selected weft tows. Therefore, a statistical analysis based on the whole fabric stack needs to be conducted.

By conducting the statistical analysis illustrated in Figure 6.6 for all fiber tows in MT2 and MT3, average values $\overline{\Delta f}_{mean}$ mean of Δf are calculated for every tow. After determining the average, maximum and minimum values of the values $\overline{\Delta f}_{mean}$, a statistical analysis is carried out for the whole fabric stack as illustrated in Figure 6.7. The result is quite similar to the ones of individual tows reported in Figure 6.6. This means that although the effect of material variability on the geometric features exists during compaction as illustrated in Figure 6.6, the fiber tows in the fabric stack deform in a similar fashion, especially when the compaction level is high.

For these two types of fiber tows, the evolution of several geometric features are similar during compaction, while the area, height and circularity show obvious differences in MT2. The mean value of most of the geometric features change slightly at MT2 for weft tows, and reach the same level as the ones of warp tows at MT3. This lag in the evolution of geometric features is similar to the finding in Figure 6.6b, which indicates that the phenomena does not only exist in individual tows which might be induced by material variability, but it exists in the whole fabric stack. It appears that additional studies are required in the future in order to explain this phenomenon.

Although the area and height change considerably during compaction, the width is barely modified, especially for the tows in MT2. Thus, the area and height are mainly affected during compaction since fiber tows are compressed in the height direction, while the influence of Poisson effect on the width is less obvious. Moreover, the width changes a little in MT2, but more significantly in MT3; which suggests that Poisson effect is more significant in the fabric stack at higher fiber volume contents.

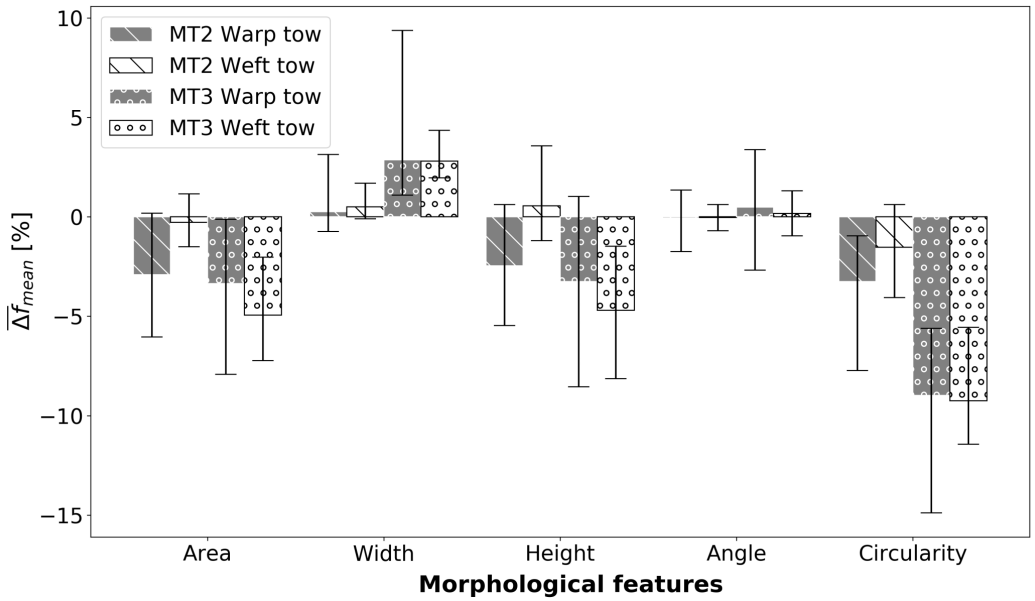

Figure 6.7 Statistical analysis showing the evolution of the morphological features of all the warp and weft tows at different levels of compaction

Similar to the finding in Figure 6.6, the maximum change in angle is still less than 5%, namely around 4 degrees, while the mean value nearly keeps zero for the whole stack. This means that the rotation of fiber tows is negligible during transverse compaction. On the contrary, circularity exhibits a significant difference at the two levels of compaction MT2 and MT3, which indicates that the shapes of cross-sections become less regular. This might be explained by complex contact configurations between the fiber tows of real fabrics, which will be further investigated in Part II.

6.7 Displacement of fiber tows

Besides the deformation of fiber tows, their movement during transverse compaction is another important issue that can be evaluated from Micro-CT images. In this section, the displacement of the central lines of fiber tows is investigated during compaction. Figure 6.8 displays the central lines derived from material twins for the three levels of compaction considered. Because of nesting induced during the lay-up process, the central lines are not oriented exactly in the same direction. During the transverse compaction process, no significant rotation or distortion of central lines is observed.

In order to analyze the displacements of central lines, the centroids in the same cross-section defined by the red dashed rectangles in Figure 6.8 are extracted from the geometric models

and plotted in the upper part of Figure 6.9. At the bottom of the stack, the centroids barely move, while significant displacements appear at the top. This can be explained by the bottom layer, which is regarded as a fixed reference in the transverse direction. During compaction, the top layers move downward and the displacements of the centroids of cross-sections are larger in the upper layers.

The second layer from the top (the blue dashed line) is extracted for further analysis. The X and Y coordinates in the cross-section are the horizontal and vertical axes of the local reference system in pixel units that will be introduced in detail in Part II. The centroids move about 25 pixels in the vertical direction, but only 2 or 3 pixels in the horizontal direction. Thus, the vertical displacements of fiber tows at this layer are more significant than their horizontal movements.

By calculating the movements of centroids of all the tows in each cross-section, the mean value of the displacements of the fiber tows located in different layers are obtained. In 2D woven fabrics, because of the woven pattern, the displacements of warp tows should be similar to the ones of weft tows, thus only the warp tows are analyzed here. As shown in Figure 6.10, both displacements ΔX and ΔY exist during compaction, but the vertical displacement ΔY is much larger than the horizontal displacement ΔX. ΔY presents an obvious trend with different fabric layer, namely changes from -25 pixels at the top (first) layer to around 0 at the bottom (eight) layer for MT3, while the change of ΔX does not display a strong relationship with the change of layer, it remains around 0 and -1 for MT2 and MT3 respectively. Therefore, for the whole stack, especially for the upper layers, the vertical displacement of fiber tows are significant, while their horizontal movements are negligible.

6.8 Conclusion

In this study three mesostructural models were created by Micro-CT AGM [1] from microtomographic images of a stack of 2D glass woven fabrics at different levels of compaction. This allowed to study the mesoscopic deformations of the fibrous reinforcement based on the real fabric architecture.

In Part I, the evolution of the morphological features of fiber tows was investigated during compaction. The results show that contacts between fiber tows have an effect on the evolution of their morphological features, which is related to the material variability of fiber tows in real fabrics. Statistical analyses were also carried out to study the average behavior of all the fiber tows during compaction. The geometric features of fabric stacks change under compaction in a consistent way. Tracking of the fiber tows positions also reveals that

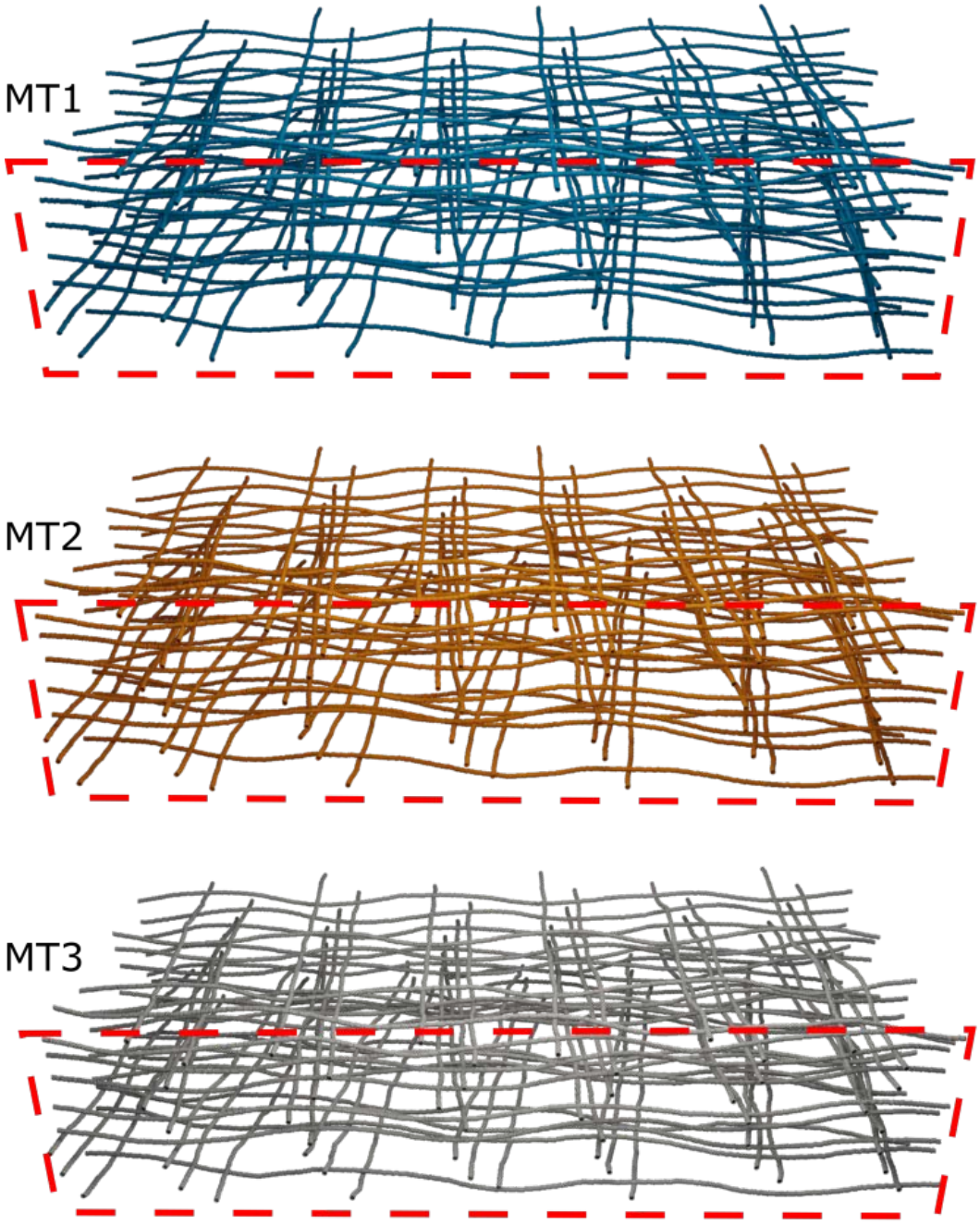

Figure 6.8 Central lines of fiber tows at three compaction levels. The red dashed rectangles indicate the cross-sections (slice = 0) of the material twins

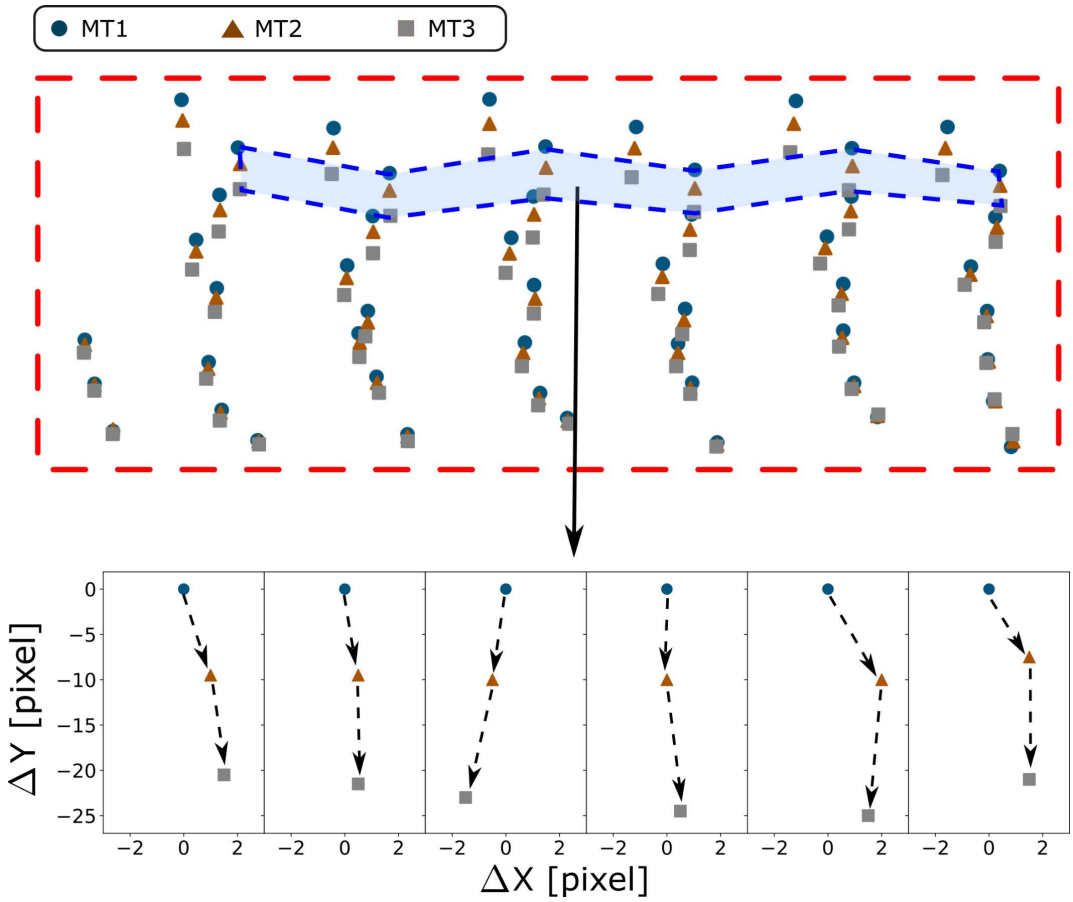

Figure 6.9 Displacement of centroids in the cross-section introduced in Figure 6.8. The blue dashed line in the upper part of the figure indicates the second fabric layer in the eight-layer stack whose centroid displacements are further analyzed in the lower part

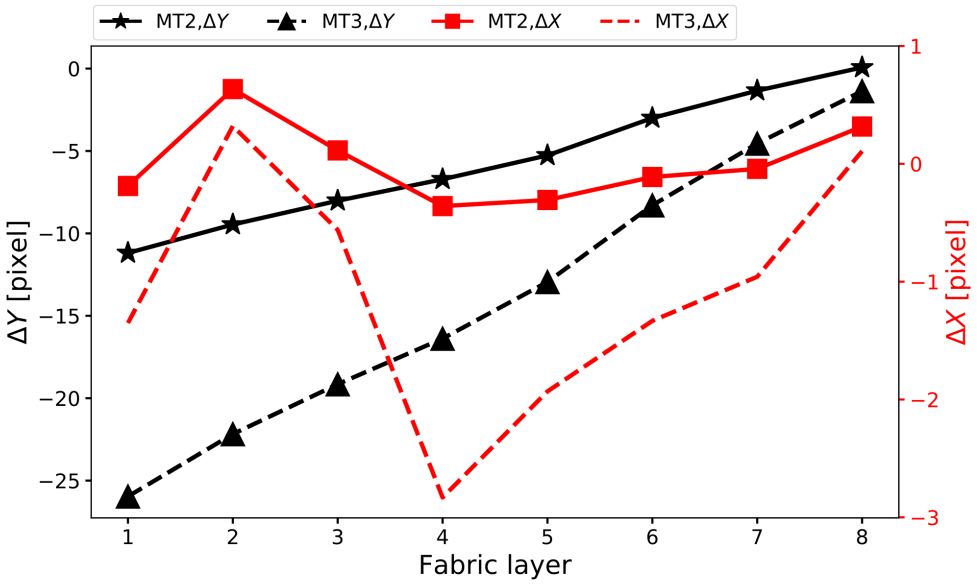

Figure 6.10 Mean value of the centroid displacements of the warp tows located in different layers

the vertical displacement of fiber tows are significant, while their horizontal movements are negligible.

Although the geometric analyses carried out in Part I provide a better understanding of mechanical phenomena occurring during textile compaction, the results remain qualitative as the deformation of fiber tows is not directly evaluated. In Part II, a new approach will be proposed to follow the displacements of contour points on the cross-sections of fiber tows at different levels of compaction. This will provide quantitative information on the textile mesoscopic deformations resulting from contacts between tows and from nesting between fabric layers. Based on material twin geometric models, it will be possible in future work to conduct numerical simulations to predict more accurately the material or flow properties of continuous fiber composites.

6.9 Acknowledgements

This work has been supported by the Department of Mechanical Engineering of Polytechnique Montreal, by a Discovery Grant of the National Science & Engineering Research Council of Canada (NSERC) and by grants of the National Natural Science Foundation of China (Grant Nos. 11920101002, 11372231 and 11772238). Authors also acknowledge the contributions of the Research Center for High Performance Polymer and Composite Systems (CREPEC), the

“Fonds de recherche du Québec - Nature et technologies” (FRQNT) and the “Fonds National de la Recherche” (FNR) of Luxembourg. Authors would also like to thank Nicolas Juillard from Texonic for providing the fibrous reinforcements and Professor Vladimir Brailovski for access to the X-ray micromograph at École de technologie supérieure (ETS), Montreal.

Bibliography

[1] W. Huang, P. Causse, V. Brailovski, H. Hu, and F. Trochu, "Reconstruction of mesostructural material twin models of engineering textiles based on Micro-CT Aided Geometric Modeling," *Composites Part A: Applied Science and Manufacturing*, vol. 124, p. 105481, 2019.

[2] L. Joubaud, V. Achim, and F. Trochu, "Numerical simulation of resin infusion and reinforcement consolidation under flexible cover," *Polymer composites*, vol. 26, no. 4, pp. 417–427, 2005.

[3] L. Joubaud, F. Trochu, and J. Le Corvec, "Analysis of resin flow under flexible cover in vacuum assisted resin infusion (VARI)," *Journal of advanced materials*, vol. 37, no. 3, pp. 3–10, 2005.

[4] X. Pham, F. Trochu, and R. Gauvin, "Simulation of compression resin transfer molding with displacement control," *Journal of reinforced plastics and composites*, vol. 17, no. 17, pp. 1525–1556, 1998.

[5] X. Pham and F. Trochu, "Simulation of compression resin transfer molding to manufacture thin composite shells," *Polymer composites*, vol. 20, no. 3, pp. 436–459, 1999.

[6] X. Pham and F. Trochu, "Analysis of the consolidation in flexible bladder process for thin composite parts by finite element method," *Journal of reinforced plastics and composites*, vol. 19, no. 3, pp. 182–218, 2000.

[7] E. Ruiz, L. Briones, E. Allard, and F. Trochu, "Flexible injection: a novel LCM technology for low cost manufacturing of high performance composites. Part I: experimental investigation," in *The 9th International Conference on Flow Processes in Composite Materials*, 2008.

[8] F. Trochu, S. Soukane, and B. Touraine, "Flexible injection: a novel LCM technology for low cost manufacturing of high performance composites. Part II: numerical model," in *9 th Int. Conf. on Flow Proc. in Comp. Mat*, 2008.

[9] P. Causse, E. Ruiz, and F. Trochu, "Spring-in behavior of curved composites manufactured by Flexible Injection," *Composites Part A: Applied Science and Manufacturing*, vol. 43, no. 11, pp. 1901–1913, 2012.

[10] N. Kuentzer, P. Simacek, S. G. Advani, and S. Walsh, "Permeability characterization of dual scale fibrous porous media," *Composites Part A: Applied Science and Manufacturing*, vol. 37, no. 11, pp. 2057–2068, 2006.

[11] E. Ruiz, V. Achim, S. Soukane, F. Trochu, and J. Bréard, "Optimization of injection flow rate to minimize micro/macro-voids formation in resin transfer molded composites," *Composites Science and Technology*, vol. 66, no. 3-4, pp. 475–486, 2006.

[12] C. Ravey, E. Ruiz, and F. Trochu, "Determination of the optimal impregnation velocity in resin transfer molding by capillary rise experiments and infrared thermography," *Composites Science and Technology*, vol. 99, pp. 96–102, 2014.

[13] M. Imbert, S. Comas-Cardona, E. Abisset-Chavanne, and D. Prono, "Experimental investigation of intra-tow fluid storage mechanisms in dual-scale fiber reinforcements," *Composites Part A: Applied Science and Manufacturing*, vol. 107, pp. 70–82, 2018.

[14] J. Bréard, Y. Henzel, F. Trochu, and R. Gauvin, "Analysis of dynamic flows through porous media. Part I: Comparison between saturated and unsaturated flows in fibrous reinforcements," *Polymer Composites*, vol. 24, no. 3, pp. 391–408, 2003.

[15] M. Sherburn, "Geometric and mechanical modelling of textiles," Ph.D. dissertation, University of Nottingham, 2007.

[16] A. C. Long and L. P. Brown, "Modelling the geometry of textile reinforcements for composites: TexGen," in *Composite Reinforcements for Optimum Performance*, 2011, pp. 239–264.

[17] I. Verpoest and S. V. Lomov, "Virtual textile composites software WiseTex: Integration with micro-mechanical, permeability and structural analysis," *Composites Science and Technology*, vol. 65, pp. 2563–2574, 2005.

[18] S. V. Lomov, D. S. Ivanov, I. Verpoest, M. Zako, T. Kurashiki, H. Nakai, and S. Hirosawa, "Meso-FE modelling of textile composites: Road map, data flow and algorithms," *Composites Science and Technology*, vol. 67, no. 9, pp. 1870–1891, 2007.

[19] Y. Cao, Y. Cai, Z. Zhao, P. Liu, L. Han, and C. Zhang, "Predicting the tensile and compressive failure behavior of angle-ply spread tow woven composites," *Composite Structures*, vol. 234, p. 111701, 2020.

[20] C. Zhang and W. K. Binienda, "A meso-scale finite element model for simulating free-edge effect in carbon/epoxy textile composite," *Mechanics of Materials*, vol. 76, pp. 1–19, 2014.

[21] X. S. Zeng, A. C. Long, F. Gommer, A. Endruweit, and M. Clifford, "Modelling compaction effect on permeability of 3D carbon reinforcements," in *18th International Conference on Composites Materials, Jeju Island, Korea*, 2011.

[22] Z. Yousaf, P. Potluri, and P. J. Withers, "Influence of tow architecture on compaction and nesting in textile preforms," *Applied Composite Materials*, vol. 24, no. 2, pp. 337–350, 2017.

[23] Q. Zeng, L. Sun, J. Ge, W. Wu, J. Liang, and D. Fang, "Damage characterization and numerical simulation of shear experiment of plain woven glass-fiber reinforced composites based on 3D geometric reconstruction," *Composite Structures*, vol. 233, p. 111746, 2020.

[24] Y. Wang and X. Sun, "Digital-element simulation of textile processes," *Composites Science and Technology*, vol. 61, no. 2, pp. 311–319, 2001.

[25] G. Zhou, X. Sun, and Y. Wang, "Multi-chain digital element analysis in textile mechanics," *Composites Science and Technology*, vol. 64, no. 2, pp. 239–244, 2004.

[26] D. Durville, "Simulation of the mechanical behaviour of woven fabrics at the scale of fibers," *International Journal of Material Forming*, vol. 3, no. 2, pp. 1241–1251, 2010.

[27] D. Durville, I. Baydoun, H. Moustacas, G. Périé, and Y. Wielhorski, "Determining the initial configuration and characterizing the mechanical properties of 3D angle-interlock fabrics using finite element simulation," *International Journal of Solids and Structures*, vol. 154, pp. 97–103, 2018.

[28] Y. Mahadik and S. R. Hallett, "Finite element modelling of tow geometry in 3D woven fabrics," *Composites Part A: Applied Science and Manufacturing*, vol. 41, no. 9, pp. 1192–1200, 2010.

[29] S. D. Green, A. C. Long, B. S. F. El Said, and S. R. Hallett, "Numerical modelling of 3D woven preform deformations," *Composite Structures*, vol. 108, pp. 747–756, 2014.

[30] S. D. Green, M. Y. Matveev, A. C. Long, D. Ivanov, and S. R. Hallett, "Mechanical modelling of 3D woven composites considering realistic unit cell geometry," *Composite Structures*, vol. 118, pp. 284–293, 2014.

[31] Q. T. Nguyen, E. Vidal-Sallé, P. Boisse, C. H. Park, A. Saouab, J. Bréard, and G. Hivet, "Mesoscopic scale analyses of textile composite reinforcement compaction," *Composites Part B: Engineering*, vol. 44, no. 1, pp. 231–241, 2013.

[32] G. Hivet and P. Boisse, "Consistent 3D geometrical model of fabric elementary cell. Application to a meshing preprocessor for 3D finite element analysis," *Finite Elements in Analysis and Design*, vol. 42, no. 1, pp. 25–49, 2005.

[33] I. Goda, M. Assidi, and J. F. Ganghoffer, "Equivalent mechanical properties of textile monolayers from discrete asymptotic homogenization," *Journal of the Mechanics and Physics of Solids*, vol. 61, no. 12, pp. 2537–2565, 2013.

[34] Y. Rahali, M. Assidi, I. Goda, A. Zghal, and J. F. Ganghoffer, "Computation of the effective mechanical properties including nonclassical moduli of 2.5D and 3D interlocks by micromechanical approaches," *Composites Part B: Engineering*, vol. 98, pp. 194–212, 2016.

[35] D. Zhang, Y. Sun, X. Wang, and L. Chen, "Meso-scale finite element analyses of three-dimensional five-directional braided composites subjected to uniaxial and biaxial loading," *Journal of Reinforced Plastics and Composites*, vol. 34, no. 24, pp. 1989–2005, 2015.

[36] F. Desplentere, S. V. Lomov, D. L. Woerdeman, I. Verpoest, M. Wevers, and A. Bogdanovich, "Micro-CT characterization of variability in 3D textile architecture," *Composites Science and Technology*, vol. 65, no. 13, pp. 1920–1930, 2005.

[37] J. S. U. Schell, M. Renggli, G. H. van Lenthe, R. Müller, and P. Ermanni, "Micro-computed tomography determination of glass fibre reinforced polymer meso-structure," *Composites Science and Technology*, vol. 66, no. 13, pp. 2016–2022, 2006.

[38] J. S. U. Schell, M. Deleglise, C. Binetruy, P. Krawczak, and P. Ermanni, "Numerical prediction and experimental characterisation of meso-scale-voids in liquid composite moulding," *Composites Part A: Applied Science and Manufacturing*, vol. 38, no. 12, pp. 2460–2470, 2007.

[39] J. Pazmino, V. Carvelli, and S. V. Lomov, "Micro-CT analysis of the internal deformed geometry of a non-crimp 3D orthogonal weave E-glass composite reinforcement," *Composites Part B: Engineering*, vol. 65, pp. 147–157, 2014.

[40] N. Naouar, E. Vidal-Sallé, J. Schneider, E. Maire, and P. Boisse, "Meso-scale FE analyses of textile composite reinforcement deformation based on X-ray computed tomography," *Composite Structures*, vol. 116, no. 1, pp. 165–176, 2014.

[41] N. Naouar, E. Vidal-Sallé, J. Schneider, E. Maire, and P. Boisse, "3D composite reinforcement meso F.E. analyses based on X-ray computed tomography," *Composite Structures*, vol. 132, pp. 1094–1104, 2015.

[42] D. Wang, N. Naouar, E. Vidal-Salle, and P. Boisse, "Longitudinal compression and poisson ratio of fiber yarns in meso-scale finite element modeling of composite reinforcements," *Composites Part B: Engineering*, vol. 141, pp. 9–19, 2018.

[43] P. Badel, E. Vidal-Sallé, E. Maire, and P. Boisse, "Simulation and tomography analysis of textile composite reinforcement deformation at the mesoscopic scale," *Composites Science and Technology*, vol. 68, no. 12, pp. 2433–2440, 2008.

[44] A. Mendoza, J. Schneider, E. Parra, E. Obert, and S. Roux, "Differentiating 3D textile composites: A novel field of application for Digital Volume Correlation," *Composite Structures*, vol. 208, pp. 735–743, 2019.

[45] A. Mendoza, J. Schneider, E. Parra, and S. Roux, "Measuring yarn deformations induced by the manufacturing process of woven composites," *Composites Part A: Applied Science and Manufacturing*, vol. 120, pp. 127–139, 2019.

[46] S. Hilal, "Caractérisation par microtomographie de la mésostructure des renforts fibreux pour la fabrication de composites par injection," Ph.D. dissertation, École Polytechinque de Montréal, 2018.

[47] X. Yu, H. Wang, and Z. Wang, "Analysis of yarn fiber volume fraction in textile composites using scanning electron microscopy and X-ray micro-computed tomography," *Journal of Reinforced Plastics and Composites*, vol. 38, no. 5, pp. 199–210, 2019.

[48] A. Vanaerschot, F. Panerai, A. Cassell, S. V. Lomov, D. Vandepitte, and N. N. Mansour, "Stochastic characterisation methodology for 3-D textiles based on micro-tomography," *Composite Structures*, vol. 173, pp. 44–52, 2017.

[49] M. A. Ali, R. Umer, K. A. Khan, S. Bickerton, and W. J. Cantwell, "Non-destructive evaluation of through-thickness permeability in 3D woven fabrics for composite fan blade applications," *Aerospace Science and Technology*, vol. 82-83, pp. 520–533, 2018.

[50] M. A. Ali, R. Umer, K. A. Khan, and W. J. Cantwell, "In-plane virtual permeability characterization of 3D woven fabrics using a hybrid experimental and numerical approach," *Composites Science and Technology*, vol. 173, pp. 99–109, 2019.

[51] M. A. Ali, R. Umer, K. A. Khan, and W. J. Cantwell, "XCT-scan assisted flow path analysis and permeability prediction of a 3D woven fabric," *Composites Part B: Engineering*, vol. 176, p. 107320, 2019.

[52] W. Huang, P. Causse, H. Hu, and F. Trochu, "Numerical and experimental investigation of saturated transverse permeability of 2D woven glass fabrics based on material twins," *Polymer Composites*, vol. 41, no. 4, pp. 1341–1355, 2020.

CHAPTER 7 ARTICLE 4 : TRANSVERSE COMPACTION OF 2D GLASS WOVEN FABRICS BASED ON MATERIAL TWINS – PART II: TOW AND FABRIC DEFORMATIONS

W. Huang, P. Causse, H. Hu*, S. Belouettar, F. Trochu*

Published in *Composite Structures, Volume 237, 111963, 1 April 2020*

7.1 Chapter overview

This chapter presents the second part of the article in two parts published in *Composite Structures*, which provides an analytical tool to analyze quantitatively the mesoscopic deformation of fiber tows at the mesoscopic scale based on material twins. According to the morphological analysis of fiber deformations during compaction presented in Chapter 6, a new correlation approach was proposed to trace the motion of contour points on the surfaces of fiber tows in the material twins created at different levels of compaction. The mesoscopic deformations of fiber tows were subsequently calculated and analyzed. The effect of contact between different layers appears to be more important than the interaction between warp and weft tows in the same layer.

7.2 Abstract

In Liquid Composite Molding (LCM), compaction of the reinforcement occurs during several stages of the entire process, including before and during resin injection, which leads to significant deformations of fibrous architecture. This article aims to study by X-ray microtomography the mesoscopic deformations of 2D glass woven fabrics under transverse compaction for a range of fiber volume fractions encountered in high performance composite applications. In Part I, material twin geometric models of dry fibrous reinforcements were created at different levels of compaction to study the evolution of the morphological features and displacements of fiber tows when compressed during processing. Part II proposes a new approach to track the motion of contour points on cross-sections of fiber tows during compaction. This will allow investigating more precisely the behavior of fiber tows by calculating their mesoscopic deformations. In particular, it will also be possible to study in more details the effect of contacts between tows and of nesting between fabric plies on the mesoscopic deformations of textile preforms during compression.

7.3 Introduction

In Part I, material twin geometric models were generated from microtomographic images at different levels of compaction and statistical analyses were carried out to evaluate quantitatively the evolution of the morphological features and displacements of fiber tows when compressed during processing. Material twins are geometric models of continuous fiber composites different from those created in other studies [1–6] which describe only the mesoporous structure of fibrous reinforcements with unseparated fiber tows. Those models remain qualitative and hence of limited interest, because the modifications of fiber architecture during compaction cannot be predicted. However, in material twins, the fiber tows of textile preforms are identified and individually labeled. This allows studying the mesoscopic deformations of fiber architecture under compaction. Note that these models turned out also to be effective in predicting the saturated transverse permeability of 2D woven fabrics [7].

One difficulty to assess material deformation by image analysis is to correlate the displacements of material points on the images at different stages of deformation. Digital Image Correlation (DIC) and Digital Volume Correlation (DVC) have been applied to process the images obtained by various observation techniques to analyze material deformations [8–14]. These approaches were developed to analyze pixel or voxel data from a series of digital images and have proved to be accurate and widely applied in mechanical analyses at the macroscopic scale. However, applications to composites at the mesoscopic or microscopic scales started only a few years [8, 12–14]. Compared with analysis at the macroscopic scale, more random noise arises in the images obtained from microtomographic scans. This leads to difficulties in accurately correlating the points on the images before and after deformation by using DIC or DVC, which may affect the quality of results.

The material twins generated from microtomographic images don't contain only raw voxel information, since tows are identified and labeled, they also provide a detailed mesostructural geometric model of fiber architecture with enhanced predictive capability compared to purely mesoporous models, in which only the mesopores are modeled. The first goal of Part II is to propose in Section 7.4 a new correlation technique to track the motion of contour points on cross-sections of fiber tows during compaction. This approach is not based on pixel intensity, thus the accuracy is not significantly affected by the noise induced during microtomographic scans. In Section 7.5, material twins allow evaluating quantitatively the mesoscopic deformations of fiber tows. In section 7.6, the proposed approach is used to study in more details the effect of contacts between tows and of nesting between fabric layers.

7.4 Approach to calculate the deformation of fiber tows

The evolution of the geometric features of fiber tows during compaction was investigated for four typical cross-sections in Part I. However, this kind of morphological analysis, although it provides a better understanding of deformations under compaction, remains qualitative and hence its predictive capability is limited. In this section, a new approach is proposed to determine the displacements of contour points in the cross-sections of fiber tows at different levels of compaction. This allows subsequently calculating the deformations of fiber tows.

7.4.1 Correlation of contour points

Figure 7.1 shows the schematics of correlating contour points at different levels of compaction. Suppose that a rectangle of width W_1 and height H_1 is compressed into a rectangle of width W_2 and height H_2, whose left top corner (the red point) is the contour point of the tow to be tracked. The angle coordinate is defined as the angle between the horizontal axis and the line connecting the contour point and the centroid (blue point). This angle decreases with compaction ($\theta_1 > \theta_2$), thus the angle coordinate cannot be directly used to correlate the points. However, by scaling the rectangles at these two stages of compaction to a same unit square, the angle coordinates θ_1 and θ_2 are both converted to θ_3. Then the contour points on the edges of the two scaled rectangles are numbered according to their respective positions. For example, the points in the left corners are numbered as the first correlated points, then the edges are divided into several parts and all the points can be numbered in order. Therefore, contour points having the same normalized angle coordinates during compaction will be correlated. Note that the scaling procedure is just used here to correlate the contour points. Thus, the calculation of displacements presented in the following sections is based on original cross-sections.

Note that the rectangle shape of cross section is presented in Figure 7.1 solely as an illustration, in order to provide a clearer description of the method. In fact, such approach is equally applicable to any arbitrary section. This approach ignores the possible rotation of contours in cross-sections orthogonal to the fiber direction. This may be considered as acceptable, because the maximum rotation of the cross-sections was found in Part I not to exceed 4 degrees. If the rotation is larger, taking into account the rotation of each cross-section in the morphological analysis is possible and would give a more precise correlation.

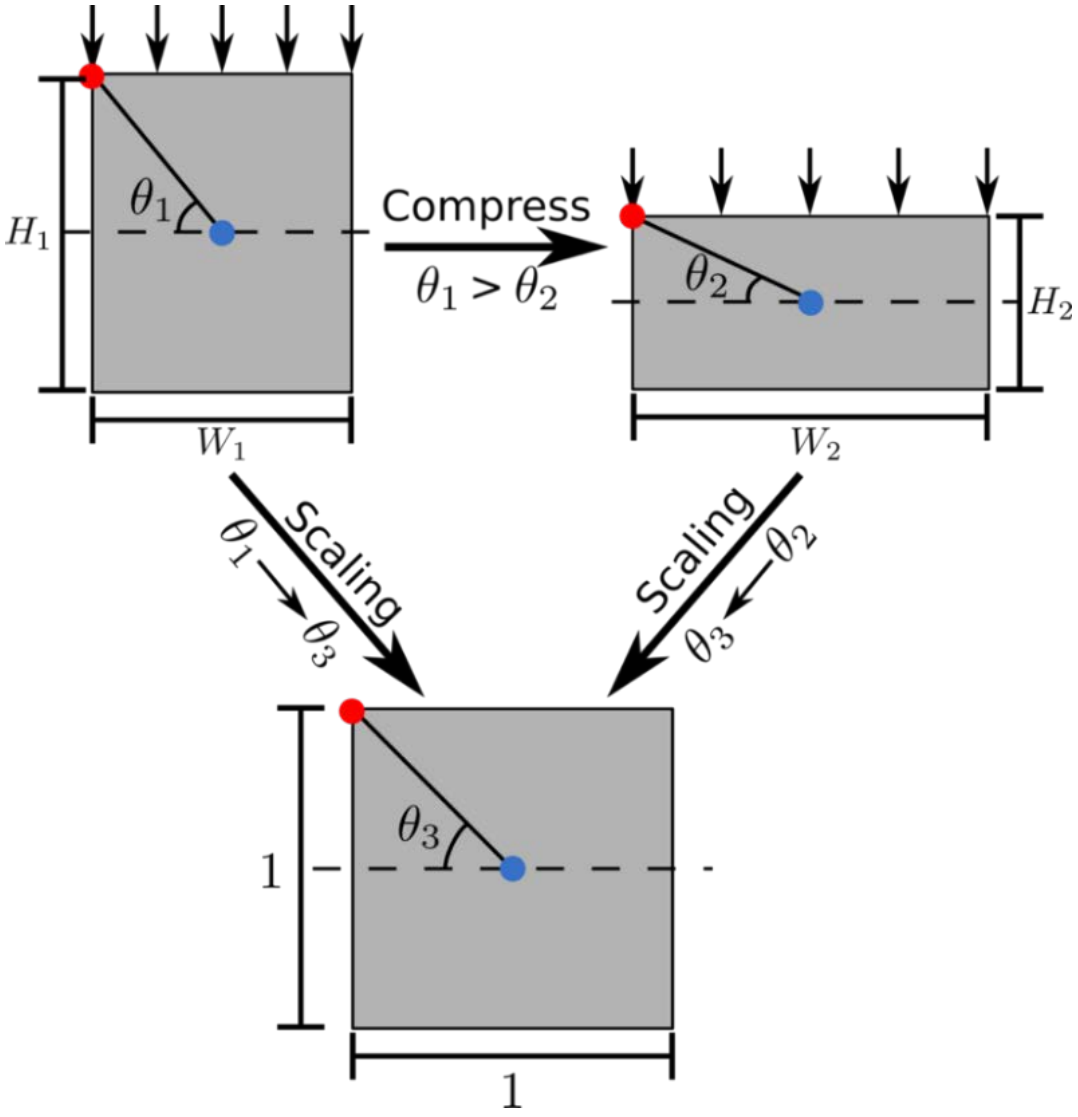

Figure 7.1 Schematics of correlating contour points at different levels of compaction

7.4.2 Displacement of contour points

After correlating contour points for different levels of compaction, their displacements can be tracked. As mentioned in Part I, both rigid movements of tows and relative displacements of contour points occur during compaction. Considering that the deformation of cross-sections only depends on the relative displacements of contour points, rigid movements of tows can be eliminated. Therefore, relative displacements may be calculated as follows:

1. Compare the positions of correlated points on the contours at different stages of compaction and calculate the absolute displacement U_a of a contour point.
2. Compare the positions of centroids at different stages of compaction and calculate the rigid displacement U_r of the contour.
3. Subtract the rigid displacement U_r from the absolute displacement U_a to obtain the relative displacement U of contour points.

Figure 7.2 presents three scaled contours with several correlated points at different levels of compaction. All the centroids of the contours are located at the origin (0,0) to eliminate rigid displacements. The displacements of correlated points are indicated by red arrows. In the upper right part of the tow boundary, contour points move towards the centroid, while contour points in the lower right part move outwards.

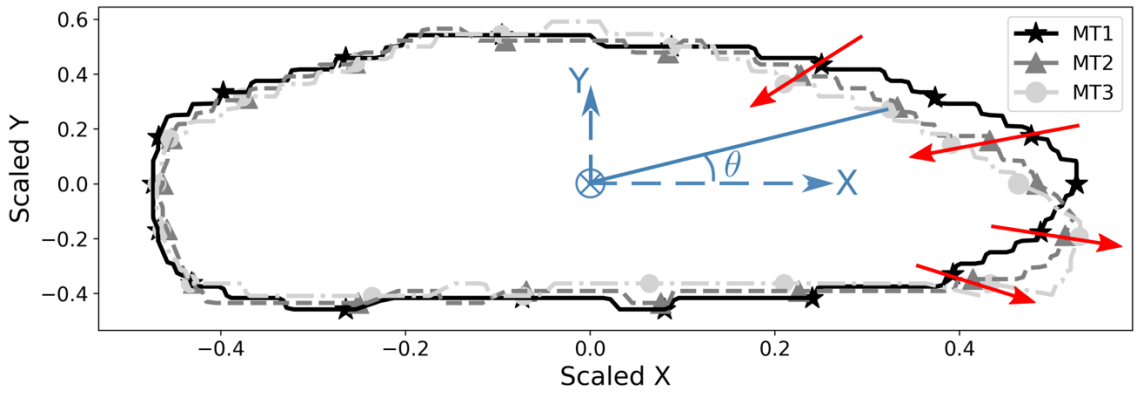

Figure 7.2 Scaled contours of one cross-section at three compaction levels. The relative movements of contour points during compaction are illustrated by red arrows. The angle coordinate θ of one contour point in MT3 is also represented in the figure.

Before calculating the deformations of fiber tows, the global and local coordinate systems need to be introduced. In Figure 7.3a, the global coordinate system (x, y, z) is presented in the lower left and the local coordinate systems (X, Y, Z) of the weft and warp tows are

plotted in red and yellow respectively. The $X-Y$ plane defines the cross-section of the fiber tow orthogonal to the Z axis in the fiber direction.

Since the deformations of fiber tows are calculated in their cross-sections, defining the displacements of contour points with respect to a local coordinate system is more appropriate for the following deformation analysis. As illustrated in Figure 7.3b, the displacements along the local coordinate axes X, Y are defined as the positive horizontal and vertical displacements U_X and U_Y respectively. Note that only the displacements of the contour points on the tow surfaces are calculated. In order to calculate the points inside the fiber tows, the method needs to be further developed.

Considering that the shape of the cross-sections of fiber tows are close to ellipse and the centroid lines of the fiber tows have been already obtained in Part I, it is more proper to describe the deformation of fiber tows under the polar coordinate system for 2D cases or the cylindrical coordinate system for 3D cases. Therefore, the radial displacement U_ρ on the contour is used to describe the local expansion or compression of the fiber tow, which is calculated based on the horizontal and vertical displacements U_X and U_Y as shown in Figure 7.3b:

$$U_\rho = U_X cos\theta + U_Y sin\theta \tag{7.1}$$

To accurately describe the deformation of fiber tows, scaled contours are equally divided by 360 points, with one contour point chosen for each degree of the angle coordinate θ. The relative radial displacement U_ρ is calculated for each point as presented in Figure 7.4 for typical weft tow in MT3. Because the material twins are low resolution voxel models generated from microtomographic images, the contours are not perfectly smooth. This explains the oscillation of the original displacement data in Figure 7.4. Therefore the displacements are smoothed in this figure by Savitzky-Golay filter [15].

As shown in Figure 7.4, there are two zones clearly presenting negative radial displacement, namely around $\theta = 90°$ and $\theta = 270°$. This means that the top and bottom parts of the cross-section are highly compressed. Meanwhile, on the sides of these two compressed zones, positive displacements appear, indicating that fiber tows tend to expand along the radial direction in these regions.

7.4.3 Deformation of fiber tows

The proposed approach allows calculating the displacements of contour points for all the cross-sections of the fiber tow. So the displacement fields of the fiber tow can be obtained as illustrated in Figure 7.5. Although the displacements are calculated for each cross-section, the

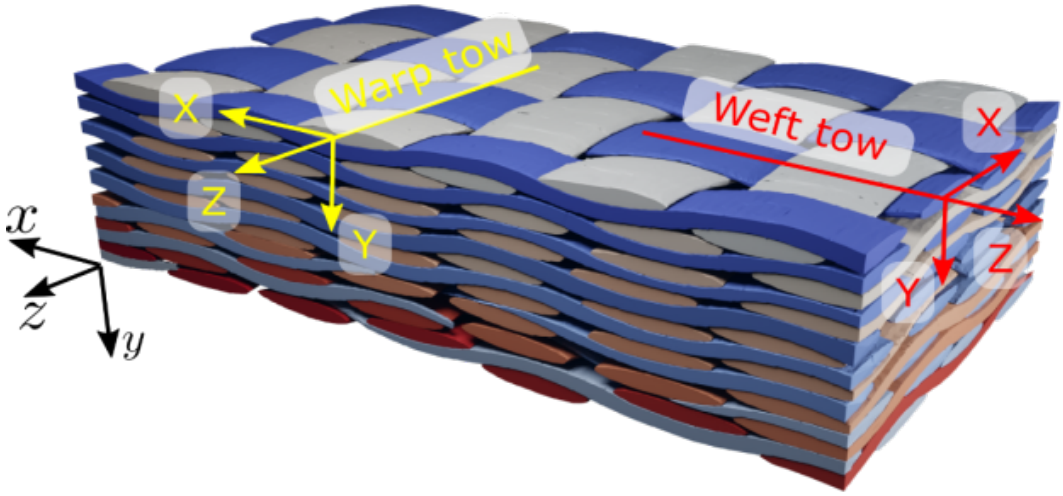

(a) Global and local coordinate systems

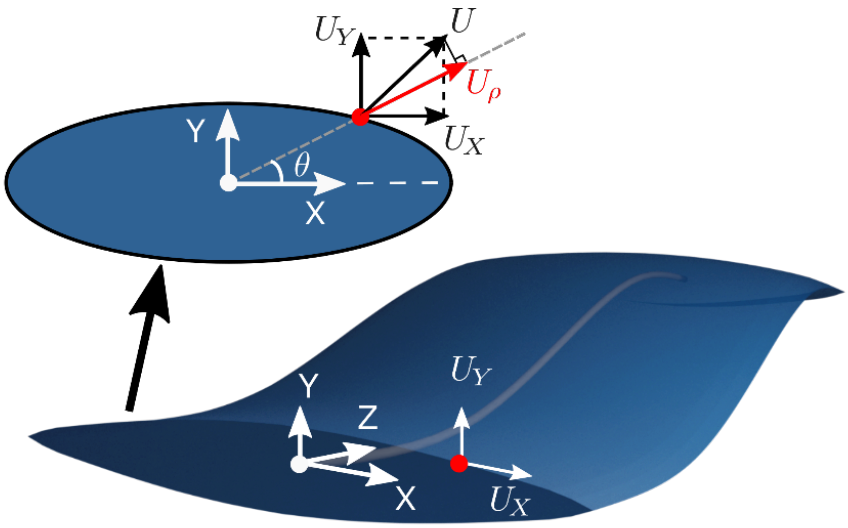

(b) Positive horizontal and vertical displacements of contour points

Figure 7.3 (a) The global coordinate system (x, y, z) is defined on the lower left side, and the local coordinate systems (X, Y, Z) of the weft and warp tows are represented in red and yellow respectively; (b) positive displacements of a contour point with respect to the local coordinates

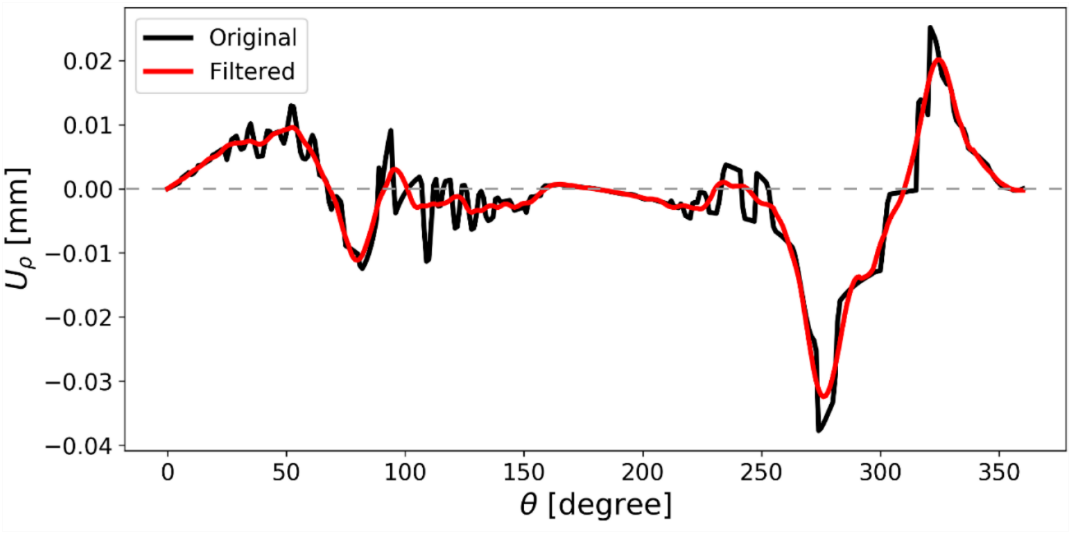

Figure 7.4 Relative radial displacement U_ρ of contour points in a weft tow for the third compaction level considered in Figure 6.1 of Part I (MT3)

displacement fields remain smooth along the fiber tow. This results from the material twin generated by dual kriging interpolation [16] and the iterative expansion approach proposed in [17]. Besides, as presented by Madra et al. [18], the surface of fiber tows can be further smoothed by introducing the nugget effect into kriging, which could improve the smoothing accuracy of calculations.

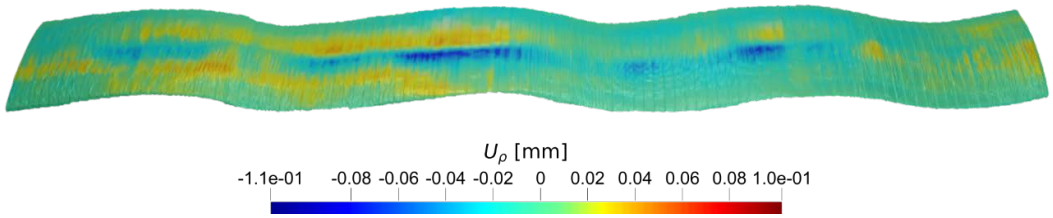

Figure 7.5 Relative radial displacement fields of a weft tow for the third compaction level considered in Figure 6.1 of Part I(MT3)

Note that the accuracy of Micro-CT AGM [17] is evaluated with respect to the resolution of the microtomographic scan. In other words, for a certain scanning resolution, this approach, together with the multiple factor morphological criterion introduced in [17], gives a material twin of relatively high accuracy. However, the accuracy of the deformation calculated by material twins relies on the scan resolution. A more accurate reconstruction of the contour can be obtained at higher resolution. This could be recommended when generating the material twins for the deformation analysis. However, if the resolution is too high, the

geometric dimensions of scanned samples will be restrained, hence probably too small to reflect material variability. Optimizing the scan resolution to keep both the absolute accuracy of the reconstructed model, while remaining representative of material variability, could be a topic of future work.

7.4.4 Evolution of the deformations in fiber tows

In this work, we are only interested in the deformation induced during transverse compaction, thus the mesostructural model MT1 considered in Figure 6.1 of Part I, for which nearly no transverse compression is applied on the fabric stack, is considered as a reference with zero deformation. Therefore, only the deformations of MT2 and MT3 will be analyzed. In order to observe the evolution of deformations, the relative displacement field of one weft tow is presented in Figure 7.6 with the same scale bar at different compaction levels. Several zones of the MT2 tow show slightly compressed deformations, which become more severe in MT3. Note that there is no obvious incorrect zone in the result (for example a compressed region in MT2 that would suddenly change to an expansion zone in MT3) even though the displacements of the two models were computed independently. Such consistency suggests that the evolution of the displacement with different compaction levels is well described by the proposed method.

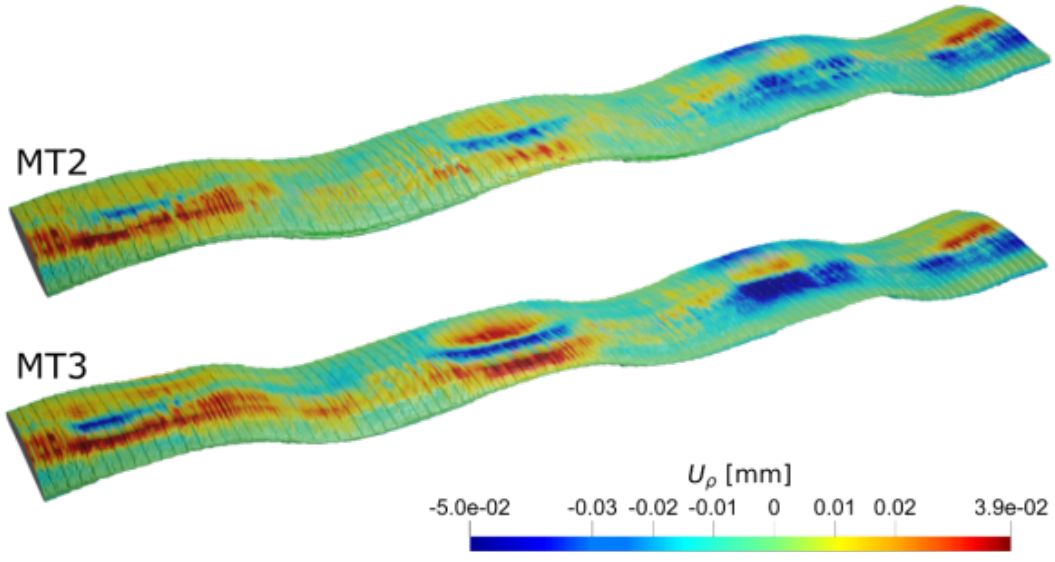

Figure 7.6 Evolution of the relative radial displacement fields of a weft tow during compaction

During sample preparation, the different layers were positioned as carefully as possible.

Therefore, without considering nesting between fabric layers, the fiber tows in neighboring layers are in contact at the crests or troughs. This explains why significant displacement mainly appears at the crests and troughs of the fiber tow (but not necessarily all), which is similar to the fiber tow presented in Figure 7.5.

The compression zones are mainly located at the center part of the surface along the fiber tow, while the expansion appears at their sides. The reason might be that the fiber tow is a bundle of fiber filaments, thus during transverse compaction, the filaments of the fiber tow are rearranged and squeezed to accommodate the compression at the microscopic scale [19, 20]. As a result, the fiber tow deforms at the mesoscopic scale in the contact zones with other tows. Some fibers near the highly compressed zones move in horizontal direction, leading to an expansion in the vicinity of the contact areas.

The fiber tow also should expand in the horizontal direction at the edges due to the Poisson effect. However, because fiber tows remain in contact with each other, the displacement is restrained at the horizontal edges. Thus, the contact between fiber tows has an influence on the deformation of the entire mesostructure. This will be further discussed Section 7.6.

7.5 Deformation of the fabric stack

In this section, the above-proposed approach is implemented to calculate the deformations of all the fiber tows in the fabric stack. The radial displacement fields of MT2 and MT3 are presented in Figure 7.7a and b, while their expanded views are displayed in Figure 7.7c and d separately. In each layer, the deformation exhibits strong local effects, which means that the displacement field of fiber tows is not uniform. Overall, the behavior previously discussed is visible in most of the tows. Compressed zones generally exist in the middle on the fiber bundles and are surrounded by regions of slight expansion. However, the intensity of this phenomenon can vary greatly along the fiber tow and between different tows. For example, for the first ply, the fiber tows on the right part severely deform under compression, compared to the ones on the left part. Therefore, the deformation distribution (linked to the pressure distribution) is not uniform in the layer. This kind of in-plane local effects are also different between layers, namely not all the fiber tows at the right part deforms severely for each layer. For example, for the fifth and sixth plies, the fiber tows located in the center of the stack exhibit the most significant deformations.

Comparing the deformation of the fiber tows in different layers, the fiber tows in the first, fifth and sixth plies deforms more severely than the tows in other layers. These differences in the deformation distribution strongly suggest that the pressure distribution differs between

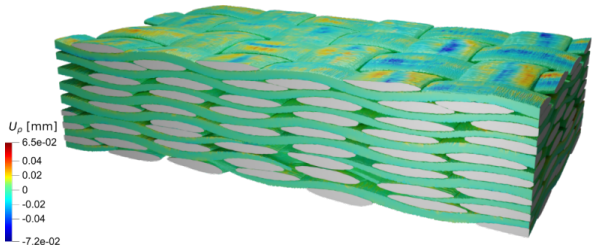

(a) Relative radial displacement U_ρ of MT2

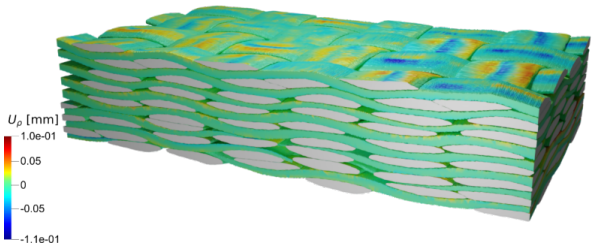

(b) Relative radial displacement U_ρ of MT3

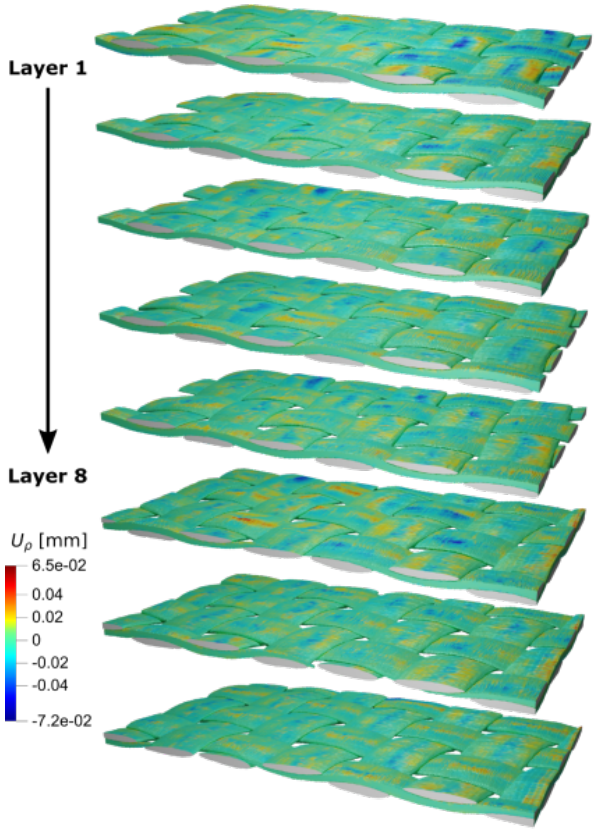

(c) Expanded view of relative radial displacement U_ρ of MT2

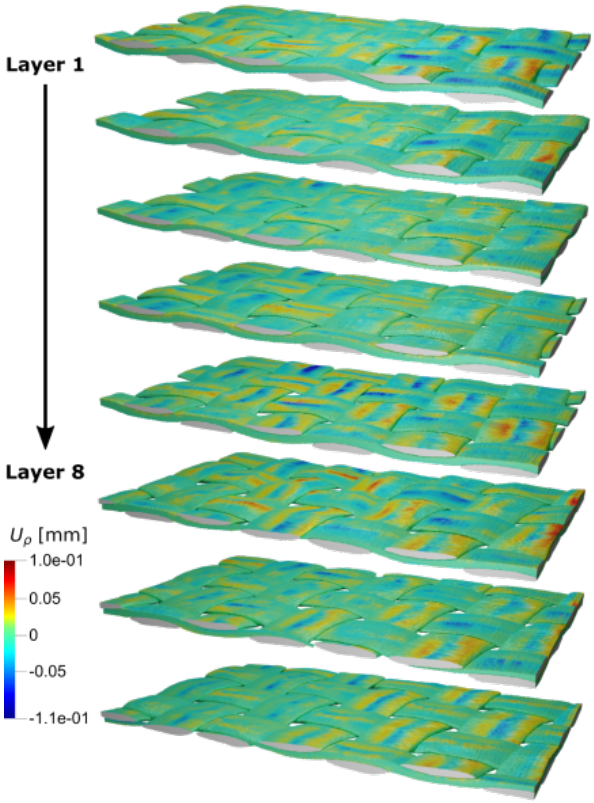

(d) Expanded view of relative radial displacement U_ρ of MT3

Figure 7.7 Relative radial displacements of contour points in the weft and warp tows of the middle eight layers of the two material twins MT2 and MT3 considered in Figure 6.1 of Part I

the layers. The local effects in the layer and the differences between the layers illustrate the material variability of real fabrics, a typical result obtained with material twins. They are induced by many factors, and the contact between fiber tows might be one of the most essential reasons. This effect will be studied in details in the following section.

7.6 Effect of contacts between tows on fiber deformation

In order to analyze the effect of contacts between fiber tows and of nesting between fabric layers, two sets of fabric layers are specifically studied in the material twins, namely layers 2 and 3, and layers 5 and 6. As shown in Figure 7.8a and b, layers 3 and 6 were analyzed and their deformations calculated, while layers 2 and 5 are the top layers which were considered to illustrate the contact between fiber tows. As discussed in [7] and illustrated in Figure 7.8b, although during sample preparation, the different layers were positioned as carefully as possible, the orientation of fibers cannot be perfectly controlled, significant nesting occurs between layers 5 and 6. This leads to the contact between fiber tows being rather complex. On the other hand, the fiber tows in layers 2 and 3 display basically the same orientation and are well aligned so that nearly no nesting exists between these two fabric layers. In this section, the selected examples will be used to analyze the effect of contact and nesting on the deformation of fiber tows.

Considering that the warp and weft tows of the 2D woven fabrics studied in this article have similar geometric features, only the deformations of the warp tows of layer 3 (the analyzed layer in Figure 7.8a) are analyzed and presented in Figure 7.9. Since nearly no nesting exists between the layers 2 and 3, the warp tows of layer 3 are only in contact with the weft tows of the layers 2 and 3. Therefore, the warp tows of layer 2 (the top layer in Figure 7.8a) are not considered. The transparent blue and brown tows are the weft tows in the analyzed layer and the top layer respectively, which corresponds to the layer colors of Figure 7.8. The blue or red rectangles are displayed in Figure 7.9 as examples to emphasize the zones with most significant deformation that are respectively in contact with the weft tows of the same layer and the ones of the top layer.

The compressive radial deformation U_ρ occurs in regions of the tow where contact exists with the other tows. Moreover, the compressive deformations where warp tows are in contact with weft tows in the top layer are more severe than the parts in contact with the ones in the same layer. In the studied domain, around six zones are compressed by the weft tows in the top layer to deform more severely than -0.08 mm, while only two zones deform significantly by the compression of the weft tows in the same layer. This suggests that the compression transferred between fabric layers is larger than the one transferred between fiber tows in the

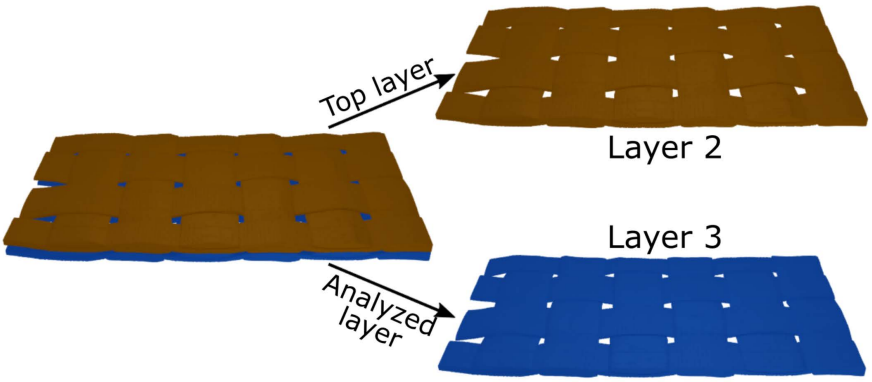

(a) Fabric layers 2 and 3

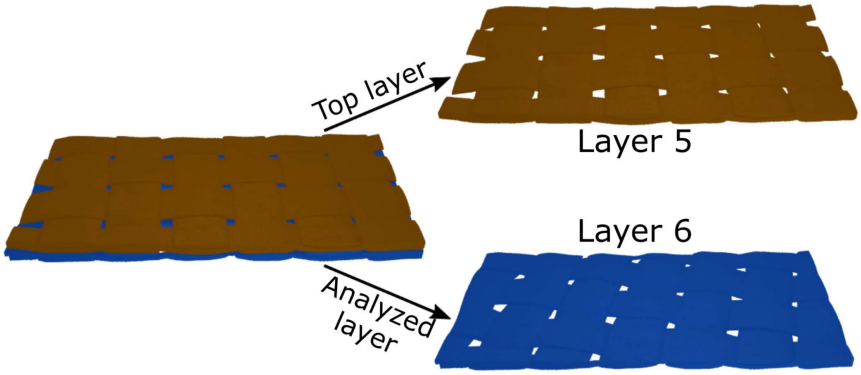

(b) Fabric layers 5 and 6

Figure 7.8 Four layers are studied to analyze the effect of contacts between tows on the local deformations of fiber bundles

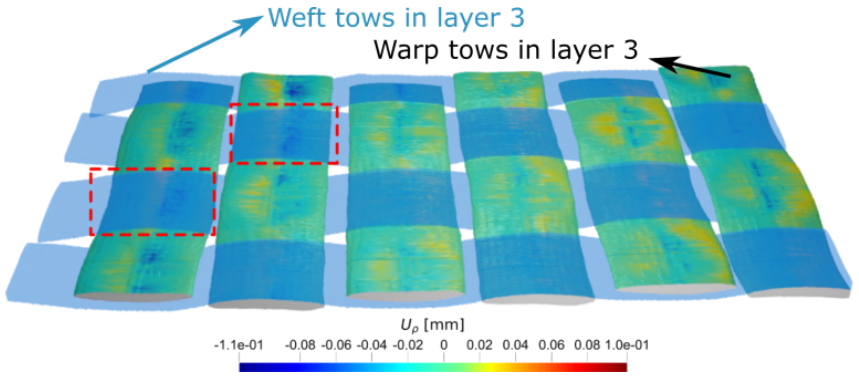

(a)

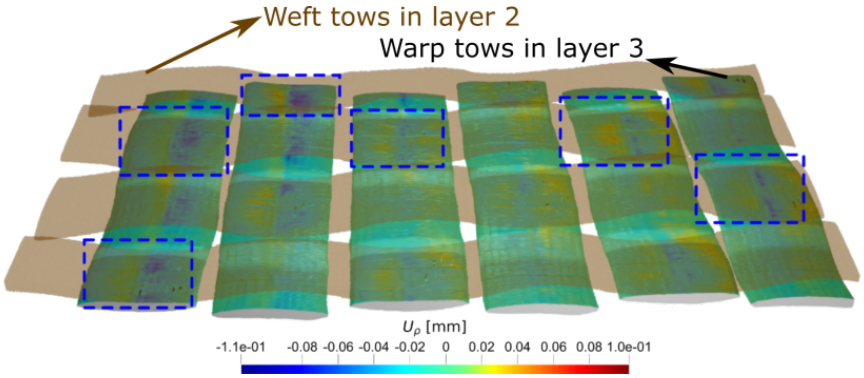

(b)

Figure 7.9 Effect of contacts between fiber tows on the deformations of warp tows in layer 3

same layer. Similar observations exist in the warp tows of layer 6 as illustrated in Figure 7.10, in which there are more zones deforming severely by the contact with tows located in layer 5.

Since significant nesting exists between layers 5 and 6, while no nesting occurs between layers 3 and 4, the distribution of the compressive radial deformation in layer 6 is quite different from the one in layer 3. Most zones of the warp tows of layer 3 are in contact with the weft tows of layer 2 as shown in Figure 7.9, thus the middle parts of the surfaces of the warp tows are compressed to deform in vertical direction. The warp tows of layer 6 are in contact with both the warp and weft tows in layer 5 due to the nesting. As illustrated in the zoomed views of Figure 7.10c, the warp tows of the layer 5 compress the warp tows of layer 6 at many regions. Therefore, the compressive radial deformation is no longer located in the middle of the surface, but in any zones of the warp tows in contact with other tows. By comparing the displacement distributions in Figure 7.9 and Figure 7.10, it can be concluded that the nesting between fabric layers leads to more complex contact between fiber tows, which further determines the different deformation distributions in fabric layers. This might be one of the sources of variability in transverse compressibility measurements using a stack of fabrics, since the orientation of fibers cannot be perfectly controlled during the measurements, resulting in nesting between fabric layers.

7.7 Conclusion

In this study, the mesoscopic deformations of 2D glass woven fabrics under transverse compaction was analyzed by X-ray microtomography. Material twins are created by Micro-CT AGM [17], a recently proposed technique from microtomographic images of the fabric stack at different levels of compaction [7]. In Part II, a new approach was proposed to track the movements of contour points on the surfaces of fiber tows at different levels of compaction. The mesoscopic deformations of fiber tows were subsequently calculated and analyzed.

Overall, the analyses show a general pattern for fiber tow deformation during compaction with compression in the contact regions and expansion of the fiber tows near the contacting zones. Moreover, the effect of contact between different layers appears to be more important than the interaction between warp and weft tows located in the same layer. This suggests than the forces transferred inside one ply and between layers are different during transverse compaction of 2D woven fabrics. However, the results are strongly affected by the material variability at different scales: within the same fiber tow, between different tows and between different layers. The effects of contacts between fiber tows are notably highly influenced by the nesting of adjacent fabric layers. This consequently affects the mechanical behavior of fabrics

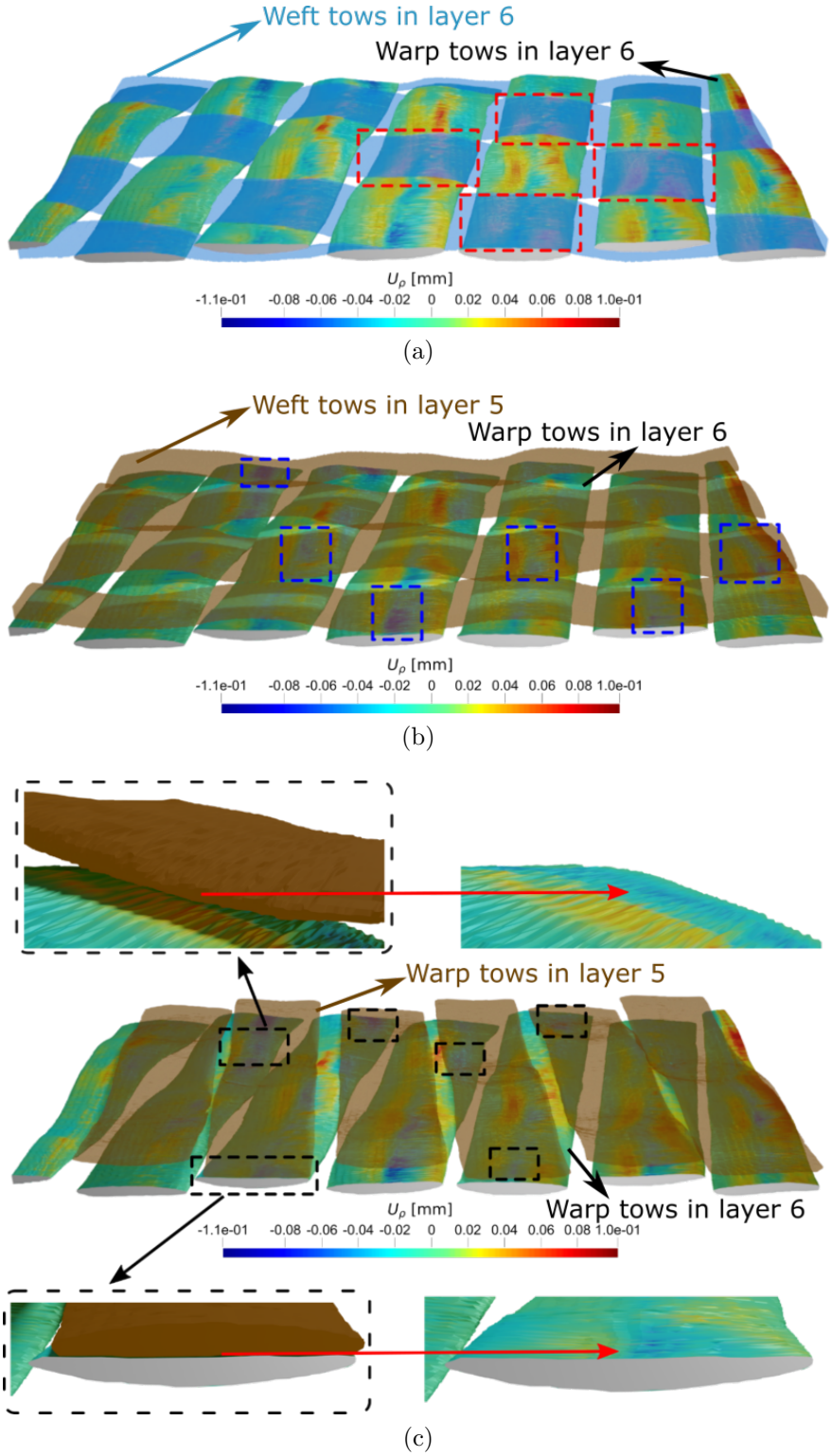

Figure 7.10 Effect of contacts between fiber tows on the deformations of warp tows in layer 6. The zoomed views in (c) illustrate contacts between the warp tows of layers 5 and 6

and might explain the high variability encountered in measurement results of transverse compressibility as it is difficult to control nesting during this kind of test.

The accuracy of tow deformations is affected by several factors such as the scan resolution, the errors induced by microtomography and the post-processing procedure used to evaluate the deformations of fiber tows. In order to get more accurate mesoscopic deformations, the related parameters and procedures need to be optimized. Comparing the results presented here with those obtained from DIC or DVC would be a meaningful future work. It would be also of great interest to compare the experimental deformations with numerical predictions. By combining material twins with multiscale models (see references [21–24] for example), applying appropriate techniques to smoothen and mesh the fiber tows with reasonable number of elements [25] and considering the compression of fiber filaments at the microscopic scale [19], computer simulations of transverse compaction taking into account the dual-scale architecture of fibrous reinforcements could be carried out.

7.8 Acknowledgements

This work has been supported by the Department of Mechanical Engineering of Polytechnique Montreal, by a Discovery Grant of the National Science & Engineering Research Council of Canada (NSERC) and by grants of the National Natural Science Foundation of China (11920101002, 11372231 and 11772238). Authors also acknowledge the contributions of the Research Center for High Performance Polymer and Composite Systems (CREPEC), the "Fonds de recherche du Québec - Nature et technologies" (FRQNT) and the "Fonds National de la Recherche" (FNR) of Luxembourg. Authors would also like to thank Nicolas Juillard from Texonic for providing the fibrous reinforcements and Professor Vladimir Brailovski for access to the X-ray microtomograph at École de technologie supérieure (ETS), Montreal.

Bibliography

[1] M. A. Ali, R. Umer, K. A. Khan, S. Bickerton, and W. J. Cantwell, "Non-destructive evaluation of through-thickness permeability in 3D woven fabrics for composite fan blade applications," *Aerospace Science and Technology*, vol. 82-83, pp. 520–533, 2018.

[2] M. A. Ali, R. Umer, K. A. Khan, and W. J. Cantwell, "In-plane virtual permeability characterization of 3D woven fabrics using a hybrid experimental and numerical approach," *Composites Science and Technology*, vol. 173, pp. 99–109, 2019.

[3] M. A. Ali, R. Umer, K. A. Khan, and W. J. Cantwell, "XCT-scan assisted flow path analysis and permeability prediction of a 3D woven fabric," *Composites Part B: Engineering*, vol. 176, p. 107320, 2019.

[4] J. S. U. Schell, M. Renggli, G. H. van Lenthe, R. Müller, and P. Ermanni, "Micro-computed tomography determination of glass fibre reinforced polymer meso-structure," *Composites Science and Technology*, vol. 66, no. 13, pp. 2016–2022, 2006.

[5] J. S. U. Schell, M. Deleglise, C. Binetruy, P. Krawczak, and P. Ermanni, "Numerical prediction and experimental characterisation of meso-scale-voids in liquid composite moulding," *Composites Part A: Applied Science and Manufacturing*, vol. 38, no. 12, pp. 2460–2470, 2007.

[6] A. S. Dharmalingam, J. Hemmer, A. S. Lectez, C. Binetruy, and S. Comas-Cardona, "Evolution of single carbon and glass fibrous tow cross-sections in dry and lubricated states during compaction perpendicular to the fibers," *Composites Part B: Engineering*, vol. 148, pp. 235–242, 2018.

[7] W. Huang, P. Causse, H. Hu, and F. Trochu, "Numerical and experimental investigation of saturated transverse permeability of 2D woven glass fabrics based on material twins," *Polymer Composites*, vol. 41, no. 4, pp. 1341–1355, 2020.

[8] A. Mendoza, J. Schneider, E. Parra, E. Obert, and S. Roux, "Differentiating 3D textile composites: A novel field of application for Digital Volume Correlation," *Composite Structures*, vol. 208, pp. 735–743, 2019.

[9] B. Koohbor, S. Mallon, A. Kidane, and M. A. Sutton, "A DIC-based study of in-plane mechanical response and fracture of orthotropic carbon fiber reinforced composite," *Composites Part B: Engineering*, vol. 66, pp. 388–399, 2014.

[10] M. Mehdikhani, E. Steensels, A. Standaert, K. A. M. Vallons, L. Gorbatikh, and S. V. Lomov, "Multi-scale digital image correlation for detection and quantification of matrix cracks in carbon fiber composite laminates in the absence and presence of voids controlled by the cure cycle," *Composites Part B: Engineering*, vol. 154, pp. 138–147, 2018.

[11] M. Tekieli, S. De Santis, G. de Felice, A. Kwiecień, and F. Roscini, "Application of Digital Image Correlation to composite reinforcements testing," *Composite Structures*, vol. 160, pp. 670–688, 2017.

[12] B. Croom, W. M. Wang, J. Li, and X. Li, "Unveiling 3D deformations in polymer composites by coupled micro x-ray computed tomography and volumetric digital image correlation," *Experimental Mechanics*, vol. 56, no. 6, pp. 999–1016, 2016.

[13] A. Mendoza, J. Schneider, E. Parra, and S. Roux, "Measuring yarn deformations induced by the manufacturing process of woven composites," *Composites Part A: Applied Science and Manufacturing*, vol. 120, pp. 127–139, 2019.

[14] A. Mendoza, J. Schneider, E. Parra, and S. Roux, "The correlation framework: bridging the gap between modeling and analysis for 3D woven composites," *Composite Structures*, vol. 229, p. 111468, 2019.

[15] A. Savitzky and M. J. E. Golay, "Smoothing and differentiation of data by simplified least squares procedures." *Analytical Chemistry*, vol. 36, no. 8, pp. 1627–1639, 1964.

[16] F. Trochu, "A contouring program based on dual kriging interpolation," *Engineering with Computers*, vol. 9, no. 3, pp. 160–177, 1993.

[17] W. Huang, P. Causse, V. Brailovski, H. Hu, and F. Trochu, "Reconstruction of mesostructural material twin models of engineering textiles based on Micro-CT Aided Geometric Modeling," *Composites Part A: Applied Science and Manufacturing*, vol. 124, p. 105481, 2019.

[18] A. Madra, P. Breitkopf, A. Rassineux, and F. Trochu, "Image-based model reconstruction and meshing of woven reinforcements in composites," *International Journal for Numerical Methods in Engineering*, vol. 112, no. 9, pp. 1235–1252, 2017.

[19] P. Latil, L. Orgéas, C. Geindreau, P. J. J. Dumont, and S. R. Du Roscoat, "Towards the 3D in situ characterisation of deformation micro-mechanisms within a compressed bundle of fibres," *Composites Science and Technology*, vol. 71, no. 4, pp. 480–488, 2011.

[20] H. Ghayoor, S. V. Hoa, and C. C. Marsden, "A micromechanical study of stress concentrations in composites," *Composites Part B: Engineering*, vol. 132, pp. 115–124, 2018.

[21] R. Xu, Y. Hui, H. Hu, Q. Huang, H. Zahrouni, T. B. Zineb, and M. Potier-Ferry, "A Fourier-related FE^2 multiscale model for instability phenomena of long fiber reinforced materials," *Composite Structures*, vol. 211, pp. 530–539, 2019.

[22] J. Yang, R. Xu, H. Hu, Q. Huang, and W. Huang, "Structural-Genome-Driven computing for composite structures," *Composite Structures*, vol. 215, pp. 446–453, 2019.

[23] M. El Hachemi, Y. Koutsawa, H. Nasser, G. Giunta, A. Daouadji, E. M. Daya, and S. Belouettar, "An intuitive computational multi-scale methodology and tool for the dynamic modelling of viscoelastic composites and structures," *Composite Structures*, vol. 144, pp. 131–137, 2016.

[24] Z. Ullah, X. Y. Zhou, L. Kaczmarczyk, E. Archer, A. McIlhagger, and E. Harkin-Jones, "A unified framework for the multi-scale computational homogenisation of 3D-textile composites," *Composites Part B: Engineering*, vol. 167, pp. 582–598, 2019.

[25] W. Wijaya, M. A. Ali, R. Umer, K. A. Khan, P. A. Kelly, and S. Bickerton, "An automatic methodology to CT-scans of 2D woven textile fabrics to structured finite element and voxel meshes," *Composites Part A: Applied Science and Manufacturing*, vol. 125, p. 105561, 2019.

CHAPTER 8 ARTICLE 5 : A FOURIER BASED REDUCED MODEL FOR WRINKLING ANALYSIS OF CIRCULAR MEMBRANES

W. Huang, Q. Huang, Y. Liu, J. Yang, H. Hu*, F. Trochu, P. Causse

Published in *Computer Methods in Applied Mechanics and Engineering, Volume 345, 1114-1137, 1 March 2019*

8.1 Chapter overview

In Chapters 4 to 7, experimental approaches and numerical tools were developed to study the mechanical and flow properties of fibrous reinforcements based on material twins. One objective of the thesis is to provide tools to study the possible defects in composite parts manufactured by LCM processes using deformable membranes (such as VARTM and FI). Thus besides the factors related to fiber architecture, process related issues also need to be considered. As mentioned in Section 1.2.3, both local and global wrinkling phenomena might appear in VARTM and FI processes. This chapter presents the article published in *Computer Methods in Applied Mechanics and Engineering*, which introduces the development of the Fourier based reduced model for the wrinkling analysis of circular membranes. The efficiency and accuracy of this approach is verified by comparing the numerical simulations with calculations carried out with ABAQUS. Besides, several wrinkling problems in circular membranes under different loads are also discussed to reveal the mechanisms of wrinkling. This article enriches the family of the Fourier-based reduced models, which provides an efficient way to study wrinkling problems in the deformable membranes used LCM processes.

8.2 Abstract

As a soft material with an almost negligible bending stiffness, a membrane may easily lose its mechanical stability. To capture its entire instability process, intensive computation is required, especially in the case of short wave length. The objective of this paper is to construct an efficient model to simulate and study the instability phenomena of circular membranes. By using the method of Fourier series with slowly variable coefficients in the circumferential direction, a new family of one-dimensional reduced finite elements are developed to study the three-dimensional problems. The nonlinear system is solved by the Asymptotic Numerical Method(ANM), which is reliable and efficient for tracing the bifurcation points and post-

buckling equilibrium path compared with other classical non-linear solution algorithms. The accuracy and efficiency of the reduced model is verified by simulating the instability phenomena in stretched annular membranes and a compressed circular plate. The relation between critical loads and bifurcation patterns and the evolution of stress components in the entire wrinkling process are discussed. This study provides new simulation schemes to explore the instability in circular membranes under complex loadings and boundary conditions.

8.3 Introduction

Membrane structures have been widely used in aerospace and civil engineering, such as solar sail, large membrane roof and wall, because of their high performance in resisting external tensional loads with much lighter weight compared with traditional structures [1]. In recent years, various kinds of membrane structures have been developed and applied in different engineering fields to meet specific requirements. For example, through mounting electronical elements on membrane structures [2], various kinds of stretchable electronics have been fabricated, including stretchable batteries [3], supercapacitors [4] and wireless epidermal sensors [5], which provide superior mechanical properties inaccessible in traditional electronics. Recent studies found wide existence of membrane structures in biological organism [6], which play essential roles in realizing specific functions, such as morphogenesis of bacterial biofilms [7], cell spreading [8], and deformation of red blood cell [9]. In some composite manufacturing processes, such as Vacuum Assisted Resin Transfer Molding (VARTM) [10–12] and Flexible Injection (FI) [13,14], membranes play a key roles in inducing the through-thickness impregnation for faster composite manufacturing process.

As a soft material with an almost negligible bending stiffness, a membrane easily loses its mechanical stability and wrinkles when subject to in-plane compressive stress. Such phenomena are widely observed both in nature and engineering. One of common example is the wrinkles emerging in the direction perpendicular to tensional direction in clamped rectangular elastic membrane [15], which can be explained by the strain incompatibility due to the Poisson effect. Additionally, as presented in Li et al. [16], membrane wrinkling can be also observed in film-substrate system.

Wrinkling can have significant effects on the mechanical and optical properties of membranes [17, 18]. This can lead to undesired problems in some engineering applications, such as the production defects in strip conveying process [19] and deep drawing process [20]. To explore the mechanism for the instability in membranes, a large amount of modeling methods have been proposed. In a pioneering work, Wagner [21] developed a tension field theory, which assumed that there was no in-plane compressive stress throughout the membrane. This

approach involves a uniaxial tension field with only one nonzero principal stress component, which is perpendicular to the wrinkled direction. To model partly wrinkled membranes, Pipkin [22] proposed a relaxed energy density to replace the strain energy function in tension field theory. This approach was then employed by Pipkin [23] to study the wrinkling of pressurized membranes. By introducing a modified deformation tensor based on a fictive non-wrinkled mode, [24] further considered the effects of large deformation and anisotropy in their model, which is capable to precisely describe the stress situation of anisotropic membrane. [25] transformed the wrinkling conditions of Roddeman [24] into a reference configuration to determine the stress state, and implemented the algorithm into a FE code for analyzing general wrinkling problem.

Although the essential reason for membrane wrinkling is the negligible bending stiffness and the in-plane compressive stress, the occurrence and evolution of the wrinkles differ among structures with different geometric shapes and materials distributions. For example, wrinkles in annular membrane usually show periodic oscillation in the circumferential direction due to its axisymmetry, while those in rectangular domain are highly dependent on specific loads and boundary conditions. The wrinkling problems in annular and circular membranes have been widely studied. Plaut [26] analyzed the large unwrinkled axisymmetric deformations of circular membranes under several different loadings using three theories, including Generalized Reissner theory, Reissner theory, Föppl-von Kármán (FvK) theory. The analytical solutions of wrinkling phenomena in annular membranes under different boundary conditions were thoroughly studied by Coman and Haughton [27], Coman [28, 29]. Géminard et al. [30] experimentally investigated the main features of wrinkles that form in a pre-stretched annular membrane under axisymmetric traction at the center. Wang et al. [31] proposed a theoretical model to predict the wrinkling and post-buckling behaviors, which is verified by experimental measurement.

Most studies mentioned above are based on analytical solutions, which correctly predict the critical wrinkling loads and modes and stress distribution before bifurcation. However, the post-buckling analysis is also very important, because it is essential to predict and control the evolution of wrinkles in its engineering application. The finite element method has been proved to be the most robust method to capture the complex evolution of wrinkles and stress distribution. For example, Argyris et al. [32] developed a TRIC (TRIangular Composite) element with aim to model post-buckling of shells based on the natural mode finite element method. Combescure [33, 34] developed a new computational scheme which permits to consider the effects of initial geometrical imperfection on the post-buckling behaviors. However, these methods either present intensive computation especially for the case with small wave length or suffer the difficulties of choosing a proper imperfection.

In order to reduce the computation for the case of small wrinkle wave length and meanwhile ease the sensitivity of post-buckling behaviors to the applied geometric imperfection, Damil and Potier-Ferry [35] proposed a reduced-order FE model based on the Fourier expansion of the displacement field. This approach showed good performance in both accuracy and efficiency for many kinds of instability problems, such as rectangular membranes [36–38], rectangular sandwich plates [39–41], and thin films on compliant substrates [42]. Besides, because the reduced model is based on the Fourier expansion, it can accurately trace the specific instability pattern without introducing imperfection in the initial model. In order to model the wrinkling phenomena of circular membranes, it is natural to consider the geometric axisymmetric property of membranes [43, 44]. However, the deformations in instability phenomena are not axisymmetric, therefore general axisymmetric elements are no longer applicable. The objective of this study is to develop a one-dimensional reduced order model based on the approach proposed by Damil and Potier-Ferry [35] to model three-dimensional wrinkling problems in circular membranes. The accuracy and efficiency of the reduced model are verified by comparing the simulation results with the ABAQUS and analytical results. Based on the modeling results of the reduced model, the instability mechanism of circular membranes for different geometries and loading conditions are thoroughly investigated. The developed model can be extended to simulate and investigate other instability phenomena in circular domain, such as wrinkling in film-substrate system [45–47], buckling of sandwich plates [48–50] or functionally graded plates [51–53].

This paper is structured as follows. In section 8.4, several basic equations are reviewed. In section 8.5, the finite element procedure is described, and the one-dimensional reduced model is constructed in cylindrical coordinates. From section 8.6 to section 8.9, the accuracy and efficiency of the reduced model are verified, and the various instability phenomena in circular domain are investigated by the reduced model. The paper ends with a discussion on main conclusions and future work.

8.4 Basic equations

As mentioned above, the bending stiffness should be taken into account to solve membrane wrinkling problems. Two types of stresses are considered including the bending stress caused by the flexion of the membrane and the membrane in-plane stress determined by the conditions of static equilibrium. Let u, v, w denote respectively the radial, circumferential and transversal components of the mid-plane displacement in cylindrical coordinates ρ ($\rho \geq 0$) and θ ($2\pi \geq \theta \geq 0$). The linear strain in the circular domain can be divided into membrane

strains ϵ_{ij}^m and bending strains ϵ_{ij}^b (see [54]):

$$\begin{aligned}
\epsilon_\rho^m &= \frac{\partial u}{\partial \rho}, && (a)\\
\epsilon_\theta^m &= \frac{1}{\rho}\left(\frac{\partial v}{\partial \theta} + u\right), && (b)\\
\epsilon_{\rho\theta}^m &= \frac{1}{2}\left[\frac{\partial v}{\partial \rho} + \frac{1}{\rho}\left(\frac{\partial u}{\partial \theta} - v\right)\right], && (c)\\
\epsilon_\rho^b &= -\frac{\partial^2 w}{\partial \rho^2}, && (d)\\
\epsilon_\theta^b &= \frac{1}{\rho^2}\left(-\frac{\partial^2 w}{\partial \theta^2} - \rho\frac{\partial w}{\partial \rho}\right), && (e)\\
\epsilon_{\rho\theta}^b &= \frac{1}{\rho^2}\left(-\rho\frac{\partial^2 w}{\partial \rho \partial \theta} + \frac{\partial w}{\partial \theta}\right). && (f)
\end{aligned} \tag{8.1}$$

Quadratic membrane strains ϵ_{ij}^q measure the variation of strain state in an infinitely small increment, and thus enable to predict buckling (see [34]). These nonlinear strains can be expressed as follows:

$$\begin{aligned}
\epsilon_\rho^q &= \frac{1}{2}\left[\left(\frac{\partial w}{\partial \rho}\right)^2 + \left(\frac{\partial u}{\partial \rho}\right)^2 + \left(\frac{\partial v}{\partial \rho}\right)^2\right], && (a)\\
\epsilon_\theta^q &= \frac{1}{2\rho^2}\left[\left(\frac{\partial w}{\partial \theta}\right)^2 + \left(\frac{\partial u}{\partial \theta} - v\right)^2 + \left(\frac{\partial v}{\partial \theta} + u\right)^2\right], && (b)\\
\epsilon_{\rho\theta}^q &= \frac{1}{2\rho}\left[\frac{\partial w}{\partial \theta}\frac{\partial w}{\partial \rho} + \frac{\partial u}{\partial \rho}\left(\frac{\partial u}{\partial \theta} - v\right) + \frac{\partial v}{\partial \rho}\left(\frac{\partial v}{\partial \theta} + u\right)\right]. && (c)
\end{aligned} \tag{8.2}$$

Instability problems in a circular domain are axisymmetric before buckling, which means the in-plane shear strain is zero and only the radial and circumferential normal strains components exist. However, when wrinkles occur, these problems are no longer axisymmetric. Thus, the in-plane shear strain should also be accounted for. The strains could be combined

as follows:

$$\begin{aligned}\{\boldsymbol{\gamma}\} &= \left\{\begin{array}{c}\epsilon_\rho\\ \epsilon_\theta\\ \gamma_{\rho\theta}\end{array}\right\} = \left\{\begin{array}{c}\epsilon_\rho^m\\ \epsilon_\theta^m\\ 2\epsilon_{\rho\theta}^m\end{array}\right\} + z\left\{\begin{array}{c}\epsilon_\rho^b\\ \epsilon_\theta^b\\ 2\epsilon_{\rho\theta}^b\end{array}\right\} + \left\{\begin{array}{c}\epsilon_\rho^q\\ \epsilon_\theta^q\\ 2\epsilon_{\rho\theta}^q\end{array}\right\}\\ &= \{\boldsymbol{\gamma}^m\} + z\{\boldsymbol{\gamma}^b\} + \{\boldsymbol{\gamma}^q\},\end{aligned} \tag{8.3}$$

In this paper, the material behavior is assumed to be linear elastic, although the methodology is also valid for nonlinear constitutive laws. The constitutive relations can be expressed as:

$$\left\{\begin{array}{l}\sigma_\rho = \dfrac{E}{1-\mu^2}\left(\epsilon_\rho + \mu\epsilon_\theta\right),\\ \sigma_\theta = \dfrac{E}{1-\mu^2}\left(\epsilon_\theta + \mu\epsilon_\rho\right),\\ \tau_{\rho\theta} = \dfrac{E}{1+\mu}\gamma_{\rho\theta},\end{array}\right. \tag{8.4}$$

where E is Young's modulus and μ is Poisson's ratio.

By combining the geometric equations (8.1) and (8.2) with the constitutive relations Eq. (8.4), the internal work of the membrane occupying the region ω can be divided into two parts, including a membrane term due to stretching and a bending contribution:

$$\left\{\begin{array}{l}\mathcal{W}_{int} = \mathcal{W}_{mem} + \mathcal{W}_{ben},\\ 2\mathcal{W}_{mem} = \displaystyle\iint_\omega \left(\langle\boldsymbol{\gamma}^m\rangle + \langle\boldsymbol{\gamma}^q\rangle\right)\left[\mathbf{L}^m\right]\left(\{\boldsymbol{\gamma}^m\} + \{\boldsymbol{\gamma}^q\}\right)\ \mathrm{d}\omega,\\ 2\mathcal{W}_{ben} = \displaystyle\iint_\omega \left\langle\boldsymbol{\gamma}^b\right\rangle\left[\mathbf{L}^b\right]\left\{\boldsymbol{\gamma}^b\right\}\ \mathrm{d}\omega,\end{array}\right. \tag{8.5}$$

in which the membrane elasticity tensor and the bending elasticity tensor are represented by the following matrices:

$$[\mathbf{L}^m] = \frac{Eh}{1-\mu^2}\begin{bmatrix}1 & \mu & 0\\ \mu & 1 & 0\\ 0 & 0 & \frac{1-\mu}{2}\end{bmatrix}, [\mathbf{L}^b] = \frac{Eh^3}{12(1-\mu^2)}\begin{bmatrix}1 & \mu & 0\\ \mu & 1 & 0\\ 0 & 0 & \frac{1-\mu}{2}\end{bmatrix}, \tag{8.6}$$

where h is the membrane thickness.

8.5 Reduced model for instability problems in circular domain

In this section, the method of Fourier series with slowly variable coefficients is briefly reviewed first. Then the finite element procedure is described to construct the one-dimensional reduced model. Finally, the nonlinear system is solved by the Asymptotic Numerical Method.

8.5.1 The method of Fourier series with slowly variable coefficients

The common instability modes observed in membranes are periodic or nearly periodic along wave length direction. To exploit this periodicity, Damil et al. [36, 37] proposed an efficient reduced model by expanding the rapidly varying displacement field of the full shell model into Fourier series and taking the slowly variable Fourier coefficients as new macroscopic unknowns [35]. For example, $\mathbf{U}(x)$ is assumed to be the vector of the unknown displacements of the full shell model in Cartesian coordinates, which rapidly varies along the x-axis. It can be transformed into the Fourier series:

$$\mathbf{U}(x) = \sum_{m=-\infty}^{+\infty} \mathbf{U}_m(x) \mathrm{e}^{\mathrm{i}mQx}, \tag{8.7}$$

where i is the imaginary unit and the Fourier coefficients $\mathbf{U}_m(x)$ denote the new macroscopic unknowns and vary slowly over a period $[x, x + 2\pi/Q]$ of oscillation with a preassigned wave number Q. At least two functions, the mean field $\mathbf{U}_0(x)$ and the envelope field of the spatial fluctuation $\mathbf{U}_{\pm 1}(x)$, are needed to describe the nearly periodic patterns of the displacement $\mathbf{U}(x)$ as suggested in [35](see Fig. 8.1).

Similar to the Fourier transformation in Cartesian coordinate system, the unknown displacement field of the circular membrane with periodic instability patterns in the circumferential direction can be expressed as follows:

$$\mathbf{U}(\rho, \theta) = \sum_{m=-\infty}^{+\infty} \mathbf{U}_m(\rho) \mathrm{e}^{\mathrm{i}mQ\theta}, \tag{8.8}$$

where Q is a preassigned integer wave-parameter($Q \in \mathbb{N}$) representing the wave number of the wrinkles in the circumferential direction. The unknown field $\mathbf{U}(\rho, \theta)$ is decoupled into $\mathbf{U}_m(\rho)$ in the radial direction and $e^{\mathrm{i}mQ\theta}$ in the circumferential direction, that is to say, the envelopes of the unknown field are independent of the angle θ and are thus axisymmetric. As a result, the original wrinkling analysis is simplified from a two dimensional problem to a one-dimensional one, where all the unknown fields are changed with the radius ρ. In this paper, only two harmonics, namely $\mathbf{U}_0(\rho)$ and $\mathbf{U}_{\pm 1}(\rho)$, are considered, which has been proved to be effective to solve instability problems in membranes [38, 42, 55].

8.5.2 Energy equations

To employ the method of Fourier series with slowly variable coefficients, the calculation rules proposed by Damil and Potier-Ferry [35] should be introduced. Given two Fourier coefficients

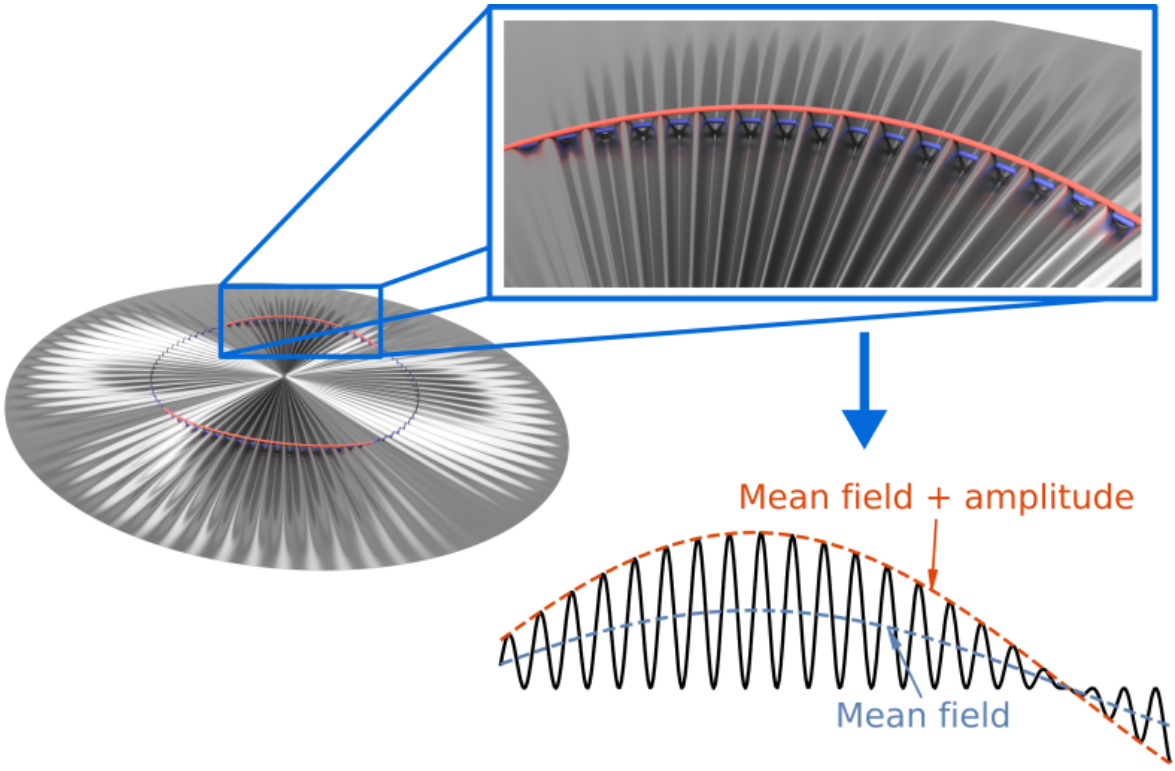

Figure 8.1 Diagram of the method of Fourier series with slowly variable coefficients

$a(\rho)$ and $b(\rho)$ as in Eq. (8.8), the following identities hold:

$$\int_0^L a(\rho)b(\rho)\mathrm{d}\rho = \int_0^L \sum_{m=-\infty}^{+\infty} a_m(\rho)b_{-m}(\rho)\mathrm{d}\rho, \tag{8.9}$$

$$\left(\frac{da}{d\rho}\right)_m = (a')_m = \left(\frac{d}{d\rho} + \mathrm{i}mQ\right) a_m = (a_m)' + \mathrm{i}mQa_m, \tag{8.10}$$

$$\left(\frac{d^2a}{d\rho^2}\right)_m = (a'')_m = \left(\frac{d}{d\rho} + \mathrm{i}mQ\right)^2 a_m = (a_m)'' + 2\mathrm{i}mQ(a_m)' - m^2Q^2a_m^2, \tag{8.11}$$

$$(ab)_m = \sum_{n=-\infty}^{+\infty} a_n b_{m-n}. \tag{8.12}$$

in which i is the imaginary unit, Q the preassigned wave number and m denotes the mth order harmonic. After introducing Eqs. (8.9)-(8.12), the geometric equations can be deduced from Eqs. (8.1) and (8.2) as follows:

$$\begin{aligned}\epsilon_{\rho m} =& \left[\frac{\partial u_m}{\partial \rho} + \frac{1}{2}\sum_{n=-1}^{1}\left(\frac{\partial w_n}{\partial \rho}\frac{\partial w_{m-n}}{\partial \rho} + \frac{\partial u_n}{\partial \rho}\frac{\partial u_{m-n}}{\partial \rho} + \frac{\partial v_n}{\partial \rho}\frac{\partial v_{m-n}}{\rho}\right)\right.\\ &\left. - z\frac{\partial^2 w_m}{\partial \rho^2}\right]\mathrm{e}^{\mathrm{i}mQ\theta},\end{aligned} \tag{8.13}$$

$$\begin{aligned}\epsilon_{\theta m} =& \left[\frac{u_m}{\rho} + \frac{1}{2\rho^2}\sum_{n=-1}^{1}\left(-n(m-n)Q^2w_nw_{m-n} + v_nv_{m-n} + u_nu_{m-n}\right)\right.\\ &\left. + \frac{z}{\rho^2}\left(m^2Q^2w_m - \rho\frac{\partial w_m}{\partial \rho}\right)\right]\mathrm{e}^{\mathrm{i}mQ\theta},\end{aligned} \tag{8.14}$$

$$\begin{aligned}2\epsilon_{\rho\theta m} =& \left[\frac{\partial v_m}{\partial \rho} - \frac{v_m}{\rho} + \frac{1}{\rho}\sum_{n=-1}^{1}\left(\mathrm{i}nQw_n\frac{\partial w_{m-n}}{\partial \rho} - v_n\frac{\partial u_{m-n}}{\partial \rho} + u_n\frac{\partial v_{m-n}}{\partial \rho}\right)\right.\\ &\left. + \frac{z}{\rho^2}\left(\mathrm{i}2mQw_m - \mathrm{i}2mQ\rho\frac{\partial w_m}{\partial \rho}\right)\right]\mathrm{e}^{\mathrm{i}mQ\theta},\end{aligned} \tag{8.15}$$

in which $m = -1, 0, 1$, because only two harmonics are considered as mentioned previously. As shown in Eqs. (8.13)-(8.15), oscillations in the circumferential direction occur for the non-zero order strain. However, the integration of the strain energy over the entire domain does not oscillate, which means the internal work should be 0 order without any exponential term. Therefore, the oscillation terms could be diminished in the internal virtual work.

In this work, periodic instability phenomena of circular film structures are investigated, where the oscillations of $u(\rho, \theta)$ and $v(\rho, \theta)$ can be neglected compared to $w(\rho, \theta)$ in the overall instability mode. Thus it can be assumed that $u(\rho, \theta) = u_0(\rho)$ and $v(\rho, \theta) = v_0(\rho)$. For the transverse displacement $w(\rho, \theta)$, the mean field $w_0(\rho)$ and the real envelope field $w_{\pm1}(\rho)$ are taken into consideration, i.e. $w(\rho, \theta) = w_0(\rho) + w_1(\rho)\mathrm{e}^{\mathrm{i}Q\theta} + w_{-1}(\rho)\mathrm{e}^{-\mathrm{i}Q\theta}$. Here $w_1(\rho)$, $w_{-1}(\rho)$

can be expressed as $w_1(\rho) = r(\rho)\mathrm{e}^{\mathrm{i}\phi}$, $w_{-1}(\rho) = r(\rho)\mathrm{e}^{-\mathrm{i}\phi}$, where $r(\rho)$ is the real part and ϕ the angle of phase modulation. Taking the phase modulation in consideration, the model might be able to solve other more complex instability problems in circular membranes, such as a circular membrane under shear load [31]. To simplify the work, the angle ϕ is assumed to be constant and equal to $\pm\dfrac{\pi}{2}$. More details on the discussion about the phase modulation is presented by Liu et al. [39]. After introducing these displacement assumptions, the unknown vector $\langle \mathbf{q} \rangle$ can be expressed as follows:

$$\langle \mathbf{q} \rangle = \left\langle \; u_0, \quad \frac{\partial u_0}{\partial \rho}, \quad v_0, \quad \frac{\partial v_0}{\partial \rho}, \quad w_0, \quad \frac{\partial w_0}{\partial \rho}, \quad \frac{\partial^2 w_0}{\partial \rho^2}, \quad w_1, \quad \frac{\partial w_1}{\partial \rho}, \quad \frac{\partial^2 w_1}{\partial \rho^2} \; \right\rangle. \tag{8.16}$$

The generalized strain vectors are expressed as $\{\mathscr{E}\}_m$, in which $m = -1, 0, 1$ denotes the strains of -1^{st}, 0^{th}, 1^{st} orders. Since $\{\mathscr{E}\}_{-1}$ and $\{\mathscr{E}\}_1$ are a pair of complex conjugates, which can be regarded as the same in the following derivation. Thus, only $\{\mathscr{E}\}_0$ and $\{\mathscr{E}\}_1$ are presented as follows:

$$\begin{aligned} \{\mathscr{E}\}_0 &= \begin{Bmatrix} \epsilon^m_{\rho 0} + \epsilon^q_{\rho 0} \\ \epsilon^m_{\theta 0} + \epsilon^q_{\theta 0} \\ 2\left(\epsilon^m_{\rho\theta 0} + \epsilon^q_{\rho\theta 0}\right) \\ \epsilon^b_{\rho 0} \\ \epsilon^b_{\theta 0} \\ 2\epsilon^b_{\rho\theta 0} \end{Bmatrix} = \begin{Bmatrix} \{\boldsymbol{\gamma}^m\}_0 + \{\boldsymbol{\gamma}^q\}_0 \\ \left\{\boldsymbol{\gamma}^b\right\}_0 \end{Bmatrix} \\ &= \left([\mathbf{H}]_0 + \frac{1}{2}\left[\mathbf{A}\left(\mathbf{q}\right)\right]_0 \right) \{\mathbf{q}\}, \end{aligned} \tag{8.17}$$

$$\begin{aligned} \{\mathscr{E}\}_1 &= \begin{Bmatrix} \epsilon^m_{\rho 1} + \epsilon^q_{\rho 1} \\ \epsilon^m_{\theta 1} + \epsilon^q_{\theta 1} \\ 2\left(\epsilon^m_{\rho\theta 1} + \epsilon^q_{\rho\theta 1}\right) \\ \epsilon^b_{\rho 1} \\ \epsilon^b_{\theta 1} \\ 2\epsilon^b_{\rho\theta 1} \end{Bmatrix} = \begin{Bmatrix} \{\boldsymbol{\gamma}^m\}_1 + \{\boldsymbol{\gamma}^q\}_1 \\ \left\{\boldsymbol{\gamma}^b\right\}_1 \end{Bmatrix} \\ &= \left([\mathbf{H}]_1 + \frac{1}{2}[\mathbf{A}(\mathbf{q})]_1 \right) \{\mathbf{q}\} + \mathbf{i}\left([\mathbf{H}]_2 + \frac{1}{2}\left[\mathbf{A}\left(\mathbf{q}\right)\right]_2 \right) \{\mathbf{q}\}, \end{aligned} \tag{8.18}$$

where the matrix $[\mathbf{H}]_t$ $(t = 0, 1, 2)$ represents the linear parts of the strains without unknown terms, while the matrix $[\mathbf{A}\left(\mathbf{q}\right)]_t$ $(t = 0, 1, 2)$ represents the quadratic nonlinear parts of the strains with the unknown terms, presented in Table 8.1.

Table 8.1 Non-zero elements of the generalized strains related matrices

Matrix (6×10)	Non-zero elements				
$[\mathbf{H}]_0$	(1,2)=1 (4,7)=−1	(2,1)=$\frac{1}{\rho}$	(3,3)=$-\frac{1}{\rho}$	(3,4)=1	(5,6)=$-\frac{1}{\rho}$
$[\mathbf{A}(\mathbf{q})]_0$	(1,2)=$\frac{\partial u_0}{\partial \rho}$ (2,3)=$\frac{v_0}{\rho^2}$ (3,4)=$\frac{\partial u_0}{\rho \partial \rho}$	(1,4)=$\frac{\partial v_0}{\partial \rho}$ (2,8)=$\frac{2Q^2 w_1}{\rho^2}$	(1,6)=$\frac{\partial w_0}{\partial \rho}$ (3,1)=$\frac{\partial v_0}{\rho \partial \rho}$	(1,9)=$\frac{2\partial w_1}{\partial \rho}$ (3,2)=$-\frac{v_0}{\rho}$	(2,1)=$\frac{u_0}{\rho^2}$ (3,3)=$-\frac{\partial u_0}{\rho \partial \rho}$
$[\mathbf{H}]_1$	(4,10)=−1	(5,8)=$\frac{Q^2}{\rho^2}$	(5,9)=$-\frac{1}{\rho}$		
$[\mathbf{A}(\mathbf{q})]_1$	(1,6)=$\frac{\partial w_1}{\partial \rho}$	(1,9)=$\frac{\partial w_0}{\partial \rho}$			
$[\mathbf{H}]_2$	(6,8)=$\frac{Q}{\rho^2}$	(6,9)=$-\frac{2Q}{\rho}$			
$[\mathbf{A}(\mathbf{q})]_2$	(3,6)=$\frac{Qw_1}{\rho}$	(3,8)=$\frac{Q}{\rho}\frac{\partial w_0}{\partial \rho}$			

The internal virtual work of the circular membrane in Eq. (8.5) can be deduced as:

$$\begin{aligned}\mathcal{W}_{int}(\delta q) =&\delta\Bigg(\iint_{\omega} \Bigg[\frac{1}{2}\Bigg[(\langle \boldsymbol{\gamma}^m\rangle_0 + \langle \boldsymbol{\gamma}^q\rangle_0)\,[\mathbf{L}^m]\,(\{\boldsymbol{\gamma}^m\}_0 + \{\boldsymbol{\gamma}^q\}_0) + \left\langle \boldsymbol{\gamma}^b\right\rangle_0 \left[\mathbf{L}^b\right]\left\{\boldsymbol{\gamma}^b\right\}_0\Bigg] \\ &+ \Bigg[(\langle \boldsymbol{\gamma}^m\rangle_1 + \langle \boldsymbol{\gamma}^q\rangle_1)\,[\mathbf{L}^m]\,(\{\boldsymbol{\gamma}^m\}_1 + \{\boldsymbol{\gamma}^q\}_1) + \left\langle \boldsymbol{\gamma}^b\right\rangle_1 \left[\mathbf{L}^b\right]\left\{\boldsymbol{\gamma}^b\right\}_1\Bigg]\Bigg]\,\mathrm{d}\omega\Bigg). \end{aligned} \tag{8.19}$$

Since the body forces are neglected in this paper, the external virtual work of the circular membrane can be written as:

$$\mathcal{W}_{ext}(\delta q) = \iint_{\omega} \lambda\,\langle \delta\mathbf{q}\rangle\,\{\mathbf{f}\}\,\mathrm{d}\omega. \tag{8.20}$$

which is due to a generalized force vector $\lambda\{\mathbf{f}\}$ with $\lambda \in \mathbb{R}$ being a load parameter. Finally, substituting Eqs. (8.17) and (8.18) into Eq. (8.19), and using the principle of virtual work:

$$\mathcal{W}_{int}(\delta q) = \mathcal{W}_{ext}(\delta q), \tag{8.21}$$

the governing equations can be deduced as:

$$\begin{cases} \langle \delta \mathbf{q} \rangle \left\{ \iint_{\omega} \left[\left({}^{T}[\mathbf{H}]_0 + [\mathbf{A}(\mathbf{q})]_0 \right) \{\mathbf{S}\}_0 + 2 \left({}^{T}[\mathbf{H}]_1 + [\mathbf{A}(\mathbf{q})]_1 \right) \{\mathbf{S}\}_1 \right. \right. \\ \qquad \left. \left. + 2 \left({}^{T}[\mathbf{H}]_2 + [\mathbf{A}(\mathbf{q})]_2 \right) \{\mathbf{S}\}_2 \right] \mathrm{d}\omega - \iint_{\omega} \lambda \{\mathbf{f}\} \, \mathrm{d}\omega \right\} = 0, \\ \{\mathbf{S}\}_t = [\mathbf{D}] \left([\mathbf{H}]_t + \frac{1}{2} [\mathbf{A}(\mathbf{q})]_t \right) \{\mathbf{q}\}, \end{cases} \tag{8.22}$$

in which the subscript $t = 0, 1, 2$ stands for the notation of relevant matrix, and the elastic coefficient matrix can be written as follows:

$$[\mathbf{D}] = \left({}^{T}[\mathbf{R}_m][\mathbf{L}^m][\mathbf{R}_m] + {}^{T}[\mathbf{R}_b][\mathbf{L}^b][\mathbf{R}_b] \right), \tag{8.23}$$

in which $[\mathbf{R}_m]$ (for the membrane strains) and $[\mathbf{R}_b]$ (for the bending strains) can be written as follows:

$$[\mathbf{R}_m] = \begin{bmatrix} 1 & 0 & 0 & 0 & 0 & 0 \\ 0 & 1 & 0 & 0 & 0 & 0 \\ 0 & 0 & 1 & 0 & 0 & 0 \end{bmatrix}, \qquad [\mathbf{R}_b] = \begin{bmatrix} 0 & 0 & 0 & 1 & 0 & 0 \\ 0 & 0 & 0 & 0 & 1 & 0 \\ 0 & 0 & 0 & 0 & 0 & 1 \end{bmatrix}. \tag{8.24}$$

8.5.3 Discretization

The finite element method is used to solve the nonlinear system of Eq. (8.22). In membrane problems, both the radial and circumferential displacements have only the first order partial derivatives, while the second order partial derivatives appear in the transverse displacements. Normally, the Lagrangian interpolation is employed for u and v, and the Hermite interpolation for w. However, considering the possible membrane locking problem as presented in Reddy [56], Choe et al. [57] suggest to use Hermite interpolation for all the displacement components. Therefore, a two-node 1D element with 8 degrees of freedom at each node is used. The vector of shape functions can be written as follows:

$$\langle \mathbf{\Gamma} \rangle = \left\langle \frac{(1-\xi)^2 (2+\xi)}{4}, \frac{le\,(1-\xi^2)\,(1-\xi)}{8}, \frac{(1+\xi)^2 (2-\xi)}{4}, \frac{le\,(-1+\xi^2)\,(1+\xi)}{8} \right\rangle. \tag{8.25}$$

in which le denotes the length of the element. Considering the unknowns in Eq. (8.26), the element nodal displacements vector $\langle \mathbf{q}^e \rangle$ can be expressed as:

$$\langle \mathbf{q}^e \rangle = \left\langle u_0^I, \ \frac{\partial u_0^I}{\partial \rho}, \ v_0^I, \ \frac{\partial v_0^I}{\partial \rho}, \ w_0^I, \ \frac{\partial w_0^I}{\partial \rho}, \ w_1^I, \ \frac{\partial w_1^I}{\partial \rho}, \ u_0^{II}, \ \frac{\partial u_0^{II}}{\partial \rho}, \ v_0^{II}, \ \frac{\partial v_0^{II}}{\partial \rho}, \ w_0^{II}, \ \frac{\partial w_0^{II}}{\partial \rho}, \ w_1^{II}, \ \frac{\partial w_1^{II}}{\partial \rho} \right\rangle, \tag{8.26}$$

then Eq. (8.26) can be expressed as a discretized form:

$$\{\mathbf{q}\} = [\mathbf{G}]\,\{\mathbf{q}^e\}\,, \tag{8.27}$$

in which, the 10×16 matrix of shape functions $[\mathbf{G}]$ can be written as:

$$[\mathbf{G}] = \begin{bmatrix} \boldsymbol{\Gamma}_{\boldsymbol{q}^e} & 0 & 0 & 0 & 0 & 0 & 0 \\ \boldsymbol{\Gamma}_{\boldsymbol{q}^e,\rho} & 0 & 0 & 0 & 0 & 0 & 0 \\ 0 & 0 & \boldsymbol{\Gamma}_{\boldsymbol{q}^e} & 0 & 0 & 0 & 0 \\ 0 & 0 & \boldsymbol{\Gamma}_{\boldsymbol{q}^e,\rho} & 0 & 0 & 0 & 0 \\ 0 & 0 & 0 & 0 & \boldsymbol{\Gamma}_{\boldsymbol{q}^e} & 0 & 0 \\ 0 & 0 & 0 & 0 & \boldsymbol{\Gamma}_{\boldsymbol{q}^e,\rho} & 0 & 0 \\ 0 & 0 & 0 & 0 & \boldsymbol{\Gamma}_{\boldsymbol{q}^e,\rho\rho} & 0 & 0 \\ 0 & 0 & 0 & 0 & 0 & 0 & \boldsymbol{\Gamma}_{\boldsymbol{q}^e} \\ 0 & 0 & 0 & 0 & 0 & 0 & \boldsymbol{\Gamma}_{\boldsymbol{q}^e,\rho} \\ 0 & 0 & 0 & 0 & 0 & 0 & \boldsymbol{\Gamma}_{\boldsymbol{q}^e,\rho\rho} \end{bmatrix}, \tag{8.28}$$

where subscripts following commas denote partial derivatives and the vector $\langle \boldsymbol{\Gamma}_{\boldsymbol{q}^e} \rangle$ is as follows:

$$\langle \boldsymbol{\Gamma}_{\boldsymbol{q}^e} \rangle = \Big\langle\ \boldsymbol{\Gamma}(1),\ \ \boldsymbol{\Gamma}(2),\ \ 0,\ \ 0,\ \ 0,\ \ 0,\ \ 0,\ \ 0,\ \ \boldsymbol{\Gamma}(3),\ \ \boldsymbol{\Gamma}(4)\ \Big\rangle\,. \tag{8.29}$$

Substituting the discretized unknown $\{\mathbf{q}\}$ in Eq. (8.27) into Eq. (8.22), the governing equations can be converted into the following form:

$$\begin{cases} \displaystyle\sum_e \langle \delta\mathbf{q}^e \rangle \left[\int_0^{le} \left({}^T[\mathbf{B}(\mathbf{q}^e)]_0\{\mathbf{S}\}_0 + 2^T[\mathbf{B}(\mathbf{q}^e)]_1\{\mathbf{S}\}_1 + 2^T[\mathbf{B}(\mathbf{q}^e)]_2\{\mathbf{S}\}_2 \right) \rho \mathrm{d}\rho - \lambda\{\mathbf{f}^e\} \right] = 0, \\ \{\mathbf{S}\}_t = [\mathbf{D}] \left([\mathbf{B}_l]_t + \dfrac{1}{2}[\mathbf{B}_{nl}(\mathbf{q}^e)]_t \right) \{\mathbf{q}^e\}, \end{cases} \tag{8.30}$$

where

$$\begin{cases} [\mathbf{B}(\mathbf{q}^e)]_t = [\mathbf{B}_l]_t + [\mathbf{B}_{nl}(\mathbf{q}^e)]_t, \\ [\mathbf{B}_l]_t = [\mathbf{H}]_t[\mathbf{G}], \\ [\mathbf{B}_{nl}(\mathbf{q}^e)]_t = [\mathbf{A}(\mathbf{q}^e)]_t[\mathbf{G}], \\ \{\mathbf{f}^e\} = \displaystyle\int_0^{le} {}^T[\mathbf{G}]\{\mathbf{f}\}\rho \mathrm{d}\rho. \end{cases} \tag{8.31}$$

8.5.4 Implementation of the ANM

In this section, we introduce the solution procedure of the governing equation by the Asymptotic Numerical Method (ANM) proposed by Cochelin et al. [58]. This method offers sev-

eral advantages in terms of computational efficiency and reliability compared with classical non-linear solution algorithms, such as the Newton-Raphson or the arc-length method. For example, the arc-length step size in the ANM is fully adaptive, and the global stiffness matrix inversion is calculated only once in each step.

Let $\{\mathbf{S}\}_t$ and $\{\mathbf{q}^e\}$ are assembled vectors of $\{\mathbf{S}_p\}_t$ and $\{\mathbf{q}_p^e\}(p = 1, 2, 3\cdots)$, then solution $(\mathbf{q}^{e(j+1)}, \mathbf{S}^{j+1}, \lambda^{j+1})$ at the step $j+1$ can be asymptotically expanded as

$$\{\mathbf{S}\}_t = \{\mathbf{S}\}_t^j + \sum_{p=1}^{n} \alpha^p \{\mathbf{S}_p\}_t = \{\mathbf{S}\}_t^j + \alpha\{\mathbf{S}_1\}_t + \alpha^2\{\mathbf{S}_2\}_t + \cdots, \tag{8.32}$$

$$\{\mathbf{q}^e\} = \{\mathbf{q}^e\}^j + \sum_{p=1}^{n} \alpha^p \{\mathbf{q}_p^e\} = \{\mathbf{q}^e\}^j + \alpha\{\mathbf{q}_1^e\} + \alpha^2\{\mathbf{q}_2^e\} + \cdots, \tag{8.33}$$

$$\lambda = \lambda^j + \sum_{p=1}^{n} \alpha^p \lambda_p = \lambda^j + \alpha\lambda_1 + \alpha^2\lambda_2 + \cdots, \tag{8.34}$$

$$\alpha = \langle \mathbf{q}_1^e \rangle \left(\{\mathbf{q}^e\} - \{\mathbf{q}^e\}^j \right) + \lambda_1 \left(\lambda - \lambda^j \right), \tag{8.35}$$

in which, $(\mathbf{q}^{ej}, \mathbf{S}^j, \lambda^j)$ is the solution at the step j and α is the path parameter. The parameter α used here was proposed by Cochelin et al. [58], whose stability and validity have been verified. Substituting the asymptotic solutions of Eqs. (8.32)-(8.35) into Eqs. (8.30) and (8.31), the governing equations are transformed into a set of equivalent equations, which can be grouped into order 1 and order p. The general form for the equations for order 1 can be expressed as:

$$\begin{cases} \sum\limits_e \langle \delta\mathbf{q}^e \rangle \int_0^{le} \Big({}^T[\mathbf{B}(\mathbf{q}^{ej})]_0\{\mathbf{S}_1\}_0 + {}^T[\mathbf{B}_{nl}(\mathbf{q}_1^e)]_0\{\mathbf{S}\}_0^j + 2{}^T[\mathbf{B}(\mathbf{q}^{ej})]_1\{\mathbf{S}_1\}_1 \\ +2{}^T[\mathbf{B}_{nl}(\mathbf{q}_1^e)]_1\{\mathbf{S}\}_1^j + 2{}^T[\mathbf{B}(\mathbf{q}^{ej})]_2\{\mathbf{S}_1\}_2 + 2{}^T[\mathbf{B}_{nl}(\mathbf{q}_1^e)]_2\{\mathbf{S}\}_2^j \Big) \rho d\rho = \sum\limits_e \langle \delta\mathbf{q}^e \rangle \lambda_1 \{\mathbf{f}^e\}, \\ \{\mathbf{S}_1\}_t = [\mathbf{D}][\mathbf{B}(\mathbf{q}^{ej})]_t\{\mathbf{q}_1^e\}, \\ 1 = \langle \mathbf{q}_1^e \rangle \{\mathbf{q}_1^e\} + \lambda_1^2. \end{cases} \tag{8.36}$$

Here, $\{\mathbf{q}_1^e\}$ is the only unknown vector to be solved. The terms ${}^T[\mathbf{B}_{nl}(\mathbf{q}_1^e)]_t\{\mathbf{S}\}_t^j$ can be rewritten as:

$${}^T[\mathbf{B}_{nl}(\mathbf{q}_1^e)]_t\{\mathbf{S}\}_t^j = {}^T[\mathbf{G}][\widetilde{\mathbf{S}}]_t^j[\mathbf{G}]\{\mathbf{q}_1^e\}, \tag{8.37}$$

in which, the non-zero elements of transform matrices $[\widetilde{\mathbf{S}}]_t^j$ $(t = 0, 1, 2)$ are listed in Table 8.2. Submitting Eq. (8.37) into Eq. (8.36), the governing equation can be written in a more simplified form:

$$\sum_e \langle \delta\mathbf{q}^e \rangle \left([\mathbf{k}(\mathbf{q}^e, \mathbf{S}_t)]\{\mathbf{q}_1^e\} - \lambda_1\{\mathbf{f}^e\} \right) = 0, \tag{8.38}$$

Table 8.2 Non-zero elements of the transform matrices

Matrix (6×10)	Non-zero elements				
$[\widetilde{\mathbf{S}}]_0^j$	(1,1)=$\frac{1}{\rho^2}S_2^j$	(1,4)=$\frac{1}{\rho}S_3^j$	(2,2)=S_1^j	(2,3)=$-\frac{1}{\rho}S_3^j$	(3,2)=$-\frac{1}{\rho}S_3^j$
	(3,3)=$\frac{1}{\rho^2}S_2^j$	(4,1)=$\frac{1}{\rho}S_3^j$	(4,4)=S_1^j	(6,6)=S_1^j	(8,8)=$\frac{2Q^2}{\rho^2}S_2^j$
	(9,9)=$2S_1^j$				
$[\widetilde{\boldsymbol{S}}]_1^j$	(6,9)=S_1^j	(9,6)=S_1^j			
$[\widetilde{\boldsymbol{S}}]_2^j$	(6,8)=$\frac{Q}{\rho}S_3^j$	(8,6)=$\frac{Q}{\rho}S_3^j$			

in which, $[\mathbf{k}(\mathbf{q}^e, \mathbf{S}_t)]$ is the element stiffness matrix,

$$\begin{aligned}[\mathbf{k}(\mathbf{q}^e, \mathbf{S}_t)] = \int_0^{le} \Big(&{}^T[\mathbf{B}(\mathbf{q}^{ej})]_0[\mathbf{D}][\mathbf{B}(\mathbf{q}^{ej})]_0 + {}^T[\mathbf{G}][\widetilde{\mathbf{S}}]_0^j[\mathbf{G}] \\ &+2^T[\mathbf{B}(\mathbf{q}^{ej})]_1[\mathbf{D}][\mathbf{B}(\mathbf{q}^{ej})]_1 + 2^T[\mathbf{G}][\widetilde{\mathbf{S}}]_1^j[\mathbf{G}] \\ &+2^T[\mathbf{B}(\mathbf{q}^{ej})]_2[\mathbf{D}][\mathbf{B}(\mathbf{q}^{ej})]_2 + 2^T[\mathbf{G}][\widetilde{\mathbf{S}}]_2^j[\mathbf{G}]\Big)\,\rho \mathrm{d}\rho. \end{aligned} \tag{8.39}$$

After combining all the element matrices and vectors, the final equation of order 1 can be obtained:

$$[\mathbf{K}(\mathbf{q}^e, \mathbf{S}_t)]\{\mathbf{Q}_1\} = \lambda_1\{\mathbf{F}\}, \tag{8.40}$$

in which, $[\mathbf{K}(\mathbf{q}^e, \mathbf{S}_t)]$ is the global stiffness matrix, $\{\mathbf{Q}_1\}$ the global displacement vector and $\{\mathbf{F}\}$ the global load vector.

Similar to order 1, the governing equations of order p can be expressed as:

$$\begin{cases} \sum\limits_e \langle \delta\mathbf{q}^e \rangle \int_0^{le} \Big({}^T[\mathbf{B}(\mathbf{q}^{ej})]_0\{\mathbf{S}_p\}_0 + {}^T[\mathbf{B}_{nl}(\mathbf{q}_p^e)]_0\{\mathbf{S}\}_0^j + 2^T[\mathbf{B}(\mathbf{q}^{ej})]_1\{\mathbf{S}_p\}_1 \\ +2^T[\mathbf{B}_{nl}(\mathbf{q}_p^e)]_1\{\mathbf{S}\}_1^j + 2^T[\mathbf{B}(\mathbf{q}^{ej})]_2\{\mathbf{S}_1\}_2 + 2^T[\mathbf{B}_{nl}(\mathbf{q}_p^e)]_2\{\mathbf{S}\}_2^j\Big)\,\rho \mathrm{d}\rho \\ = \sum\limits_e \langle \delta\mathbf{q}^e \rangle \left(\lambda_p\{\mathbf{f}^e\} + \{\mathbf{f}_p^{enl}\}_0 + 2\{\mathbf{f}_p^{enl}\}_1 + 2\{\mathbf{f}_p^{enl}\}_2\right), \\ \{\mathbf{S}_p\}_t = [\mathbf{D}][\mathbf{B}(\mathbf{q}^{ej})]_t\{\mathbf{q}_p^e\} + \left\{\mathbf{S}_p^{nl}\right\}_t, \\ 0 = \langle \mathbf{q}_1^e \rangle \{\mathbf{q}_p^e\} + \lambda_1\lambda_p, \end{cases} \tag{8.41}$$

where

$$\begin{cases} \left\{\mathbf{f}_p^{enl}\right\}_t = -\sum\limits_{r=1}^{p-1} \int_0^{le} \left({}^T[\mathbf{B}_{nl}(\mathbf{q}_{p-r}^e)]_t\{\mathbf{S}_p\}_t\right) \rho \mathrm{d}\rho, \\ \left\{\mathbf{S}_p^{nl}\right\}_t = \dfrac{1}{2}[\mathbf{D}] \sum\limits_{r=1}^{p-1} [\mathbf{B}_{nl}(\mathbf{q}_{p-r}^e)]_t \{\mathbf{q}_r^e\}. \end{cases} \tag{8.42}$$

There are some additional terms in Eq. (8.41) compared with Eq. (8.36). They are nonlinear force terms and are moved to the right side of the equation.

$$\sum_e \langle \delta \mathbf{q}^e \rangle \left([\mathbf{k}(\mathbf{q}^{ej}, \mathbf{S}_t)] \{\mathbf{q}_p^e\} - \lambda_p \{\mathbf{f}^e\} - \left\{\mathbf{f}_p^{eNL}\right\}_0 - 2\left\{\mathbf{f}_p^{eNL}\right\}_1 - 2\left\{\mathbf{f}_p^{eNL}\right\}_2 \right) = 0, \tag{8.43}$$

in which, the element nonlinear force vector $\left\{\mathbf{f}_p^{eNL}\right\}_t$ can be expressed as:

$$\left\{\mathbf{f}_p^{eNL}\right\}_t = \left\{\mathbf{f}_p^{enl}\right\}_t - \int_0^{le} \left({}^T[\mathbf{B}(\mathbf{q}^{ej})]_t \{\mathbf{S}_p^{nl}\}_t \right) \rho d\rho. \tag{8.44}$$

After combining all the element matrices, the final equation of order p can be derived as:

$$[\mathbf{K}(\mathbf{q}^e, \mathbf{S}_t)] \{\mathbf{Q}_p\} = \lambda_p \{\mathbf{F}\} + \{\mathbf{F}_p^{nl}\}, \tag{8.45}$$

in which $[\mathbf{K}(\mathbf{q}^e, \mathbf{S}_t)]$ is the global stiffness matrix, that is the same as the one of order 1. $\{\mathbf{Q}_p\}$ is the global displacement vector, $\{\mathbf{F}\}$ the global load vector, and $\{\mathbf{F}_p^{nl}\}$ the global nonlinear force vector. Due to the same stiffness matrix for the equations at different orders, only one inversion of the stiffness matrix is needed in each step.

After solving all the orders in one step, the results $\{\mathbf{Q}_p\}$(p≥1) can be submitted into Eq. (8.33):

$$\{\mathbf{Q}\}^{j+1} = \{\mathbf{Q}\}^j + \sum_{p=1}^{n} \alpha^p \{\mathbf{Q}_p\} = \{\mathbf{Q}\}^j + \alpha\{\mathbf{Q}_1\} + \alpha^2\{\mathbf{Q}_2\} + \cdots, \tag{8.46}$$

in which the maximum value of the path parameter α is defined as [58]:

$$\alpha = \left(\zeta \frac{\|\mathbf{Q}_1\|}{\|cQ_n\|} \right)^{\frac{1}{n-1}}, \tag{8.47}$$

where ζ is the precision parameter, which is preliminarily assigned by the user.

8.6 Annular membrane under in-plane radial tensile load

In this section, the instability problem of an annular membrane under radial traction is studied. As shown in Fig. 8.2, the external edge of the membrane is simply supported, while the transverse displacement of the internal edge is fixed. A uniformly distributed radial tensile load is applied along the internal edge. The wrinkling pattern, bifurcation curve etc. obtained by the Fourier reduced model are compared with the 3D finite element model in ABAQUS (referred to as the 'full shell model' in this paper) to verify the accuracy and

efficiency of the reduced model. Then, the buckling and post-buckling behaviors, such as evolution of wrinkles and stress are analyzed based on the simulation of the reduced model. The material properties and geometric dimensions of the membrane are listed in Table. 8.3.

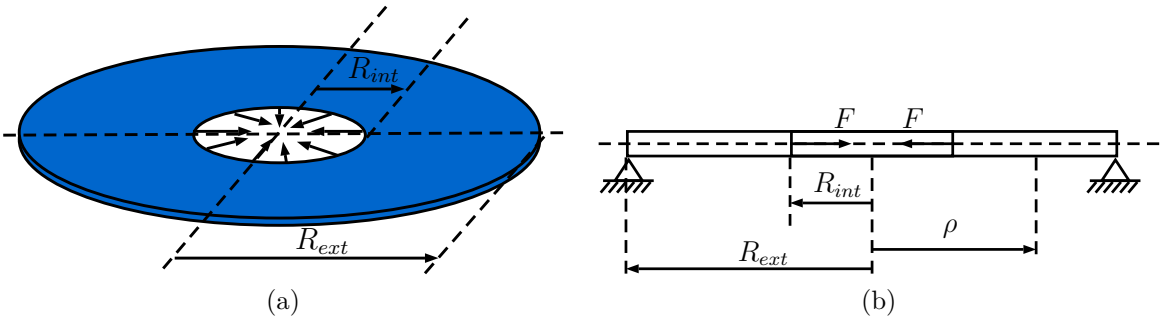

Figure 8.2 An annular membrane under in-plane radial tensile load along the internal edge

Table 8.3 Material properties and geometric dimensions of the annular membrane

Young's modulus E(MPa)	Poisson's ratio μ	Thickness h(mm)	Internal radius R_{int}(mm)	External radius R_{ext}(mm)
69,000	0.3	1	400	1000

8.6.1 Verification

Let X and Y be the half-waves in the radial direction and waves in the circumferential direction, respectively, and $RXCY$ represent the buckling modes with different wave numbers. By using both the reduced model and the full shell model to predict the bifurcation loads of the mode $R1C13$ with various numbers of elements, a mesh convergence study is performed to determine the minimum number of elements for the discretization. As shown in Table. 8.4, in the convergence test of the reduced model, the reference is the result with 16 elements. It is precise enough to use 4 elements in the reduced model to simulate the phenomenon in this section. However, if the wrinkles arise in both the radial and circumferential directions, for example the problem investigated in section 8.9, higher number of elements is necessary. As shown in Table. 8.5, in the convergence test of the full shell model, the reference is the result with 16 elements and 60 elements in the radial and circumferential direction respectively, and the lowest critical buckling mode of the example is $R1C13$. When the number of elements used in the circumferential direction is lower than 52, the full shell model cannot correctly

predict the lowest buckling mode, although the results are precise. Thus, considering the accuracy, at least 52×8 elements are needed to discretize the full shell model. The corresponding 3D deformed shapes are given in Fig. 8.3, in which the two simulation results show almost the same buckling mode.

Table 8.4 Error of the bifurcation load predicted by the reduced model with respect to the number of elements in the radial direction

Number of elements	2	3	4	5	6	16
Bifurcation load (N/mm)	46.178	43.874	43.423	43.319	43.290	43.261
Relative error	6.74%	1.42%	0.37%	0.13%	0.06%	——

Table 8.5 Error of the bifurcation load and lowest buckling mode predicted by the full shell model with respect to the number of elements in the radial and circumferential directions

	Elements in the radial direction					Elements in the circumferential direction				
Number of elements	4	6	8	10	16	28	36	44	52	60
Bifurcation load (N/mm)	45.370	43.817	43.453	43.343	43.274	44.421	43.733	43.557	43.488	43.274
Relative error	4.84%	1.25%	0.41%	0.16%	——	2.65%	1.06%	0.65%	0.49%	——
Lowest buckling mode	R1C13	R1C13	R1C13	R1C13	R1C13	R1C12	R1C12	R1C12	R1C13	R1C13

To trigger the post-buckling analysis in ABAQUS, the geometric imperfection, consisting of the interested buckling eigenmodes obtained by the linear buckling analysis (BUCKLE), is introduced in the initial state of the annular membrane by multiplying by a scale factor κ. This factor is taken as about $0.0001\% - 0.01\%$ of the membrane thickness h to get accurate instability curves and precise bifurcation points in this paper. In contrast, a simpler initial perturbation, namely a uniform transverse force about 10^{-6} of the applied load F, is applied in the reduced model.

The bifurcation curves of $R1C13$ calculated by the two models are illustrated in Fig. 8.4. As shown in the table in the figure, there is nearly no difference between the critical loads obtained by the full shell model(FM) and reduced model(RM). Even in the post-buckling process when transverse displacement reaches the same magnitude as the membrane thickness, the reduced model still performs well. As shown in the zoomed inset near the bifurcation point, the reduced model with ANM solver tracks the loading path precisely and smoothly compared with the full shell model. Besides, thanks to the ANM solver, the calculation steps of the reduced model are much fewer compared to the full shell model. Meanwhile, the reduced model only required 40 degrees of freedom (DOFs), about 0.2% of the full model, to

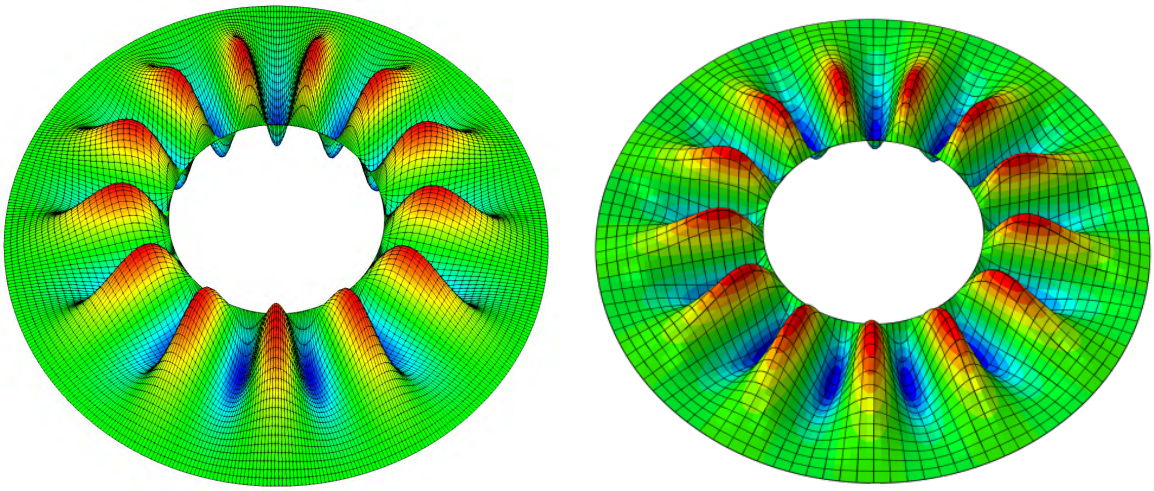

(a) (b)

Figure 8.3 Instability pattern $R1C13$ of the annular membrane under radial tensile load predicted by two different models: (a) the reduced model; (b) the full shell mod

obtain accurate enough results. Therefore, the reduced model shows a significant improvement in computational efficiency regarding to the number of loading steps and number of DOFs.

Fig. 8.5 presents the relative transverse displacements at the bifurcation point along the radial direction simulated by the two models. In order to obtain smooth deflection curve based on the displacement data in the radial direction, dual kriging [59] was used to interpolate the nodes. As seen in Fig. 8.5, the two groups of results show a good agreement.

8.6.2 Stress distribution

Here, we further discuss the stress distribution obtained by the reduced model. As shown in Fig. 8.6, the circumferential stress of the membrane simulated by the two models in the post-buckling stage is periodic around the circumference. The minimum value of the stress, i.e., the maximum compressive stress, is located near the internal edge.

In order to verify the stress results, the evolution of the circumferential and radial stress components on the top and bottom surface of the crest are given in Fig. 8.7. It can be seen that the reduced model performs well in predicting the stresses in the entire loading process. Before the bifurcation point, the two stresses on the top and bottom surfaces are the same and vary linearly with the increase of tensile load. Near the bifurcation point, the membrane buckles to accommodate the in-plane strain incompatibility generated by the negative radial displacement. As a consequence, one surface of the membrane starts to be stretched while

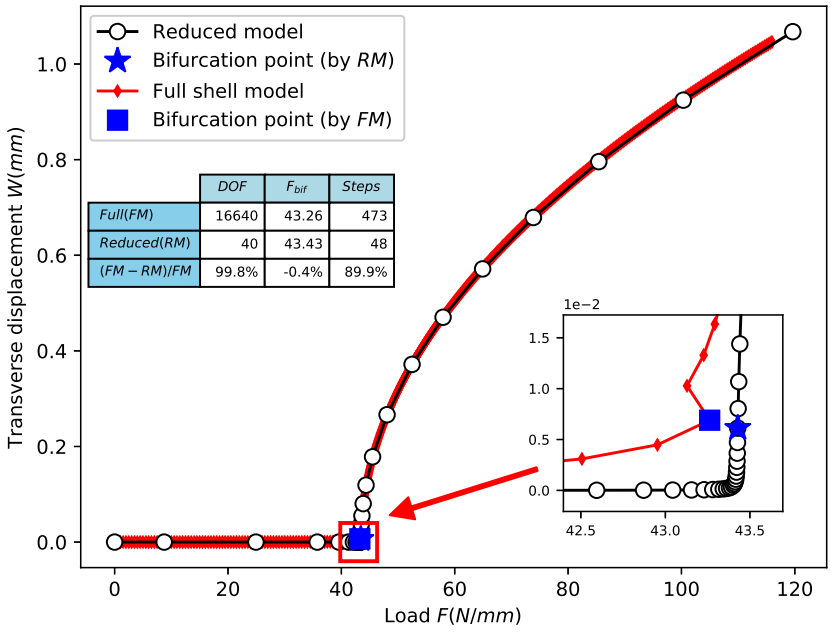

Figure 8.4 Bifurcation analysis of the annular membrane under radial tensile load along the internal edge

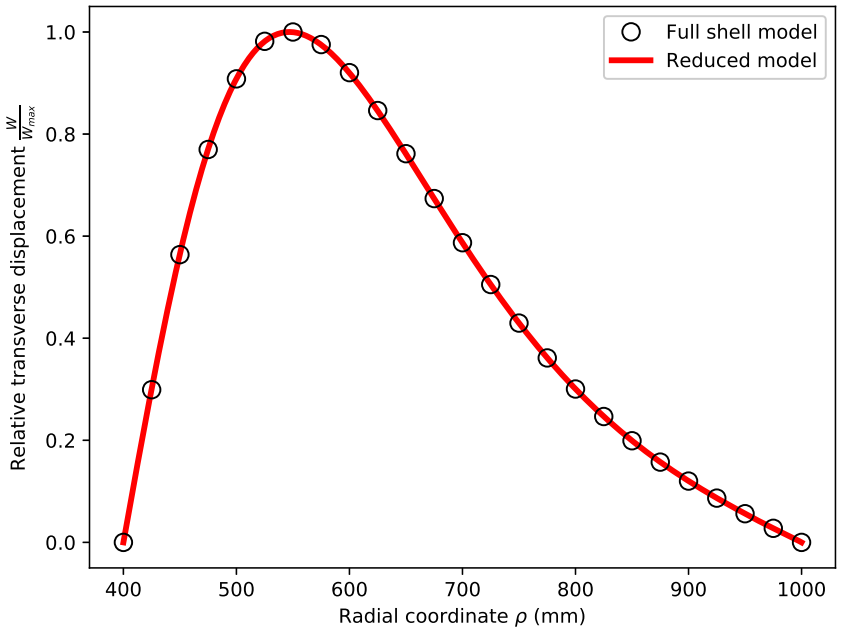

Figure 8.5 Transverse displacements in the radial direction of the cross section $\theta = 0$ at the bifurcation point

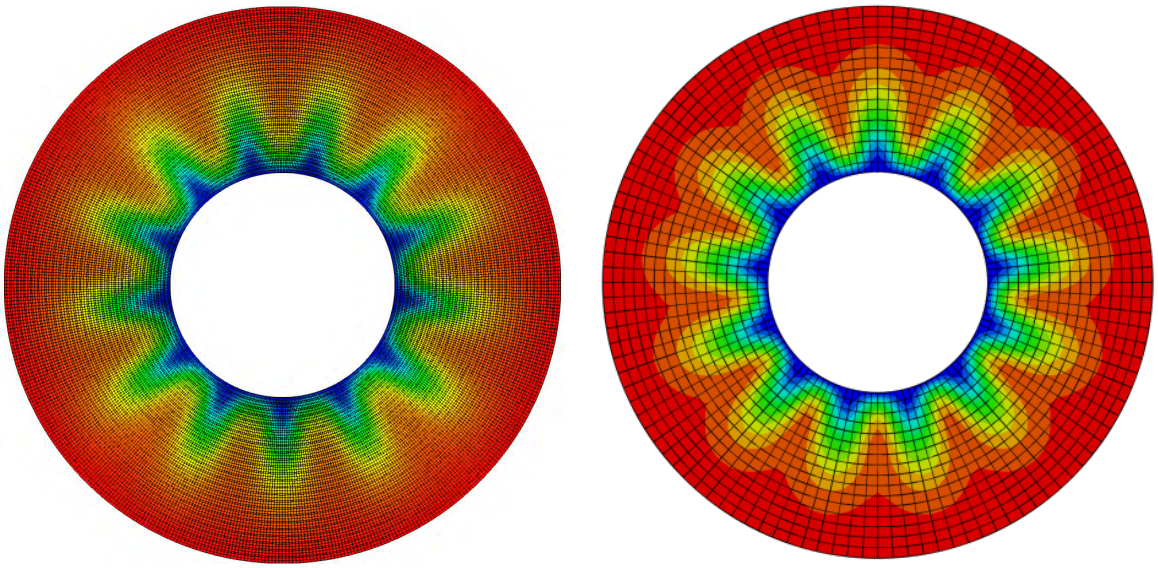

(a) (b)

Figure 8.6 Circumferential stress distribution in the post-buckling stage simulated by the two models: (a) reduced model; (b) full shell model

the other one gets further compressed. As shown in the Fig. 8.7, at the crest, the stress on the top surface increases with the load, while the one on the bottom surface decreases. It should be noted that the compressive stress on the top surface does not change to the tensile stress immediately, until the load reaches a specific value.

8.7 Annular membrane under transverse load

As shown in Fig. 8.8, the reduced model is used to simulate a pure bending problem, which is an annular membrane under transverse load, to verify that the model is able to precisely simulate the flexion of the membrane. Linear shell element (S4R) and quadratic shell element (S8R5) are used in ABAQUS to simulate the deformation of the annular membrane under transverse compressive load as references to verify the reduced model in this example. In order to investigate the membrane locking phenomenon, reduced models with two different discretization schemes are compared: one is the scheme used in the present article, i.e., all displacement unknowns are interpolated by the Hermite shape function (Reduced model (Hermite) in Fig. 8.9); another one is to use the linear Lagrange interpolation for radial and circumferential displacements u_0 and v_0, and the Hermite interpolation for transverse displacements w_0 and w_1 (Reduced model (Lagrange) in Fig. 8.9).

As shown in Fig. 8.9 the reduced model (Hermite) precisely simulates the evolution of both

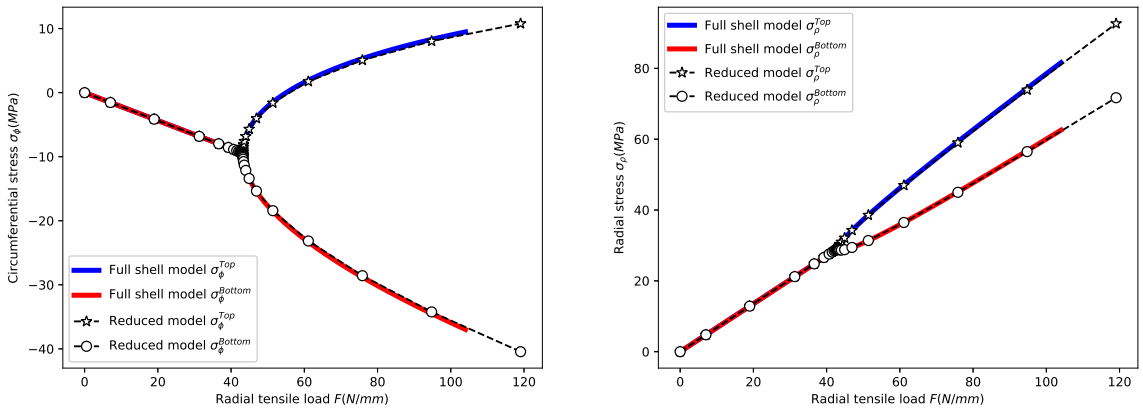

(a) (b)

Figure 8.7 Evolutions of stresses on the top and bottom surfaces of the crest: (a) circumferential stresses; (b) radial stresses

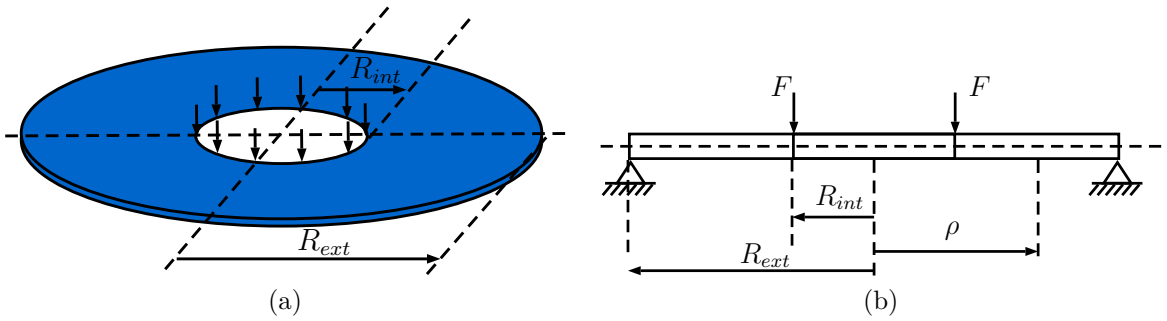

(a) (b)

Figure 8.8 An annular membrane under transverse load along the internal edge

transverse and radial displacements. Therefore, the reduced model (Hermite) proposed in the present article is verified for the simulation of the bending of an annular membrane. However, it can be seen that the reduced model (Lagrange) does not precisely simulate the deformation, especially for the radial displacement. It is obvious that the reduced model (Lagrange) is stiffer than the reduced model (Hermite). This phenomenon is known as the membrane locking as mentioned in [56], in which Reddy suggested to use the linear and the Hermite cubic interpolation for u and w, respectively, and the reduced integration to avoid the membrane locking. In the present article, we followed the suggestion of [57] to use the Hermite interpolation for all the displacements in the reduced model, also avoiding the membrane locking problems. It should be noted that the effect of membrane locking phenomenon is more severe for the radial displacement compared to the transverse displacement.

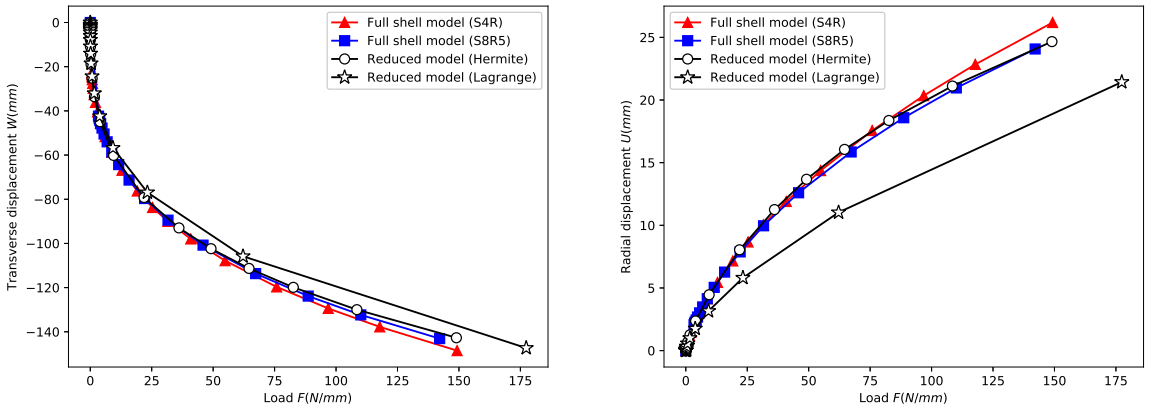

(a) (b)

Figure 8.9 Evolution of displacements at $\rho = R_{int}$: (a) transverse displacement; (b) radial displacement

8.8 Annular membrane under diagonal tensile load

After the validation of the reduced model under in-plane and out-of-plane loads, the reduced model is used to simulate a more complex example, which is an annular membrane under diagonal radial tensile load along the internal edge as shown in Fig. 8.10. This example is selected to verify that the model is able to simulate the instability phenomenon consisting of a local wrinkling and a global bending. The applied force is decomposed into a horizontal component and a vertical one.

This example is modified based on the wrinkling in a stretched thin sheet under lateral

pressure and a similar example can be found in Vermorel et al. [60], where the dynamic effects were considered. The angle between the diagonal tensile load and the initial mid-surface is around 6° in this example.

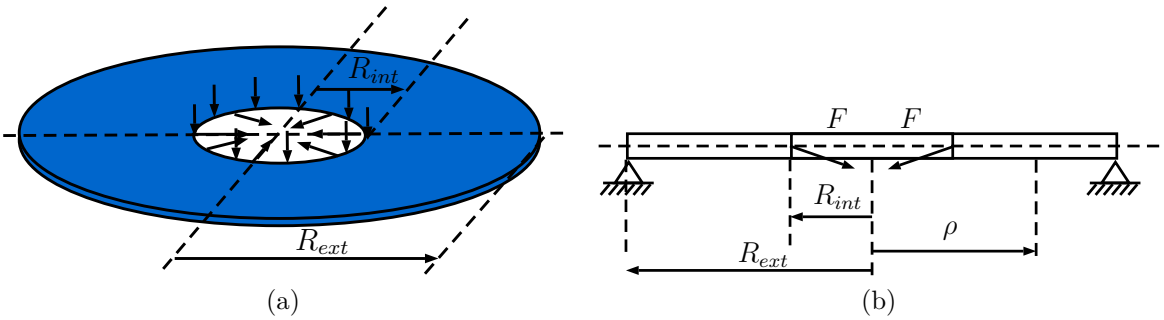

Figure 8.10 An annular membrane under diagonal radial tensile load along the internal edge

Fig. 8.11 shows the deformation of the annular membrane, which is composed of a uniform bending w_0 and a local instability w_1. The relationship between the displacements and the load is illustrated in Fig. 8.12. As shown in Fig. 8.12a, the radial displacement u_0 increases when $F < 62.6N/mm$, and it tends to decrease linearly after $F > 386.5N/mm$. The reason might be that the bending stiffness of the thin sheet is negligible compared with the in-plane stiffness, which means that deformation stage for $F < 62.6N/mm$ represents a pure bending mode. Therefore, at this stage, the global bending w_0 appears while the in-plane deformation is negligible, as shown in Fig. 8.12b, leading to a positive radial displacement u_0. When w_0 reaches the lowest value around $66.5mm$ with the load around $2518N/mm$, the membrane deforms into a shape with an angle about 6° with respect to the horizontal plane, which is close to the angle of diagonal tensile load. As shown in Fig. 8.12c, w_1 starts to increase significantly after the same point, which means the wrinkling phenomenon occurs. Therefore the bifurcation point is around $2518N/mm$. As shown in Fig. 8.12, after bifurcation point, w_0 increases slightly and tends to remain in the same level, while w_1 increases significantly. The deformation of this example can be summarized as follows: the sheet deforms to an angle close to the angle of the diagonal load, which can produce high enough in-plane tensile stresses to resist the external load; then the diagonal tensile load lies in the plane of the deformed membrane, which would generate the same instability pattern as the in-plane tensile load example discussed in section 8.6.

Fig. 8.13 shows the stress evolution of the membrane in the entire process. It can be seen that after the bifurcation point the evolution of both the radial and circumferential stresses on the top and bottom surfaces is similar to the trend obtained in the example discussed in section 8.6.2. However, it should be noted that the circumferential stress increases at the

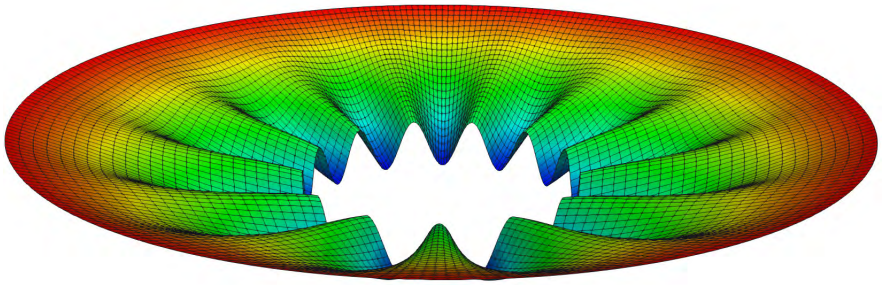

Figure 8.11 Deformation of the annular membrane under diagonal radial tensile load with an angle around 6°

beginning stage and gets the highest value around $F = 175N/mm$, then decreases to negative value, which differs from the one discussed in section 8.6.2. This can be explained as follows. From Eqs. (8.1) and (8.2), the radial and circumferential strains can be written as:

$$\begin{cases} \epsilon_\rho = \dfrac{\partial u}{\partial \rho} + \dfrac{1}{2}\left[\left(\dfrac{\partial w}{\partial \rho}\right)^2 + \left(\dfrac{\partial u}{\partial \rho}\right)^2 + \left(\dfrac{\partial v}{\partial \rho}\right)^2\right] - z\dfrac{\partial^2 w}{\partial \rho^2}, \\ \epsilon_\theta = \dfrac{1}{\rho}\left(\dfrac{\partial v}{\partial \theta} + u\right) + \dfrac{1}{2\rho^2}\left[\left(\dfrac{\partial w}{\partial \theta}\right)^2 + \left(\dfrac{\partial u}{\partial \theta} - v\right)^2 + \left(\dfrac{\partial v}{\partial \theta} + u\right)^2\right] - z\dfrac{1}{\rho^2}\left(\dfrac{\partial^2 w}{\partial \theta^2} + \rho\dfrac{\partial w}{\partial \rho}\right). \end{cases} \tag{8.48}$$

There is an axisymmetric bending before the bifurcation, which means $u(\rho)$ and $w(\rho)$ should be considered. As shown in Fig. 8.13, the stresses on the top and bottom surfaces are nearly the same before bifurcation, therefore the terms related to z can be neglected. After introducing the constitutive relationship and neglecting the terms of second order $\dfrac{1}{2}\left(\dfrac{u}{\rho}\right)^2$ and $\dfrac{\mu}{2}\left(\dfrac{\partial u}{\partial \rho}\right)^2$, the circumferential stress σ_θ can be simplied from Eq. (8.48) as follows:

$$\sigma_\theta \approx \frac{E}{1-\mu^2}\left[\frac{u}{\rho} + \mu\frac{\partial u}{\partial \rho} + \frac{\mu}{2}\left(\frac{\partial w}{\partial \rho}\right)^2\right]. \tag{8.49}$$

As analyzed above, radial displacement u_0 is positive when $F < 428N/mm$, and bending

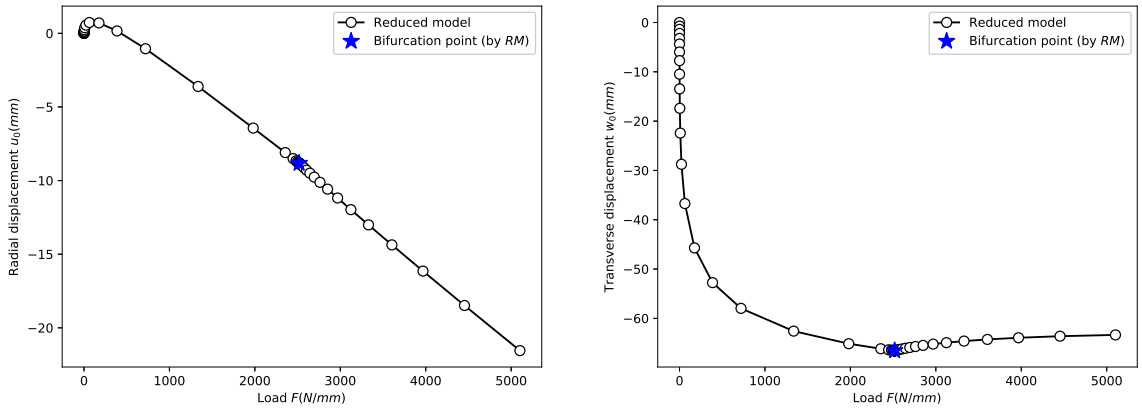

(a)

(b)

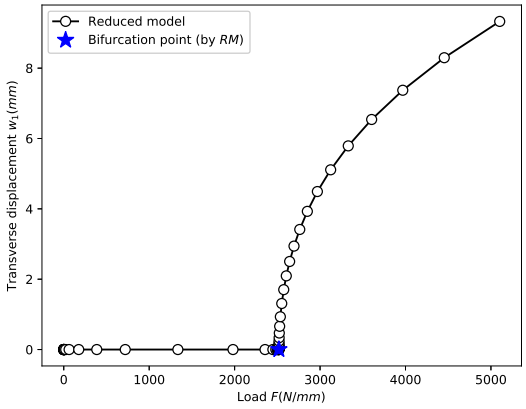

(c)

Figure 8.12 Evolution of displacements of the crest: (a) radial displacement u_0; (b) transverse displacement w_0; (c) transverse displacement w_1

displacement w_0 is uniform, which leads to the increasing positive circumferential stress at the early stage. When $F > 175N/mm$, the slope of w tends to decline gently while the radial displacement u stops increasing and tends to decrease linearly as a function of F. Therefore, the circumferential stress starts to decrease. When the circumferential stress reaches a specific negative value, the wrinkling occurs. After the bifurcation point, the stress evolution is similar to the one discussed in section 8.6.2.

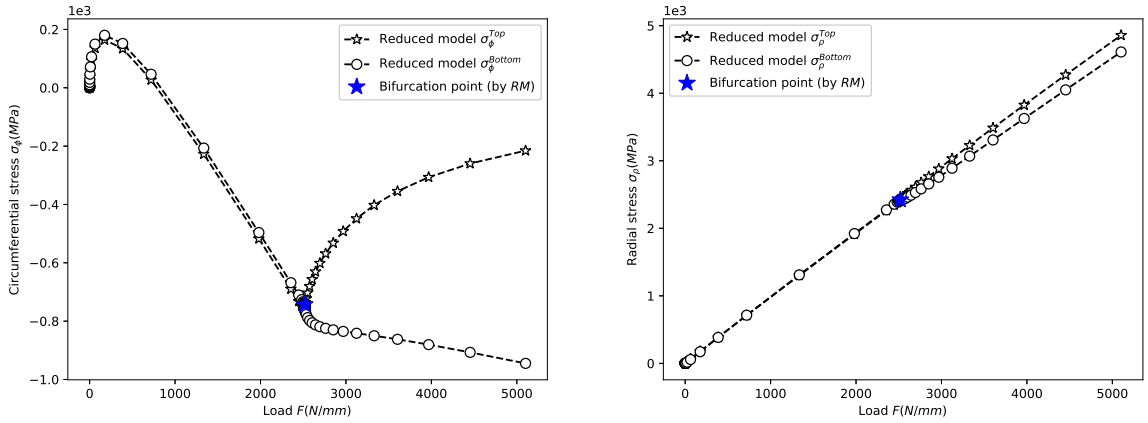

(a) (b)

Figure 8.13 Evolutions of stresses on the top and bottom surfaces of the crest: (a) circumferential stresses; (b) radial stresses

8.9 Circular plate under in-plane radial compressive load

A circular plate under uniform compressive load along the external edge, as shown in Fig.8.14, is investigated in this section to verify that the reduced model can be employed in the instability problems of circular thin plates. The analytical solution of the example obtained by Alfutov [61] is introduced as a benchmark for our result. The stress distribution in the entire process is simulated by using the reduced model. The material properties and geometric dimensions are given in Table. 8.6.

Table 8.6 Material properties and geometric dimensions of the circular plate

Young's modulus E(MPa)	Poisson's ratio μ	Thickness h(mm)	Radius R(mm)
69,000	0.3	10	1000

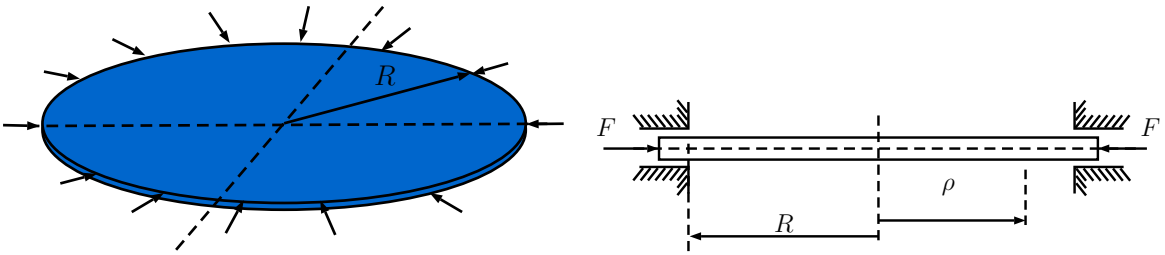

(a) (b)

Figure 8.14 A circular plate under radial compressive load along the external edge

8.9.1 Verification

In this example, there is a uniform distribution of compressive stress in the entire field. The von Kármán nonlinear equation is applied based on the assumption that the transverse displacement is small compared to the in-plane dimensions of the plate before bifurcation:

$$D\left(\frac{\partial^2}{\partial\rho^2}+\frac{1}{\rho}\frac{\partial}{\partial\rho}+\frac{1}{\rho^2}\frac{\partial^2}{\partial\theta^2}\right)\left(\frac{\partial^2 w}{\partial\rho^2}+\frac{1}{\rho}\frac{\partial w}{\partial\rho}+\frac{1}{\rho^2}\frac{\partial^2 w}{\partial\theta^2}\right)-T_\rho^0\frac{\partial^2 w}{\partial\rho^2}-T_\theta^0\left(\frac{1}{\rho}\frac{\partial w}{\partial\rho}+\frac{1}{\rho^2}\frac{\partial^2 w}{\partial\theta^2}\right)=0. \tag{8.50}$$

Then submitting the expansion function of $w(\rho,\theta)$ (Eq. (8.8)) and introducing the loading condition, the following expansion form can be derived:

$$\left(\frac{d^2}{d\rho^2}+\frac{1}{\rho}\frac{d}{d\rho}-\frac{m^2Q^2}{\rho^2}\right)\left(\frac{d^2 w_m}{d\rho^2}+\frac{1}{\rho}\frac{dw_m}{d\rho}-\frac{m^2Q^2 w_m}{\rho^2}\right)+k^2\left(\frac{d^2 w_m}{d\rho^2}+\frac{1}{\rho}\frac{dw_m}{d\rho}-\frac{m^2Q^2 w_m}{\rho^2}\right)=0, \tag{8.51}$$

in which $m=0,1$, $k^2=\dfrac{q}{D}$ and Q is the preassigned circumferential wave number as mentioned above. Both the eigenfunctions and eigenvalues can be obtained from the solutions of the equation, in which the smallest eigenvalue is related to the critical load of the lowest instability pattern.

Eq. (8.51) is the famous Bessel's differential equation, which has solutions named Bessel functions of the first kind, denoted as $J_{mQ}(k\rho)$, in the case of an integer mQ. As derived by Alfutov [61], the roots $k\rho$ of $J_{mQ+1}(k\rho)=0$ are the eigenvalues of related instability patterns, and several of them are listed in Table 8.7. The columns are named as the first roots, the second roots and the third roots respectively, which represent the numbers of half-wave in the radial direction, while the rows represent the circumferential wave numbers Q. The critical compressive loads can be obtained based on these roots by using $k^2=\dfrac{q}{D}$:

$$F_{bif}=\frac{(k\rho)^2 D}{R^2}. \tag{8.52}$$

Table 8.7 The roots value of the first kind Bessel Function

Q	First roots	Second roots	Third roots
0	3.8317	7.0155	10.1734
1	5.1356	8.4172	11.6198
2	6.3801	9.7610	13.0152
3	7.5883	11.0647	14.3725

The instability patterns $R1C3$ and $R3C5$ simulated by the reduced model and the full shell model are presented in Fig. 8.15. The reduced model precisely describes the instability patterns, no matter if the wrinkles arise in the radial or in the circumferential directions.

Fig. 8.16 shows the comparison of solutions among the analytical method, the full shell model and the reduced model, which are in good agreement. In this example, for the case $\frac{h}{R} = 10^{-2}$, the accuracy of the model is acceptable. However, based on more calculations for the case with larger thickness (the results are not shown here), the difference between the reduced model and other models become significant, especially for the high instability patterns. This is because the reduced model is based on several basic assumptions valid only for thin plates. Therefore, the assumptions are no longer accurate enough for the kinematics of the reduced model when the thickness gets to a certain level.

8.9.2 Stress distribution

The evolution of the stress distribution on the top and bottom surface of the crest for the instability pattern $R3C5$ is shown in Fig. 8.17. As mentioned above, before the bifurcation, there is a uniform distribution of compressive stress in the entire field. As shown in Fig. 8.17, the radial and circumferential stresses are the same negative value at the linear stage. When wrinkles occur, the stresses on the top surface increase while the ones on the bottom surface decrease. Meanwhile, it can be seen that although the radial stresses show the same change as circumferential stresses, but they are lower in the post-buckling process. The stress redistribution can be observed with the increase of load, which might cause multiple bifurcations [62].

8.10 Conclusions

Based on the method of Fourier series with slowly variable coefficients [35] and the asymptotic numerical method [58], a one-dimensional reduced model is constructed to model circumferential periodic instability patterns in circular domains. The reduced model is verified to be

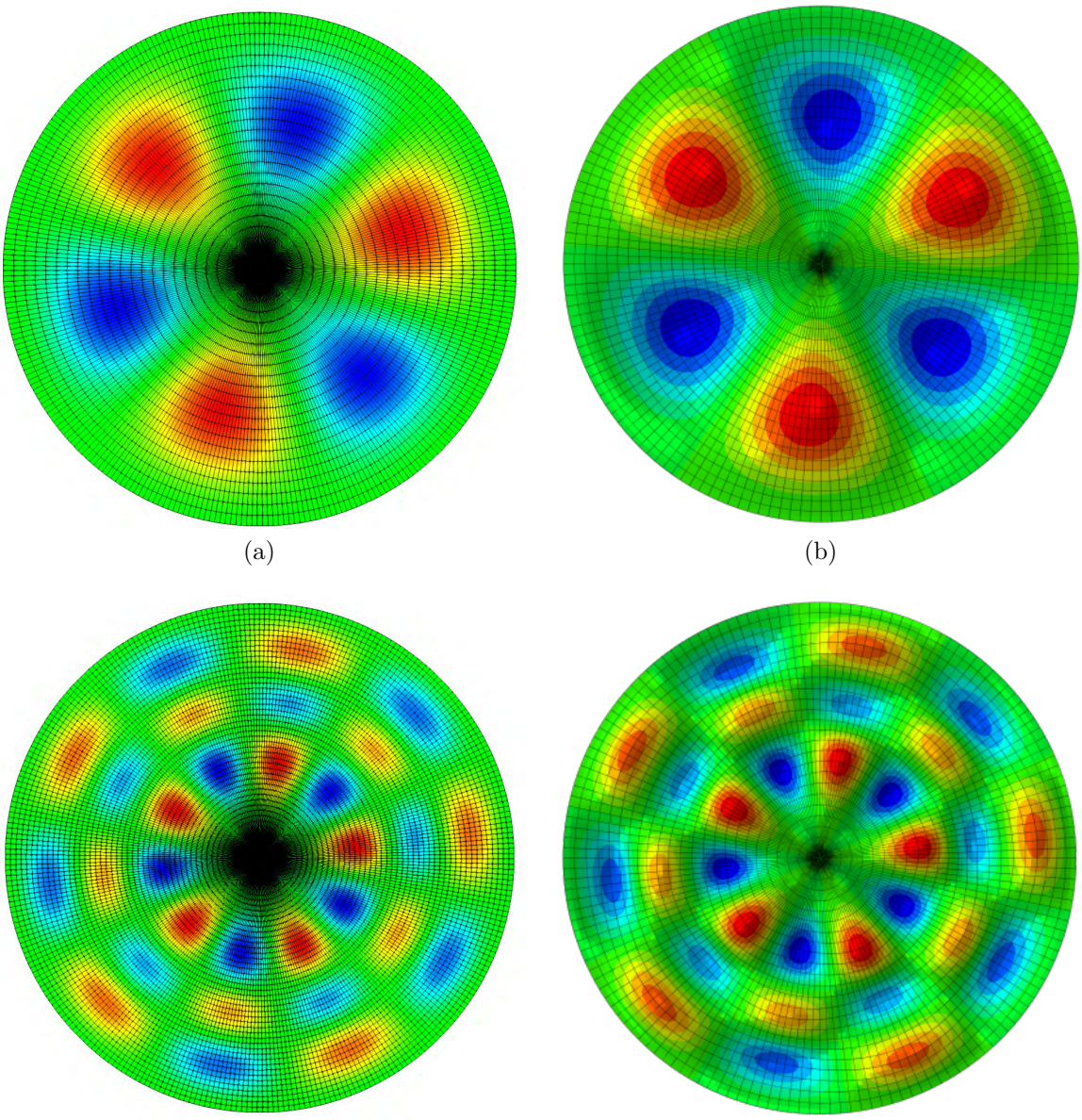

(a) (b)

(c) (d)

Figure 8.15 Instability patterns of the circular plate under compressive load along the external edge predicted by two different models: (a) reduced model $R1C3$; (b) full shell model $R1C3$; (c) reduced model $R3C5$; (d) full shell model $R3C5$

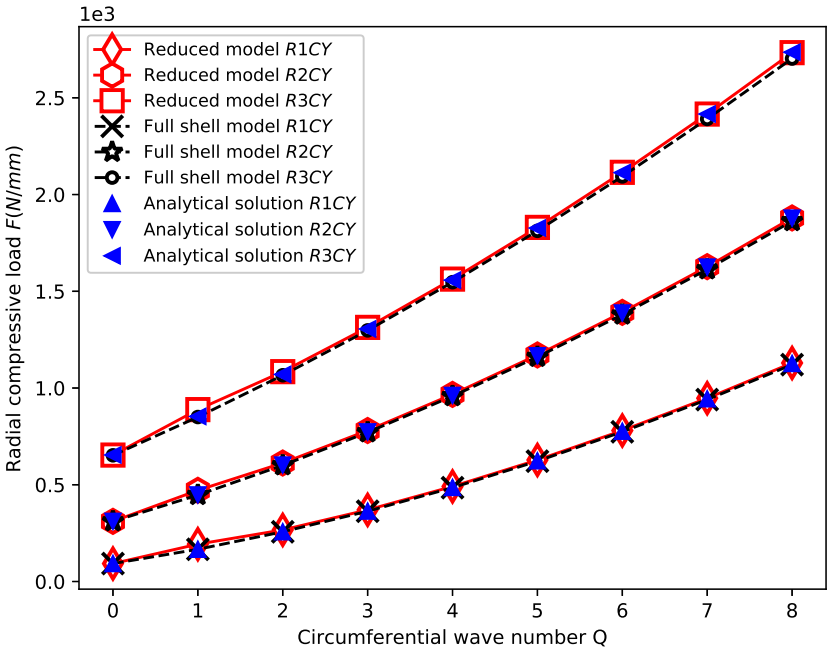

Figure 8.16 Critical loads of different instability patterns predicted by analytical solutions and numerical simulations

efficient and accurate by comparing its results with those of ABAQUS for an annular membrane under various loads. With reduction of 99.8% DOFs, the reduced model still precisely simulate the evolution of displacement and stress. Furthermore, the wrinkling patterns are predicted without introducing imperfection to the initial model. Since the Hermite interpolation is used for all the displacements, the reduced model is accurate in the simulation of pure bending example without membrane locking problem. In the examples of annular membrane under diagonal stretch and circular plate under in-plane compression, the reduced model simulates the complex deformations and evolutions of stresses in different post-buckling processes. Therefore, the reduced model shows the potential to precisely predict the buckling patterns and efficiently simulate the post-buckling processes of various wrinkling phenomena in circular domain.

Further modification can be made to extend the application scope of the reduced model. For example, the Fourier expansion on the radial displacement can be considered to make it easier to trace radial wrinkle patterns with large wave number. The phase modulation in the macroscopic unknowns is another important factor to be considered, which enables modeling more complex wrinkle patterns such as the one produced by shear loads [31]. The proposed modeling method is also promising to model other periodic instability problems in circular

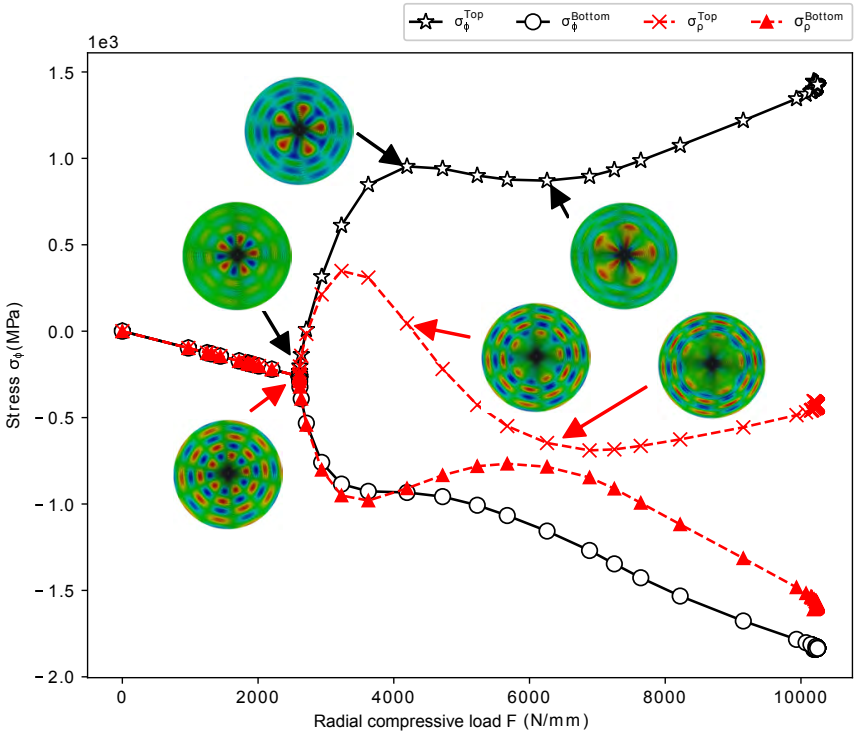

Figure 8.17 Evolutions of stresses on the top and bottom surfaces of the crests

domains, such as circular film-substrate systems [47], circular sandwich plates [49] or circular functionally graded shells [52, 63–65].

Acknowledgements

This work has been supported by the National Natural Science Foundation of China (Grant Nos. 11772238 and 11702198). The authors also acknowledge the financial support of the National Science & Engineering Research Council of Canada (NSERC).

Bibliography

[1] C. H. Jenkins, *Gossamer spacecraft: Membrane and inflatable structures technology for space applications*. American Institute of Aeronautics and Astronautics, 2001.

[2] J. A. Rogers, T. Someya, and Y. Huang, "Materials and mechanics for stretchable electronics," *science*, vol. 327, no. 5973, pp. 1603–1607, 2010.

[3] Y. Zhang, Y. Huang, and J. A. Rogers, "Mechanics of stretchable batteries and supercapacitors," *Current Opinion in Solid State and Materials Science*, vol. 19, no. 3, pp. 190–199, 2015.

[4] Z. Yi, L. G. Bettini, G. Tomasello, P. Kumar, P. Piseri, I. Valitova, P. Milani, F. Soavi, and F. Cicoira, "Flexible conducting polymer transistors with supercapacitor function," *Journal of Polymer Science Part B: Polymer Physics*, vol. 55, no. 1, pp. 96–103, 2017.

[5] X. Huang, Y. Liu, H. Cheng, W. Shin, J. A. Fan, Z. Liu, C. Lu, G. Kong, K. Chen, D. Patnaik, S. Lee, S. Hage-Ali, Y. Huang, and J. A. Rogers, "Materials and designs for wireless epidermal sensors of hydration and strain," *Advanced Functional Materials*, vol. 24, pp. 3846–3854, 2014.

[6] G. A. Holzapfel, R. Eberlein, P. Wriggers, and H. W. Weizsäcker, "Large strain analysis of soft biological membranes: Formulation and finite element analysis," *Computer Methods in Applied Mechanics and Engineering*, vol. 132, pp. 45–61, 1996.

[7] C. Zhang, B. Li, J. Tang, X. Wang, Z. Qin, and X. Feng, "Experimental and theoretical studies on the morphogenesis of bacterial biofilms," *Soft Matter*, vol. 13, pp. 7389–7397, 2017.

[8] Z. Zhao, Z. Liu, J. Du, G. Xu, and X. Feng, "A dynamic biochemomechanical model of geometry-confined cell spreading," *Biophysical Journal*, vol. 112, pp. 2377–2386, 2017.

[9] A. S. Ademiloye, L. W. Zhang, and K. M. Liew, "A multiscale framework for large deformation modeling of RBC membranes," *Computer Methods in Applied Mechanics and Engineering*, vol. 329, pp. 144–167, 2018.

[10] C. Williams, J. Summerscales, and S. Grove, "Resin infusion under flexible tooling (RIFT): A review," *Composites Part A: Applied Science and Manufacturing*, vol. 27, pp. 517–524, 1996.

[11] B. W. Grimsley, P. Hubert, X. Song, R. J. Cano, A. C. Loos, and R. B. Pipes, "Flow and compaction during the vacuum assisted resin transfer molding process," Tech. Rep., 2001.

[12] N. C. Correia, F. Robitaille, A. C. Long, C. D. Rudd, P. Šimáček, and S. G. Advani, "Analysis of the vacuum infusion moulding process: I. Analytical formulation," *Composites Part A: Applied Science and Manufacturing*, vol. 36, pp. 1645–1656, 2005.

[13] F. Trochu, S. Soukane, and B. Touraine, "Flexible injection: a novel LCM technology for low cost manufacturing of high performance composites. Part II: numerical model," in *9 th Int. Conf. on Flow Proc. in Comp. Mat*, 2008.

[14] P. Causse, E. Ruiz, and F. Trochu, "Influence of preforming on the quality of curved composite parts manufactured by flexible injection," *International Journal of Material Forming*, vol. 6, pp. 341–362, 2013.

[15] E. Cerda, K. Ravi-Chandar, and L. Mahadevan, "Thin films: Wrinkling of an elastic sheet under tension," *Nature*, vol. 419, no. 6907, pp. 579–580, 2002.

[16] B. Li, Y. Cao, X. Feng, and H. Gao, "Mechanics of morphological instabilities and surface wrinkling in soft materials: A review," *Soft Matter*, vol. 8, pp. 5728–5745, 2012.

[17] N. Bowden, S. Brittain, A. G. Evans, J. W. Hutchinson, and G. M. Whitesides, "Spontaneous formation of ordered structures in thin films of metals supported on an elastomeric polymer," *Nature*, vol. 393, no. May, pp. 146–149, 1998.

[18] E. Cerda and L. Mahadevan, "Geometry and physics of wrinkling," *Physical Review Letters*, vol. 90, no. 7, p. 074302, 2003.

[19] N. Jacques, A. Elias, M. Potier-Ferry, and H. Zahrouni, "Buckling and wrinkling during strip conveying in processing lines," *Journal of Materials Processing Technology*, vol. 190, no. 1-3, pp. 33–40, 2007.

[20] A. Agrawal, N. V. Reddy, and P. M. Dixit, "Prediction of wrinkling and determination of minimum blankholding pressure in multistage deep drawing," *Journal of Manufacturing Science and Engineering*, vol. 133, no. 6, p. 061023, 2011.

[21] H. Wagner, "Flat sheet metal girders with very thin metal web. Part I : General theories and assumptions," *Zeitschrift für Motortechnik und Luftschiffahrt*, vol. 20, no. 8, pp. 200–207, 1929.

[22] A. C. Pipkin, "Integration of an equation in membrane theory," *Zeitschrift für angewandte Mathematik und Physik ZAMP*, vol. 19, no. 5, pp. 818–819, 1968.

[23] D. J. Steigmann and A. C. Pipkin, "Wrinkling of pressurized membranes," *Journal of Applied Mechanics*, vol. 56, no. 3, p. 624, 1989.

[24] D. G. Roddeman, J. Drukker, C. W. J. Oomens, and J. D. Janssen, "The wrinkling of thin membranes : Part I — theory," *Journal of Applied Mechanics*, vol. 54, pp. 884–887, 1987.

[25] H. Schoop, L. Taenzer, and J. Hornig, "Wrinkling of nonlinear membranes," *Computational Mechanics*, vol. 29, no. 1, pp. 68–74, 2002.

[26] R. H. Plaut, "Linearly elastic annular and circular membranes under radial, transverse, and torsional loading. Part I: Large unwrinkled axisymmetric deformations," *Acta Mechanica*, vol. 202, pp. 79–99, 2009.

[27] C. D. Coman and D. M. Haughton, "Localized wrinkling instabilities in radially stretched annular thin films," *Acta Mechanica*, vol. 185, pp. 179–200, 2006.

[28] C. D. Coman, "On the applicability of tension field theory to a wrinkling instability problem," *Acta Mechanica*, vol. 190, pp. 57–72, 2007.

[29] C. D. Coman, "Some applications of the WKB method to the wrinkling of bi-annular plates in tension," *Acta Mechanica*, vol. 224, pp. 399–423, 2013.

[30] J. C. Géminard, R. Bernai, and F. Melo, "Wrinkle formations in axi-symmetrically stretched membranes," *European Physical Journal E*, vol. 15, pp. 117–126, 2004.

[31] C. G. Wang, Y. P. Liu, L. Lan, L. Li, and H. F. Tan, "Post-wrinkling analysis of a torsionally sheared annular thin film by using a compound series method," *International Journal of Mechanical Sciences*, vol. 110, pp. 22–33, 2016.

[32] J. Argyris, L. Tenek, and L. Olofsson, "TRIC: a simple but sophisticated 3-node triangular element based on 6 rigid-body and 12 straining modes for fast computational simulations of arbitrary isotropic and laminated composite shells," *Computer Methods in Applied Mechanics and Engineering*, vol. 145, pp. 11–85, 1997.

[33] A. G. Combescure, "Static and dynamic buckling of large thin shells," *Nuclear Engineering and Design*, vol. 92, pp. 339–354, 1986.

[34] A. G. Combescure, "Modeling elastic-plastic buckling of sandwich axisymmetric shells: On the limits of " shell " models and analytical solutions," *Advanced Modeling and Simulation in Engineering Sciences*, pp. 1–27, 2014.

[35] N. Damil and M. Potier-Ferry, "Influence of local wrinkling on membrane behaviour: A new approach by the technique of slowly variable Fourier coefficients," *Journal of the Mechanics and Physics of Solids*, vol. 58, no. 8, pp. 1139–1153, 2010.

[36] N. Damil, M. Potier-ferry, and H. Hu, "New nonlinear multi-scale models for wrinkled membranes," *Comptes Rendus Mecanique*, vol. 341, no. 8, pp. 616–624, 2013.

[37] N. Damil, M. Potier-Ferry, and H. Hu, "Membrane wrinkling revisited from a multi-scale point of view," *Advanced Modeling and Simulation in Engineering Sciences*, vol. 1, no. 1, p. 6, 2014.

[38] Q. Huang, H. Hu, K. Yu, M. Potier-Ferry, S. Belouettar, and N. Damil, "Macroscopic simulation of membrane wrinkling for various loading cases," *International Journal of Solids and Structures*, vol. 64-65, pp. 246–258, 2015.

[39] Y. Liu, K. Yu, H. Hu, S. Belouettar, M. Potier-Ferry, and N. Damil, "A new Fourier-related double scale analysis for instability phenomena in sandwich structures," *International Journal of Solids and Structures*, vol. 49, no. 22, pp. 3077–3088, 2012.

[40] K. Yu, H. Hu, S. Chen, S. Belouettar, and M. Potier-Ferry, "Multi-scale techniques to analyze instabilities in sandwich structures," *Composite Structures*, vol. 96, pp. 751–762, 2013.

[41] Q. Huang, Y. Liu, H. Hu, Q. Shao, K. Yu, G. Giunta, S. Belouettar, and M. Potier-Ferry, "A Fourier-related double scale analysis on the instability phenomena of sandwich plates," *Computer Methods in Applied Mechanics and Engineering*, vol. 318, pp. 270–295, 2017.

[42] Q. Huang, J. Yang, W. Huang, Y. Liu, H. Hu, G. Giunta, and S. Belouettar, "A new Fourier-related double scale analysis for wrinkling analysis of thin films on compliant substrates," *Composite Structures*, vol. 160, pp. 613–624, 2017.

[43] J. T. Oden and J. E. Key, "Numerical analysis of finite axisymmetric deformations of incompressible elastic solid of revolution," *International Journal of Solids and Structures*, vol. 6, pp. 497–518, 1970.

[44] F. C. Bardi, S. Kyriakides, and H. D. Yun, "Plastic buckling of circular tubes under axial compression – part II: Analysis," *International Journal of Mechanical Sciences*, vol. 48, pp. 842–854, 2006.

[45] Y. Cao, F. Jia, Y. Zhao, X. Feng, and S. Yu, "Buckling and post-buckling of a stiff film resting on an elastic graded substrate," *International Journal of Solids and Structures*, vol. 49, pp. 1656–1664, 2012.

[46] J. Yang, Q. Huang, H. Hu, G. Giunta, S. Belouettar, and M. Potier-Ferry, "A new family of finite elements for wrinkling analysis of thin films on compliant substrates," *Composite Structures*, vol. 119, pp. 568–577, 2015.

[47] X. Huang, H. Zhao, W. Xie, W. Hong, and X. Feng, "Radial wrinkles on film-substrate system induced by local prestretch: A theoretical analysis," *International Journal of Solids and Structures*, vol. 58, pp. 12–19, 2015.

[48] K. Yu, H. Hu, H. Tang, G. Giunta, M. Potier-Ferry, and S. Belouettar, "A novel two-dimensional finite element to study the instability phenomena of sandwich plates," *Computer Methods in Applied Mechanics and Engineering*, vol. 283, pp. 1117–1137, 2015.

[49] N. Naderi Beni and M. Botshekanan Dehkordi, "An extension of Carrera unified formulation in polar coordinate for analysis of circular sandwich plate with FGM core using GDQ method," *Composite Structures*, vol. 185, pp. 421–434, 2018.

[50] F. A. Fazzolari and E. Carrera, "Advanced variable kinematics Ritz and Galerkin formulations for accurate buckling and vibration analysis of anisotropic laminated composite plates," *Composite Structures*, vol. 94, pp. 50–67, 2011.

[51] J. N. Reddy and J. Berry, "Nonlinear theories of axisymmetric bending of functionally graded circular plates with modified couple stress," *Composite Structures*, vol. 94, pp. 3664–3668, 2012.

[52] L. Ke, J. Yang, S. Kitipornchai, and M. A. Bradford, "Bending, buckling and vibration of size-dependent functionally graded annular microplates," *Composite Structures*, vol. 94, pp. 3250–3257, 2012.

[53] L. W. Zhang, K. M. Liew, and J. N. Reddy, "Postbuckling behavior of bi-axially compressed arbitrarily straight-sided quadrilateral functionally graded material plates," *Computer Methods in Applied Mechanics and Engineering*, vol. 300, pp. 593–610, 2016.

[54] O. C. Zienkiewicz, *The finite element method*. McGraw-Hill, 1977.

[55] H. Hu, N. Damil, and M. Potier-Ferry, "A bridging technique to analyze the influence of boundary conditions on instability patterns," *Journal of Computational Physics*, vol. 230, pp. 3753–3764, 2011.

[56] J. N. Reddy, *An introduction to nonlinear finite element analysis*. UK: Oxford, 2004.

[57] J. Choe, Q. Huang, J. Yang, and H. Hu, "An efficient approach to investigate the post-buckling behaviors of sandwich structures," *Composite Structures*, vol. 201, pp. 377–388, 2018.

[58] B. Cochelin, N. Damil, and M. Potier-Ferry, *Méthode asymptotique numérique*. Hermes Lavoissier, 2007.

[59] F. Trochu, "A contouring program based on dual kriging interpolation," *Engineering with Computers*, vol. 9, no. 3, pp. 160–177, 1993.

[60] R. Vermorel, N. Vandenberghe, and E. Villermaux, "Impacts on thin elastic sheets," *Proceedings of the Royal Society A: Mathematical, Physical and Engineering Sciences*, vol. 465, pp. 823–842, 2009.

[61] N. A. Alfutov, *Stability of elastic structures*. Springer Science & Business Media, 2013.

[62] F. Xu, M. Potier-Ferry, S. Belouettar, and H. Hu, "Multiple bifurcations in wrinkling analysis of thin films on compliant substrates," *International Journal of Non-Linear Mechanics*, vol. 76, pp. 203–222, 2015.

[63] M. Mehri, H. Asadi, and Q. Wang, "Buckling and vibration analysis of a pressurized CNT reinforced functionally graded truncated conical shell under an axial compression using HDQ method," *Computer Methods in Applied Mechanics and Engineering*, vol. 303, pp. 75–100, 2016.

[64] H. Shen, "Thermal buckling and postbuckling behavior of functionally graded carbon nanotube-reinforced composite cylindrical shells," *Composites Part B: Engineering*, vol. 43, pp. 1030–1038, 2012.

[65] K. M. Liew, Z. X. Lei, J. L. Yu, and L. W. Zhang, "Postbuckling of carbon nanotube-reinforced functionally graded cylindrical panels under axial compression using a meshless approach," *Computer Methods in Applied Mechanics and Engineering*, vol. 268, pp. 1–17, 2014.

CHAPTER 9 ARTICLE 6 : WRINKLING ANALYSIS OF CIRCULAR MEMBRANES BY A FOURIER BASED REDUCED MODEL

W. Huang, W. Yan, R. Xu, Q. Huang*, J. Yang*, F. Trochu, H. Hu

Submitted to *Thin-Walled Structures on 14 July 2020*

9.1 Chapter overview

Chapter 8 developed a Fourier based reduced model for efficient and accurate numerical simulations of wrinkling problems in circular membranes. Due to the fact that only two harmonics (namely 0^{th} and $\pm 1^{st}$ orders) are considered in the reduced model, it is necessary to select the wave number before simulations. This chapter presents the article submitted to *Thin-Walled Structures*, in which the reduced model is further improved by accounting for several Fourier harmonics. The improved reduced model can automatically choose the lowest instability pattern to ensure the system to be in a state of minimum energy, which facilitates the study of cases with unknown wrinkling patterns. The instability mechanisms of an annular membrane under in-plane stretching is investigated, indicating that the appearance of wrinkles in circular membranes does not depend on Poisson's effect.

9.2 Abstract

As a soft material with an almost negligible bending stiffness, membranes may easily lose their mechanical stability. Generally, the wave lengths of the wrinkles are quite small, leading to the intensive computation in numerical simulations. To deal with the issue, a Fourier based reduced model is recently developed by [1] showing good performance in both accuracy and efficiency for the simulation of circular membrane wrinkling. The objective of this paper is to improve the reduced model by accounting for several Fourier harmonics, then employ it to study the wrinkling phenomenon in the circular domain. By accounting for several Fourier harmonics, the reduced model can automatically distinguish the lowest instability pattern, which facilitates the study of the cases of unknown wrinkling patterns. The instability mechanisms of an annular membrane under in-plane stretching is also investigated. The results show that the appearance of the wrinkles in circular membranes does not rely on the Poisson's effect, although the value of Poisson's ratio and the geometric dimensions have great influence on the wrinkling patterns. Finally, the instability problem of a circular thin

plate under the in-plane compression is studied. The effects of the boundary condition and the wrinkling pattern on the crest position and the critical load are investigated.

9.3 Introduction

Membrane structures have been widely used in aerospace and civil engineering, because of their high performance in resisting tensional loads with much lighter weight compared with traditional structures. In recent years, the application of membrane structures has been broaden to different engineering fields. In order to meet specific structures, various kinds of membrane structures have been designed. For example, by assembling electronical elements on membranes [2], various stretchable electronics are fabricated, including stretchable organic electrochemical transistors [3], supercapacitors [4] and wireless epidermal sensors [5]. They present superior mechanical and wearable properties inaccessible in traditional electronics. In some composite manufacturing processes, such as Flexible Injection (FI) [6] and Vacuum Assisted Resin Transfer Molding (VARTM) [7], membranes play a key roles in inducing the through-thickness compaction [8, 9] and impregnation [10] for faster manufacturing process of woven fabric reinforced composites [11].

Membranes easily lose the mechanical stability and wrinkles when subject to in-plane compressive stress [12–14] due to their almost negligible bending stiffness. Such phenomena have significant effects on the mechanical and optical properties of membranes, leading to undesired problems in engineering applications, such as the production defects in strip conveying process [15] and deep drawing process [16]. To explore the mechanism for the instability in membranes, a large amount of analytical studies [17–20], experimental analyses [21, 22] and numerical simulations [23–28] have been conducted. The finite element method has been proved to be a robust and efficient way to capture the complex evolution of wrinkles and stress distribution. However, the general FE models either present intensive computation especially for the case with small wave length or suffer the difficulties of choosing a proper imperfection.

In order to deal with the issues, Damil and Potier-Ferry [29] proposed a reduced-order FE model based on the Fourier expansion of the displacement field. This approach reduce the computation and ease the sensitivity of post-buckling behaviors to the applied geometric imperfection, and have been adopted to study various kinds of instability problems, such as rectangular membranes [30–33], rectangular sandwich plates [34–36], and thin films on compliant substrates [37]. Recently, Huang et al. [1] employed this approach to develop a reduced model to study the wrinkling problems in circular membranes, which shows good performance in both accuracy and efficiency. However, only two harmonics (namely 0^{th} and

$\pm 1^{st}$ orders) are considered in the reduced model. This paper aims at improving the reduced model by accounting for several Fourier harmonics to facilitates the selection of the unknown lowest instability pattern. The reduced model is used to investigate the instability mechanism of the stretched annular membrane. Moreover, the effects of Poisson's ratio and the geometric dimensions on the wrinkling patterns are also discussed. Finally, the instability problem of a circular thin plate under the in-plane compression is studied.

This paper is structured as follows. In section 9.4, the finite element procedure is described, and the reduced model is constructed in cylindrical coordinates. In section 9.5 and section 9.6, the model is used to study the wrinkling phenomena of the stretched annular membrane and the compressed circular thin plate. The paper ends with a discussion on main conclusions.

9.4 Reduced model for instability problems in circular domain

In this section, first basic equations are reviewed; then the method of Fourier series with slowly variable coefficients is briefly reviewed; after that, the finite element procedure to construct the reduced model is described; finally, the nonlinear system is solved by the Asymptotic Numerical Method.

9.4.1 Basic functions

The geometric relation is divided into linear and non-linear parts, in which the linear strain in the circular domain is formed of membrane strains ϵ_{ij}^m and bending strains ϵ_{ij}^b (see [38]):

$$\begin{aligned}
\epsilon_\rho^m &= \frac{\partial u}{\partial \rho}, && (a)\\
\epsilon_\theta^m &= \frac{1}{\rho}\left(\frac{\partial v}{\partial \theta} + u\right), && (b)\\
\epsilon_{\rho\theta}^m &= \frac{1}{2}\left[\frac{\partial v}{\partial \rho} + \frac{1}{\rho}\left(\frac{\partial u}{\partial \theta} - v\right)\right], && (c)\\
\epsilon_\rho^b &= -\frac{\partial^2 w}{\partial \rho^2}, && (d)\\
\epsilon_\theta^b &= \frac{1}{\rho^2}\left(-\frac{\partial^2 w}{\partial \theta^2} - \rho\frac{\partial w}{\partial \rho}\right), && (e)\\
\epsilon_{\rho\theta}^b &= \frac{1}{\rho^2}\left(-\rho\frac{\partial^2 w}{\partial \rho \partial \theta} + \frac{\partial w}{\partial \theta}\right), && (f)
\end{aligned} \tag{9.1}$$

where u, v, w denote respectively the radial, circumferential and transversal components of the mid-plane displacement in cylindrical coordinates ρ ($\rho \geq 0$) and θ ($2\pi \geq \theta \geq 0$). Quadratic membrane strains ϵ_{ij}^q measuring the variation of strain state in an infinitely small increment [26] are expressed as follows:

$$\begin{aligned}
\epsilon_\rho^q &= \frac{1}{2}\left[\left(\frac{\partial w}{\partial \rho}\right)^2 + \left(\frac{\partial u}{\partial \rho}\right)^2 + \left(\frac{\partial v}{\partial \rho}\right)^2\right], && (a)\\
\epsilon_\theta^q &= \frac{1}{2\rho^2}\left[\left(\frac{\partial w}{\partial \theta}\right)^2 + \left(\frac{\partial u}{\partial \theta} - v\right)^2 + \left(\frac{\partial v}{\partial \theta} + u\right)^2\right], && (b)\\
\epsilon_{\rho\theta}^q &= \frac{1}{2\rho}\left[\frac{\partial w}{\partial \theta}\frac{\partial w}{\partial \rho} + \frac{\partial u}{\partial \rho}\left(\frac{\partial u}{\partial \theta} - v\right) + \frac{\partial v}{\partial \rho}\left(\frac{\partial v}{\partial \theta} + u\right)\right]. && (c)
\end{aligned} \tag{9.2}$$

The strains are then combined as follows:

$$\begin{aligned}\{\boldsymbol{\gamma}\} &= \left\{ \begin{array}{c} \epsilon_\rho \\ \epsilon_\theta \\ \gamma_{\rho\theta} \end{array} \right\} = \left\{ \begin{array}{c} \epsilon_\rho^m \\ \epsilon_\theta^m \\ 2\epsilon_{\rho\theta}^m \end{array} \right\} + z \left\{ \begin{array}{c} \epsilon_\rho^b \\ \epsilon_\theta^b \\ 2\epsilon_{\rho\theta}^b \end{array} \right\} + \left\{ \begin{array}{c} \epsilon_\rho^q \\ \epsilon_\theta^q \\ 2\epsilon_{\rho\theta}^q \end{array} \right\} \\ &= \{\boldsymbol{\gamma}^m\} + z\{\boldsymbol{\gamma}^b\} + \{\boldsymbol{\gamma}^q\},\end{aligned} \tag{9.3}$$

In this paper, the material behavior is assumed to be linear elastic. However, note that the methodology is also valid for nonlinear constitutive laws. The constitutive relations are expressed as:

$$\left\{ \begin{array}{l} \sigma_\rho = \dfrac{E}{1-\mu^2} \left(\epsilon_\rho + \mu\epsilon_\theta\right), \\ \sigma_\theta = \dfrac{E}{1-\mu^2} \left(\epsilon_\theta + \mu\epsilon_\rho\right), \\ \tau_{\rho\theta} = \dfrac{E}{1+\mu}\gamma_{\rho\theta}, \end{array} \right. \tag{9.4}$$

where E is Young's modulus and μ is Poisson's ratio. The internal work of the membrane occupying the region ω is divided into two parts, including a membrane term due to stretching and a bending contribution:

$$\left\{ \begin{array}{l} \mathcal{W}_{int} = \mathcal{W}_{mem} + \mathcal{W}_{ben}, \\ 2\mathcal{W}_{mem} = \displaystyle\iint_\omega \left(\langle\boldsymbol{\gamma}^m\rangle + \langle\boldsymbol{\gamma}^q\rangle\right) \left[\mathbf{L}^m\right] \left(\{\boldsymbol{\gamma}^m\} + \{\boldsymbol{\gamma}^q\}\right) \, d\omega, \\ 2\mathcal{W}_{ben} = \displaystyle\iint_\omega \left\langle\boldsymbol{\gamma}^b\right\rangle \left[\mathbf{L}^b\right] \left\{\boldsymbol{\gamma}^b\right\} \, d\omega, \end{array} \right. \tag{9.5}$$

in which the two elasticity tensors $[\mathbf{L}^m]$ and $\left[\mathbf{L}^b\right]$ are written as:

$$[\mathbf{L}^m] = \frac{Eh}{1-\mu^2} \begin{bmatrix} 1 & \mu & 0 \\ \mu & 1 & 0 \\ 0 & 0 & \frac{1-\mu}{2} \end{bmatrix}, [\mathbf{L}^b] = \frac{Eh^3}{12(1-\mu^2)} \begin{bmatrix} 1 & \mu & 0 \\ \mu & 1 & 0 \\ 0 & 0 & \frac{1-\mu}{2} \end{bmatrix}, \tag{9.6}$$

where h is the membrane thickness.

9.4.2 The method of Fourier series with slowly variable coefficients

The common instability modes observed in membranes are periodic or nearly periodic along wave length direction. To exploit this periodicity, Damil and Potier-Ferry [29] proposed the method of Fourier series with slowly variable coefficients to expand the rapidly varying displacement field of the full shell model into Fourier series and to consider the slowly variable

Fourier coefficients as new unknowns. The method has been widely adopted to generate the efficient reduced model in Cartesian coordinates to study the wrinkling phenomena in rectangular domains [30–37]. The method was recently employed by Huang et al. [1] to construct the reduced model to study the wrinkling phenomena in circular domains. The unknown displacement field of the circular membrane with periodic instability patterns in the circumferential direction is expressed as follows (see Fig. 9.1):

$$\mathbf{U}(\rho,\theta) = \sum_{m=-\infty}^{+\infty} \mathbf{U}_m(\rho)\mathrm{e}^{\mathrm{i}mQ\theta}, \tag{9.7}$$

where i is the imaginary unit, m denotes the m^{th} order harmonic, and Q ($Q \in \mathbb{N}$) is a pre-assigned integer wave-parameter presenting the wave number of the wrinkles in the circumferential direction. The unknown field $\mathbf{U}(\rho,\theta)$ is decoupled into $e^{\mathrm{i}mQ\theta}$ in the circumferential direction and $\mathbf{U}_m(\rho)$ in the radial direction. As a result, the original wrinkling analysis is simplified to a one-dimensional problem, where all the unknown fields are changed with the radius ρ.

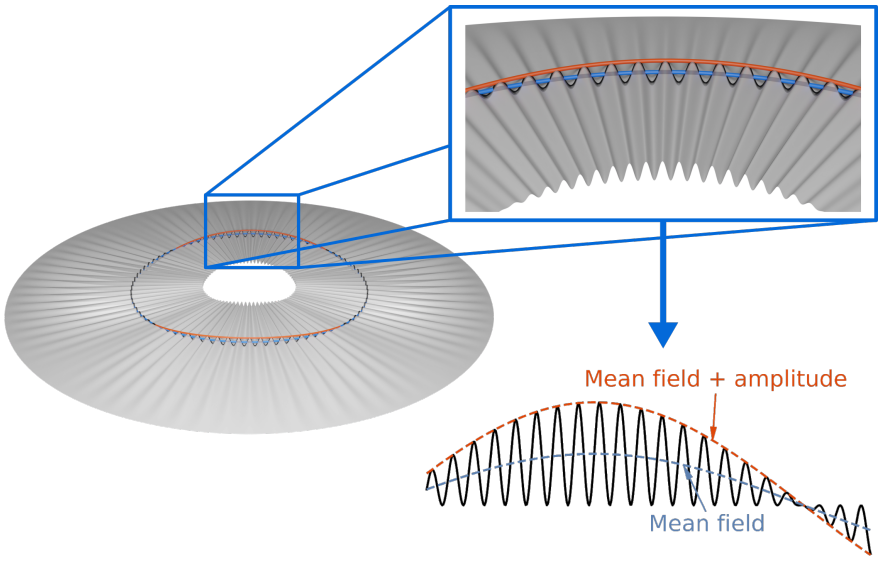

Figure 9.1 Diagram of the method of Fourier series with slowly variable coefficients

9.4.3 Energy equations

The calculation rules proposed by [29] is introduced to construct the reduced model. Given two Fourier coefficients $a(\rho)$ and $b(\rho)$ as in Eq. (9.7), the following identities hold:

$$\int_0^L a(\rho)b(\rho)d\rho = \int_0^L \sum_{m=-\infty}^{+\infty} a_m(\rho)b_{-m}(\rho)d\rho, \tag{9.8}$$

$$\left(\frac{da}{d\rho}\right)_m = (a')_m = \left(\frac{d}{d\rho} + \mathrm{i}mQ\right) a_m = (a_m)' + \mathrm{i}mQa_m, \tag{9.9}$$

$$\left(\frac{d^2a}{d\rho^2}\right)_m = (a'')_m = \left(\frac{d}{d\rho} + \mathrm{i}mQ\right)^2 a_m = (a_m)'' + 2\mathrm{i}mQ(a_m)' - m^2Q^2a_m^2, \tag{9.10}$$

$$(ab)_m = \sum_{n=-\infty}^{+\infty} a_n b_{m-n}. \tag{9.11}$$

after introducing Eqs. (9.8)-(9.11), the geometric equations are deduced from Eqs. (9.1) and (9.2) as follows:

$$\begin{aligned}\epsilon_{\rho m} =& \left[\frac{\partial u_m}{\partial \rho} + \frac{1}{2}\sum_{n=-n_j}^{n_j}\left(\frac{\partial w_n}{\partial \rho}\frac{\partial w_{m-n}}{\partial \rho} + \frac{\partial u_n}{\partial \rho}\frac{\partial u_{m-n}}{\partial \rho} + \frac{\partial v_n}{\partial \rho}\frac{\partial v_{m-n}}{\rho}\right)\right.\\ &\left. - z\frac{\partial^2 w_m}{\partial \rho^2}\right]\mathrm{e}^{\mathrm{i}mQ\theta},\end{aligned} \tag{9.12}$$

$$\begin{aligned}\epsilon_{\theta m} =& \left[\frac{u_m}{\rho} + \frac{1}{2\rho^2}\sum_{n=-n_j}^{n_j}\left(-n(m-n)Q^2w_nw_{m-n} + v_nv_{m-n} + u_nu_{m-n}\right)\right.\\ &\left. + \frac{z}{\rho^2}\left(m^2Q^2w_m - \rho\frac{\partial w_m}{\partial \rho}\right)\right]\mathrm{e}^{\mathrm{i}mQ\theta},\end{aligned} \tag{9.13}$$

$$\begin{aligned}2\epsilon_{\rho\theta m} =& \left[\frac{\partial v_m}{\partial \rho} - \frac{v_m}{\rho} + \frac{1}{\rho}\sum_{n=-n_j}^{n_j}\left(\mathrm{i}nQw_n\frac{\partial w_{m-n}}{\partial \rho} - v_n\frac{\partial u_{m-n}}{\partial \rho} + u_n\frac{\partial v_{m-n}}{\partial \rho}\right)\right.\\ &\left. + \frac{z}{\rho^2}\left(\mathrm{i}2mQw_m - \mathrm{i}2mQ\rho\frac{\partial w_m}{\partial \rho}\right)\right]\mathrm{e}^{\mathrm{i}mQ\theta},\end{aligned} \tag{9.14}$$

in which n_j is the Fourier expansion orders considered for the reduced model. In the current work, considering that only the transverse displacement w shows obvious periodic oscillation in the circumferential direction, it is assumed that $u(\rho,\theta) = u_0(\rho)$ and $v(\rho,\theta) = v_0(\rho)$. For the transverse displacement $w(\rho,\theta)$, several Fourier harmonics are considered, which is different from the previous work [1]. After introducing these displacement assumptions, the unknown

vector $\langle \mathbf{q} \rangle$ is expressed as follows:

$$\langle \mathbf{q} \rangle = < u_0, \quad \frac{\partial u_0}{\partial \rho} \quad v_0, \quad \frac{\partial v_0}{\partial \rho} \quad w_0, \quad \frac{\partial w_0}{\partial \rho}, \quad \frac{\partial^2 w_0}{\partial \rho^2}, \quad ... \quad w_{n_j}, \quad \frac{\partial w_{n_j}}{\partial \rho}, \quad \frac{\partial^2 w_{n_j}}{\partial \rho^2} > . \tag{9.15}$$

The generalized strain vectors are expressed as $\{\mathscr{E}\}_m$ $(m = 0, 1, 2, ...)$, the strain of m^{th} order. $\{\mathscr{E}\}_{-|n|}$ and $\{\mathscr{E}\}_{|n|}$ $(n = 1, 2, 3, ...)$ are a pair of complex conjugates that are regarded as the same in the following derivation. $\{\mathscr{E}\}_0$ and $\{\mathscr{E}\}_n$ are written as follows:

$$\begin{aligned} \{\mathscr{E}\}_0 &= \begin{Bmatrix} \epsilon^m_{\rho 0} + \epsilon^q_{\rho 0} \\ \epsilon^m_{\theta 0} + \epsilon^q_{\theta 0} \\ 2\left(\epsilon^m_{\rho\theta 0} + \epsilon^q_{\rho\theta 0}\right) \\ \epsilon^b_{\rho 0} \\ \epsilon^b_{\theta 0} \\ 2\epsilon^b_{\rho\theta 0} \end{Bmatrix} = \begin{Bmatrix} \{\boldsymbol{\gamma}^m\}_0 + \{\boldsymbol{\gamma}^q\}_0 \\ \left\{\boldsymbol{\gamma}^b\right\}_0 \end{Bmatrix} \\ &= \left([\mathbf{H}]_0 + \frac{1}{2} [\mathbf{A}(\mathbf{q})]_0 \right) \{\mathbf{q}\}, \end{aligned} \tag{9.16}$$

$$\begin{aligned} \{\mathscr{E}\}_n &= \begin{Bmatrix} \epsilon^m_{\rho n} + \epsilon^q_{\rho n} \\ \epsilon^m_{\theta n} + \epsilon^q_{\theta n} \\ 2\left(\epsilon^m_{\rho\theta n} + \epsilon^q_{\rho\theta n}\right) \\ \epsilon^b_{\rho n} \\ \epsilon^b_{\theta n} \\ 2\epsilon^b_{\rho\theta n} \end{Bmatrix} = \begin{Bmatrix} \{\boldsymbol{\gamma}^m\}_n + \{\boldsymbol{\gamma}^q\}_n \\ \left\{\boldsymbol{\gamma}^b\right\}_n \end{Bmatrix} \\ &= \left([\mathbf{H}]_n + \frac{1}{2} [\mathbf{A}(\mathbf{q})]_n \right) \{\mathbf{q}\} + \mathbf{i} \left([\mathscr{H}]_n + \frac{1}{2} [\mathscr{A}(\mathbf{q})]_n \right) \{\mathbf{q}\}, \end{aligned} \tag{9.17}$$

where the matrix $[\mathbf{H}]_0$, $[\mathbf{H}]_n$ and $[\mathscr{H}]_n$represents the linear parts of the strains without unknown terms, while the matrix $[\mathbf{A}(\mathbf{q})]_0$, $[\mathbf{A}(\mathbf{q})]_n$ and $[\mathscr{A}(\mathbf{q})]_n$ represent the quadratic nonlinear parts of the strains with the unknown terms presented in Table 9.1, in which $r \in [n - n_j, n_j]$ and n_j is the number of Fourier orders considered for the transverse displacement w. The operator of addition assignment "+=" indicates adding another value to the element's value and assigning the new value to the element.

Table 9.1 Non-zero elements of the generalized strains related matrices

Matrix $(6\times(7+3n_j))$	Non-zero elements			
$[\mathbf{H}]_0$	(1,2)=1 (4,7)=−1	(2,1)=$\frac{1}{\rho}$ (5,6)=$-\frac{1}{\rho}$	(3,3)=$-\frac{1}{\rho}$	(3,4)=1
$[\mathbf{A}(\mathbf{q})]_0$	(1,2) = $\frac{\partial u_0}{\partial\rho}$ (2,3)=$\frac{v_0}{\rho^2}$ (3,3)=$-\frac{\partial u_0}{\rho\partial\rho}$	(1,4) = $\frac{\partial v_0}{\partial\rho}$ (2,5+3|r|)+=$\frac{r^2Q^2w_{\|r\|}}{\rho^2}$ (3,4)=$\frac{u_0}{\rho}$	(1,6+3|r|) += $\frac{\partial w_{\|r\|}}{\partial\rho}$ (3,1)=$\frac{\partial v_0}{\rho\partial\rho}$	(2,1)=$\frac{u_0}{\rho^2}$ (3,2)=$-\frac{v_0}{\rho}$
$[\mathbf{H}]_n$	(4,7+3n)=−1	(5,5+3n)=$\frac{n^2Q^2}{\rho^2}$	(5,6+3n)=$-\frac{1}{\rho}$	
$[\mathbf{A}(\mathbf{q})]_n$	(1,6+3|r|)+=$\frac{\partial w_{\|n-r\|}}{\partial\rho}$		(2,5+3|r|)+=$\frac{[-r(n-r)Q^2]w_{\|n-r\|}}{\rho^2}$	
$[\mathscr{H}]_n$	(6,5+3n)=$\frac{nQ}{\rho^2}$		(6,6+3n)=$-\frac{2nQ}{\rho}$	
$[\mathscr{A}(\mathbf{q})]_n$	(3,5+3|r|)+=$\frac{rQ\partial w_{\|n-r\|}}{\rho\partial\rho}$		(3,6+3|n−r|)+=$\frac{rQw_{\|r\|}}{\rho}$	

The internal virtual work of the circular membrane in Eq. (9.5) is deduced as:

$$\begin{aligned}\mathcal{W}_{int}(\delta q) =&\delta\Bigg(\iint_\omega\left[\frac{1}{2}\left[\left(\langle\boldsymbol{\gamma}^m\rangle_0+\langle\boldsymbol{\gamma}^q\rangle_0\right)[\mathbf{L}^m]\left(\{\boldsymbol{\gamma}^m\}_0+\{\boldsymbol{\gamma}^q\}_0\right)+\left\langle\boldsymbol{\gamma}^b\right\rangle_0\left[\mathbf{L}^b\right]\left\{\boldsymbol{\gamma}^b\right\}_0\right]\right.\\&\left.+\sum_{n=1}^{n_j}\left[\left(\langle\boldsymbol{\gamma}^m\rangle_n+\langle\boldsymbol{\gamma}^q\rangle_n\right)[\mathbf{L}^m]\left(\{\boldsymbol{\gamma}^m\}_n+\{\boldsymbol{\gamma}^q\}_n\right)+\left\langle\boldsymbol{\gamma}^b\right\rangle_n\left[\mathbf{L}^b\right]\left\{\boldsymbol{\gamma}^b\right\}_n\right]\right]d\omega\Bigg).\end{aligned}\tag{9.18}$$

After substituting Eqs. (9.16) and (9.17) into Eq. (9.18), and adopting the principle of virtual work:

$$\mathcal{W}_{int}(\delta q)=\mathcal{W}_{ext}(\delta q),\tag{9.19}$$

the governing equations are deduced as:

$$\begin{cases}\langle\delta\mathbf{q}\rangle\left\{\iint_\omega\left[\left({}^T[\mathbf{H}]_0+[\mathbf{A}(\mathbf{q})]_0\right)\{\mathbf{S}\}_0+2\sum_{n=1}^{n_j}\left({}^T[\mathbf{H}]_n+[\mathbf{A}(\mathbf{q})]_n\right)\{\mathbf{S}\}_n\right.\right.\\\qquad\left.\left.+2\sum_{n=1}^{n_j}\left({}^T[\mathscr{H}]_n+[\mathscr{A}(\mathbf{q})]_n\right)\{\mathscr{S}\}_n\right]d\omega-\iint_\omega\lambda\{\mathbf{f}\}\,d\omega\right\}=0,\\\{\mathbf{S}\}_n=[\mathbf{D}]\left([\mathbf{H}]_n+\frac{1}{2}[\mathbf{A}(\mathbf{q})]_n\right)\{\mathbf{q}\},\\\{\mathscr{S}\}_n=[\mathbf{D}]\left([\mathscr{H}]_n+\frac{1}{2}[\mathscr{A}(\mathbf{q})]_n\right)\{\mathbf{q}\},\end{cases}\tag{9.20}$$

where $\lambda\{\mathbf{f}\}$ is a generalized force vector with $\lambda\in\mathbb{R}$ being a load parameter, and the elastic

coefficient matrix is written as follows:

$$[\mathbf{D}] = \left({}^{T}[\mathbf{R}^m][\mathbf{L}^m][\mathbf{R}^m] + {}^{T}[\mathbf{R}^b][\mathbf{L}^b][\mathbf{R}^b] \right), \tag{9.21}$$

in which $[\mathbf{R}^m]$ (for the membrane strains) and $[\mathbf{R}^b]$ (for the bending strains) are written as follows:

$$[\mathbf{R}^m] = \begin{bmatrix} 1 & 0 & 0 & 0 & 0 & 0 \\ 0 & 1 & 0 & 0 & 0 & 0 \\ 0 & 0 & 1 & 0 & 0 & 0 \end{bmatrix}, \qquad [\mathbf{R}^b] = \begin{bmatrix} 0 & 0 & 0 & 1 & 0 & 0 \\ 0 & 0 & 0 & 0 & 1 & 0 \\ 0 & 0 & 0 & 0 & 0 & 1 \end{bmatrix}. \tag{9.22}$$

9.4.4 Discretization

Similar to the discretization procedure in the previous work [1], Hermite interpolation is employed for all the displacement components to prevent the possible membrane locking problem. Since n_j Fourier expansion orders are considered for the transverse displacement w in the current work, a two-node 1D element with $(6 + 2 \times n_j)$ degrees of freedom at each node is adopted. The vector of shape functions can be written as follows:

$$\langle \mathbf{\Gamma} \rangle = \left\langle \frac{(1-\xi)^2 (2+\xi)}{4}, \frac{le\,(1-\xi^2)\,(1-\xi)}{8}, \frac{(1+\xi)^2 (2-\xi)}{4}, \frac{le\,(-1+\xi^2)\,(1+\xi)}{8} \right\rangle. \tag{9.23}$$

in which le denotes the length of element. Considering the unknowns in Eq. (9.15), the element nodal displacements vector $\langle \mathbf{q}^e \rangle$ can be expressed as:

$$\begin{aligned} \langle \mathbf{q}^e \rangle = < \; & u_0^I, \; \frac{\partial u_0^I}{\partial \rho}, \; v_0^I, \; \frac{\partial v_0^I}{\partial \rho}, \; w_0^I, \; \frac{\partial w_0^I}{\partial \rho}, \; \ldots \; w_{n_j}^I, \; \frac{\partial w_{n_j}^I}{\partial \rho}, \; u_0^{II}, \; \frac{\partial u_0^{II}}{\partial \rho}, \; v_0^{II}, \; \frac{\partial v_0^{II}}{\partial \rho}, \\ & w_0^{II}, \; \frac{\partial w_0^{II}}{\partial \rho}, \; \ldots \; w_{n_j}^{II}, \; \frac{\partial w_{n_j}^{II}}{\partial \rho} \; >, \end{aligned} \tag{9.24}$$

then Eq. (9.15) is expressed as a discretized form:

$$\{\mathbf{q}\} = [\mathbf{G}]\,\{\mathbf{q}^e\}, \tag{9.25}$$

in which, the $(7+3n_j)\times(12+4n_j)$ matrix of shape functions $[\mathbf{G}]$ can be written as:

$$[\mathbf{G}]=\begin{bmatrix}
\boldsymbol{\Gamma}_{\boldsymbol{q}^e} & 0 & 0 & 0 & 0 & 0 & 0 & 0 & ... \\
\boldsymbol{\Gamma}_{\boldsymbol{q}^e,\rho} & 0 & 0 & 0 & 0 & 0 & 0 & 0 & ... \\
0 & 0 & \boldsymbol{\Gamma}_{\boldsymbol{q}^e} & 0 & 0 & 0 & 0 & 0 & ... \\
0 & 0 & \boldsymbol{\Gamma}_{\boldsymbol{q}^e,\rho} & 0 & 0 & 0 & 0 & 0 & ... \\
0 & 0 & 0 & 0 & \boldsymbol{\Gamma}_{\boldsymbol{q}^e} & 0 & 0 & 0 & ... \\
0 & 0 & 0 & 0 & \boldsymbol{\Gamma}_{\boldsymbol{q}^e,\rho} & 0 & 0 & 0 & ... \\
0 & 0 & 0 & 0 & \boldsymbol{\Gamma}_{\boldsymbol{q}^e,\rho\rho} & 0 & 0 & 0 & ... \\
0 & 0 & 0 & 0 & 0 & 0 & \boldsymbol{\Gamma}_{\boldsymbol{q}^e} & 0 & ... \\
0 & 0 & 0 & 0 & 0 & 0 & \boldsymbol{\Gamma}_{\boldsymbol{q}^e,\rho} & 0 & ... \\
0 & 0 & 0 & 0 & 0 & 0 & \boldsymbol{\Gamma}_{\boldsymbol{q}^e,\rho\rho} & 0 & ... \\
\vdots & \vdots & \vdots & \vdots & \vdots & \vdots & \vdots & \vdots & \ddots
\end{bmatrix}, \tag{9.26}$$

where subscripts following commas denote partial derivatives and the vector $\langle\boldsymbol{\Gamma}_{\boldsymbol{q}^e}\rangle$ is as follows:

$$\langle\boldsymbol{\Gamma}_{\boldsymbol{q}^e}\rangle=\Big\langle\ \boldsymbol{\Gamma}(1),\ \ \boldsymbol{\Gamma}(2),\ \ 0,\ \ ...\ \ 0,\ \ \boldsymbol{\Gamma}(3),\ \ \boldsymbol{\Gamma}(4)\ \Big\rangle. \tag{9.27}$$

in which $4+2n_j$ zeros exist between $\boldsymbol{\Gamma}(2)$ and $\boldsymbol{\Gamma}(3)$. Substituting the discretized unknown $\{\mathbf{q}\}$ in Eq. (9.25) into Eq. (9.20), the governing equations can be converted into the following form:

$$\begin{cases}
\displaystyle\sum_e \langle\delta\mathbf{q}^e\rangle\left[\int_0^{le}\left({}^T[\mathbf{B}(\mathbf{q}^e)]_0\{\mathbf{S}\}_0+2\sum_{n=1}^{n_j}{}^T[\mathbf{B}(\mathbf{q}^e)]_n\{\mathbf{S}\}_n+2\sum_{n=1}^{n_j}{}^T[\boldsymbol{\mathscr{B}}(\mathbf{q}^e)]_n\{\boldsymbol{\mathscr{S}}\}_n\right)\rho d\rho-\lambda\{\mathbf{f}^e\}\right]=0,\\
\{\mathbf{S}\}_n=[\mathbf{D}]\left([\mathbf{B}_l]_n+\dfrac{1}{2}[\mathbf{B}_{nl}(\mathbf{q}^e)]_n\right)\{\mathbf{q}^e\},\\
\{\boldsymbol{\mathscr{S}}\}_n=[\mathbf{D}]\left([\boldsymbol{\mathscr{B}}_l]_n+\dfrac{1}{2}[\boldsymbol{\mathscr{B}}_{nl}(\mathbf{q}^e)]_n\right)\{\mathbf{q}^e\},
\end{cases} \tag{9.28}$$

where

$$\begin{cases}
[\mathbf{B}(\mathbf{q}^e)]_t=[\mathbf{B}_l]_t+[\mathbf{B}_{nl}(\mathbf{q}^e)]_t,\\
[\mathbf{B}_l]_t=[\mathbf{H}]_t[\mathbf{G}],\\
[\mathbf{B}_{nl}(\mathbf{q}^e)]_t=[\mathbf{A}(\mathbf{q}^e)]_t[\mathbf{G}],\\
[\boldsymbol{\mathscr{B}}(\mathbf{q}^e)]_n=[\boldsymbol{\mathscr{B}}_l]_n+[\boldsymbol{\mathscr{B}}_{nl}(\mathbf{q}^e)]_n,\\
[\boldsymbol{\mathscr{B}}_l]_n=[\boldsymbol{\mathscr{H}}]_n[\mathbf{G}],\\
[\boldsymbol{\mathscr{B}}_{nl}(\mathbf{q}^e)]_n=[\boldsymbol{\mathscr{A}}(\mathbf{q}^e)]_n[\mathbf{G}],\\
\{\mathbf{f}^e\}=\displaystyle\int_0^{le}{}^T[\mathbf{G}]\{\mathbf{f}\}\rho d\rho.
\end{cases} \tag{9.29}$$

in which $t \in [0, n_j]$. The asymptotic numerical method proposed by [39] is used to solve the set of equations. Details on the use of the ANM for the resolution of non-linear equations are given in 9.8.

9.5 Annular membrane under in-plane tensile load

In this section, the reduced model accounting for several Fourier coefficients, which is different from the model used in [1], is firstly employed to study the instability phenomena of the annular membrane under radial tensile load (see Fig. 9.2). The external edge of the membrane is simply supported and the transverse displacement of the internal edge is fixed, while a uniformly distributed radial tensile load is applied along the internal edge. Then a discussion is conducted on the difference between wrinkling mechanism of the annular membrane and that of the rectangular membrane under unidirectionally tensile load. The effects of the Poisson's ratio and the geometric dimensions on the wrinkling pattern are also investigated. The material properties and geometric dimensions of the annular membrane are listed in Table 9.2.

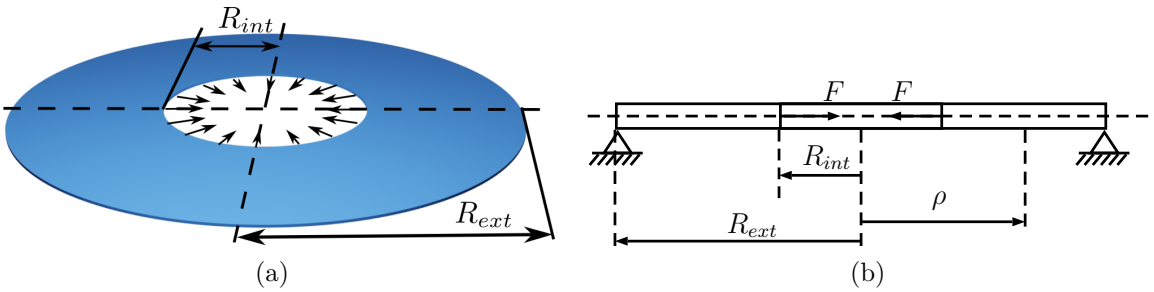

Figure 9.2 An annular membrane under in-plane radial tensile load along the internal edge

Table 9.2 Material properties and geometric dimensions of the annular membranes

Young's modulus E(MPa)	Poisson's ratio μ	Thickness h(mm)	External radius R_{ext}(mm)	Internal radius R_{int}(mm)	Instability pattern
69,000	0.3	1	1000	390	$R1C12$
				400	$R1C13$

9.5.1 Verification

$RXCY$ represents the buckling modes with different wave numbers, in which X and Y denote the half-waves in the radial direction and waves in the circumferential direction, respectively.

Since the geometric dimensions plays an important role in membrane buckling [32], the annular membranes of different internal radius are studied, whose lowest instability patterns are different as shown in Table 9.2. By using the reduced model to predict the bifurcation loads of the mode $R1C12$ with various numbers of elements, a mesh convergence study is performed to determine the minimum number of elements for the discretization. The model with seven Fourier coefficients (namely the highest order harmonic is 6^{th} in Eq. (9.7)) is adopted for the study, while the preassigned wave number $Q = 2$. Fig. 9.3 presents the result of the convergence study, the transverse displacement W is the summation of all the harmonics. It is precise enough to use 4 elements in the reduced model to simulate the phenomenon in this section.

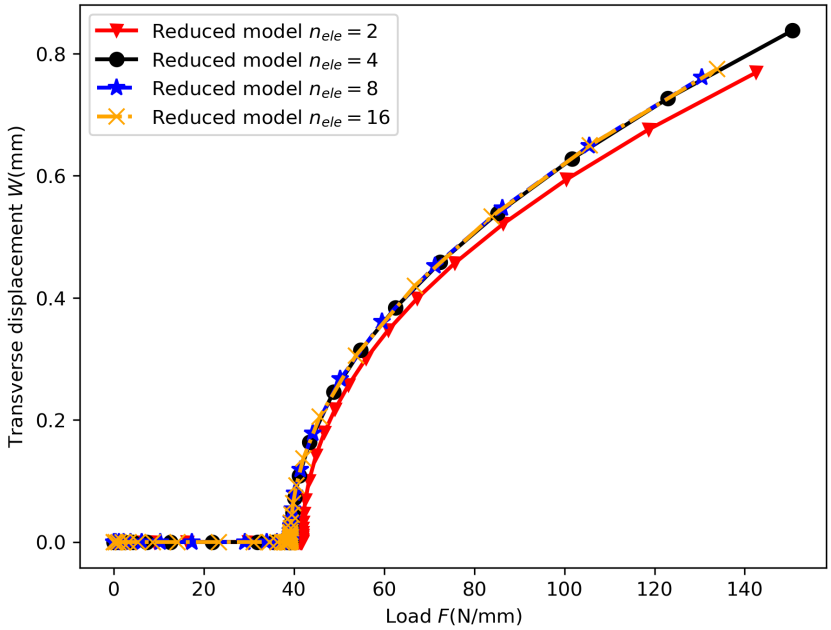

Figure 9.3 Convergence study of the reduced model with respect to the number of elements in the radial direction

In order to verify the accuracy of the reduced model, a simulation is conducted based on 3D finite element model in ABAQUS (referred to as the 'full shell model' in this paper), and the result is regarded as the benchmark. The convergence test of the full shell model has been done in [1], and 52×8 elements are employed to discretize the full shell model. Fig. 9.4 shows the deformed shapes of the annular membranes predicted by the both models, and the two simulation results show almost the same buckling mode $R1C12$.

Usually, only the zero harmonic U_0 (mean field) and the first harmonic U_1 (envelope of the oscillation) are adopted [1, 29, 32, 34, 35]. When applying those reduced models, it is

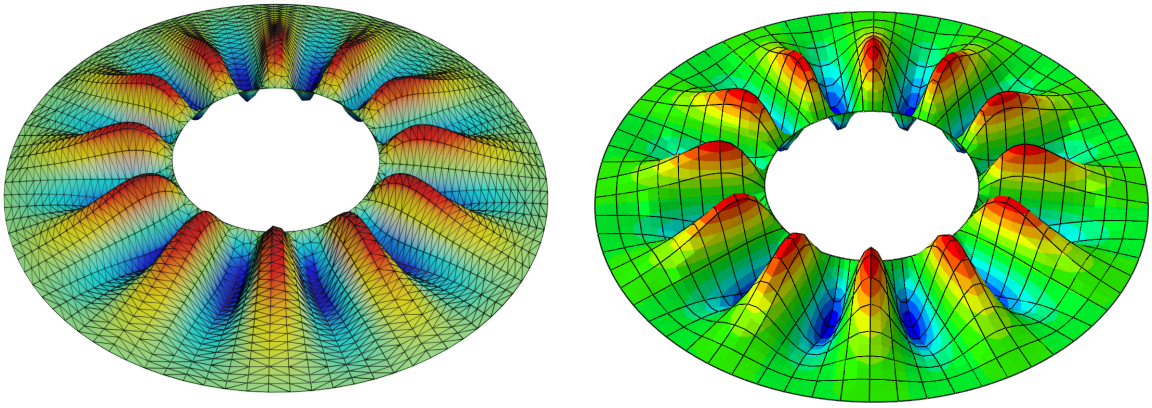

(a) (b)

Figure 9.4 Instability pattern $R1C12$ of the annular membrane under radial tensile load predicted by two different models: (a) the reduced model; (b) the full shell model

necessary to preassign a proper wave number Q to obtain the interested wrinkling patterns. For example, in order to obtain $R1C12$, the wave number needs to be $Q = 12$. As introduced by [37], the lowest buckling mode of thin films on compliant substrates can be automatically predicted by the model accounting for several Fourier harmonics. To verify that the model constructed in the current study is able to realize the same function, the reduced model accounting for seven Fourier harmonics is adopted to simulate the $R1C12$ cases, while the wave numbers are set to be $Q = 2$ and $Q = 3$.

The bifurcation curves of $R1C12$ calculated by the reduced model and the full shell model are illustrated in Fig. 9.4, in which W_m denotes the transverse displacement of the m^{th} order harmonic. No matter $Q = 2$ or $Q = 3$, the result of the reduced model is quite precise. Even in the post-buckling process when W reaches the same magnitude as the membrane thickness, the reduced model still performs well. Besides, although seven harmonics are considered here for the transverse displacement W, the reduced model is highly efficient and only requires 90 degrees of freedom (DOFs), about 0.5% of the full shell model (DOFs = 16640). Note that the only difference between Fig. 9.4a and 9.4b is the main fluctuation harmonic. To be more specific, the transverse displacement of 6^{th} harmonic changes significantly after bifurcation point when $Q = 2$, while the one of 4^{th} harmonic increases obviously when $Q = 3$. Both cases obtain the wrinkling pattern $R1C12$ and predict the same bifurcation curve. Therefore, for the simulation of annular membrane wrinkling, the reduced model with several Fourier harmonics automatically chooses the proper Fourier coefficient to ensure the system to be in a state of minimum energy.

Even though the automatic selection of the fluctuation harmonic facilitates the study of the

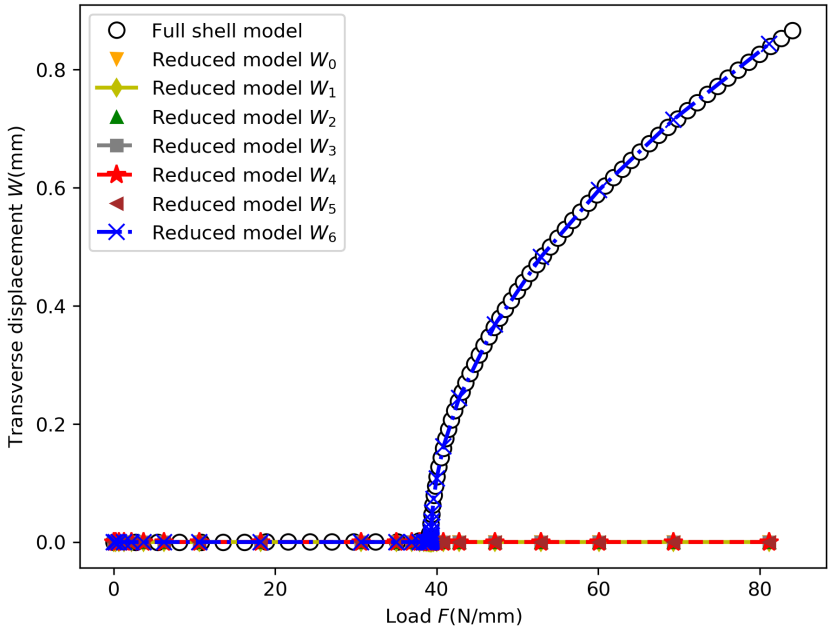

(a)

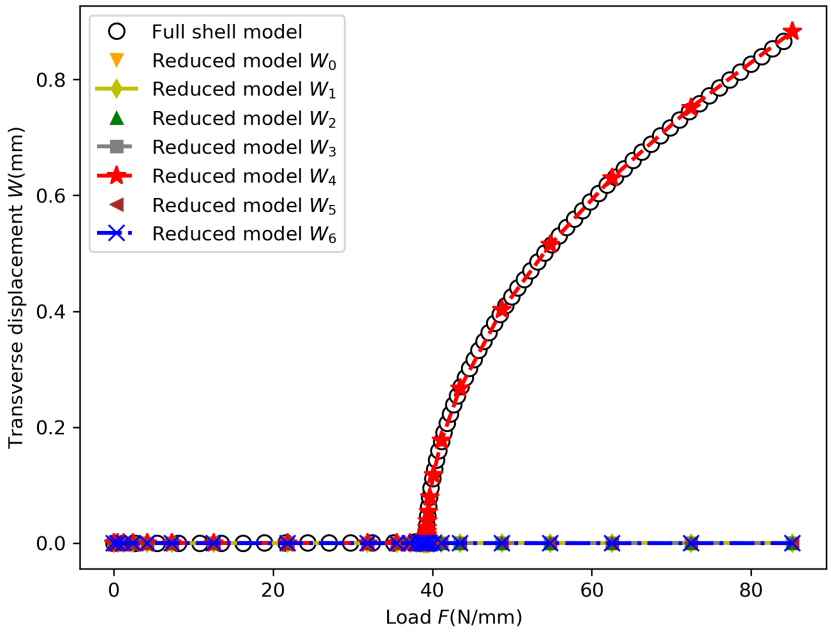

(b)

Figure 9.5 Bifurcation curves of $R1C12$ obtained by the full shell model and the reduced models with different preassigned wave numbers Q

cases of unknown wrinkling patterns, the reduced model might be ineffective for some cases, for example, when the wave number Q of the wrinkling pattern $R1CY$ is a prime number. For the case of $R_{int} = 400$ shown in Table 9.2, the lowest instability pattern is $R1C13$. Two reduced models can be used to simulate this case: 1) the model accounting only the 0^{th} and 1^{st} when $Q = 13$; 2) the model accounting from the 0^{th} to the 13^{th} harmonics when $Q = 1$. The first one is discussed in [1], and the second one is adopted to predict the bifurcation curve as shown in Fig. 9.6. The transverse displacements of the 0^{th} to 12^{th} harmonics keep constant for the whole process, while only W_{13} increases significantly after bifurcation point. The reduced model still chooses the correct main fluctuation harmonic, although the usage of fourteen Fourier coefficients diminish its efficiency. In the following section, the stress evolution of the annular membrane is investigated to provide an enhanced understanding of the instability mechanism.

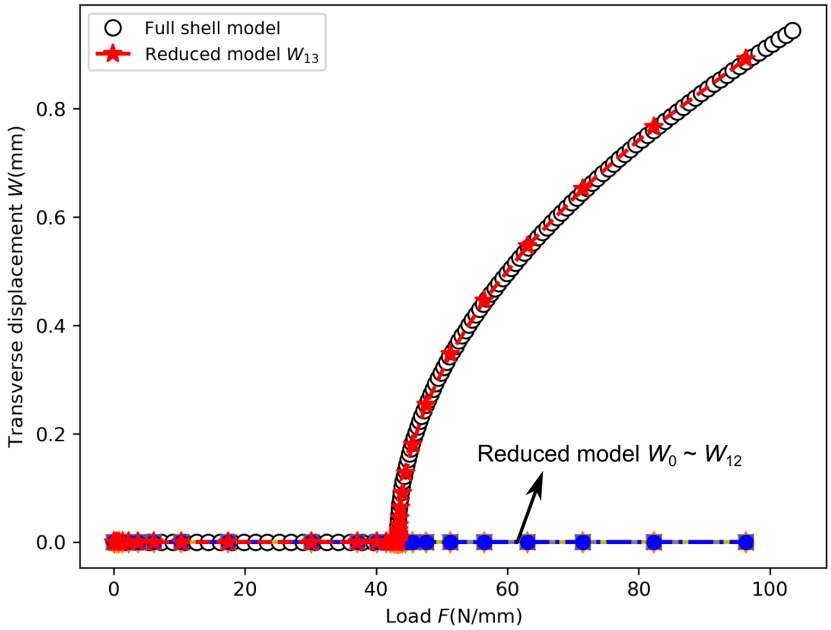

Figure 9.6 Bifurcation curve of $R1C13$ obtained by the full shell model and by the reduced model accounting fourteen harmonics when the wave number $Q = 1$

9.5.2 Instability mechanisms

From Eqs. (9.1) and (9.2), the complete form of the radial and circumferential strains are expressed as follows:

$$\begin{cases} \epsilon_\rho = \dfrac{\partial u}{\partial \rho} + \dfrac{1}{2}\left[\left(\dfrac{\partial w}{\partial \rho}\right)^2 + \left(\dfrac{\partial u}{\partial \rho}\right)^2 + \left(\dfrac{\partial v}{\partial \rho}\right)^2\right] - z\dfrac{\partial^2 w}{\partial \rho^2}, \\ \epsilon_\theta = \dfrac{1}{\rho}\left(\dfrac{\partial v}{\partial \theta} + u\right) + \dfrac{1}{2\rho^2}\left[\left(\dfrac{\partial w}{\partial \theta}\right)^2 + \left(\dfrac{\partial u}{\partial \theta} - v\right)^2 + \left(\dfrac{\partial v}{\partial \theta} + u\right)^2\right] - z\dfrac{1}{\rho^2}\left(\dfrac{\partial^2 w}{\partial \theta^2} + \rho\dfrac{\partial w}{\partial \rho}\right). \end{cases} \tag{9.30}$$

Before the bifurcation point, the deformation of the annular membrane is axisymmetric in the linear stage. Thus the circumferential displacement v and the derivative of the radial displacement $\dfrac{\partial u}{\partial \theta}$ are negligible. Based on the assumption that the membrane is perfectly plane before the loss of stability, the terms related to the transverse displacement w can also be neglected. Then Eq. (9.30) is simplified as follows:

$$\begin{cases} \epsilon_\rho = \dfrac{\partial u}{\partial \rho} + \dfrac{1}{2}\left(\dfrac{\partial u}{\partial \rho}\right)^2, \\ \epsilon_\theta = \dfrac{u}{\rho} + \dfrac{1}{2}\left(\dfrac{u}{\rho}\right)^2. \end{cases} \tag{9.31}$$

Considering that the compressive circumferential stress is the origin of the wrinkling for the numerical cases discussed above. Therefore, for the following analysis, only the circumferential stress is studied. After introducing Eq. (9.31) into the constitutive relationship, in which the shear strain is neglected, the circumferential stress is deduced as follows:

$$\begin{aligned} \sigma_\theta &= \frac{E}{1-\mu^2}\left(\epsilon_\theta + \mu\epsilon_\rho\right) \\ &= \frac{E}{1-\mu^2}\left[\frac{u}{\rho} + \frac{1}{2}\left(\frac{u}{\rho}\right)^2 + \mu\frac{\partial u}{\partial \rho} + \frac{\mu}{2}\left(\frac{\partial u}{\partial \rho}\right)^2\right]. \end{aligned} \tag{9.32}$$

As shown in Fig. 9.7, $\dfrac{u}{\rho}$ and $\mu\dfrac{\partial u}{\partial \rho}$ are of the same order of magnitude being much smaller than 1. After neglecting the terms of second order $\dfrac{1}{2}\left(\dfrac{u}{\rho}\right)^2$ and $\dfrac{\mu}{2}\left(\dfrac{\partial u}{\partial \rho}\right)^2$, σ_θ can be simplified as

follows:

$$\sigma_\theta \approx \frac{E}{1-\mu^2}\left[\frac{u}{\rho}+\mu\frac{\partial u}{\partial \rho}\right]. \tag{9.33}$$

This shows that the main effective term of circumferential stress σ_θ is the radial displacement u. The similar conclusion can be obtained from the famous Lamé's equations and many other studies [17–19]. Fig. 9.7 presents that when a tensile load at the internal edge causes a negative radial displacement u, a compressive zone appears near the internal edge no matter if the Poisson's ratio of the material is positive, zero or even negative. This implies that the wrinkling phenomena in circular membranes is not highly sensitive to Poisson's effect. This also explains why no wrinkle appears if the internal edge is fixed while the external edge is stretched in the radial direction, which is an simple but practical way to prevent the wrinkling problems of annular membranes.

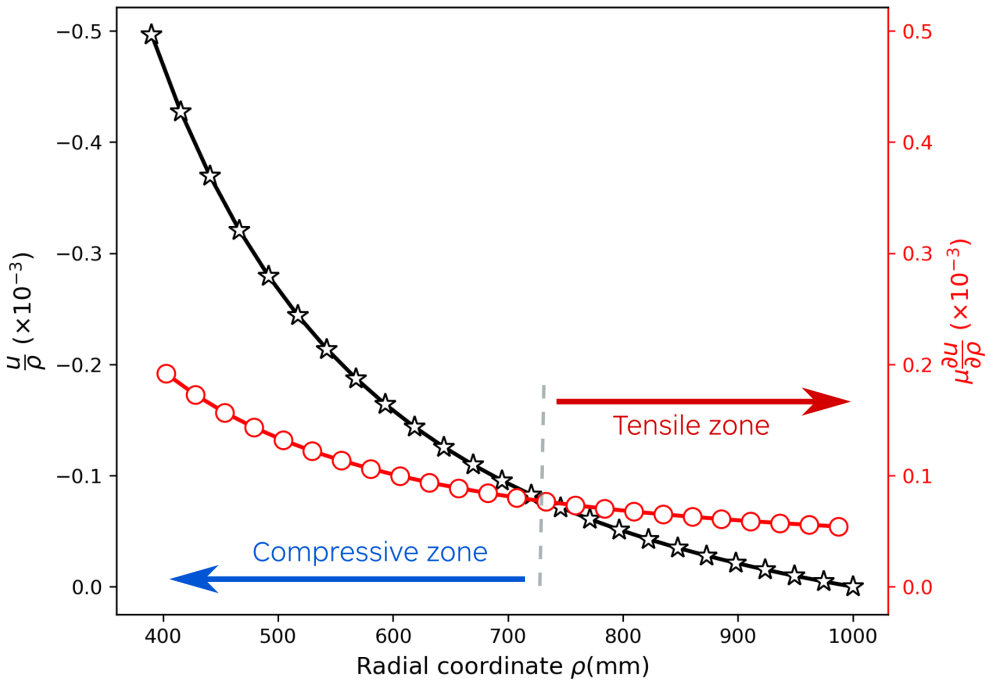

Figure 9.7 Evolution of the two terms related to the radial displacements in Eq. (9.33) along the radial direction

Since the instability pattern is highly sensitive to the stress distribution, the reduced model is used to simulate the stress. Fig. 9.8 illustrates the redistribution of circumferential stress, and the evolution of the stresses on the top and bottom surfaces of the crest during the whole process. The movement and deformation of an arc line AB is presented to describe the appearance of wrinkling in Fig. 9.8a. In order to clearly illustrate the mechanism, a deformation scaling factor is used to visually enlarge the deformation. Due to the tensile load,

the line AB moves towards the internal edge. Before the bifurcation point, the compressive stresses on the top and bottom surfaces are the same and vary linearly with the increase of the tensile load. Suppose that when the line AB moves to A'B', it reaches the bifurcation point, thus the line A'B' buckles to accommodate the in-plane strain incompatibility generated by the negative radial displacement. As the consequence, the top surface of the membrane starts to be stretched while the bottom surface gets further compressed. From an intuitive perspective, the circle's circumference decreases from the external to the internal edges, thus when the arc AB moves towards A'B', it must shrink in the plane or buckle out of the plane to meet the geometric constraint.

As discussed above, the relationship between the displacement and circumferential stresses plays a key role in the instability process. As shown in Fig. 9.9, the wave length and the wave number of circumferential stress are the same as those of the transverse displacement. Meanwhile, when comparing the transverse displacement and the circumferential stress on the top surface, their phases are the same, whereas when compared to the stress on the bottom, the phase differs by half a period. Therefore, the top surface of the crest and the bottom surface of the trough around the circumference tend to be stretched in the post-buckling stage.

This wrinkling phenomenon is different from the similar reference example in Cartesian coordinates, which is the rectangular membrane under an in-plane uniaxial tensile load [14, 32]. Although these two examples both describe unidirectionally stretched membranes with lateral wrinkling, their instability mechanisms are different. The negative radial displacement is the origin of the circumferential compressive stress of the annular membrane, which is on the load direction and does not depend on the Poisson effect. But the main reason causing the compressive stress of the rectangular membrane is the shrinkage along the lateral direction vertical to the tensile load, which is induced by Poisson's effect as illustrated in Fig. 9.10. The figure also presents a membrane of negative Poisson's ratio under an in-plane uniaxial tensile load. The small transverse displacements existing in the example of $\mu = -0.3$ is because the rectangular membrane cases are simulated by ABAQUS. It is necessary here to introduce very small initial imperfections related to the buckling patterns before performing the numerical simulations. Although the transverse displacement is negligible compared with the obvious ones in the example of $\mu = 0.3$, the distribution of the displacement U_x shows that the membrane expands in the lateral direction under the tensile load in the negative Poisson's ratio case. No compressive stress exists in the zone of interest and thus no wrinkle appears. However, as mentioned above, the wrinkles always appear in the annular membrane no matter if the Poisson's ratio is positive or negative.

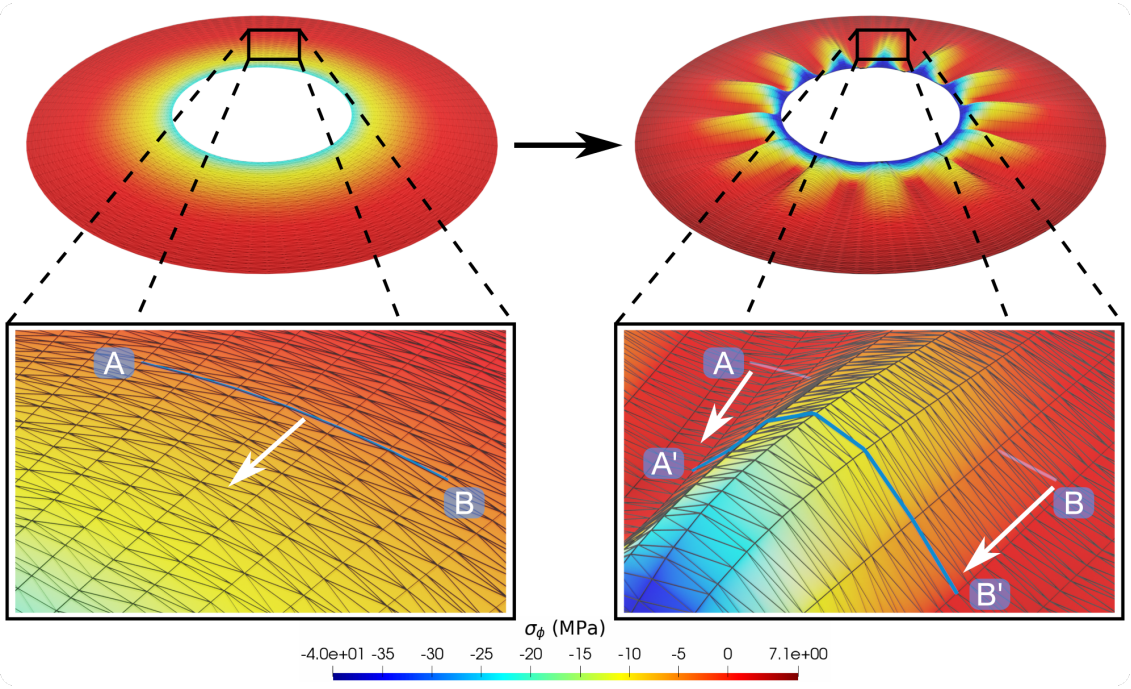

(a)

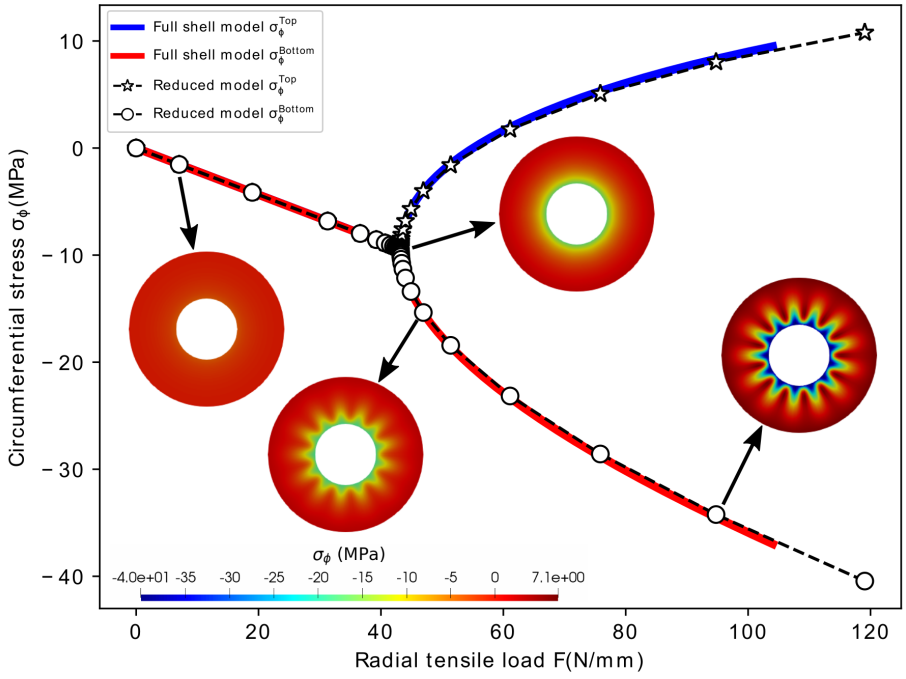

(b)

Figure 9.8 Circumferential stress evolution: (a) illustration of the instability mechanism; (b) evolutions of circumferential stresses on the top and bottom surfaces of the crest simulated by the two models

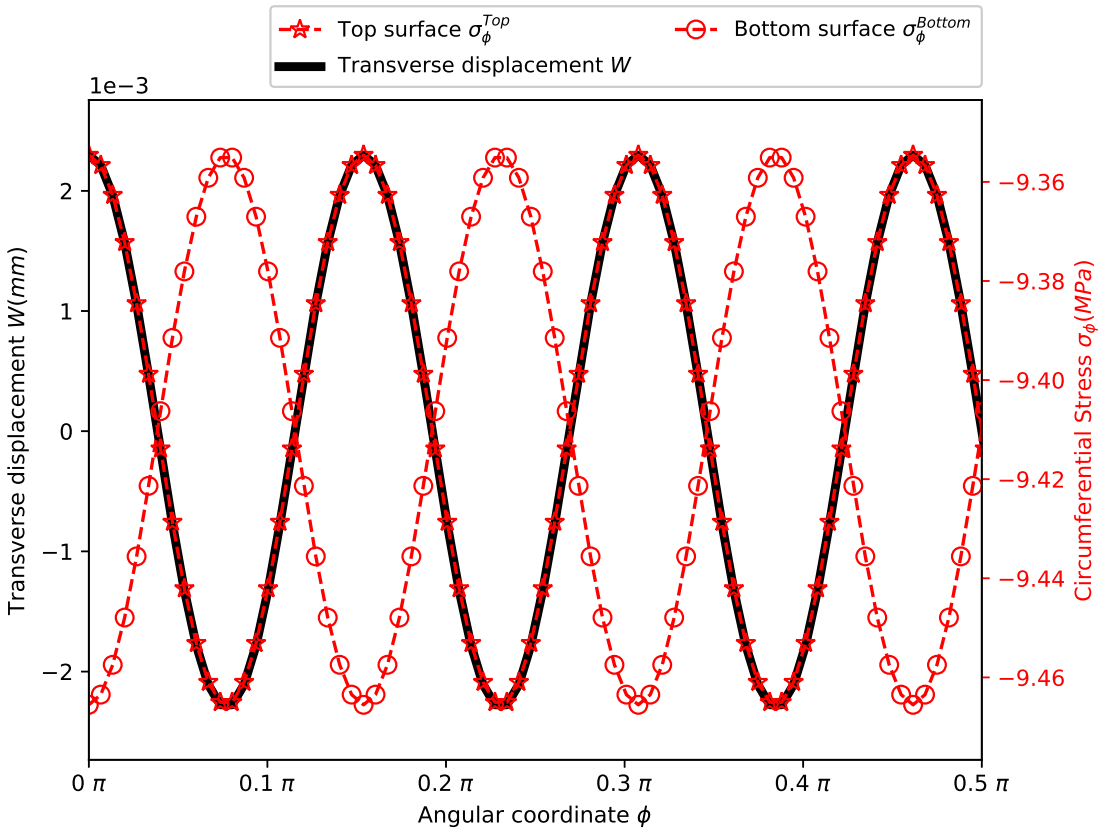

Figure 9.9 Transverse displacements and circumferential stresses around the circumference at the bifurcation point

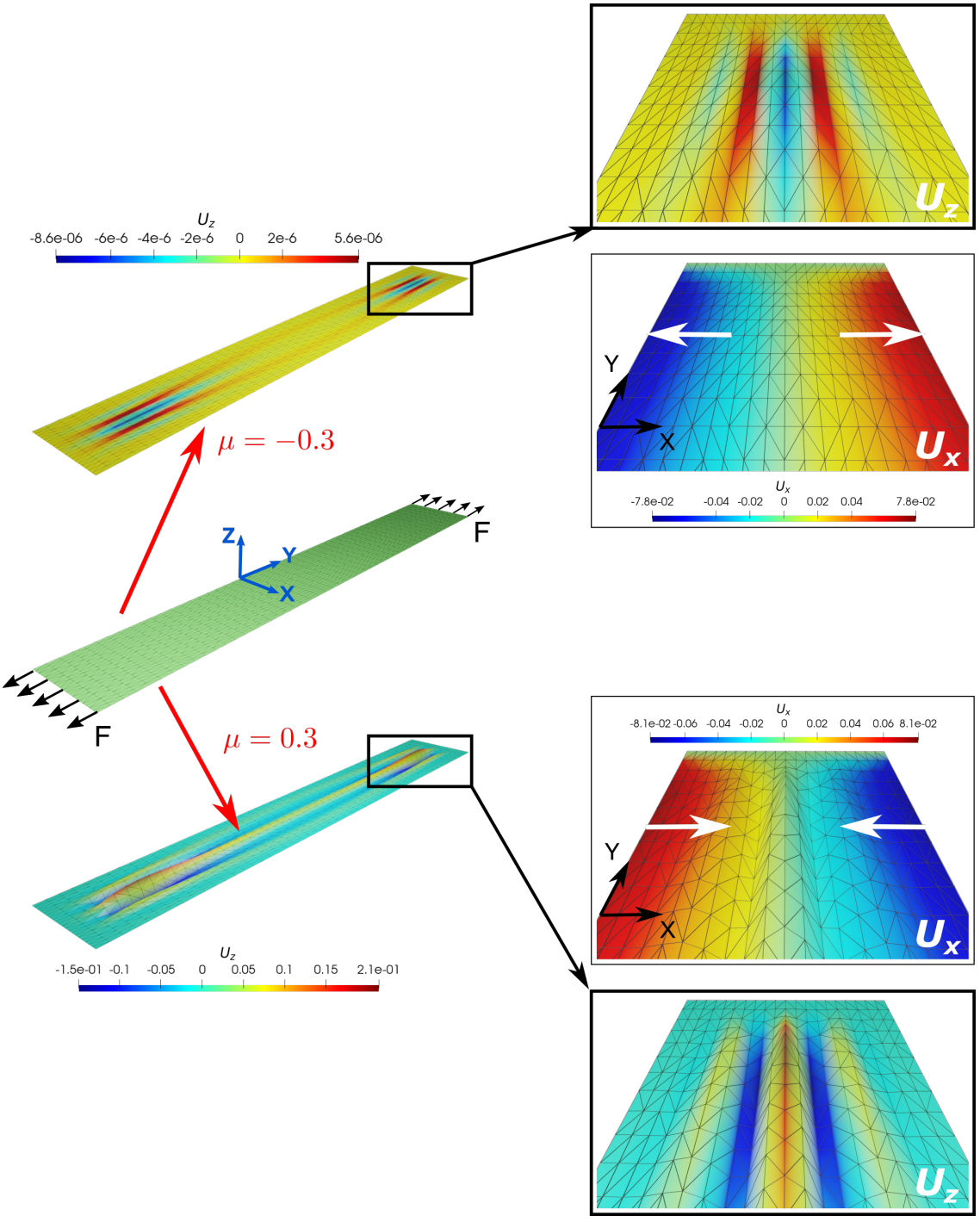

Figure 9.10 Displacement fields of two rectangular membranes of positive and negative Poisson's ratios under an in-plane uniaxial tensile load simulated by ABAQUS

9.5.3 Effect of geometric dimensions

As mentioned above, even though the automatic selection of the fluctuation harmonic facilitates the study of cases with unknown wrinkling patterns, the reduced model might be ineffective in some cases. The lowest instability pattern is affected by many factors, e.g., boundary conditions, geometric dimensions and material properties. In order to overcome this drawback, the relationship between the geometric dimensions and the lowest instability patterns is investigated by the reduced model in this section. A MATLAB script is developed to simulate the cases with increasing internal radius R_{int} to automatically judge the lowest instability patterns. As shown in Fig. 9.11 and Fig. 9.12, two important attributes are presented, namely the circumferential wave number Q and the critical load F_{bif}. Since Poisson's ratio also affects the lowest instability pattern as a material property, the results with three different Poisson's ratios are compared.

As shown in Fig. 9.11a, with the increase of $\frac{R_{int}}{R_{ext}}$, Q varies as an exponential function $Q = A\mathrm{e}^{B\frac{R_{int}}{R_{ext}}} + C$. This facilitates the selection of the lowest instability pattern according to $\frac{R_{int}}{R_{ext}}$. Note that the higher Poisson's ratio the material has, the more rapidly the wave number increases. Therefore, the coefficients of the exponential function are related to Poisson's ratio, and their relationship is presented in Fig. 9.11b. The parameters A and C are well fitted by linear functions, while B is precisely fitted by an exponential function. Combining this function with the reduced model, the lowest instability patterns of unknown cases can be assigned automatically. Note that only the Poisson's ratio is considered here, the other factors should be taken into consideration in the future to improve the applicability of the model.

Fig. 9.12 shows the evolution of the critical tensile load with the increase of the radius ratio $\frac{R_{int}}{R_{ext}}$. For the case $\mu = 0.3$, the critical instability load F_{bif} presents an interesting "U" shape. With the decrease of Poisson's ratio, the curve tends to take a "L" shape, especially when $\mu = -0.3$. When $\frac{R_{int}}{R_{ext}} < 0.10$, the critical instability load F_{bif} decreases sharply with $\frac{R_{int}}{R_{ext}}$. Then all the curves tend to reach their plateau stages. This means that when the radius ratio lies in this plateau range, one cannot prevent wrinkling by changing the radius ratio, since the critical instability load remains at a low level. When $\frac{R_{int}}{R_{ext}} = 0.30$, the curve with $\mu = 0.3$ starts to increase continuously. The critical tensile load increases significantly when $\frac{R_{int}}{R_{ext}} > 0.4$, due to the rapid increase of the wave number with the radius ratio as shown in Fig. 9.11. The curve with $\mu = 0.0$ starts to increase significantly when $\frac{R_{int}}{R_{ext}} = 0.60$, while the curve with $\mu = -0.3$ remains stable in the range of $0.1 < \frac{R_{int}}{R_{ext}} < 0.7$. Therefore, when it comes to improving the wrinkling resistance by changing the radius ratio, it is much easier with the annular membrane of high Poisson's ratio than the one of low Poisson's ratio. Therefore, in practical applications, using the annular membranes of high Poisson's ratios and low (or

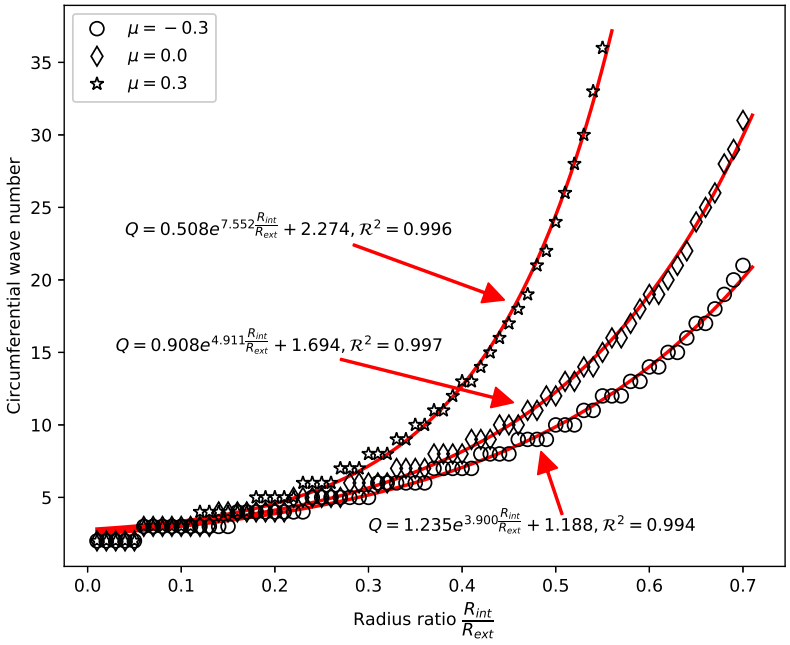

(a)

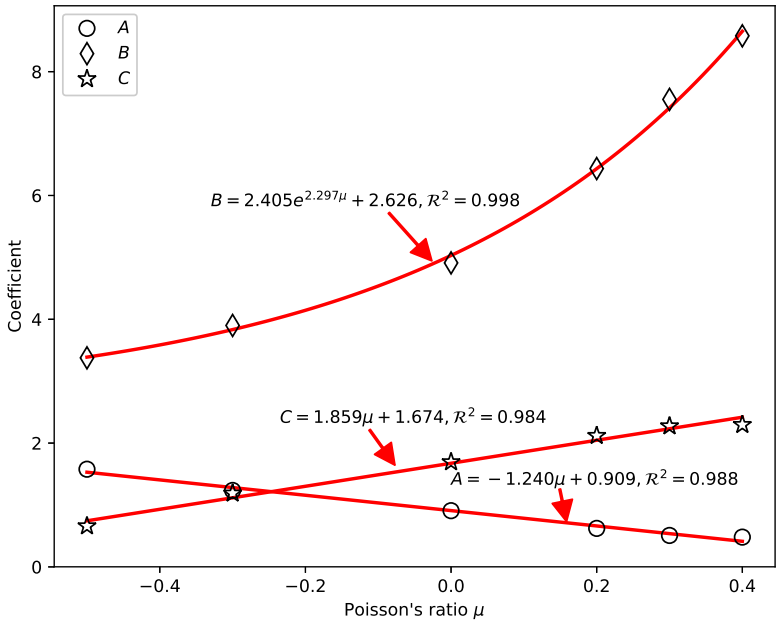

(b)

Figure 9.11 Relationship between the radius ratio and the wave number of the lowest instability pattern: (a) circumferential wave number is a function of radius ratio; (b) coefficients of the exponential function are the functions of μ

high) radius ratios, is a simple, but effective, way to improve the wrinkling resistance, which is also mentioned in [17].

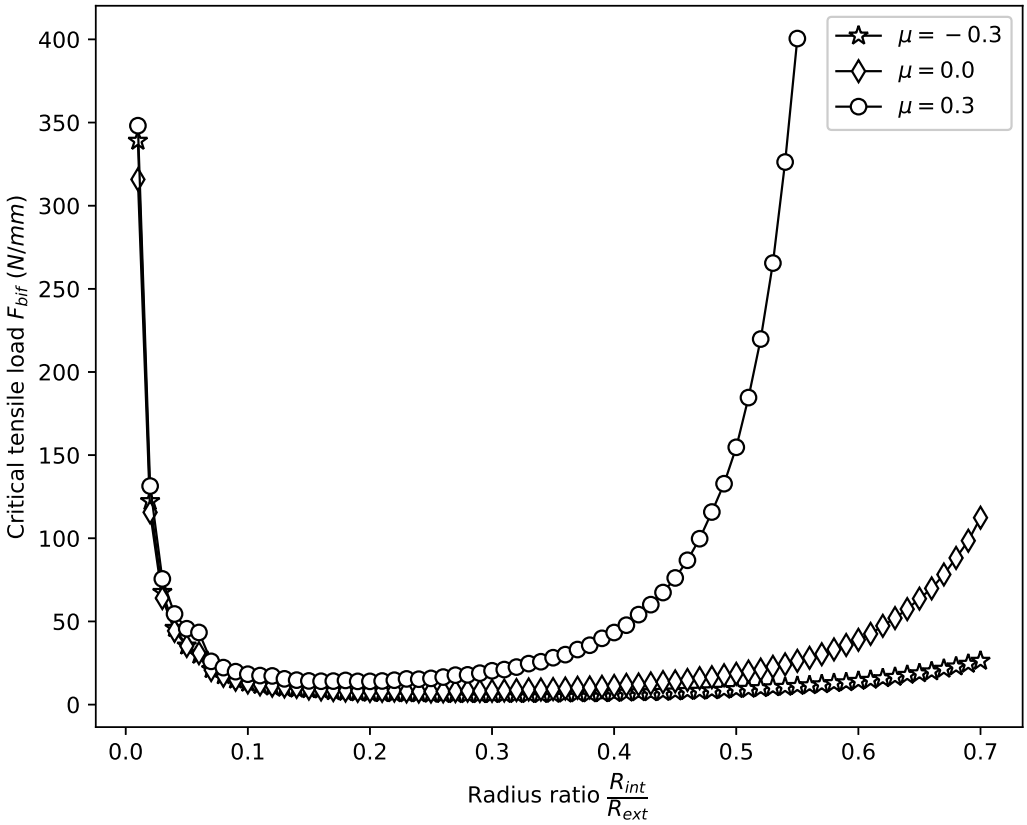

Figure 9.12 Relationship between the radius ratio and the critical instability load of the lowest instability pattern

9.5.4 Effect of Poisson's ratio

As discussed above, the wrinkling phenomena always arise when the annular membrane is stretched at the internal edge no matter if the Poisson's ratio is negative or positive. However, the value of Poisson's ratio should somehow affect wrinkling. Therefore, in this section, the effect of Poisson's ratio is further investigated.

Table 9.3 displays both the lowest instability patterns, which corresponds to the lowest critical loads, and the specific instability pattern $R1C13$ of five Poisson's ratios decreasing from 0.40 to -0.40. The critical load of the same instability pattern $R1C13$ decreases from $100.48N/mm$ to $11.89N/mm$, and the circumferential wave number of the lowest instability pattern decreases from 17 to 7. The critical instability load F_{bif} of $R1C13$ does not mono-

tonically decrease with Poisson's ratio μ. When $\mu = -0.4$, the critical load of instability of $R1C13$ is $F_{bif} = 11.89N/mm$, which is higher than $F_{bif} = 11.88N/mm$ in the case of $\mu = -0.30$. $R1C13$ is the higher instability pattern when $\mu < 0.3$ and the lowest instability pattern when $\mu = 0.3$, but becomes the higher instability pattern again when $\mu > 0.3$.

Table 9.3 Instability patterns for different Poisson's ratio μ

Poisson's ratio μ	Instability patterns	Tensile load $F(N/mm)$
0.40	R1C17 (Lowest pattern)	100.48
	R1C13 (Higher pattern)	131.22
0.30	R1C13 (Lowest pattern)	43.17
0.00	R1C8 (Lowest pattern)	11.22
	R1C13 (Higher pattern)	15.51
-0.30	R1C7 (Lowest pattern)	7.06
	R1C13 (Higher pattern)	11.88
-0.40	R1C7 (Lowest pattern)	6.57
	R1C13 (Higher pattern)	11.89

To further analyze the results, other calculation for Poisson's ratios μ ranging from -0.45 to 0.40 with the interval of 0.05 are carried out. As discussed above, the main effective term of circumferential stress is the radial displacement. Therefore, the relationship between the critical load and the radial displacement at the internal edge is studied. As shown in Fig. 9.13, both the critical load F_{bif} and the radial displacement u vary as the functions of Poisson's ratio. When $\mu < -0.40$, the critical instability load decreases with Poisson's ratio μ; whereas when $\mu \geq -0.40$, it increases. Except in the case of $\mu = 0.30$, the critical load F_{bif} of $R1C13$ is always higher than that of the lowest instability pattern. A similar trend can be observed in the curve of the radial displacement u_{int} at the internal edge, but u_{int} remains nearly constant when $\mu < -0.40$.

9.5.5 Summary

The above discussion shows that the reduced model accounting for several Fourier harmonics provides accurate and computationally efficient results to simulate the entire instability process. Meanwhile, the proper lowest wrinkling pattern can be automatically selected with the reduced model. Moreover, the instability mechanism of the annular membrane under tensile load at the internal edge is discussed as the appearance of wrinkles in this example is not determined by Poisson's ratio. An exponential function related to the geometric dimensions

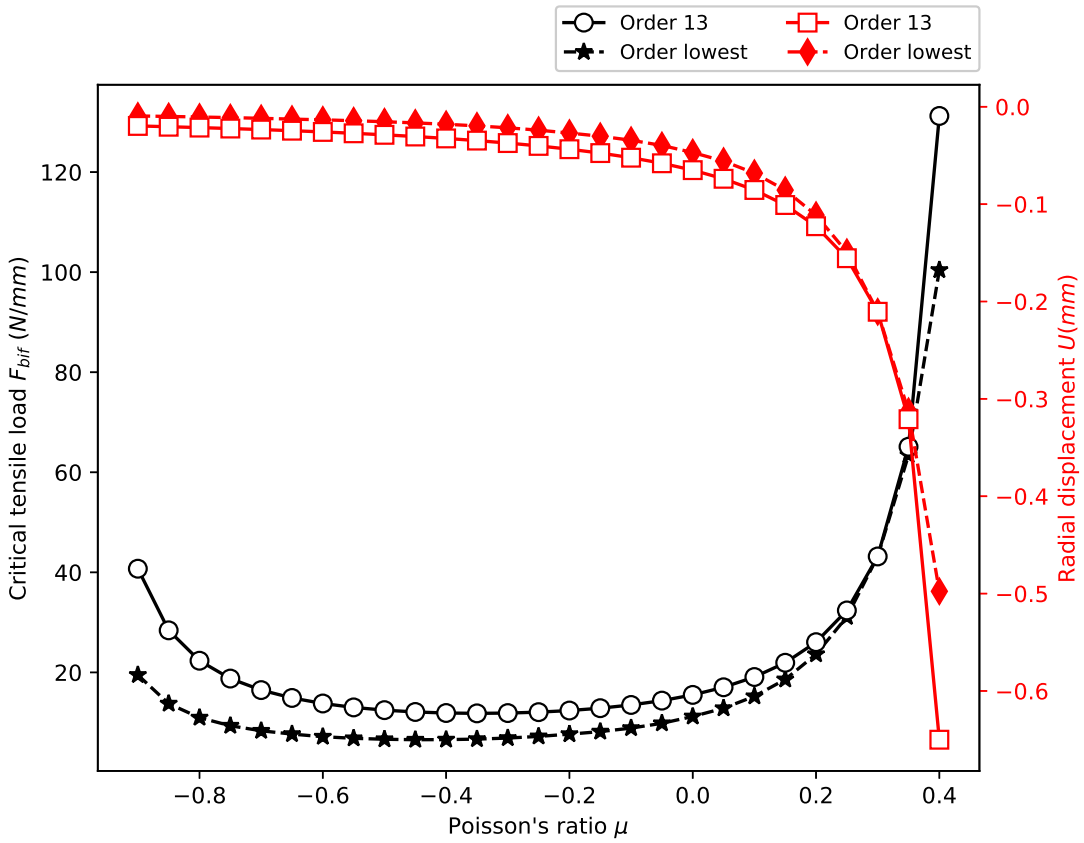

Figure 9.13 Critical loads of instability and transverse displacements at the internal edge with the variation of Poisson's ratio

and Poisson's ratio is developed to predict the wave number of the lowest instability pattern so as to further improve the reduced model.

9.6 Solution for circular plate buckling problem

As shown in Fig.9.14, a circular plate under the uniform compressive load along the external edge is investigated in this section. The transverse displacement and stress distribution are predicted with the reduced model. The material properties and geometric dimensions are given in Table 9.4.

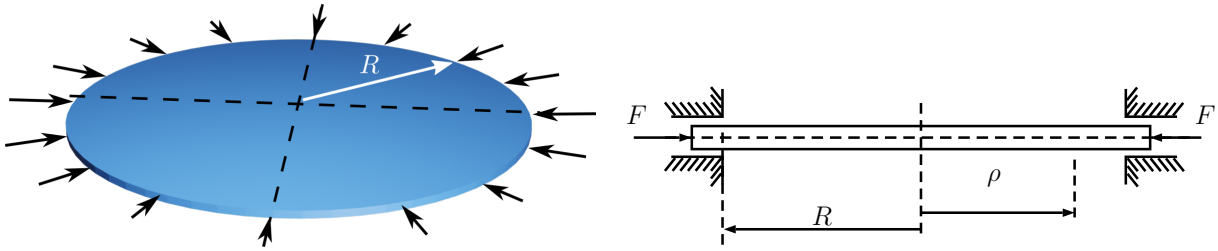

Figure 9.14 A circular plate under radial compressive load along the external edge

Table 9.4 Material properties and geometric dimensions of the circular plate

Young's modulus E (MPa)	Poisson's ratio μ	Thickness h (mm)	Radius R (mm)
$69,000$	0.3	10	1000

9.6.1 Transverse displacement

The relationship between the critical load and the position of the crest is investigated here, because they are both related to the instability pattern. The instability patterns of waves in the circumferential direction and several half-waves in the radial direction are simulated by the reduced model, such as $R1C3$ and $R3C5$ presented in Fig. 9.15.

Fig. 9.16 shows the transverse displacement distributions in the radial direction for the cases of different instability patterns and boundary conditions. As shown in Fig. 9.16a, the circumferential wave number changes from 3 to 9, while the crest position moves to the external edge. On the contrary, as shown in Fig. 9.16b, when the radial wave number increases from 1 to 4, the crest position moves to the internal edge. Besides, in both figures,

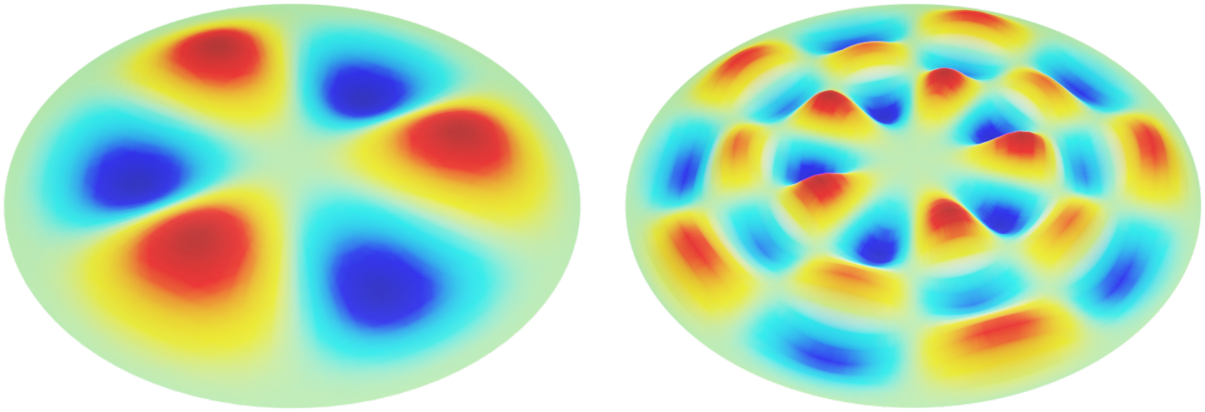

(a) $R1C3$ (b) $R3C5$

Figure 9.15 Instability patterns of circular plates under compressive load along the external edge predicted by the reduced model

the crest is closer to the internal edge when the edge of the plate is clamped compared to simply supported boundaries. Therefore, the relative location of the crest is affected by both the wave numbers in the two directions and the boundary conditions.

Fig. 9.17 quantitatively shows the relationship between the wave number and the crest position discussed above. The half-wave number in the radial direction and the wave number in the circumferential direction change from 1 to 9 simultaneously. Under different boundary conditions, the crest position varies as well as the exponential function of the wave number in both directions. For each case, the position always converges to a constant value with the increase of the wave number. These functions make it possible to directly predict the crest position of different instability pattern according to the wave number.

The relationship between the critical load F_{bif} and the relative location of the crest $\frac{\rho_{crest}}{R}$is quantitatively analyzed in Fig. 9.18. The eigenvalue $\sqrt{\frac{R^2 F_{bif}}{D}}$ related to the critical load is used for the analysis, which is not affected by the geometric dimensions. The results of four different cases are well fitted by exponential functions. Using the same idea to analyze other more complex examples without analytical solutions, it might be a rapid and effective way to predict the critical loads of instability by measuring the positions of crests with special optical devices, e.g., digital image correlation (DIC) measurement systems.

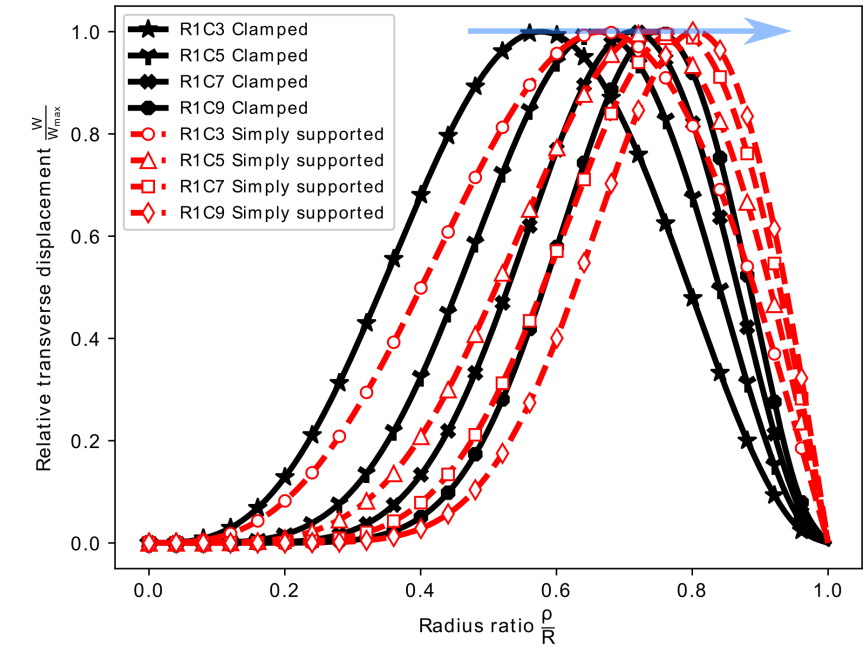

(a)

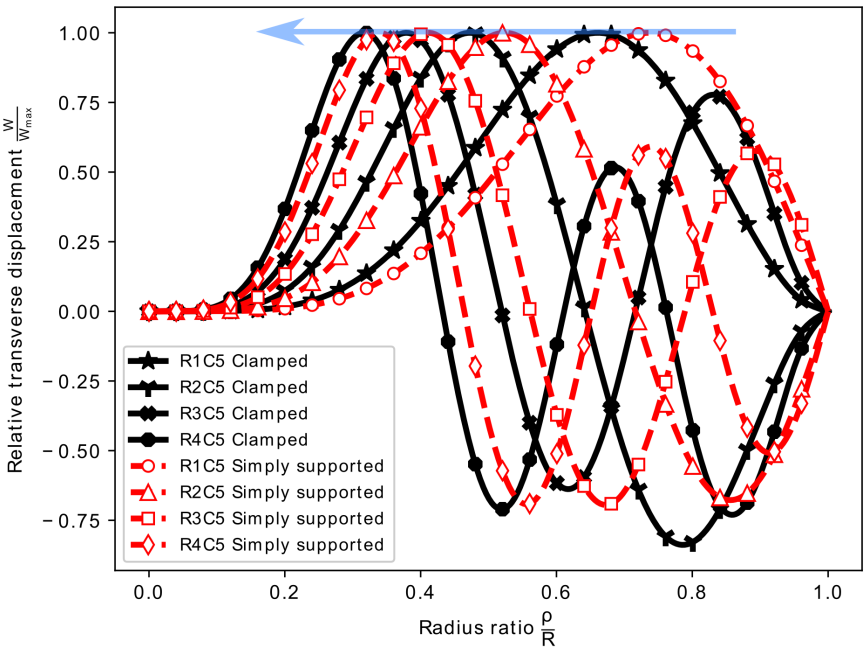

(b)

Figure 9.16 Transverse displacements in the radial direction for different instability patterns: (a) different circumferential instability patterns; (b) different radial instability patterns

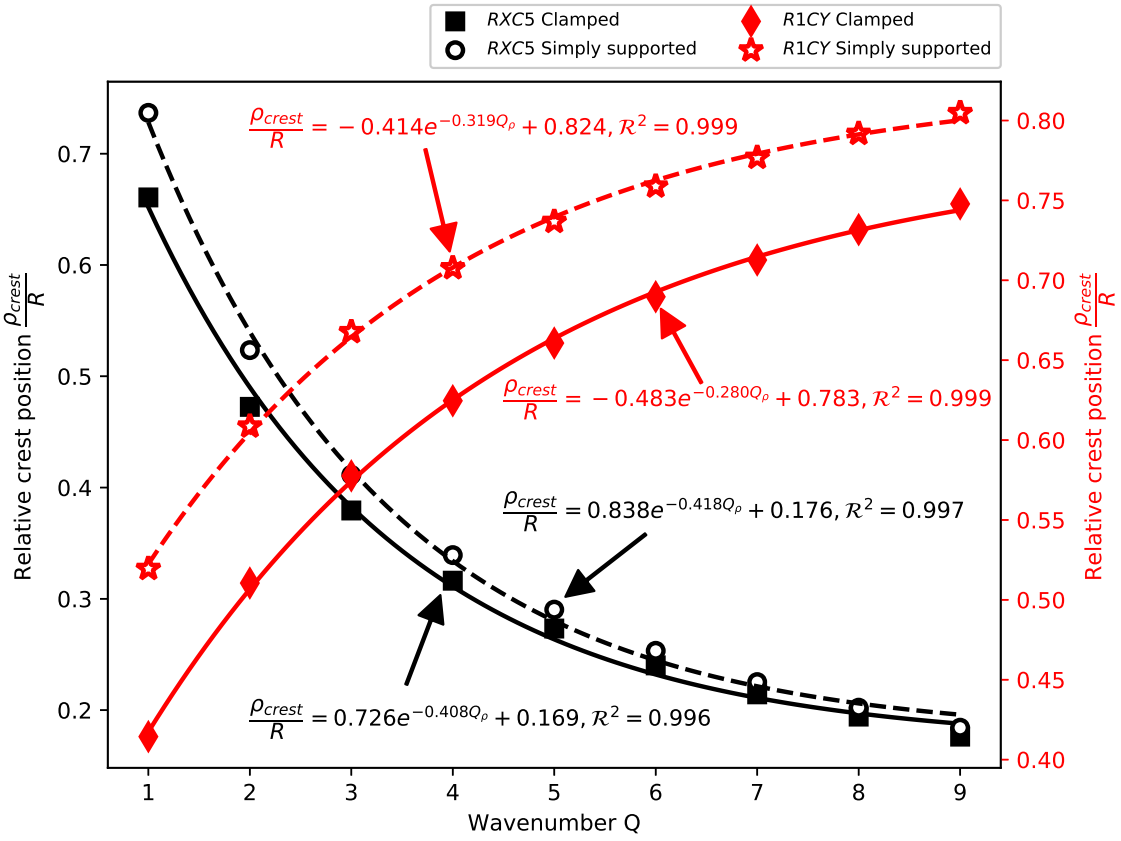

Figure 9.17 Relationship between the positions of the crests and the wave numbers under different boundary conditions

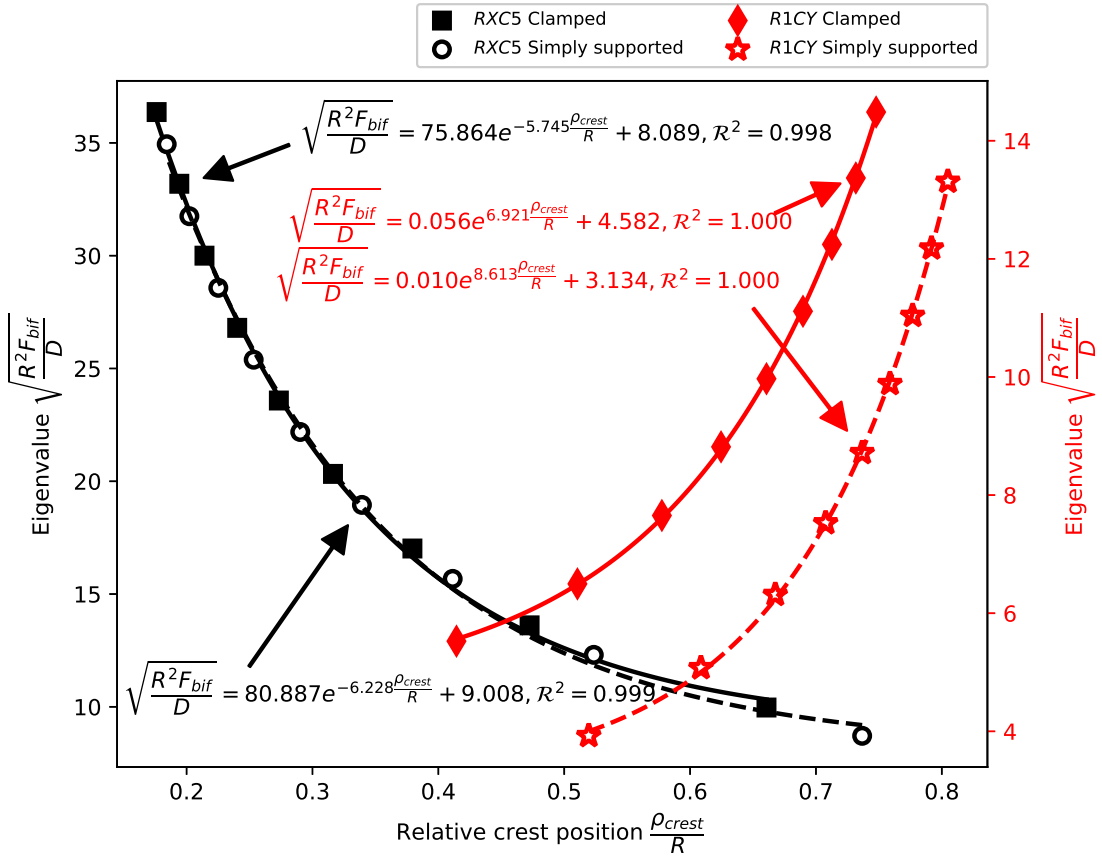

Figure 9.18 Relationship between the eigenvalue and the positions of the crests in the cases of different boundary conditions

9.6.2 Stress distributions

The instability pattern $R3C5$ is simulated by the reduced model to study the stress distributions. As shown in Fig. 9.19, near the bifurcation point, both stresses exhibit a periodic pattern in the circumferential direction and a nearly periodic one in the radial direction. The region of maximum circumferential stress appears in the vicinity of the center, while there does not seem to be any unique region of maximum radial stress.

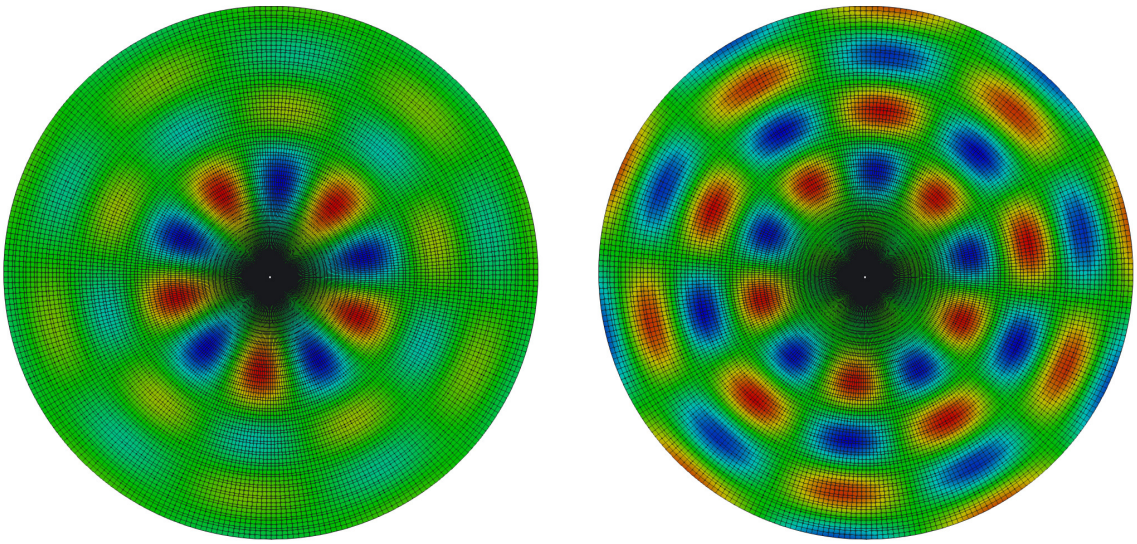

(a) (b)

Figure 9.19 Stress distributions on the top surface near the bifurcation point: (a) circumferential stress distribution; (b) radial stress distribution

As shown in Fig. 9.20 for the instability pattern $R3C5$, both the radial and circumferential stresses present nearly periodic pattern in the radial direction. The stresses on the top surface tend to be higher at the peak, while the ones on the bottom surface tend to be higher at the trough. Therefore, the direction of the transverse displacement determines the surface to be stretched, i.e., the top surface of the crest and the bottom surface of the trough tend to be stretched in the post-buckling stage. The amplitude of the radial stress remains at the same level, while that of the circumferential stress decreases in the radial direction. The explanation could be connected with the wave lengths of the radial wrinkles which are nearly the same along the radial direction, while the ones of the circumferential wrinkles change along the radial direction.

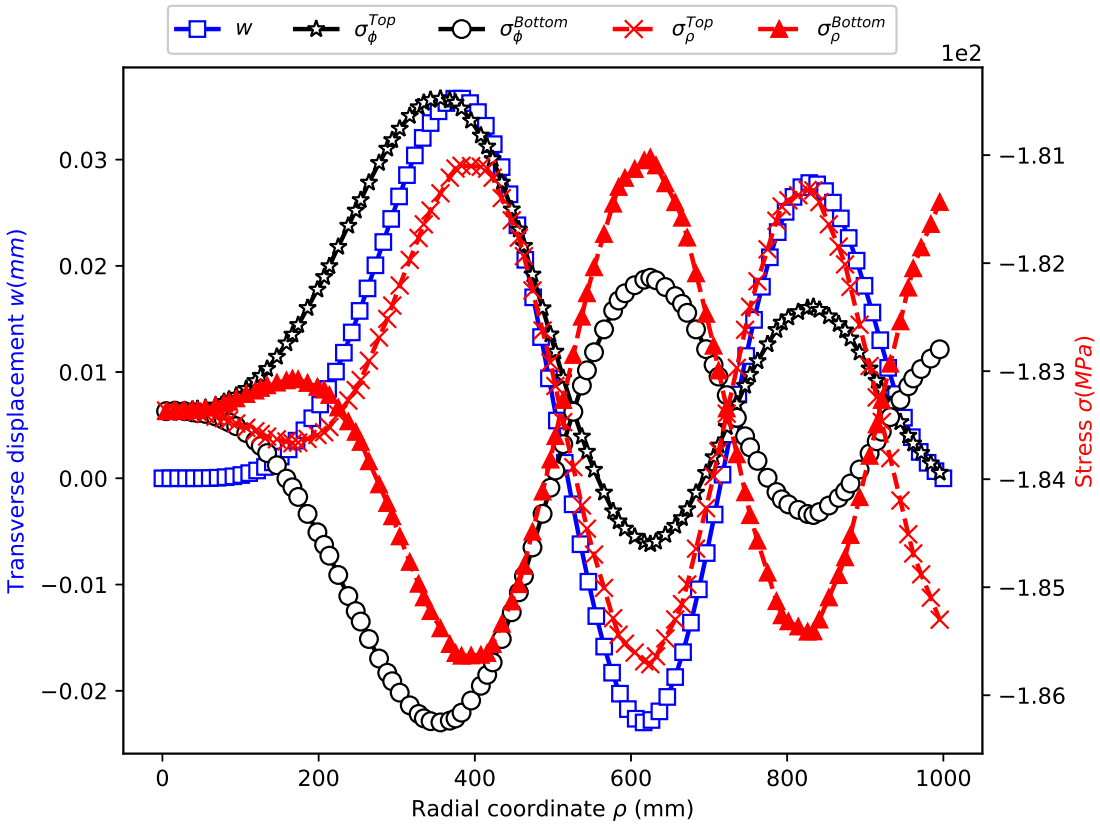

Figure 9.20 Transverse displacements and stresses in the radial direction near the bifurcation point

9.7 Conclusions

Based on the recently developed approach [1], a improved reduced model accounting for several Fourier harmonics is constructed to solve circumferential periodic instability problems of circular thin-walled structures. For the simulation of annular membrane wrinkling, the reduced model automatically chooses the lowest instability pattern to ensure the system to be in a state with minimum energy, which facilitates the study of cases with unknown wrinkling patterns. The instability mechanisms of a stretched annular membrane have been investigated. The results show that the appearance of wrinkles in circular membranes does not rely on Poisson's effect, which is different from a similar reference example in Cartesian coordinates, namely a rectangular membrane under in-plane uniaxial tensile load [14, 32]. However, the value of Poisson's ratio and the geometric dimensions have a great influence on wrinkling patterns. Finally, the instability problem of a circular thin plate under the in-plane compression was investigated. The relative location of the crest is affected by both the wave numbers in the two directions and the boundary conditions. It always converges to a constant value with the increase of the wave number.

Acknowledgements

This work has been supported by the National Natural Science Foundation of China (Grant Nos. 11920101002 and 11772238). The authors also acknowledge the financial support of the National Science & Engineering Research Council of Canada (NSERC).

9.8 Appendix A. Implementation of the ANM

The established nonlinear system is solved by the Asymptotic Numerical Method (ANM) proposed by [39]. Suppose that $\{\mathbf{S}\}_t$ $(t \in [0, n_j])$, $\{\mathscr{S}\}_n$ $(n \in [1, n_j])$ and $\{\mathbf{q}^e\}$ are the assembly of the vectors $\{\mathbf{S}_p\}_t$, $\{\mathscr{S}_p\}_n$ and $\{\mathbf{q}_p^e\}$ $(p = 1, 2, 3 \cdots)$. The solution at the end of step j is assumed to be known to determine the solution at the end of step $(j + 1)$. Thus the

unknowns vectors can be expressed as:

$$\{\mathbf{S}\}_t = \{\mathbf{S}\}_t^j + \sum_{p=1}^{n_a} \alpha^p \{\mathbf{S}_p\}_t = \{\mathbf{S}\}_t^j + \alpha\{\mathbf{S}_1\}_t + \alpha^2\{\mathbf{S}_2\}_t + \cdots, \tag{9.34}$$

$$\{\boldsymbol{\mathscr{S}}\}_n = \{\boldsymbol{\mathscr{S}}\}_n^j + \sum_{p=1}^{n_a} \alpha^p \{\boldsymbol{\mathscr{S}}_p\}_n = \{\boldsymbol{\mathscr{S}}\}_n^j + \alpha\{\boldsymbol{\mathscr{S}}_1\}_n + \alpha^2\{\boldsymbol{\mathscr{S}}_2\}_n + \cdots, \tag{9.35}$$

$$\{\mathbf{q}^e\} = \{\mathbf{q}^e\}^j + \sum_{p=1}^{n_a} \alpha^p \{\mathbf{q}_p^e\} = \{\mathbf{q}^e\}^j + \alpha\{\mathbf{q}_1^e\} + \alpha^2\{\mathbf{q}_2^e\} + \cdots, \tag{9.36}$$

$$\lambda = \lambda^j + \sum_{p=1}^{n_a} \alpha^p \lambda_p = \lambda^j + \alpha\lambda_1 + \alpha^2\lambda_2 + \cdots, \tag{9.37}$$

$$\alpha = \langle \mathbf{q}_1^e \rangle \left(\{\mathbf{q}^e\} - \{\mathbf{q}^e\}^j \right) + \lambda_1 \left(\lambda - \lambda^j \right), \tag{9.38}$$

in which α is the path parameter. Substituting the approached solutions of Eqs. (9.34)-(9.38) into Eqs. (9.28) and (9.29), a complete expansion form of governing equations can be deduced. Then each calculation step can be separated into order 1 and order p (p≥2):

Order 1

$$\begin{cases} \sum\limits_e \langle \delta\mathbf{q}^e \rangle \int_0^{le} \left\{ {}^T[\mathbf{B}(\mathbf{q}^{ej})]_0\{\mathbf{S}_1\}_0 + {}^T[\mathbf{B}_{nl}(\mathbf{q}_1^e)]_0\{\mathbf{S}\}_0^j + 2\sum\limits_{n=1}^{n_j} \left[{}^T[\mathbf{B}(\mathbf{q}^{ej})]_n\{\mathbf{S}_1\}_n + {}^T[\mathbf{B}_{nl}(\mathbf{q}_1^e)]_n\{\mathbf{S}\}_n^j \right] \right. \\ \left. +2\sum\limits_{n=1}^{n_j} \left[{}^T[\boldsymbol{\mathscr{B}}(\mathbf{q}^{ej})]_n\{\boldsymbol{\mathscr{S}}_1\}_n + {}^T[\boldsymbol{\mathscr{B}}_{nl}(\mathbf{q}_1^e)]_n\{\boldsymbol{\mathscr{S}}\}_n^j \right] \right\} \rho d\rho = \sum\limits_e \langle \delta\mathbf{q}^e \rangle \lambda_1 \{\mathbf{f}^e\}, \\ \{\mathbf{S}_1\}_n = [\mathbf{D}][\mathbf{B}(\mathbf{q}^{ej})]_n\{\mathbf{q}_1^e\}, \\ \{\boldsymbol{\mathscr{S}}_1\}_n = [\mathbf{D}][\boldsymbol{\mathscr{B}}(\mathbf{q}^{ej})]_n\{\mathbf{q}_1^e\}, \\ 1 = \langle \mathbf{q}_1^e \rangle \{\mathbf{q}_1^e\} + \lambda_1^2. \end{cases} \tag{9.39}$$

Note that $\{\mathbf{q}^e\}^j$ is the known vector and $\{\mathbf{q}_1^e\}$ is the unknown vector. The terms ${}^T[\mathbf{B}_{nl}(\mathbf{q}_1^e)]_t\{\mathbf{S}\}_t^j$ and ${}^T[\boldsymbol{\mathscr{B}}_{nl}(\mathbf{q}_1^e)]_n\{\boldsymbol{\mathscr{S}}\}_n^j$ are rewritten as:

$$\begin{cases} {}^T[\mathbf{B}_{nl}(\mathbf{q}_1^e)]_t\{\mathbf{S}\}_t^j = {}^T\ [\mathbf{G}][\widetilde{\mathbf{S}}]_t^j[\mathbf{G}]\{\mathbf{q}_1^e\}, \\ {}^T[\boldsymbol{\mathscr{B}}_{nl}(\mathbf{q}_1^e)]_n\{\boldsymbol{\mathscr{S}}\}_n^j = {}^T\ [\mathbf{G}][\widetilde{\boldsymbol{\mathscr{S}}}]_n^j[\mathbf{G}]\{\mathbf{q}_1^e\}, \end{cases} \tag{9.40}$$

where $t \in [0, n_j]$, $n \in [1, n_j]$ and the non-zero elements of transform matrices $[\widetilde{\mathbf{S}}]_t^j$ and $[\widetilde{\boldsymbol{\mathscr{S}}}]_n^j$ are listed in Table 9.5, in which $r \in [n - n_j, n_j]$. Submitting Eq. (9.40) into Eq. (9.39), the following equation with element matrices is obtained:

$$\sum_e \langle \delta\mathbf{q}^e \rangle \left([\mathbf{k}(\mathbf{q}^e, \mathbf{S}_t, \boldsymbol{\mathscr{S}}_n)]\{\mathbf{q}_1^e\} - \lambda_1\{\mathbf{f}^e\} \right) = 0, \tag{9.41}$$

in which, $[\mathbf{k}(\mathbf{q}^e, \mathbf{S}_t, \mathscr{S}_n)]$ is the element stiffness matrix,

$$[\mathbf{k}(\mathbf{q}^e, \mathbf{S}_t, \mathscr{S}_n)] = \int_0^{le} \Bigg({}^T[\mathbf{B}(\mathbf{q}^{ej})]_0[\mathbf{D}][\mathbf{B}(\mathbf{q}^{ej})]_0 + {}^T[\mathbf{G}][\widetilde{\mathbf{S}}]_0^j[\mathbf{G}] + 2\sum_{n=1}^{n_j} \left[{}^T[\mathbf{B}(\mathbf{q}^{ej})]_n[\mathbf{D}][\mathbf{B}(\mathbf{q}^{ej})]_n + {}^T[\mathbf{G}][\widetilde{\mathbf{S}}]_n^j[\mathbf{G}] \right] + 2\sum_{n=1}^{n_j} \left[{}^T[\mathscr{B}(\mathbf{q}^{ej})]_n[\mathbf{D}][\mathscr{B}(\mathbf{q}^{ej})]_n + {}^T[\mathbf{G}][\widetilde{\mathscr{S}}]_n^j[\mathbf{G}] \right] \Bigg) \rho d\rho. \tag{9.42}$$

Table 9.5 Elements of the transform matrices $[\widetilde{\mathbf{S}}]_t^j$ and $[\widetilde{\mathscr{S}}]_n^j$

Matrix $((7+3n_j)\times(7+3n_j))$	Non-zero elements	
$[\widetilde{\boldsymbol{S}}]_0^j$	(1,1)=$\frac{S_2^j}{\rho^2}$ (1,4)=$\frac{S_3^j}{\rho}$	(2,2)=S_1^j (2,3)=$-\frac{S_3^j}{\rho}$
	(3,3)=$\frac{S_2^j}{\rho^2}$ (4,4)=S_1^j	(3,2)=$-\frac{S_3^j}{\rho}$ (4,1)=$\frac{S_3^j}{\rho}$
	(5+3|r|,5+3|r|)+=$\frac{r^2Q^2S_2^j}{\rho^2}$	(6+3|r|,6+3|r|)+=S_1^j
$[\widetilde{\boldsymbol{S}}]_n^j$	(5+3|r|,5+3|n − r|)+=$\frac{r(r-n)Q^2S_2^j}{\rho^2}$	(6+3|r|,6+3|n − r|)+=S_1^j
$[\widetilde{\mathscr{S}}]_n^j$	(5+3|r|,6+3|n − r|)+=$\frac{rQS_3^j}{\rho}$	(6+3|n − r|,5+3|r|)+=$\frac{rQS_3^j}{\rho}$

After combining all the element matrices and vectors, the final equation of order 1 can be obtained:

$$[\mathbf{K}(\mathbf{q}^e, \mathbf{S}_t, \mathscr{S}_n)]\{\mathbf{Q}_1\} = \lambda_1\{\mathbf{F}\}, \tag{9.43}$$

where $[\mathbf{K}(\mathbf{q}^e, \mathbf{S}_t, \mathscr{S}_n)]$ is the global stiffness matrix, $\{\mathbf{Q}_1\}$ the global displacement vector and $\{\mathbf{F}\}$ the global load vector.

Order p

The governing equations of order p is written as following:

$$\begin{cases} \sum_e \langle \delta \mathbf{q}^e \rangle \int_0^{le} \left\{ {}^T[\mathbf{B}(\mathbf{q}^{ej})]_0 \{\mathbf{S}_p\}_0 + {}^T[\mathbf{B}_{nl}(\mathbf{q}_p^e)]_0 \{\mathbf{S}\}_0^j + 2\sum_{n=1}^{n_j} \left[{}^T[\mathbf{B}(\mathbf{q}^{ej})]_n \{\mathbf{S}_p\}_n + {}^T[\mathbf{B}_{nl}(\mathbf{q}_p^e)]_n \{\mathbf{S}\}_n^j \right] \right. \\ \left. +2\sum_{n=1}^{n_j} \left[{}^T[\boldsymbol{\mathscr{B}}(\mathbf{q}^{ej})]_n \{\boldsymbol{\mathscr{S}}_p\}_n + {}^T[\boldsymbol{\mathscr{B}}_{nl}(\mathbf{q}_p^e)]_n \{\boldsymbol{\mathscr{S}}\}_n^j \right] \right\} \rho d\rho \\ = \sum_e \langle \delta \mathbf{q}^e \rangle \left[\lambda_p \{\mathbf{f}^e\} + \{\mathbf{f}_p^{enl}\}_0 + 2\sum_{n=1}^{n_j} \left(\{\mathbf{f}_p^{enl}\}_n + \{\boldsymbol{\mathscr{F}}_p^{enl}\}_n \right) \right], \\ \{\mathbf{S}_p\}_t = [\mathbf{D}][\mathbf{B}(\mathbf{q}^{ej})]_t \{\mathbf{q}_p^e\} + \left\{\mathbf{S}_p^{nl}\right\}_t, \\ \{\boldsymbol{\mathscr{S}}_p\}_n = [\mathbf{D}][\boldsymbol{\mathscr{B}}(\mathbf{q}^{ej})]_n \{\mathbf{q}_p^e\} + \left\{\boldsymbol{\mathscr{S}}_p^{nl}\right\}_n, \\ 0 = \langle \mathbf{q}_1^e \rangle \{\mathbf{q}_p^e\} + \lambda_1 \lambda_p, \end{cases} \tag{9.44}$$

in which

$$\begin{cases} \left\{\mathbf{f}_p^{enl}\right\}_t = -\sum_{g=1}^{p-1} \int_0^{le} \left({}^T[\mathbf{B}_{nl}(\mathbf{q}_{p-g}^e)]_t \{\mathbf{S}_p\}_t \right) \rho d\rho, \\ \left\{\mathbf{S}_p^{nl}\right\}_t = \frac{1}{2}[\mathbf{D}] \sum_{g=1}^{p-1} [\mathbf{B}_{nl}(\mathbf{q}_{p-g}^e)]_t \left\{\mathbf{q}_g^e\right\}, \\ \left\{\boldsymbol{\mathscr{F}}_p^{enl}\right\}_n = -\sum_{g=1}^{p-1} \int_0^{le} \left({}^T[\boldsymbol{\mathscr{B}}_{nl}(\mathbf{q}_{p-g}^e)]_n \{\boldsymbol{\mathscr{S}}_p\}_n \right) \rho d\rho, \\ \left\{\boldsymbol{\mathscr{S}}_p^{nl}\right\}_n = \frac{1}{2}[\mathbf{D}] \sum_{g=1}^{p-1} [\boldsymbol{\mathscr{B}}_{nl}(\mathbf{q}_{p-g}^e)]_n \left\{\mathbf{q}_g^e\right\}. \end{cases} \tag{9.45}$$

Some additional terms exist in Eq. (9.44) compared to Eq. (9.39), which are non-linear force terms and are moved to the right side of the equation.

$$\sum_e \langle \delta \mathbf{q}^e \rangle \left[[\mathbf{k}(\mathbf{q}^{ej}, \mathbf{S}_t, \boldsymbol{\mathscr{S}}_n)] \{\mathbf{q}_p^e\} - \lambda_p \{\mathbf{f}^e\} - \left\{\mathbf{f}_p^{eNL}\right\}_0 - 2\sum_{n=1}^{n_j} \left(\{\mathbf{f}_p^{eNL}\}_n + \{\boldsymbol{\mathscr{F}}_p^{eNL}\}_n \right) \right] = 0, \tag{9.46}$$

in which, the element nonlinear force vectors $\left\{\mathbf{f}_p^{eNL}\right\}_t$ and $\left\{\boldsymbol{\mathscr{F}}_p^{eNL}\right\}_n$ are written as:

$$\begin{cases} \left\{\mathbf{f}_p^{eNL}\right\}_t = \left\{\mathbf{f}_p^{enl}\right\}_t - \int_0^{le} \left({}^T[\mathbf{B}(\mathbf{q}^{ej})]_t \{\mathbf{S}_p^{nl}\}_t \right) \rho d\rho, \\ \left\{\boldsymbol{\mathscr{F}}_p^{eNL}\right\}_n = \left\{\boldsymbol{\mathscr{F}}_p^{enl}\right\}_n - \int_0^{le} \left({}^T[\boldsymbol{\mathscr{B}}(\mathbf{q}^{ej})]_n \{\boldsymbol{\mathscr{S}}_p^{nl}\}_n \right) \rho d\rho. \end{cases} \tag{9.47}$$

After combining all the element matrices, the final equation of order p can be derived as:

$$[\mathbf{K}(\mathbf{q}^e, \mathbf{S}_t, \boldsymbol{\mathscr{S}}_n)] \{\mathbf{Q}_p\} = \lambda_p \{\mathbf{F}\} + \{\mathbf{F}_p^{nl}\}, \tag{9.48}$$

in which $[\mathbf{K}(\mathbf{q}^e, \mathbf{S}_t, \boldsymbol{\mathscr{S}}_n)]$ is the global stiffness matrix, that is the same as the one in the first

order. $\{\mathbf{Q}_p\}$ is the global displacement vector, $\{\mathbf{F}\}$ the global load vector, and $\{\mathbf{F}_p^{nl}\}$ the global nonlinear force vector.

After solving all the orders in one step, the results $\{\mathbf{Q}_p\}$(p≥1) are submitted into Eq. (9.36):

$$\{\mathbf{Q}\}^{j+1} = \{\mathbf{Q}\}^j + \sum_{p=1}^{n_a} \alpha^p \{\mathbf{Q}_p\} = \{\mathbf{Q}\}^j + \alpha\{\mathbf{Q}_1\} + \alpha^2\{\mathbf{Q}_2\} + \cdots , \tag{9.49}$$

where the maximum value of the path parameter α is defined as the same principle as in [39],

$$\alpha = \left(\zeta \frac{\|\mathbf{Q}_1\|}{\|\mathbf{Q}_{n_a}\|}\right)^{\frac{1}{n_a - 1}} . \tag{9.50}$$

where ζ is the precise parameter initially assigned by the user.

Bibliography

[1] W. Huang, Q. Huang, Y. Liu, J. Yang, H. Hu, F. Trochu, and P. Causse, "A Fourier based reduced model for wrinkling analysis of circular membranes," *Computer Methods in Applied Mechanics and Engineering*, vol. 345, pp. 1114–1137, 2019.

[2] J. A. Rogers, T. Someya, and Y. Huang, "Materials and mechanics for stretchable electronics," *science*, vol. 327, no. 5973, pp. 1603–1607, 2010.

[3] Y. Li, S. Zhang, X. Li, V. R. N. Unnava, and F. Cicoira, "Highly stretchable PEDOT:PSS organic electrochemical transistors achieved via polyethylene glycol addition," *Flexible and Printed Electronics*, vol. 4, no. 4, p. 044004, 2019.

[4] Z. Yi, L. G. Bettini, G. Tomasello, P. Kumar, P. Piseri, I. Valitova, P. Milani, F. Soavi, and F. Cicoira, "Flexible conducting polymer transistors with supercapacitor function," *Journal of Polymer Science Part B: Polymer Physics*, vol. 55, no. 1, pp. 96–103, 2017.

[5] G. Xu, C. Cheng, Z. Liu, W. Yuan, X. Wu, Y. Lu, S. S. Low, J. Liu, L. Zhu, D. Ji *et al.*, "Battery-free and wireless epidermal electrochemical system with all-printed stretchable electrode array for multiplexed in situ sweat analysis," *Advanced Materials Technologies*, vol. 4, no. 7, p. 1800658, 2019.

[6] P. Causse, E. Ruiz, and F. Trochu, "Influence of preforming on the quality of curved composite parts manufactured by flexible injection," *International Journal of Material Forming*, vol. 6, pp. 341–362, 2013.

[7] C. Williams, J. Summerscales, and S. Grove, "Resin infusion under flexible tooling (RIFT): A review," *Composites Part A: Applied Science and Manufacturing*, vol. 27, pp. 517–524, 1996.

[8] W. Huang, P. Causse, H. Hu, S. Belouettar, and F. Trochu, "Transverse compaction of 2D glass woven fabrics based on material twins – Part I : Geometric analysis," *Composite Structures*, vol. 237, p. 111929, 2020.

[9] W. Huang, P. Causse, H. Hu, S. Belouettar, and F. Trochu, "Transverse compaction of 2D glass woven fabrics based on material twins – Part II: Tow and fabric deformations," *Composite Structures*, vol. 237, p. 111963, 2020.

[10] W. Huang, P. Causse, H. Hu, and F. Trochu, "Numerical and experimental investigation of saturated transverse permeability of 2D woven glass fabrics based on material twins," *Polymer Composites*, vol. 41, no. 4, pp. 1341–1355, 2020.

[11] W. Huang, P. Causse, V. Brailovski, H. Hu, and F. Trochu, "Reconstruction of mesostructural material twin models of engineering textiles based on Micro-CT Aided Geometric Modeling," *Composites Part A: Applied Science and Manufacturing*, vol. 124, p. 105481, 2019.

[12] N. Bowden, S. Brittain, A. G. Evans, J. W. Hutchinson, and G. M. Whitesides, "Spontaneous formation of ordered structures in thin films of metals supported on an elastomeric polymer," *Nature*, vol. 393, no. May, pp. 146–149, 1998.

[13] B. Li, Y. Cao, X. Feng, and H. Gao, "Mechanics of morphological instabilities and surface wrinkling in soft materials: A review," *Soft Matter*, vol. 8, pp. 5728–5745, 2012.

[14] E. Cerda, K. Ravi-Chandar, and L. Mahadevan, "Thin films: Wrinkling of an elastic sheet under tension," *Nature*, vol. 419, no. 6907, pp. 579–580, 2002.

[15] N. Jacques, A. Elias, M. Potier-Ferry, and H. Zahrouni, "Buckling and wrinkling during strip conveying in processing lines," *Journal of Materials Processing Technology*, vol. 190, no. 1-3, pp. 33–40, 2007.

[16] A. Agrawal, N. V. Reddy, and P. M. Dixit, "Prediction of wrinkling and determination of minimum blankholding pressure in multistage deep drawing," *Journal of Manufacturing Science and Engineering*, vol. 133, no. 6, p. 061023, 2011.

[17] R. H. Plaut, "Linearly elastic annular and circular membranes under radial, transverse, and torsional loading. Part I: Large unwrinkled axisymmetric deformations," *Acta Mechanica*, vol. 202, pp. 79–99, 2009.

[18] C. D. Coman and D. M. Haughton, "Localized wrinkling instabilities in radially stretched annular thin films," *Acta Mechanica*, vol. 185, pp. 179–200, 2006.

[19] C. D. Coman, "On the applicability of tension field theory to a wrinkling instability problem," *Acta Mechanica*, vol. 190, pp. 57–72, 2007.

[20] C. D. Coman, "Some applications of the WKB method to the wrinkling of bi-annular plates in tension," *Acta Mechanica*, vol. 224, pp. 399–423, 2013.

[21] J. C. Géminard, R. Bernai, and F. Melo, "Wrinkle formations in axi-symmetrically stretched membranes," *European Physical Journal E*, vol. 15, pp. 117–126, 2004.

[22] C. G. Wang, Y. P. Liu, L. Lan, L. Li, and H. F. Tan, "Post-wrinkling analysis of a torsionally sheared annular thin film by using a compound series method," *International Journal of Mechanical Sciences*, vol. 110, pp. 22–33, 2016.

[23] J. Argyris, L. Tenek, and L. Olofsson, "TRIC: a simple but sophisticated 3-node triangular element based on 6 rigid-body and 12 straining modes for fast computational simulations of arbitrary isotropic and laminated composite shells," *Computer Methods in Applied Mechanics and Engineering*, vol. 145, pp. 11–85, 1997.

[24] A. G. Combescure, "Static and dynamic buckling of large thin shells," *Nuclear Engineering and Design*, vol. 92, pp. 339–354, 1986.

[25] H. Hu, N. Damil, and M. Potier-Ferry, "A bridging technique to analyze the influence of boundary conditions on instability patterns," *Journal of Computational Physics*, vol. 230, pp. 3753–3764, 2011.

[26] A. G. Combescure, "Modeling elastic-plastic buckling of sandwich axisymmetric shells: On the limits of " shell " models and analytical solutions," *Advanced Modeling and Simulation in Engineering Sciences*, pp. 1–27, 2014.

[27] X. Wang, J. Ma, S. Law, and Q. Yang, "Numerical analysis of wrinkle-influencing factors of thin membranes," *International Journal of Solids and Structures*, vol. 97, pp. 458–474, 2016.

[28] Q. Huang, J. Yang, W. Huang, G. Giunta, S. Belouettar, and H. Hu, "The boundary effects on stretch-induced membrane wrinkling," *Thin-Walled Structures*, vol. 154, p. 106838, 2020.

[29] N. Damil and M. Potier-Ferry, "Influence of local wrinkling on membrane behaviour: A new approach by the technique of slowly variable Fourier coefficients," *Journal of the Mechanics and Physics of Solids*, vol. 58, no. 8, pp. 1139–1153, 2010.

[30] N. Damil, M. Potier-ferry, and H. Hu, "New nonlinear multi-scale models for wrinkled membranes," *Comptes Rendus Mecanique*, vol. 341, no. 8, pp. 616–624, 2013.

[31] N. Damil, M. Potier-Ferry, and H. Hu, "Membrane wrinkling revisited from a multi-scale point of view," *Advanced Modeling and Simulation in Engineering Sciences*, vol. 1, no. 1, p. 6, 2014.

[32] Q. Huang, H. Hu, K. Yu, M. Potier-Ferry, S. Belouettar, and N. Damil, "Macroscopic simulation of membrane wrinkling for various loading cases," *International Journal of Solids and Structures*, vol. 64-65, pp. 246–258, 2015.

[33] K. Attipou, H. Hu, F. Mohri, M. Potier-Ferry, and S. Belouettar, "Thermal wrinkling of thin membranes using a Fourier-related double scale approach," *Thin-Walled Structures*, vol. 94, pp. 532–544, 2015.

[34] Y. Liu, K. Yu, H. Hu, S. Belouettar, M. Potier-Ferry, and N. Damil, "A new Fourier-related double scale analysis for instability phenomena in sandwich structures," *International Journal of Solids and Structures*, vol. 49, no. 22, pp. 3077–3088, 2012.

[35] K. Yu, H. Hu, S. Chen, S. Belouettar, and M. Potier-Ferry, "Multi-scale techniques to analyze instabilities in sandwich structures," *Composite Structures*, vol. 96, pp. 751–762, 2013.

[36] Q. Huang, Y. Liu, H. Hu, Q. Shao, K. Yu, G. Giunta, S. Belouettar, and M. Potier-Ferry, "A Fourier-related double scale analysis on the instability phenomena of sandwich plates," *Computer Methods in Applied Mechanics and Engineering*, vol. 318, pp. 270–295, 2017.

[37] Q. Huang, J. Yang, W. Huang, Y. Liu, H. Hu, G. Giunta, and S. Belouettar, "A new Fourier-related double scale analysis for wrinkling analysis of thin films on compliant substrates," *Composite Structures*, vol. 160, pp. 613–624, 2017.

[38] O. C. Zienkiewicz, *The finite element method*. McGraw-Hill, 1977.

[39] B. Cochelin, N. Damil, and M. Potier-Ferry, *Méthode asymptotique numérique*. Hermes Lavoissier, 2007.

CHAPTER 10 GENERAL DISCUSSION

This chapter provides a general discussion on the work carried out and presented in this thesis. To structure the discussion, four key issues were addressed in detail: generation of digital material twins, evaluation and account for material variability in composites, analyses based on digital material twins and simulation of membrane wrinkling in LCM processes.

10.1 Generation of digital material twins

Thanks to microtomographic observations of the material structure and to the Micro-CT AGM methodology, a new concept called "*digital material twin*" was proposed to construct a detailed and structured geometric model of textile architecture. To facilitate the operations required to achieve this goal, an original software called CompoCT was developed as a platform for Micro-CT AGM. It provides three views of the specimen, thus the accuracy of selection can be improved to identify tows, especially to distinguish between the boundaries of contacting tows. This is different from the manual separation carried out in other studies [1–5], in which the selection of contour points is generally based on only one view of the image.

During the reconstruction, the possible intersection of tows remains a problematic issue. As a matter of fact, tows in contact or close to one another may intersect when interpolated. This might lead to numerical problems during simulations. By employing the iterative expansion approach proposed in the current work, this problem can be solved. A clear boundary between two tows in contact can be obtained, although the original contours of tows intersect at the initial iteration state. Besides, no intersection is observed between the tows with different orientations. Following this approach voxel models of digital material twins were successfully generated for further analysis.

10.2 Evaluation and account for material variability in composites

The digital material twin created is a structured voxel file, in which all fiber tows are identified. This allows carrying out a thorough analysis of the geometric features of the fiber tows contained in the specimen. Since the model is generated from the real fabric, it takes into account the statistical variability of the material structure. Therefore, the numerical predictions of saturated through-thickness permeability also illustrate the variability of the material much like experiments, which was generally not possible in previous studies [6–11].

Handling material variability is a distinctive feature of digital material twin, which provides a novel way to study and account for the variability in experiments. For example, in the international Benchmark III [12], a huge difference was observed among the results obtained by different research teams. Several possible sources of errors have been proposed, but none of them was investigated quantitatively. From the results presented in Chapter 5, the nesting between fabric layers can significantly affect permeability results. This is related to the mesostructure of fibrous reinforcements resulting from the uncontrollable variability during lay-up. Digital material twins provide a way to quantitatively study the effects of mesostructure on the flow properties of fibrous reinforcements. Besides, in the analysis of transverse compaction, local effects in single layers and differences between layers illustrate the material variability of real fabrics, a typical result obtained with digital material twins. Therefore, material variability plays a very important role as it affects the mechanical and flow properties of fibrous reinforcements.

10.3 Analyses based on digital material twins

In order to quantitatively analyze the deformation of fiber tows during compaction based on microtomographic images, it is necessary to correlate the displacements of material points on the images at different stages of deformation. Digital Image Correlation (DIC) and Digital Volume Correlation (DVC) are widely used to process the images obtained by various observation techniques to analyze material deformations. However, when these approaches are used to process microtomographic images, the accuracy cannot be confirmed, since random noise arises in the images obtained from microtomographic scans. The correlation approach developed in the current work is not only based on voxel data like in other approaches, but it also uses the geometric information of the fiber tows extracted from the digital material twin. This additional information provides also a possibility to improve the accuracy of the correlation approach. Note that, in the current work, this approach ignores the possible rotation of contours in cross-sections orthogonal to the fiber direction. This may be considered as acceptable, because the maximum rotation of the cross-sections was found not to exceed 4 degrees. However, this could be taken into account in the future.

10.4 Simulations of membrane wrinkling in LCM processes

As mentioned before, other factors can also lead to defects in final composites parts during manufacture. In VARTM and FI, membranes play a key role to induce through-thickness impregnation for faster composite manufacturing processes. However, as a soft material with

an almost negligible bending stiffness, a membrane easily loses its mechanical stability and wrinkles when subject to in-plane compressive stress. In this work, a reduced computational model was developed to efficiently and accurately simulate the whole wrinkling processes in circular membranes. Although this reduced model was developed initially for membranes, it can be improved and extended to study the wrinkling phenomena of other structures. Although the essential reason for membrane wrinkling is the negligible bending stiffness and the in-plane compressive stress, the occurrence and evolution of wrinkles differ among structures of different materials and geometric shapes. The resin under the deformable membrane can be regarded as the soft substrate, which may affect the wrinkling phenomena in the membrane on top of the fiber bed. Moreover, both global and local wrinkles might appear in the membrane, for example global wrinkling in the transverse direction for a rectangular membrane and local wrinkling in specific parts of circular membranes. Therefore, it is necessary to integrate the reduced model developed in the current work together with other reduced models [13–16] to simulate the complex coupled wrinkling phenomena in LCM processes.

Bibliography

[1] F. Desplentere, S. V. Lomov, D. L. Woerdeman, I. Verpoest, M. Wevers, and A. Bogdanovich, "Micro-CT characterization of variability in 3D textile architecture," *Composites Science and Technology*, vol. 65, no. 13, pp. 1920–1930, 2005.

[2] J. Pazmino, V. Carvelli, and S. V. Lomov, "Micro-CT analysis of the internal deformed geometry of a non-crimp 3D orthogonal weave E-glass composite reinforcement," *Composites Part B: Engineering*, vol. 65, pp. 147–157, 2014.

[3] M. Karahan, S. V. Lomov, A. E. Bogdanovich, D. Mungalov, and I. Verpoest, "Internal geometry evaluation of non-crimp 3D orthogonal woven carbon fabric composite," *Composites Part A: Applied Science and Manufacturing*, vol. 41, no. 9, pp. 1301–1311, 2010.

[4] A. Vanaerschot, B. N. Cox, S. V. Lomov, and D. Vandepitte, "Multi-scale modelling strategy for textile composites based on stochastic reinforcement geometry," *Computer Methods in Applied Mechanics and Engineering*, vol. 310, pp. 906–934, 2016.

[5] X. Yu, H. Wang, and Z. Wang, "Analysis of yarn fiber volume fraction in textile composites using scanning electron microscopy and X-ray micro-computed tomography," *Journal of Reinforced Plastics and Composites*, vol. 38, no. 5, pp. 199–210, 2019.

[6] H. S. Sas, E. B. Wurtzel, P. Simacek, and S. G. Advani, "Effect of relative ply orientation on the through-thickness permeability of unidirectional fabrics," *Composites Science and Technology*, vol. 96, pp. 116–121, 2014.

[7] A. Nabovati, E. W. Llewellin, and A. C. M. Sousa, "A general model for the permeability of fibrous porous media based on fluid flow simulations using the lattice Boltzmann method," *Composites Part A: Applied Science and Manufacturing*, vol. 40, no. 6-7, pp. 860–869, 2009.

[8] M. Karaki, A. Hallal, R. Younes, F. Trochu, P. Lafon, A. Hayek, A. Kobeissy, and A. Fayad, "A comparative analytical, numerical and experimental analysis of the microscopic permeability of fiber bundles in composite materials," *International Journal of Composite Materials*, vol. 7, no. 3, pp. 82–102, 2017.

[9] F. Loix, P. Badel, L. Orgéas, C. Geindreau, and P. Boisse, "Woven fabric permeability: From textile deformation to fluid flow mesoscale simulations," *Composites science and Technology*, vol. 68, no. 7-8, pp. 1624–1630, 2008.

[10] B. Verleye, R. Croce, M. Griebel, M. Klitz, S. V. Lomov, G. Morren, H. Sol, I. Verpoest, and D. Roose, "Permeability of textile reinforcements: Simulation, influence of shear and validation," *Composites Science and Technology*, vol. 68, no. 13, pp. 2804–2810, 2008.

[11] X. Zeng, L. P. Brown, A. Endruweit, M. Matveev, and A. C. Long, "Geometrical modelling of 3D woven reinforcements for polymer composites: Prediction of fabric permeability and composite mechanical properties," *Composites Part A: Applied Science and Manufacturing*, vol. 56, pp. 150–160, 2014.

[12] D. May, A. Aktas, and A. Yong, "International benchmark exercises of textile permeability and compressibility characterization," in *ECCM18 - 18th European Conference on Composite Materials*, 2018.

[13] N. Damil, M. Potier-ferry, and H. Hu, "New nonlinear multi-scale models for wrinkled membranes," *Comptes Rendus Mecanique*, vol. 341, no. 8, pp. 616–624, 2013.

[14] N. Damil, M. Potier-Ferry, and H. Hu, "Membrane wrinkling revisited from a multiscale point of view," *Advanced Modeling and Simulation in Engineering Sciences*, vol. 1, no. 1, p. 6, 2014.

[15] Q. Huang, H. Hu, K. Yu, M. Potier-Ferry, S. Belouettar, and N. Damil, "Macroscopic simulation of membrane wrinkling for various loading cases," *International Journal of Solids and Structures*, vol. 64-65, pp. 246–258, 2015.

[16] Q. Huang, J. Yang, W. Huang, Y. Liu, H. Hu, G. Giunta, and S. Belouettar, "A new Fourier-related double scale analysis for wrinkling analysis of thin films on compliant substrates," *Composite Structures*, vol. 160, pp. 613–624, 2017.

CHAPTER 11 CONCLUSION AND RECOMMENDATIONS

This chapter provides a general synthesis of the work. The approach adopted and the results are first summed up. Then the limitations of the current work and recommendations for future work are discussed.

11.1 Summary of Works

First, a Micro-CT Aided Geometric Modeling approach (Micro-CT AGM) was proposed to reconstruct mesostructural geometric models of continuous fiber reinforcements from micro-tomographic images. A new concept called "*digital material twin*" was proposed to provide a detailed morphological description of the material structure, which possesses several interesting features: (1) the mesoscopic structure of fiber tows is reproduced with assessed accuracy; (2) the fiber tows are identified and labeled in the voxel image, thus enabling a thorough voxel based analysis of their geometrical features; (3) material variability is taken into account, which allows conducting representative numerical simulations of mechanical or flow properties.

A new software called CompoCT was developed as a platform for this specific modeling procedure. In addition, a multiple factor criterion based on a series of morphological features of fiber tows, was proposed to assess the accuracy of the geometric models created with respect to the original Micro-CT scan. Following this approach, precise mesostructural geometric models of a 2D woven fabric and a 3D orthogonal textile were successfully reconstructed at a relatively low scanning resolution.

Thanks to digital material twins, it is possible to carry out virtual permeability measurements of woven fabrics. To verify the virtual permeability evaluation, existing experimental measurement procedures were improved by considering several key issues, namely:

1) Highly permeable metallic distribution grids were placed on the top and bottom surfaces of the preforms to generate a unidirectional transverse flow as uniform as possible.

2) Low injection pressure was applied to prevent fiber deformation.

3) The effect of nesting between the distribution grids and the fabric layers was quantified and considered in the calculation of fiber volume content.

Overall, simulation results exhibit a good agreement with experiments. Besides, numerical results show that digital material twins can assess the material variability of real fabrics. This

provides a powerful tool to reveal potential sources of variability observed in the transverse permeability measurements.

Based on three digital material twins created for increasing fiber volume contents, the evolution of the morphological features of fiber tows was investigated. The results show that contacts between fiber tows have an effect on the evolution of their morphological features. In order to quantitatively assess the mesoscopic deformations of fiber tows and discuss the effect of nesting on the mechanical behavior of fabrics under transverse compaction, a new correlation approach was proposed to track the movements of contour points on the surfaces of fiber tows at different levels of compaction. Overall, the analyses show a general pattern of fiber tow deformation during compaction with compression in the contact regions and expansion of the tows near the contacting zones. Moreover, the effect of contact between different layers appears to be more important than the interaction between warp and weft tows located in the same layer. Besides, contact between fiber tows is highly influenced by nesting of adjacent fabric layers. This consequently affects the mechanical behavior of fabrics and might explain the high variability encountered in measurements of transverse compressibility as nesting is always difficult to control.

Based on the method of Fourier series with slowly variable coefficients and the asymptotic numerical method, a one-dimensional reduced model was constructed to model circumferential periodic instability patterns in circular domains. The reduced model was verified to be efficient and accurate by comparing its results with those of ABAQUS for an annular membrane under various loads. Besides, the reduced model shows the potential to precisely predict buckling patterns and efficiently simulate the post-buckling process of various wrinkling phenomena in circular domains. Therefore, it can not only predict the critical wrinkling load, but also simulate the stress distribution for the entire process. The development of the model enriches the Fourier-based reduced model family. It provides also an effective and precise tool to investigate wrinkling in LCM processes with a deformable membrane.

11.2 Contributions

Based on the work mentioned, this thesis brings several original contributions:

1. A new concept named "*digital material twin*" was proposed. This concept provides a detailed morphological description of the material structure.

2. A novel geometric modeling approach (Micro-CT AGM) was devised to generate digital material twins of woven fibrous reinforcements. A new software called CompoCT was developed to carry out the tasks related to this purpose.

3. Based on digital material twins, an accurate measurement approach was proposed to measure the saturated permeability of fibrous reinforcements both numerically and experimentally.

4. A new contour point correlation method was developed to track the contour points of material twins, which provides a tool to analyze the deformation of fiber tows at the mesoscopic scale.

5. A Fourier based reduced model was constructed for efficient and accurate analysis of membrane wrinkling in LCM processes.

In general, several numerical and experimental procedures were developed at different scales to analyze critical mechanical issues in LCM processes, especially for transverse flows such as in VARTM and FI. This work should improve the numerical predictions of composite manufacturing processes based on transverse liquid impregnation and contribute to develop more efficient LCM processes with improved part quality.

11.3 Limitations & Recommendations

Although the proposed new approach is comprehensive and systematic, certain limitations exist in its current implementation. One of the most critical limitation is connected with the contours of tows that must be obtained manually to reconstruct geometric models from a relatively lower resolution image, hence requiring significant time. One future key issue would be to implement precise automatic or semi-automatic segmentation approaches at lower resolution to accelerate the creation of the digital material twins.

Although the numerical prediction of the saturated transverse permeability shows a good agreement with experimental measurements, only mesoscopic flows were considered in the current work. This might lead to non-negligible errors in the prediction at low fiber volume content or for some textiles with a special microscopic architecture. Moreover, the unsaturated permeability that occurs in liquid impregnation processes has not yet been studied with digital material twins. Therefore, an interesting application would consist of simulating dual-scale flows through fibrous reinforcements. To that end, digital material twins could be used also to generate sub-mesoscopic or microscopic flow model.

When evaluating the mesoscopic deformations of fiber tows based on material twins, only the radial displacements of contour points on the tow surfaces are calculated, the internal deformation or the strain distribution of the entire fiber tows are not discussed in the thesis. Considering that *Digital Image Correlation* (DIC) and *Digital Volume Correlation* (DVC) can

be used to calculate the strain field on the 3D images, it would be interesting to investigate the possibility of combining the correlation approach proposed here with DIC or DVC to obtain a precise strain distribution in the fabric. Meanwhile, if pressure (or stress) measurement device is embedded in the in-situ compaction device, it is possible to further analyze the mechanical behavior and stress distribution of fabrics under compaction. Moreover, by designing new in-situ loading and observation devices, the mechanical behavior of fibrous reinforcements under different loading conditions can be investigated in the framework of the thesis.

Finally, the Fourier-based reduced model can be used to analyze several examples with simple boundary conditions. However, as a basic tool, this model can be improved to be more general in the future by introducing new approaches, for example the Arlequin bridging technique, a multi-scale method in which different models are crossed and glued together. The final objective is to efficiently simulate the stress distribution in deformable membranes during the entire manufacturing process, thus enabling to control the level of wrinkles.

REFERENCES

[1] "https://poly-matrix.hu/zartszerszamos-eljaras-rtm-resin-transfer-moulding."

[2] M. R. Abusrea and K. Arakawa, "Enhanced tensile strength cfrp adhesive joint constructed from carbon fiber-reinforced plastic and dry carbon fiber laminates," in *Proceedings of the 17th International Conference on Composite Materials (ICCM17)*, 2016.

[3] P. Causse, E. Ruiz, and F. Trochu, "Spring-in behavior of curved composites manufactured by Flexible Injection," *Composites Part A: Applied Science and Manufacturing*, vol. 43, no. 11, pp. 1901–1913, 2012.

[4] "https://www.rtmcomposites.com/blog/process-troubleshooting-air-pockets-causing-mold-defects."

[5] "https://www.patterson-rothwell.co.uk/in-pursuit-of-the-perfect-injection-moulded-part-nine-delamination."

[6] V. S. Loiselle, "Fabrication par injection flexible de pièces coniques pour des applications aérospatiales," Ph.D. dissertation, École Polytechnique de Montréal, 2013.

[7] "http://www.easycomposites.cn/beginners-guide-to-out-of-autoclave-part-3.aspx."

[8] P. Simacek and S. G. Advani, "Modeling resin flow and fiber tow saturation induced by distribution media collapse in VARTM," *Composites science and technology*, vol. 67, no. 13, pp. 2757–2769, 2007.

[9] A. Dixit and H. S. Mali, "Modeling techniques for predicting the mechanical properties of woven-fabric textile composites: a review," *Mechanics of composite Materials*, vol. 49, no. 1, pp. 1–20, 2013.

[10] S. D. Green, A. C. Long, B. S. F. El Said, and S. R. Hallett, "Numerical modelling of 3D woven preform deformations," *Composite Structures*, vol. 108, pp. 747–756, 2014.

[11] Y. Mahadik and S. R. Hallett, "Finite element modelling of tow geometry in 3D woven fabrics," *Composites Part A: Applied Science and Manufacturing*, vol. 41, no. 9, pp. 1192–1200, 2010.

[12] F. Gommer, A. Endruweit, and A. C. Long, "Quantification of micro-scale variability in fibre bundles," *Composites Part A: Applied Science and Manufacturing*, vol. 87, pp. 131–137, 2016.

[13] Y. Wang and X. Sun, "Digital-element simulation of textile processes," *Composites Science and Technology*, vol. 61, no. 2, pp. 311–319, 2001.

[14] G. Zhou, X. Sun, and Y. Wang, "Multi-chain digital element analysis in textile mechanics," *Composites Science and Technology*, vol. 64, no. 2, pp. 239–244, 2004.

[15] N. Naouar, E. Vidal-Sallé, J. Schneider, E. Maire, and P. Boisse, "Meso-scale FE analyses of textile composite reinforcement deformation based on X-ray computed tomography," *Composite Structures*, vol. 116, no. 1, pp. 165–176, 2014.

[16] S. Scholz, J. W. Gillespie, and D. Heider, "Measurement of transverse permeability using gaseous and liquid flow," *Composites Part A: Applied Science and Manufacturing*, vol. 38, no. 9, pp. 2034–2040, 2007.

[17] F. Klunker, M. Danzi, and P. Ermanni, "Fiber deformation as a result of fluid injection: modeling and validation in the case of saturated permeability measurements in through thickness direction," *Journal of Composite Materials*, vol. 49, no. 9, pp. 1091–1105, 2015.

[18] P. Potluri and T. V. Sagar, "Compaction modelling of textile preforms for composite structures," *Composite Structures*, vol. 86, no. 1-3, pp. 177–185, 2008.

[19] E. Cerda and L. Mahadevan, "Geometry and physics of wrinkling," *Physical Review Letters*, vol. 90, no. 7, p. 074302, 2003.

[20] F. Brau, H. Vandeparre, A. Sabbah, C. Poulard, A. Boudaoud, and P. Damman, "Multiple-length-scale elastic instability mimics parametric resonance of nonlinear oscillators," *Nature Physics*, vol. 7, no. 1, pp. 56–60, 2011.

[21] Y. Liu, K. Yu, H. Hu, S. Belouettar, M. Potier-Ferry, and N. Damil, "A new Fourier-related double scale analysis for instability phenomena in sandwich structures," *International Journal of Solids and Structures*, vol. 49, no. 22, pp. 3077–3088, 2012.

[22] Q. Huang, Y. Liu, H. Hu, Q. Shao, K. Yu, G. Giunta, S. Belouettar, and M. Potier-Ferry, "A Fourier-related double scale analysis on the instability phenomena of sandwich plates," *Computer Methods in Applied Mechanics and Engineering*, vol. 318, pp. 270–295, 2017.

[23] Q. Huang, J. Yang, W. Huang, Y. Liu, H. Hu, G. Giunta, and S. Belouettar, "A new Fourier-related double scale analysis for wrinkling analysis of thin films on compliant substrates," *Composite Structures*, vol. 160, pp. 613–624, 2017.

[24] Q. Huang, H. Hu, K. Yu, M. Potier-Ferry, S. Belouettar, and N. Damil, "Macroscopic simulation of membrane wrinkling for various loading cases," *International Journal of Solids and Structures*, vol. 64-65, pp. 246–258, 2015.

[25] E. Ruiz and F. Trochu, "Manufacture of composites by a flexible injection process using a double or multiple cavity mold," Jan. 11 2011, uS Patent 7,866,969.

[26] E. Ruiz, L. Briones, E. Allard, and F. Trochu, "Flexible injection: a novel LCM technology for low cost manufacturing of high performance composites. Part I: experimental investigation," in *The 9th International Conference on Flow Processes in Composite Materials*, 2008.

[27] F. Trochu, S. Soukane, and B. Touraine, "Flexible injection: a novel LCM technology for low cost manufacturing of high performance composites. Part II: numerical model," in *9 th Int. Conf. on Flow Proc. in Comp. Mat*, 2008.

[28] K. J. Bowles and S. Frimpong, "Void effects on the interlaminar shear strength of unidirectional graphite-fiber-reinforced composites," *Journal of composite materials*, vol. 26, no. 10, pp. 1487–1509, 1992.

[29] D. P. C. Aiman, M. F. Yahya, and J. Salleh, "Impact properties of 2D and 3D woven composites: a review," in *AIP Conference Proceedings*, vol. 1774, no. 1. AIP Publishing LLC, 2016, p. 020002.

[30] K. H. Leong, B. Lee, I. Herszberg, and M. K. Bannister, "The effect of binder path on the tensile properties and failure of multilayer woven CFRP composites," *Composites Science and Technology*, vol. 60, no. 1, pp. 149–156, 2000.

[31] F. Desplentere, S. V. Lomov, D. L. Woerdeman, I. Verpoest, M. Wevers, and A. Bogdanovich, "Micro-CT characterization of variability in 3D textile architecture," *Composites Science and Technology*, vol. 65, no. 13, pp. 1920–1930, 2005.

[32] X. L. Xiao, A. Endruweit, X. S. Zeng, J. L. Hu, and A. Long, "Through-thickness permeability study of orthogonal and angle-interlock woven fabrics," *Journal of Materials Science*, vol. 50, no. 3, pp. 1257–1266, 2015.

[33] Y. Miao, E. Zhou, Y. Wang, and B. A. Cheeseman, "Mechanics of textile composites: Micro-geometry," *Composites Science and Technology*, vol. 68, no. 7-8, pp. 1671–1678, 2008.

[34] L. Huang, Y. Wang, Y. Miao, D. Swenson, Y. Ma, and C. Yen, "Dynamic relaxation approach with periodic boundary conditions in determining the 3-D woven textile microgeometry," *Composite Structures*, vol. 106, pp. 417–425, 2013.

[35] Z. Yousaf, P. Potluri, P. J. Withers, D. Mollenhauer, E. Zhou, and S. Duning, "Digital element simulation of aligned tows during compaction validated by computed tomography (CT)," *International Journal of Solids and Structures*, vol. 154, pp. 78–87, 2018.

[36] A. Drach, B. Drach, and I. Tsukrov, "Processing of fiber architecture data for finite element modeling of 3D woven composites," *Advances in Engineering Software*, vol. 72, pp. 18–27, 2014.

[37] S. Joglekar and M. Pankow, "Modeling of 3D woven composites using the digital element approach for accurate prediction of kinking under compressive loads," *Composite Structures*, vol. 160, pp. 547–559, 2017.

[38] S. D. Green, M. Y. Matveev, A. C. Long, D. Ivanov, and S. R. Hallett, "Mechanical modelling of 3D woven composites considering realistic unit cell geometry," *Composite Structures*, vol. 118, pp. 284–293, 2014.

[39] B. El Said, S. Green, and S. R. Hallett, "Kinematic modelling of 3D woven fabric deformation for structural scale features," *Composites Part A: Applied Science and Manufacturing*, vol. 57, pp. 95–107, 2014.

[40] A. J. Thompson, B. El Said, D. Ivanov, J. P. H. Belnoue, and S. R. Hallett, "High fidelity modelling of the compression behaviour of 2D woven fabrics," *International Journal of Solids and Structures*, vol. 154, pp. 104–113, 2018.

[41] M. Sherburn, "Geometric and mechanical modelling of textiles," Ph.D. dissertation, University of Nottingham, 2007.

[42] A. C. Long and L. P. Brown, "Modelling the geometry of textile reinforcements for composites: TexGen," in *Composite Reinforcements for Optimum Performance*, 2011, pp. 239–264.

[43] I. Verpoest and S. V. Lomov, "Virtual textile composites software WiseTex: Integration with micro-mechanical, permeability and structural analysis," *Composites Science and Technology*, vol. 65, pp. 2563–2574, 2005.

[44] S. V. Lomov, "Modelling the geometry of textile reinforcements for composites: Wisetex," in *Composite reinforcements for optimum performance*. Elsevier, 2011, pp. 200–238.

[45] E. N. Landis and D. T. Keane, "X-ray microtomography," *Materials characterization*, vol. 61, no. 12, pp. 1305–1316, 2010.

[46] N. Naouar, E. Vidal-Sallé, J. Schneider, E. Maire, and P. Boisse, "3D composite reinforcement meso F.E. analyses based on X-ray computed tomography," *Composite Structures*, vol. 132, pp. 1094–1104, 2015.

[47] J. Bigun, T. Bigun, and K. Nilsson, "Recognition by symmetry derivatives and the generalized structure tensor," *IEEE Transactions on Pattern Analysis and Machine Intelligence*, vol. 26, no. 12, pp. 1590–1605, 2004.

[48] R. M. Haralick and L. G. Shapiro, *Computer and robot vision*. Addison-wesley Reading, 1992, vol. 1.

[49] P. J. Schilling, B. R. Karedla, A. K. Tatiparthi, M. A. Verges, and P. D. Herrington, "X-ray computed microtomography of internal damage in fiber reinforced polymer matrix composites," *Composites Science and Technology*, vol. 65, no. 14, pp. 2071–2078, 2005.

[50] J. S. U. Schell, M. Renggli, G. H. van Lenthe, R. Müller, and P. Ermanni, "Micro-computed tomography determination of glass fibre reinforced polymer meso-structure," *Composites Science and Technology*, vol. 66, no. 13, pp. 2016–2022, 2006.

[51] J. S. U. Schell, M. Deleglise, C. Binetruy, P. Krawczak, and P. Ermanni, "Numerical prediction and experimental characterisation of meso-scale-voids in liquid composite moulding," *Composites Part A: Applied Science and Manufacturing*, vol. 38, no. 12, pp. 2460–2470, 2007.

[52] A. Madra, N. El Hajj, and M. Benzeggagh, "X-ray microtomography applications for quantitative and qualitative analysis of porosity in woven glass fiber reinforced thermoplastic," *Composites Science and Technology*, vol. 95, pp. 50–58, 2014.

[53] M. A. Ali, R. Umer, K. A. Khan, S. Bickerton, and W. J. Cantwell, "Non-destructive evaluation of through-thickness permeability in 3D woven fabrics for composite fan blade applications," *Aerospace Science and Technology*, vol. 82-83, pp. 520–533, 2018.

[54] M. A. Ali, R. Umer, K. A. Khan, and W. J. Cantwell, "In-plane virtual permeability characterization of 3D woven fabrics using a hybrid experimental and numerical approach," *Composites Science and Technology*, vol. 173, pp. 99–109, 2019.

[55] M. A. Ali, R. Umer, K. A. Khan, and W. J. Cantwell, "XCT-scan assisted flow path analysis and permeability prediction of a 3D woven fabric," *Composites Part B: Engineering*, vol. 176, p. 107320, 2019.

[56] A. Mendoza, J. Schneider, E. Parra, E. Obert, and S. Roux, "Differentiating 3D textile composites: A novel field of application for Digital Volume Correlation," *Composite Structures*, vol. 208, pp. 735–743, 2019.

[57] A. Mendoza, J. Schneider, E. Parra, and S. Roux, "Measuring yarn deformations induced by the manufacturing process of woven composites," *Composites Part A: Applied Science and Manufacturing*, vol. 120, pp. 127–139, 2019.

[58] I. Straumit, S. V. Lomov, and M. Wevers, "Quantification of the internal structure and automatic generation of voxel models of textile composites from X-ray computed tomography data," *Composites Part A: Applied Science and Manufacturing*, vol. 69, pp. 150–158, 2015.

[59] A. Madra, P. Breitkopf, A. Rassineux, and F. Trochu, "Image-based model reconstruction and meshing of woven reinforcements in composites," *International Journal for Numerical Methods in Engineering*, vol. 112, no. 9, pp. 1235–1252, 2017.

[60] P. Ferland, D. Guittard, and F. Trochu, "Concurrent methods for permeability measurement in resin transfer molding," *Polymer Composites*, vol. 17, no. 1, pp. 149–158, 1996.

[61] J. R. Weitzenböck, R. A. Shenoi, and P. A. Wilson, "Radial flow permeability measurement. Part A: Theory," *Composites Part A: Applied Science and Manufacturing*, vol. 30, no. 6, pp. 781–796, 1999.

[62] J. R. Weitzenböck, R. A. Shenoi, and P. A. Wilson, "Radial flow permeability measurement. Part B: Application," *Composites part A: Applied Science and Manufacturing*, vol. 30, no. 6, pp. 797–813, 1999.

[63] S. H. Ahn, W. I. Lee, and G. S. Springer, "Measurement of the three-dimensional permeability of fiber preforms using embedded fiber optic sensors," *Journal of Composite Materials*, vol. 29, no. 6, pp. 714–733, 1995.

[64] M. Li, S. K. Wang, Y. Z. Gu, Y. X. Li, K. Potter, and Z. G. Zhang, "Evaluation of through-thickness permeability and the capillary effect in vacuum assisted liquid molding process," *Composites Science and Technology*, vol. 72, no. 8, pp. 873–878, 2012.

[65] P. B. Nedanov and S. G. Advani, "A method to determine 3D permeability of fibrous reinforcements," *Journal of Composite Materials*, vol. 36, no. 2, pp. 241–254, 2002.

[66] J. Leisen and H. W. Beckham, "Quantitative magnetic resonance imaging of fluid distribution and movement in textiles," *Textile research journal*, vol. 71, no. 12, pp. 1033–1045, 2001.

[67] V. Neacsu, J. Leisen, H. W. Beckham, and S. G. Advani, "Use of magnetic resonance imaging to visualize impregnation across aligned cylinders due to capillary forces," *Experiments in fluids*, vol. 42, no. 3, pp. 425–440, 2007.

[68] A. Endruweit, P. Glover, K. Head, and A. C. Long, "Mapping of the fluid distribution in impregnated reinforcement textiles using Magnetic Resonance Imaging: Application and discussion," *Composites Part A: Applied Science and Manufacturing*, vol. 42, no. 10, pp. 1369–1379, 2011.

[69] A. Endruweit, T. Luthy, and P. Ermanni, "Investigation of the influence of textile compression on the out-of-plane permeability of a bidirectional glass fiber fabric," *Polymer Composites*, vol. 23, no. 4, pp. 538–554, 2002.

[70] P. Ouagne and J. Bréard, "Continuous transverse permeability of fibrous media," *Composites Part A: Applied Science and Manufacturing*, vol. 41, no. 1, pp. 22–28, 2010.

[71] P. Ouagne, T. Ouahbi, C. H. Park, J. Bréard, and A. Saouab, "Continuous measurement of fiber reinforcement permeability in the thickness direction: Experimental technique and validation," *Composites Part B: Engineering*, vol. 45, no. 1, pp. 609–618, 2013.

[72] S. V. Lomov, I. Verpoest, T. Peeters, D. Roose, and M. Zako, "Nesting in textile laminates: geometrical modelling of the laminate," *Composites Science and Technology*, vol. 63, no. 7, pp. 993–1007, 2003.

[73] D. Becker and P. Mitschang, "Measurement system for on-line compaction monitoring of textile reaction to out-of-plane impregnation," *Advanced Composites Letters*, vol. 23, no. 2, p. 096369351402300202, 2014.

[74] B. Willenbacher, A. Kabachi, D. May, P. Mitschang, and P. Ermanni, "Flow induced sample deformations in out-of-plane permeability measurement," in *ECCM18 - 18th European Conference on Composite Materials*, 2018.

[75] M. Bodaghi, S. V. Lomov, P. Simacek, N. C. Correia, and S. G. Advani, "On the variability of permeability induced by reinforcement distortions and dual scale flow in liquid composite moulding: A review," *Composites Part A: Applied Science and Manufacturing*, 2019.

[76] A. Endruweit, X. Zeng, M. Matveev, and A. C. Long, "Effect of yarn cross-sectional shape on resin flow through inter-yarn gaps in textile reinforcements," *Composites Part A: Applied Science and Manufacturing*, vol. 104, pp. 139–150, 2018.

[77] N. Kuentzer, P. Simacek, S. G. Advani, and S. Walsh, "Permeability characterization of dual scale fibrous porous media," *Composites Part A: Applied Science and Manufacturing*, vol. 37, no. 11, pp. 2057–2068, 2006.

[78] E. Ruiz, V. Achim, S. Soukane, F. Trochu, and J. Bréard, "Optimization of injection flow rate to minimize micro/macro-voids formation in resin transfer molded composites," *Composites Science and Technology*, vol. 66, no. 3-4, pp. 475–486, 2006.

[79] C. Ravey, E. Ruiz, and F. Trochu, "Determination of the optimal impregnation velocity in resin transfer molding by capillary rise experiments and infrared thermography," *Composites Science and Technology*, vol. 99, pp. 96–102, 2014.

[80] M. Imbert, S. Comas-Cardona, E. Abisset-Chavanne, and D. Prono, "Experimental investigation of intra-tow fluid storage mechanisms in dual-scale fiber reinforcements," *Composites Part A: Applied Science and Manufacturing*, vol. 107, pp. 70–82, 2018.

[81] J. Bréard, Y. Henzel, F. Trochu, and R. Gauvin, "Analysis of dynamic flows through porous media. Part I: Comparison between saturated and unsaturated flows in fibrous reinforcements," *Polymer Composites*, vol. 24, no. 3, pp. 391–408, 2003.

[82] B. Yang, S. Wang, and Y. Wang, "Effect of nesting in laminates on the through-thickness permeability of woven fabrics," *Applied Composite Materials*, vol. 25, no. 5, pp. 1237–1253, 2018.

[83] E. E. Swery, T. Allen, S. Comas-Cardona, Q. Govignon, C. Hickey, J. Timms, L. Tournier, A. Walbran, P. Kelly, and S. Bickerton, "Efficient experimental characterisation of the permeability of fibrous textiles," *Journal of Composite Materials*, vol. 50, no. 28, pp. 4023–4038, 2016.

[84] H. S. Sas, E. B. Wurtzel, P. Simacek, and S. G. Advani, "Effect of relative ply orientation on the through-thickness permeability of unidirectional fabrics," *Composites Science and Technology*, vol. 96, pp. 116–121, 2014.

[85] X. S. Zeng, A. C. Long, F. Gommer, A. Endruweit, and M. Clifford, "Modelling compaction effect on permeability of 3D carbon reinforcements," in *18th International Conference on Composites Materials, Jeju Island, Korea*, 2011.

[86] S. Drapier, A. Pagot, A. Vautrin, and P. Henrat, "Influence of the stitching density on the transverse permeability of non-crimped new concept (NC2) multiaxial reinforcements: Measurements and predictions," *Composites Science and Technology*, vol. 62, no. 15, pp. 1979–1991, 2002.

[87] M. Danzi, F. Klunker, and P. Ermanni, "Experimental validation of through-thickness resin flow model in the consolidation of saturated porous media," *Journal of Composite Materials*, vol. 51, no. 17, pp. 2467–2475, 2017.

[88] D. May, A. Aktas, and A. Yong, "International benchmark exercises of textile permeability and compressibility characterization," in *ECCM18 - 18th European Conference on Composite Materials*, 2018.

[89] C. M. van Wyk, "Note on the compressibility of wool," *Journal of the Textile Institute Transactions*, vol. 37, no. 12, pp. T285–T292, 1946.

[90] R. A. Saunders, C. Lekakou, and M. G. Bader, "Compression and microstructure of fibre plain woven cloths in the processing of polymer composites," *Composites Part A: Applied Science and Manufacturing*, vol. 29, no. 4, pp. 443–454, 1998.

[91] S. V. Lomov and I. Verpoest, "Compression of woven reinforcements: A mathematical model," *Journal of Reinforced Plastics and Composites*, vol. 19, no. 16, pp. 1329–1350, 2000.

[92] Y. J. Jeong and T. J. Kang, "Analysis of compressional deformation of woven fabric using finite element method," *Journal of the Textile Institute*, vol. 92, no. 1, pp. 1–15, 2001.

[93] P. Badel, E. Vidal-Sallé, E. Maire, and P. Boisse, "Simulation and tomography analysis of textile composite reinforcement deformation at the mesoscopic scale," *Composites Science and Technology*, vol. 68, no. 12, pp. 2433–2440, 2008.

[94] H. Lin, M. Sherburn, J. Crookston, A. C. Long, M. J. Clifford, and I. A. Jones, "Finite element modelling of fabric compression," *Modelling and Simulation in Materials Science and Engineering*, vol. 16, no. 3, p. 035010, 2008.

[95] R. Maurin, P. Davies, N. Baral, and C. Baley, "Transverse properties of carbon fibres by nano-indentation and micro-mechanics," *Applied Composite Materials*, vol. 15, no. 2, p. 61, 2008.

[96] X. Zeng, L. P. Brown, A. Endruweit, M. Matveev, and A. C. Long, "Geometrical modelling of 3D woven reinforcements for polymer composites: Prediction of fabric permeability and composite mechanical properties," *Composites Part A: Applied Science and Manufacturing*, vol. 56, pp. 150–160, 2014.

[97] Q. T. Nguyen, E. Vidal-Sallé, P. Boisse, C. H. Park, A. Saouab, J. Bréard, and G. Hivet, "Mesoscopic scale analyses of textile composite reinforcement compaction," *Composites Part B: Engineering*, vol. 44, no. 1, pp. 231–241, 2013.

[98] G. Hivet and P. Boisse, "Consistent 3D geometrical model of fabric elementary cell. Application to a meshing preprocessor for 3D finite element analysis," *Finite Elements in Analysis and Design*, vol. 42, no. 1, pp. 25–49, 2005.

[99] I. Goda, M. Assidi, and J. F. Ganghoffer, "Equivalent mechanical properties of textile monolayers from discrete asymptotic homogenization," *Journal of the Mechanics and Physics of Solids*, vol. 61, no. 12, pp. 2537–2565, 2013.

[100] Y. Rahali, M. Assidi, I. Goda, A. Zghal, and J. F. Ganghoffer, "Computation of the effective mechanical properties including nonclassical moduli of 2.5D and 3D interlocks by micromechanical approaches," *Composites Part B: Engineering*, vol. 98, pp. 194–212, 2016.

[101] D. Zhang, Y. Sun, X. Wang, and L. Chen, "Meso-scale finite element analyses of three-dimensional five-directional braided composites subjected to uniaxial and biaxial loading," *Journal of Reinforced Plastics and Composites*, vol. 34, no. 24, pp. 1989–2005, 2015.

[102] E. Cerda, K. Ravi-Chandar, and L. Mahadevan, "Thin films: Wrinkling of an elastic sheet under tension," *Nature*, vol. 419, no. 6907, pp. 579–580, 2002.

[103] B. Li, Y. Cao, X. Feng, and H. Gao, "Mechanics of morphological instabilities and surface wrinkling in soft materials: A review," *Soft Matter*, vol. 8, pp. 5728–5745, 2012.

[104] X. Chen and J. W. Hutchinson, "Herringbone buckling patterns of compressed thin films on compliant substrates," *Journal of Applied Mechanics*, vol. 71, p. 597, 2004.

[105] J. W. Wang, B. Li, Y. P. Cao, and X. Q. Feng, "Surface wrinkling patterns of film–substrate systems with a structured interface," *Journal of Applied Mechanics*, vol. 82, p. 051009, 2015.

[106] N. Bowden, S. Brittain, A. G. Evans, J. W. Hutchinson, and G. M. Whitesides, "Spontaneous formation of ordered structures in thin films of metals supported on an elastomeric polymer," *Nature*, vol. 393, no. May, pp. 146–149, 1998.

[107] N. Jacques, A. Elias, M. Potier-Ferry, and H. Zahrouni, "Buckling and wrinkling during strip conveying in processing lines," *Journal of Materials Processing Technology*, vol. 190, no. 1-3, pp. 33–40, 2007.

[108] H. Wagner, "Flat sheet metal girders with very thin metal web. Part I : General theories and assumptions," *Zeitschrift für Motortechnik und Luftschiffahrt*, vol. 20, no. 8, pp. 200–207, 1929.

[109] A. C. Pipkin, "Integration of an equation in membrane theory," *Zeitschrift für angewandte Mathematik und Physik ZAMP*, vol. 19, no. 5, pp. 818–819, 1968.

[110] D. J. Steigmann and A. C. Pipkin, "Wrinkling of pressurized membranes," *Journal of Applied Mechanics*, vol. 56, no. 3, p. 624, 1989.

[111] D. G. Roddeman, J. Drukker, C. W. J. Oomens, and J. D. Janssen, "The wrinkling of thin membranes : Part I — theory," *Journal of Applied Mechanics*, vol. 54, pp. 884–887, 1987.

[112] R. H. Plaut, "Linearly elastic annular and circular membranes under radial, transverse, and torsional loading. Part I: Large unwrinkled axisymmetric deformations," *Acta Mechanica*, vol. 202, pp. 79–99, 2009.

[113] C. D. Coman, "On the applicability of tension field theory to a wrinkling instability problem," *Acta Mechanica*, vol. 190, pp. 57–72, 2007.

[114] C. D. Coman, "Some applications of the WKB method to the wrinkling of bi-annular plates in tension," *Acta Mechanica*, vol. 224, pp. 399–423, 2013.

[115] J. C. Géminard, R. Bernai, and F. Melo, "Wrinkle formations in axi-symmetrically stretched membranes," *European Physical Journal E*, vol. 15, pp. 117–126, 2004.

[116] C. G. Wang, Y. P. Liu, L. Lan, L. Li, and H. F. Tan, "Post-wrinkling analysis of a torsionally sheared annular thin film by using a compound series method," *International Journal of Mechanical Sciences*, vol. 110, pp. 22–33, 2016.

[117] F. Xu, M. Potier-Ferry, S. Belouettar, and H. Hu, "Multiple bifurcations in wrinkling analysis of thin films on compliant substrates," *International Journal of Non-Linear Mechanics*, vol. 76, pp. 203–222, 2015.

[118] J. T. Oden and J. E. Key, "Numerical analysis of finite axisymmetric deformations of incompressible elastic solid of revolution," *International Journal of Solids and Structures*, vol. 6, pp. 497–518, 1970.

[119] A. G. Combescure, "Static and dynamic buckling of large thin shells," *Nuclear Engineering and Design*, vol. 92, pp. 339–354, 1986.

[120] A. G. Combescure, "Modeling elastic-plastic buckling of sandwich axisymmetric shells: On the limits of " shell " models and analytical solutions," *Advanced Modeling and Simulation in Engineering Sciences*, pp. 1–27, 2014.

[121] N. Damil and M. Potier-Ferry, "Influence of local wrinkling on membrane behaviour: A new approach by the technique of slowly variable Fourier coefficients," *Journal of the Mechanics and Physics of Solids*, vol. 58, no. 8, pp. 1139–1153, 2010.

[122] N. Damil, M. Potier-ferry, and H. Hu, "New nonlinear multi-scale models for wrinkled membranes," *Comptes Rendus Mecanique*, vol. 341, no. 8, pp. 616–624, 2013.

[123] N. Damil, M. Potier-Ferry, and H. Hu, "Membrane wrinkling revisited from a multi-scale point of view," *Advanced Modeling and Simulation in Engineering Sciences*, vol. 1, no. 1, p. 6, 2014.

[124] K. Yu, H. Hu, S. Chen, S. Belouettar, and M. Potier-Ferry, "Multi-scale techniques to analyze instabilities in sandwich structures," *Composite Structures*, vol. 96, pp. 751–762, 2013.

[125] S. Hilal, "Caractérisation par microtomographie de la mésostructure des renforts fibreux pour la fabrication de composites par injection," Ph.D. dissertation, École Polytechinque de Montréal, 2018.

[126] J. Pazmino, V. Carvelli, and S. V. Lomov, "Micro-CT analysis of the internal deformed geometry of a non-crimp 3D orthogonal weave E-glass composite reinforcement," *Composites Part B: Engineering*, vol. 65, pp. 147–157, 2014.

[127] A. Madra, J. Adrien, P. Breitkopf, E. Maire, and F. Trochu, "A clustering method for analysis of morphology of short natural fibers in composites based on X-ray microtomography," *Composites Part A: Applied Science and Manufacturing*, vol. 102, pp. 184–195, 2017.

[128] M. J. Emerson, K. M. Jespersen, A. B. Dahl, K. Conradsen, and L. P. Mikkelsen, "Individual fibre segmentation from 3D X-ray computed tomography for characterising

the fibre orientation in unidirectional composite materials," *Composites Part A: Applied Science and Manufacturing*, vol. 97, pp. 83–92, 2017.

[129] H. Rolland, N. Saintier, P. Wilson, J. Merzeau, and G. Robert, "In situ X-ray tomography investigation on damage mechanisms in short glass fibre reinforced thermoplastics: Effects of fibre orientation and relative humidity," *Composites Part B: Engineering*, vol. 109, pp. 170–186, 2017.

[130] Y. Wan, I. Straumit, J. Takahashi, and S. V. Lomov, "Micro-CT analysis of internal geometry of chopped carbon fiber tapes reinforced thermoplastics," *Composites Part A: Applied Science and Manufacturing*, vol. 91, pp. 211–221, 2016.

[131] Y. Wan, I. Straumit, J. Takahashi, and S. V. Lomov, "Micro-CT analysis of the orientation unevenness in randomly chopped strand composites in relation to the strand length," *Composite Structures*, vol. 206, pp. 865–875, 2018.

[132] N. M. Larson and F. W. Zok, "Insights from in-situ X-ray computed tomography during axial impregnation of unidirectional fiber beds," *Composites Part A: Applied Science and Manufacturing*, vol. 107, pp. 124–134, 2018.

[133] Y. Liu, I. Straumit, D. Vasiukov, S. V. Lomov, and S. Panier, "Prediction of linear and non-linear behavior of 3D woven composite using mesoscopic voxel models reconstructed from X-ray micro-tomography," *Composite Structures*, vol. 179, pp. 568–579, 2017.

[134] N. Isart, J. A. Mayugo, N. Blanco, L. Ripoll, A. Solà, and M. Soler, "Geometric model for 3D through-thickness orthogonal interlock composites," *Composite Structures*, vol. 119, pp. 787–798, 2015.

[135] N. Isart, B. El Said, D. S. Ivanov, S. R. Hallett, J. A. Mayugo, and N. Blanco, "Internal geometric modelling of 3D woven composites: A comparison between different approaches," *Composite Structures*, vol. 132, pp. 1219–1230, 2015.

[136] F. Trochu, "A contouring program based on dual kriging interpolation," *Engineering with Computers*, vol. 9, no. 3, pp. 160–177, 1993.

[137] M. Karahan, S. V. Lomov, A. E. Bogdanovich, D. Mungalov, and I. Verpoest, "Internal geometry evaluation of non-crimp 3D orthogonal woven carbon fabric composite," *Composites Part A: Applied Science and Manufacturing*, vol. 41, no. 9, pp. 1301–1311, 2010.

[138] A. Vanaerschot, B. N. Cox, S. V. Lomov, and D. Vandepitte, "Multi-scale modelling strategy for textile composites based on stochastic reinforcement geometry," *Computer Methods in Applied Mechanics and Engineering*, vol. 310, pp. 906–934, 2016.

[139] X. Yu, H. Wang, and Z. Wang, "Analysis of yarn fiber volume fraction in textile composites using scanning electron microscopy and X-ray micro-computed tomography," *Journal of Reinforced Plastics and Composites*, vol. 38, no. 5, pp. 199–210, 2019.

[140] S. V. Lomov, D. S. Ivanov, I. Verpoest, M. Zako, T. Kurashiki, H. Nakai, and S. Hirosawa, "Meso-FE modelling of textile composites: Road map, data flow and algorithms," *Composites Science and Technology*, vol. 67, no. 9, pp. 1870–1891, 2007.

[141] J. Schindelin, I. Arganda-Carreras, E. Frise, V. Kaynig, M. Longair, T. Pietzsch, S. Preibisch, C. Rueden, S. Saalfeld, B. Schmid *et al.*, "Fiji: an open-source platform for biological-image analysis," *Nature Methods*, vol. 9, no. 7, pp. 676–682, 2012.

[142] R. Rezakhaniha, A. Agianniotis, J. T. C. Schrauwen, A. Griffa, D. Sage, C. V. C. Bouten, F. N. Van De Vosse, M. Unser, and N. Stergiopulos, "Experimental investigation of collagen waviness and orientation in the arterial adventitia using confocal laser scanning microscopy," *Biomechanics and Modeling in Mechanobiology*, vol. 11, no. 3-4, pp. 461–473, 2012.

[143] J. Ollion, J. Cochennec, F. Loll, C. Escudé, and T. Boudier, "TANGO: a generic tool for high-throughput 3D image analysis for studying nuclear organization," *Bioinformatics*, vol. 29, no. 14, pp. 1840–1841, 2013.

[144] R. Xu, C. Bouby, H. Zahrouni, T. Ben Zineb, H. Hu, and M. Potier-Ferry, "A multiscale analysis on the superelasticity behavior of architected shape memory alloy materials," *Materials*, vol. 11, no. 9, p. 1746, 2018.

[145] R. Xu, Y. Hui, H. Hu, Q. Huang, H. Zahrouni, T. B. Zineb, and M. Potier-Ferry, "A Fourier-related FE^2 multiscale model for instability phenomena of long fiber reinforced materials," *Composite Structures*, vol. 211, pp. 530–539, 2019.

[146] J. Yang, R. Xu, H. Hu, Q. Huang, and W. Huang, "Structural-Genome-Driven computing for composite structures," *Composite Structures*, vol. 215, pp. 446–453, 2019.

[147] L. Joubaud, V. Achim, and F. Trochu, "Numerical simulation of resin infusion and reinforcement consolidation under flexible cover," *Polymer composites*, vol. 26, no. 4, pp. 417–427, 2005.

[148] L. Joubaud, F. Trochu, and J. Le Corvec, "Analysis of resin flow under flexible cover in vacuum assisted resin infusion (VARI)," *Journal of advanced materials*, vol. 37, no. 3, pp. 3–10, 2005.

[149] X. Pham, F. Trochu, and R. Gauvin, "Simulation of compression resin transfer molding with displacement control," *Journal of reinforced plastics and composites*, vol. 17, no. 17, pp. 1525–1556, 1998.

[150] X. Pham and F. Trochu, "Simulation of compression resin transfer molding to manufacture thin composite shells," *Polymer composites*, vol. 20, no. 3, pp. 436–459, 1999.

[151] X. Pham and F. Trochu, "Analysis of the consolidation in flexible bladder process for thin composite parts by finite element method," *Journal of reinforced plastics and composites*, vol. 19, no. 3, pp. 182–218, 2000.

[152] L. Fang, J. Jiang, J. Wang, C. Deng, D. Li, and F. Liu, "Effect of layer shift on the out-of-plane permeability of 0/90 noncrimp fabrics," *Journal of Reinforced Plastics and Composites*, vol. 33, no. 22, pp. 2073–2094, 2014.

[153] J. Jiang, Y. Su, L. Zhou, Q. Guo, C. Xu, G. Deng, X. Chen, X. Yao, and L. Fang, "Effect of nesting on the permeability of multilayer unidirectional fabrics," *Applied Composite Materials*, vol. 24, no. 3, pp. 625–642, 2017.

[154] A. Nabovati, E. W. Llewellin, and A. C. M. Sousa, "A general model for the permeability of fibrous porous media based on fluid flow simulations using the lattice Boltzmann method," *Composites Part A: Applied Science and Manufacturing*, vol. 40, no. 6-7, pp. 860–869, 2009.

[155] M. Karaki, A. Hallal, R. Younes, F. Trochu, P. Lafon, A. Hayek, A. Kobeissy, and A. Fayad, "A comparative analytical, numerical and experimental analysis of the microscopic permeability of fiber bundles in composite materials," *International Journal of Composite Materials*, vol. 7, no. 3, pp. 82–102, 2017.

[156] F. Loix, P. Badel, L. Orgéas, C. Geindreau, and P. Boisse, "Woven fabric permeability: From textile deformation to fluid flow mesoscale simulations," *Composites science and Technology*, vol. 68, no. 7-8, pp. 1624–1630, 2008.

[157] B. Verleye, R. Croce, M. Griebel, M. Klitz, S. V. Lomov, G. Morren, H. Sol, I. Verpoest, and D. Roose, "Permeability of textile reinforcements: Simulation, influence of shear and validation," *Composites Science and Technology*, vol. 68, no. 13, pp. 2804–2810, 2008.

[158] X. S. Zeng, A. Endruweit, L. P. Brown, and A. C. Long, "Numerical prediction of in-plane permeability for multilayer woven fabrics with manufacture-induced deformation," *Composites Part A: Applied Science and Manufacturing*, vol. 77, pp. 266–274, 2015.

[159] W. Huang, P. Causse, V. Brailovski, H. Hu, and F. Trochu, "Reconstruction of mesostructural material twin models of engineering textiles based on Micro-CT Aided Geometric Modeling," *Composites Part A: Applied Science and Manufacturing*, vol. 124, p. 105481, 2019.

[160] "VGStudio MAX 3.0. Volume Graphics Inc.; https://www.volumegraphics.com."

[161] Y. Cao, Y. Cai, Z. Zhao, P. Liu, L. Han, and C. Zhang, "Predicting the tensile and compressive failure behavior of angle-ply spread tow woven composites," *Composite Structures*, vol. 234, p. 111701, 2020.

[162] C. Zhang and W. K. Binienda, "A meso-scale finite element model for simulating free-edge effect in carbon/epoxy textile composite," *Mechanics of Materials*, vol. 76, pp. 1–19, 2014.

[163] Z. Yousaf, P. Potluri, and P. J. Withers, "Influence of tow architecture on compaction and nesting in textile preforms," *Applied Composite Materials*, vol. 24, no. 2, pp. 337–350, 2017.

[164] Q. Zeng, L. Sun, J. Ge, W. Wu, J. Liang, and D. Fang, "Damage characterization and numerical simulation of shear experiment of plain woven glass-fiber reinforced composites based on 3D geometric reconstruction," *Composite Structures*, vol. 233, p. 111746, 2020.

[165] D. Durville, "Simulation of the mechanical behaviour of woven fabrics at the scale of fibers," *International Journal of Material Forming*, vol. 3, no. 2, pp. 1241–1251, 2010.

[166] D. Durville, I. Baydoun, H. Moustacas, G. Périé, and Y. Wielhorski, "Determining the initial configuration and characterizing the mechanical properties of 3D angle-interlock fabrics using finite element simulation," *International Journal of Solids and Structures*, vol. 154, pp. 97–103, 2018.

[167] D. Wang, N. Naouar, E. Vidal-Salle, and P. Boisse, "Longitudinal compression and poisson ratio of fiber yarns in meso-scale finite element modeling of composite reinforcements," *Composites Part B: Engineering*, vol. 141, pp. 9–19, 2018.

[168] A. Vanaerschot, F. Panerai, A. Cassell, S. V. Lomov, D. Vandepitte, and N. N. Mansour, "Stochastic characterisation methodology for 3-D textiles based on micro-tomography," *Composite Structures*, vol. 173, pp. 44–52, 2017.

[169] W. Huang, P. Causse, H. Hu, and F. Trochu, "Numerical and experimental investigation of saturated transverse permeability of 2D woven glass fabrics based on material twins," *Polymer Composites*, vol. 41, no. 4, pp. 1341–1355, 2020.

[170] A. S. Dharmalingam, J. Hemmer, A. S. Lectez, C. Binetruy, and S. Comas-Cardona, "Evolution of single carbon and glass fibrous tow cross-sections in dry and lubricated states during compaction perpendicular to the fibers," *Composites Part B: Engineering*, vol. 148, pp. 235–242, 2018.

[171] B. Koohbor, S. Mallon, A. Kidane, and M. A. Sutton, "A DIC-based study of in-plane mechanical response and fracture of orthotropic carbon fiber reinforced composite," *Composites Part B: Engineering*, vol. 66, pp. 388–399, 2014.

[172] M. Mehdikhani, E. Steensels, A. Standaert, K. A. M. Vallons, L. Gorbatikh, and S. V. Lomov, "Multi-scale digital image correlation for detection and quantification of matrix cracks in carbon fiber composite laminates in the absence and presence of voids controlled by the cure cycle," *Composites Part B: Engineering*, vol. 154, pp. 138–147, 2018.

[173] M. Tekieli, S. De Santis, G. de Felice, A. Kwiecień, and F. Roscini, "Application of Digital Image Correlation to composite reinforcements testing," *Composite Structures*, vol. 160, pp. 670–688, 2017.

[174] B. Croom, W. M. Wang, J. Li, and X. Li, "Unveiling 3D deformations in polymer composites by coupled micro x-ray computed tomography and volumetric digital image correlation," *Experimental Mechanics*, vol. 56, no. 6, pp. 999–1016, 2016.

[175] A. Mendoza, J. Schneider, E. Parra, and S. Roux, "The correlation framework: bridging the gap between modeling and analysis for 3D woven composites," *Composite Structures*, vol. 229, p. 111468, 2019.

[176] A. Savitzky and M. J. E. Golay, "Smoothing and differentiation of data by simplified least squares procedures." *Analytical Chemistry*, vol. 36, no. 8, pp. 1627–1639, 1964.

[177] P. Latil, L. Orgéas, C. Geindreau, P. J. J. Dumont, and S. R. Du Roscoat, "Towards the 3D in situ characterisation of deformation micro-mechanisms within a compressed bundle of fibres," *Composites Science and Technology*, vol. 71, no. 4, pp. 480–488, 2011.

[178] H. Ghayoor, S. V. Hoa, and C. C. Marsden, "A micromechanical study of stress concentrations in composites," *Composites Part B: Engineering*, vol. 132, pp. 115–124, 2018.

[179] M. El Hachemi, Y. Koutsawa, H. Nasser, G. Giunta, A. Daouadji, E. M. Daya, and S. Belouettar, "An intuitive computational multi-scale methodology and tool for the dynamic modelling of viscoelastic composites and structures," *Composite Structures*, vol. 144, pp. 131–137, 2016.

[180] Z. Ullah, X. Y. Zhou, L. Kaczmarczyk, E. Archer, A. McIlhagger, and E. Harkin-Jones, "A unified framework for the multi-scale computational homogenisation of 3D-textile composites," *Composites Part B: Engineering*, vol. 167, pp. 582–598, 2019.

[181] W. Wijaya, M. A. Ali, R. Umer, K. A. Khan, P. A. Kelly, and S. Bickerton, "An automatic methodology to CT-scans of 2D woven textile fabrics to structured finite element and voxel meshes," *Composites Part A: Applied Science and Manufacturing*, vol. 125, p. 105561, 2019.

[182] C. H. Jenkins, *Gossamer spacecraft: Membrane and inflatable structures technology for space applications*. American Institute of Aeronautics and Astronautics, 2001.

[183] J. A. Rogers, T. Someya, and Y. Huang, "Materials and mechanics for stretchable electronics," *science*, vol. 327, no. 5973, pp. 1603–1607, 2010.

[184] Y. Zhang, Y. Huang, and J. A. Rogers, "Mechanics of stretchable batteries and supercapacitors," *Current Opinion in Solid State and Materials Science*, vol. 19, no. 3, pp. 190–199, 2015.

[185] Z. Yi, L. G. Bettini, G. Tomasello, P. Kumar, P. Piseri, I. Valitova, P. Milani, F. Soavi, and F. Cicoira, "Flexible conducting polymer transistors with supercapacitor function," *Journal of Polymer Science Part B: Polymer Physics*, vol. 55, no. 1, pp. 96–103, 2017.

[186] X. Huang, Y. Liu, H. Cheng, W. Shin, J. A. Fan, Z. Liu, C. Lu, G. Kong, K. Chen, D. Patnaik, S. Lee, S. Hage-Ali, Y. Huang, and J. A. Rogers, "Materials and designs for wireless epidermal sensors of hydration and strain," *Advanced Functional Materials*, vol. 24, pp. 3846–3854, 2014.

[187] G. A. Holzapfel, R. Eberlein, P. Wriggers, and H. W. Weizsäcker, "Large strain analysis of soft biological membranes: Formulation and finite element analysis," *Computer Methods in Applied Mechanics and Engineering*, vol. 132, pp. 45–61, 1996.

[188] C. Zhang, B. Li, J. Tang, X. Wang, Z. Qin, and X. Feng, "Experimental and theoretical studies on the morphogenesis of bacterial biofilms," *Soft Matter*, vol. 13, pp. 7389–7397, 2017.

[189] Z. Zhao, Z. Liu, J. Du, G. Xu, and X. Feng, "A dynamic biochemomechanical model of geometry-confined cell spreading," *Biophysical Journal*, vol. 112, pp. 2377–2386, 2017.

[190] A. S. Ademiloye, L. W. Zhang, and K. M. Liew, "A multiscale framework for large deformation modeling of RBC membranes," *Computer Methods in Applied Mechanics and Engineering*, vol. 329, pp. 144–167, 2018.

[191] C. Williams, J. Summerscales, and S. Grove, "Resin infusion under flexible tooling (RIFT): A review," *Composites Part A: Applied Science and Manufacturing*, vol. 27, pp. 517–524, 1996.

[192] B. W. Grimsley, P. Hubert, X. Song, R. J. Cano, A. C. Loos, and R. B. Pipes, "Flow and compaction during the vacuum assisted resin transfer molding process," Tech. Rep., 2001.

[193] N. C. Correia, F. Robitaille, A. C. Long, C. D. Rudd, P. Šimáček, and S. G. Advani, "Analysis of the vacuum infusion moulding process: I. Analytical formulation," *Composites Part A: Applied Science and Manufacturing*, vol. 36, pp. 1645–1656, 2005.

[194] P. Causse, E. Ruiz, and F. Trochu, "Influence of preforming on the quality of curved composite parts manufactured by flexible injection," *International Journal of Material Forming*, vol. 6, pp. 341–362, 2013.

[195] A. Agrawal, N. V. Reddy, and P. M. Dixit, "Prediction of wrinkling and determination of minimum blankholding pressure in multistage deep drawing," *Journal of Manufacturing Science and Engineering*, vol. 133, no. 6, p. 061023, 2011.

[196] H. Schoop, L. Taenzer, and J. Hornig, "Wrinkling of nonlinear membranes," *Computational Mechanics*, vol. 29, no. 1, pp. 68–74, 2002.

[197] C. D. Coman and D. M. Haughton, "Localized wrinkling instabilities in radially stretched annular thin films," *Acta Mechanica*, vol. 185, pp. 179–200, 2006.

[198] J. Argyris, L. Tenek, and L. Olofsson, "TRIC: a simple but sophisticated 3-node triangular element based on 6 rigid-body and 12 straining modes for fast computational simulations of arbitrary isotropic and laminated composite shells," *Computer Methods in Applied Mechanics and Engineering*, vol. 145, pp. 11–85, 1997.

[199] F. C. Bardi, S. Kyriakides, and H. D. Yun, "Plastic buckling of circular tubes under axial compression – part II: Analysis," *International Journal of Mechanical Sciences*, vol. 48, pp. 842–854, 2006.

[200] Y. Cao, F. Jia, Y. Zhao, X. Feng, and S. Yu, "Buckling and post-buckling of a stiff film resting on an elastic graded substrate," *International Journal of Solids and Structures*, vol. 49, pp. 1656–1664, 2012.

[201] J. Yang, Q. Huang, H. Hu, G. Giunta, S. Belouettar, and M. Potier-Ferry, "A new family of finite elements for wrinkling analysis of thin films on compliant substrates," *Composite Structures*, vol. 119, pp. 568–577, 2015.

[202] X. Huang, H. Zhao, W. Xie, W. Hong, and X. Feng, "Radial wrinkles on film-substrate system induced by local prestretch: A theoretical analysis," *International Journal of Solids and Structures*, vol. 58, pp. 12–19, 2015.

[203] K. Yu, H. Hu, H. Tang, G. Giunta, M. Potier-Ferry, and S. Belouettar, "A novel two-dimensional finite element to study the instability phenomena of sandwich plates," *Computer Methods in Applied Mechanics and Engineering*, vol. 283, pp. 1117–1137, 2015.

[204] N. Naderi Beni and M. Botshekanan Dehkordi, "An extension of Carrera unified formulation in polar coordinate for analysis of circular sandwich plate with FGM core using GDQ method," *Composite Structures*, vol. 185, pp. 421–434, 2018.

[205] F. A. Fazzolari and E. Carrera, "Advanced variable kinematics Ritz and Galerkin formulations for accurate buckling and vibration analysis of anisotropic laminated composite plates," *Composite Structures*, vol. 94, pp. 50–67, 2011.

[206] J. N. Reddy and J. Berry, "Nonlinear theories of axisymmetric bending of functionally graded circular plates with modified couple stress," *Composite Structures*, vol. 94, pp. 3664–3668, 2012.

[207] L. Ke, J. Yang, S. Kitipornchai, and M. A. Bradford, "Bending, buckling and vibration of size-dependent functionally graded annular microplates," *Composite Structures*, vol. 94, pp. 3250–3257, 2012.

[208] L. W. Zhang, K. M. Liew, and J. N. Reddy, "Postbuckling behavior of bi-axially compressed arbitrarily straight-sided quadrilateral functionally graded material plates," *Computer Methods in Applied Mechanics and Engineering*, vol. 300, pp. 593–610, 2016.

[209] O. C. Zienkiewicz, *The finite element method.* McGraw-Hill, 1977.

[210] H. Hu, N. Damil, and M. Potier-Ferry, "A bridging technique to analyze the influence of boundary conditions on instability patterns," *Journal of Computational Physics*, vol. 230, pp. 3753–3764, 2011.

[211] J. N. Reddy, *An introduction to nonlinear finite element analysis.* UK: Oxford, 2004.

[212] J. Choe, Q. Huang, J. Yang, and H. Hu, "An efficient approach to investigate the post-buckling behaviors of sandwich structures," *Composite Structures*, vol. 201, pp. 377–388, 2018.

[213] B. Cochelin, N. Damil, and M. Potier-Ferry, *Méthode asymptotique numérique.* Hermes Lavoissier, 2007.

[214] R. Vermorel, N. Vandenberghe, and E. Villermaux, "Impacts on thin elastic sheets," *Proceedings of the Royal Society A: Mathematical, Physical and Engineering Sciences*, vol. 465, pp. 823–842, 2009.

[215] N. A. Alfutov, *Stability of elastic structures.* Springer Science & Business Media, 2013.

[216] M. Mehri, H. Asadi, and Q. Wang, "Buckling and vibration analysis of a pressurized CNT reinforced functionally graded truncated conical shell under an axial compression using HDQ method," *Computer Methods in Applied Mechanics and Engineering*, vol. 303, pp. 75–100, 2016.

[217] H. Shen, "Thermal buckling and postbuckling behavior of functionally graded carbon nanotube-reinforced composite cylindrical shells," *Composites Part B: Engineering*, vol. 43, pp. 1030–1038, 2012.

[218] K. M. Liew, Z. X. Lei, J. L. Yu, and L. W. Zhang, "Postbuckling of carbon nanotube-reinforced functionally graded cylindrical panels under axial compression using a meshless approach," *Computer Methods in Applied Mechanics and Engineering*, vol. 268, pp. 1–17, 2014.

[219] W. Huang, Q. Huang, Y. Liu, J. Yang, H. Hu, F. Trochu, and P. Causse, "A Fourier based reduced model for wrinkling analysis of circular membranes," *Computer Methods in Applied Mechanics and Engineering*, vol. 345, pp. 1114–1137, 2019.

[220] Y. Li, S. Zhang, X. Li, V. R. N. Unnava, and F. Cicoira, "Highly stretchable PEDOT:PSS organic electrochemical transistors achieved via polyethylene glycol addition," *Flexible and Printed Electronics*, vol. 4, no. 4, p. 044004, 2019.

[221] G. Xu, C. Cheng, Z. Liu, W. Yuan, X. Wu, Y. Lu, S. S. Low, J. Liu, L. Zhu, D. Ji *et al.*, "Battery-free and wireless epidermal electrochemical system with all-printed stretchable electrode array for multiplexed in situ sweat analysis," *Advanced Materials Technologies*, vol. 4, no. 7, p. 1800658, 2019.

[222] W. Huang, P. Causse, H. Hu, S. Belouettar, and F. Trochu, "Transverse compaction of 2D glass woven fabrics based on material twins – Part I : Geometric analysis," *Composite Structures*, vol. 237, p. 111929, 2020.

[223] W. Huang, P. Causse, H. Hu, S. Belouettar, and F. Trochu, "Transverse compaction of 2D glass woven fabrics based on material twins – Part II: Tow and fabric deformations," *Composite Structures*, vol. 237, p. 111963, 2020.

[224] X. Wang, J. Ma, S. Law, and Q. Yang, "Numerical analysis of wrinkle-influencing factors of thin membranes," *International Journal of Solids and Structures*, vol. 97, pp. 458–474, 2016.

[225] Q. Huang, J. Yang, W. Huang, G. Giunta, S. Belouettar, and H. Hu, "The boundary effects on stretch-induced membrane wrinkling," *Thin-Walled Structures*, vol. 154, p. 106838, 2020.

[226] K. Attipou, H. Hu, F. Mohri, M. Potier-Ferry, and S. Belouettar, "Thermal wrinkling of thin membranes using a Fourier-related double scale approach," *Thin-Walled Structures*, vol. 94, pp. 532–544, 2015.